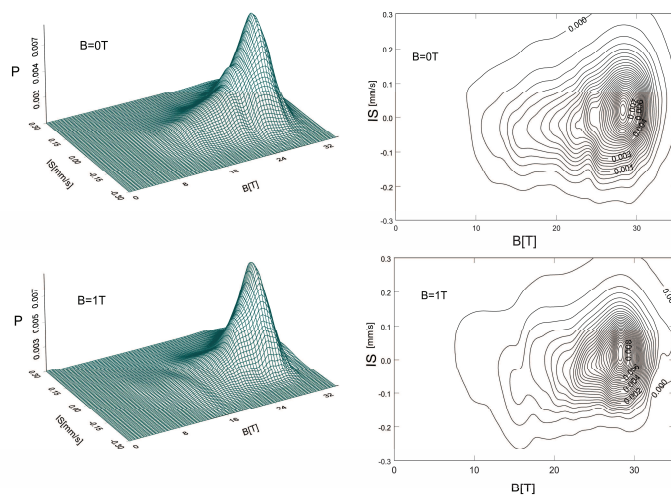


AUTOREFERAT DO ROZPRAWY HABILITACYJNEJ

Dr Dariusz Maciej Satuła

Uniwersytet w Białymstoku
Wydział Fizyki



Białystok 2012

Dane personalne

Dariusz Maciej Satuła

ur. 9 maja 1965r w Olsztynie
zam. 15-818 Białystok, ul. Jesionowa 2/4
E-mail: satula@alpha.uwb.edu.pl
Tel. 85 7457242

Miejsce stałego zatrudnienia i stanowisko

Uniwersytet w Białymstoku, Wydział Fizyki, 15-424 Białystok, ul. Lipowa 41

Stanowisko: adiunkt

Wysztalcenie i stopnie naukowe

Doktorat 1998 – Uniwersytet Warszawski, Wydział Fizyki,
Warszawa, ul. Hoża 69
Rozprawa doktorska: „**Problem selektywności obsadzeń, rozkładów momentów magnetycznych i pól nadsubtelnych na żelazie w stopach Fe-Cr-Z (Z=Si,Al)**”.
Promotor prof. dr hab. Ludwik Dobrzyński

Magisterskie 1989 – Uniwersytet Warszawski Filia w Białymstoku, Wydział Matematyczno-Przyrodniczy, 15-424 Białystok, ul. Lipowa 41
Praca magisterska: „**Badania oddziaływań nadsubtelnych w stopach amorficznych $\text{Co}_x\text{Ni}_{70-x}\text{Fe}_5\text{Si}_{15}\text{B}_{10}$ techniką efektu Mössbauera**”.
Promotor prof. dr hab. Ludwik Dobrzyński

D. Satuła

Historia zatrudnienia

- 1999 - do dziś adiunkt, Uniwersytet w Białymstoku, Wydział Fizyki
1990 - 1999 asystent, Uniwersytet w Białymstoku, Wydział Fizyki
1989 - 1990 stanowisko techniczne, Uniwersytet w Białymstoku, Wydział Fizyki

Staże i praca naukowa za granicą oraz współpraca międzynarodowa

- 2005 - 2009 - współpraca z Politechniką Darmstadt, Niemcy
2004 - współpraca z Freie Universitate Berlin – badania cząstek magnetytu
2001 - 2004 - liczne wyjazdy związane z badaniami synchrotronowymi w DESY, Hamburg,
 Niemcy
1999 - pięciomiesięczne stypendium na Uppsala University, Szwecja

Wyróżnienia w pracy naukowej i działalności organizacyjnej

- Nagroda Rektora Uniwersytetu w Białymstoku za pracę naukową
Białystok 2010
Nagroda Rektora Uniwersytetu w Białymstoku za pracę naukową
Białystok 2009
Nagroda Rektora Uniwersytetu w Białymstoku za pracę naukową
Białystok 2008
Nagroda Rektora Uniwersytetu w Białymstoku za działalność organizacyjną
Białystok 2007
Nagroda Rektora Uniwersytetu w Białymstoku za pracę naukową
Białystok 2005
Nagroda Rektora Uniwersytetu w Białymstoku za pracę naukową
Białystok 2003
Nagroda Rektora Uniwersytetu w Białymstoku za pracę naukową
Białystok 2000

D. Sztuka

Realizowane granty krajowe i zagraniczne:

- 1) główny wykonawca grantu MNiSW (N N202 172335) pt. „**Metoda niezmienników w spektroskopii mössbauerowskiej i zastosowanie do mikroskopowych badań wybranych układów magnetycznych**”, 2008-2011,
- 2) wykonawca projektu I-20060174 EC, DESY, Hamburg, pt. “**EXAFS investigation of Cr_{3-x}Co_xSi alloys**”,
- 3) wykonawca projektu badawczego I-01-042 09.05.2001-31.12.2002, DESY, Hamburg, pt. “**Investigation of directions of the hyperfine fields in Er-Fe-B**”,
- 4) główny wykonawca grantu KBN 2P03B 115 16, 1.03.1999-1.03.2001, pt. „**Badanie własności magnetycznych układów nieuporządkowanych technikami spolaryzowanego źródła mössbauerowskiego, magnetometrii, transportu i rozpraszania komptonowskiego**”,
- 5) wykonawca projektu klasy AB (II-03-003) DESY, Hamburg, pt. “**Circularly Polarized Beam for Nuclear Resonant Scattering**” (IHP-Contract HPRI-CT-1999-00040/2001-00140),
- 6) wykonawca grantu 2P03B03610, 01.01.1996-30.06.1998, pt. „**Badanie struktury elektronowej i własności magnetycznych niektórych stopów d-elektronowych**”.

Dorobek naukowy

Jestem współautorem **69** oryginalnych prac naukowych w recenzowanych czasopismach o międzynarodowej renomie (wykaz w załączniku 1). Do najważniejszych czasopism należą:

Physical Review B	- 2 prace
Journal of Physics C	- 5 prac
Journal of the Physical Society of Japan	- 2 prace
Journal of Alloys and Compounds	- 3 prace
Superconductor Science and Technology	- 1 praca
Journal of Applied Physics	- 1 praca
International Journal of Modern Physics B	- 1 praca
Acta Physica Polonica A	- 10 prac

D. Sztuka

Journal of Magnetism and Magnetic Materials	- 13 prac
Hyperfine Interaction	- 10 prac
Nuclear Instruments and Methods in Physics Research B	- 3 prace
Nukleonica	- 5 prac
Journal Applied Physics	- 1 praca
Physica B	- 3 prace

Według **Web of Science** prace te były cytowane 263 razy

Indeks **H** - 9.0

Oprócz regularnych publikacji, uzyskane wyniki naukowe przedstawione były przeze mnie w postaci 9 plakatów na międzynarodowych konferencjach naukowych i opublikowane zostały w wydaniach konferencyjnych.

Spośród prac naukowych 54 opublikowane zostały w latach 1999-2011 tj. po obronie pracy doktorskiej. W tym okresie przedstawiłem 4 wykłady na międzynarodowych i krajowych konferencjach.

D. Sztuka

Przebieg pracy naukowej

- przed doktorem

Pracę naukową rozpocząłem będąc na piątym roku studiów fizyki, na stanowisku technicznym, w Filii Uniwersytetu Warszawskiego w Białymstoku (obecnie Uniwersytet w Białymstoku) w Pracowni Metod Jądrowych Fizyki Ciała Stałego - pod kierownictwem prof. Ludwika Dobrzyńskiego. W tym okresie zajmowałem się poszerzeniem bazy badawczej pracowni. Pracowałem nad uruchomieniem i przetestowaniem układów chłodzących stosowanych w spektroskopii mössbauerowskiej i zapewnieniem stabilizacji temperatury w tych układach. Jednocześnie prowadziłem badania stopów amorficznych $\text{Co}_{70-x}\text{Ni}_x\text{Fe}_5\text{Si}_{15}\text{B}_{10}$ techniką spektroskopii mössbauerowskiej, będących przedmiotem mojej pracy magisterskiej, zatytułowanej „**Badania oddziaływań nadsubtelnych w stopach amorficznych $\text{Co}_x\text{Ni}_{70-x}\text{Fe}_5\text{Si}_{15}\text{B}_{10}$ techniką efektu Mössbauera**”. Promotorem pracy magisterskiej był prof. Ludwik Dobrzyński. Pracę obroniłem w roku 1989, a uzyskane wyniki zostały opublikowane w regularnym czasopiśmie o zasięgu międzynarodowym [1].

Od 01.10.1990 roku zostałem zatrudniony na stanowisku asystenta Filii Uniwersytetu Warszawskiego w Białymstoku, w Pracowni Metod Jądrowych Fizyki Ciała Stałego. Moja praca naukowa związana była bezpośrednio z badaniami oddziaływań nadsubtelnych techniką efektu Mössbauera. Podstawowym obszarem mojej działalności były badania stopów $\text{Fe}_{3-x}\text{Cr}_x\text{Si}$ i $\text{Fe}_{3-x}\text{Cr}_x\text{Al}$, które ze względu na swoją strukturę krystaliczną jak i własność selektywnego podstawiania atomów domieszki, stanowią atrakcyjny obiekt badań fizyki magnetyzmu pasmowego. Najważniejsze cechy badanych stopów to możliwość lokowania się atomów żelaza w nierównoważne podsieci struktury krystalicznej i związane z tym różnice w najbliższym otoczeniu żelaza, wpływające w istotny sposób na lokalne momenty magnetyczne i pola nadsubtelne. Podstawowymi technikami badawczymi jakie zostały zastosowane były: dyfrakcja neutronów, dyfrakcja promieniowania X , spektroskopia mössbauerowska i pomiary magnetyczne. Wyniki badań opublikowane zostały w 6 artykułach wydanych w czasopismach o zasięgu międzynarodowym [2, 3, 4, 6, 7, 12]. Powyższe prace stały się podstawą mojej rozprawy doktorskiej zatytułowanej „**Problem selektywności obsadzeń, rozkładu momentów magnetycznych i pól nadsubtelnych na żelazie w stopach Fe-Cr-Z (Z = Si, Al)**”, którą obroniłem na Wydziale Fizyki Uniwersytetu Warszawskiego 21.12.1998 r. Promotorem pracy doktorskiej był prof. Ludwik Dobrzyński. W swojej rozprawie wykazałem, że istnieje zasadnicza różnica zachowania się domieszki Cr w izostrukuralnych stopach $\text{Fe}_{3-x}\text{Cr}_x\text{Si}$ i $\text{Fe}_{3-x}\text{Cr}_x\text{Al}$. W $\text{Fe}_{3-x}\text{Cr}_x\text{Si}$ brak jest preferencji obsadzeń atomów Cr w odpowiednie węzły struktury krystalicznej i jednocześnie obserwowany jest ujemny moment magnetyczny na atomach Cr. W stopach $\text{Fe}_{3-x}\text{Cr}_x\text{Al}$ atomy Cr lokują się preferencyjnie w pozycje B i w granicach niepewności pomiarowej nie niosą momentu magnetycznego. Można zatem wnioskować, że struktury elektronowe obu badanych stopów nie są tak bardzo podobne, jak donosi literatura, a wpływ atomów metaloidu na własności magnetyczne i strukturalne jest bardzo istotny.

D. Sutała

W tym czasie nie ograniczałem się jedynie do badań bezpośrednio związanych z pracą doktorską. W pracowni, z moim udziałem, prowadzone były ponadto badania materiałów otrzymywanych metodą mechanicznego stapiania Fe-N, magnetycznych własności stopów UFe_xAl_{12-x} , Pd_2TiAl domieszkowanego izotopem ^{57}Fe i innych. Efektem było opublikowanie 8 artykułów w czasopismach o zasięgu międzynarodowym, których byłem współautorem [5, 8, 9, 10, 11, 13, 14, 16]. W tym okresie, uczestniczyłem również w dwóch stażach naukowych w Uppsala University (Szwecja). Pobyt ten zaowocował współpracą międzynarodową pomiędzy oboma ośrodkami. Rezultatem wspólnych prac badawczych było opublikowanie 3 artykułów w wydawnictwach o zasięgu międzynarodowym [27, 28, 30]. Bardzo ważnym osiągnięciem w tym czasie było opracowanie metody analizy danych mössbauerowskich uzyskanych z użyciem monochromatycznej wiązki spolaryzowanej kołowo [16]. Zastosowanie promieniowania spolaryzowanego kołowo w przypadku badań stopów UFe_xAl_{12-x} pozwoliło na stwierdzenie, że tylko około $\frac{1}{4}$ z momentu magnetycznego atomów Fe wnosi wkład do namagnesowania [18]. Badania mössbauerowskie i dyfrakcji neutronów pozwoliły stwierdzić, iż składowa ferromagnetyczna atomów Fe wynosi $0.3\mu_B$. Z punktu widzenia rozwoju technicznego Pracowni bardzo ważnym elementem było skonstruowanie i uruchomienie młyna do tzw. stapiania mechanicznego. Konstrukcja młyna pozwalała na przeprowadzanie procesu mechanicznego stapiania z zastosowaniem różnych atmosfer gazowych [5].

- po doktoracie

Od 01.09.1999 roku zostałem zatrudniony na stanowisku adiunkta Uniwersytetu w Białymstoku w Zakładzie Fizyki Ciała Stałego. Głównym celem mojej działalności naukowej stały się badania własności układów nieuporządkowanych magnetycznie, materiałów z istnieniem konkurencyjnych oddziaływań wymiennych oraz materiałów niskowymiarowych. Jednym z powodów zainteresowania się tego typu materiałami było skonstruowanie w naszej Pracowni unikatowego w skali światowej układu do pomiarów mössbauerowskich z wykorzystaniem promieniowania spolaryzowanego kołowo. Metoda ta, w odróżnieniu od klasycznej spektroskopii mössbauerowskiej, pozwala na obserwację zwrotu pola nadsubtelnego. Pierwsze prace polegały na rozwinięciu metodologii opracowania wyników pomiarowych otrzymanych metodą polarymetrii mössbauerowskiej w szczególności w przypadkach próbek, w których występują szerokie rozkłady pól nadsubtelnych. Jak się okazało, bardzo efektywną metodą opracowania danych mössbauerowskich jest jednoczesne opracowywanie wyników otrzymanych z użyciem promieniowania niespolaryzowanego jak i spolaryzowanego. Takie postępowanie powoduje, że otrzymywane rekonstrukcje rozkładów pól nadsubtelnych są bardziej wiarygodne. Efektem prac badawczych w tym zakresie jest 14 artykułów wydanych w recenzowanych czasopismach o zasięgu międzynarodowym, których jestem współautorem [16, 17, 22, 23, 24, 27, 28, 31, 32, 34, 40, 42, 45, 52]. Równoległe rozwinięta została polarymetria *CEMS* bardzo ważna z punktu widzenia badań magnetyzmu cienkich warstw [47, 52]. Kolejnym elementem związanym z polarymetrią mössbauerowską było opracowanie metody otrzymywania synchrotronowej wiązki spolaryzowanej kołowo. Określono parametry wiązki synchrotronowej, dla której pomiary takie byłyby efektywne [38]. Naturalnym rozszerzeniem bazy eksperymentalnej naszej pracowni było skonstruowanie układu do otrzymywania wiązki spolaryzowanej liniowo. W pracy [65] prezentowany jest zrealizowany przeze mnie układ do otrzymywania monochromatycznej wiązki spolaryzowanej liniowo. Opracowana została także metoda analizy tak mierzonych widm mössbauerowskich oraz przedstawiono wyniki pierwszych pomiarów.

D. Sukieta

Aktualnie jedną z moich tematów badawczych jest problematyka związana z badaniem stopów typu inwar. Sam problem ma już bardzo długą historię, lecz do tej pory ściśle wytłumaczenie braku rozszerzalności objętościowej stopów inwarowych, obserwowanych w szerokim zakresie temperatur, jest nieznane. Jedną z hipotez wiąże to zjawisko z istnieniem atomów żelaza w dwóch konfiguracjach elektronowych tzw. konfiguracji wysoko i nisko spinowej. Ze względu na mikroskopowy charakter zjawiska i przewidywanych teoretycznie różnych kątowych rozkładów momentów magnetycznych w obu konfiguracjach żelaza polarymetria mössbauerowska jest techniką idealną do badania takich własności. W moich pracach [31, 34] wykazałem, że rozkłady kątowe magnetycznych pól nadsubtelnych na Fe w stopach inwarowych Fe-Ni są niezależne od wartości pola nadsubtelnego. Analizę przeprowadziłem dwiema metodami. Jedną polegała na dopasowaniu widm zakładając rozkład pola nadsubtelnego jako superpozycję trzech rozkładów gaussowskich o różnych parametrach nadsubtelnych (B, IS, σ_B) gdzie B - magnetyczne pole nadsubtelne, IS - przesunięcie izomeryczne, σ_B - odchylenie standardowe rozkładu B . Analizowane były widma uzyskane z pomiarów z użyciem monochromatycznej wiązki spolaryzowanej kołowo jak i wiązki niespolaryzowanej. Drugie podejście zrealizowane zostało z wykorzystaniem metody maksymalnej entropii, która nie wymaga formułowania założeń co do kształtu rozkładu pola nadsubtelnego jak i założenia korelacji pomiędzy polami nadsubtelnym, a pozwala na rekonstrukcję rozkładów $P(B, IS, z)$ gdzie, z - parametr tekstury magnetycznej. Oba podejścia nie pokazały różnych rozkładów kątowych magnetycznych pól nadsubtelnych na atomach żelaza w stopach inwarowych Fe-Ni.

Kolejnym polem moich ostatnich zainteresowań naukowych jest badanie układów o rozmiarach nanometrów. Związane jest to ze współpracą z ośrodkiem Freie Universität Berlin i Instytutem Chemii Uniwersytetu w Białymstoku. Mnogość i różnorodność nowych zjawisk występujących w układach nanometrycznych, w szczególności wpływ powierzchni na własności magnetyczne substancji jest bardzo interesującą tematyką. Dotychczasowa współpraca zaowocowała czterema publikacjami w wydawnictwach o zasięgu międzynarodowym [36, 44, 49, 64]. Cennym wynikiem jest zbadanie wpływu środowiska, w którym zachodzi strącanie nanocząstek na rozkłady ich wielkości. Okazało się np. iż strącanie nanocząstek magnetytu w środowisku wodnym prowadzi do otrzymywania nanocząstek o większych rozmiarach w porównaniu do wielkości otrzymanych w procedurze przeprowadzonej w środowisku alkoholowym. Istotnym wynikiem jest również obserwowany w pracy [49] bardzo duży wpływ mikrostruktury nanocząstek na ich własności magnetyczne. Zmiana mikrostruktury powoduje zmianę własności magnetycznych samych nanocząstek jak i oddziaływań kolektywnych pomiędzy zbiorem nanocząstek.

Opis otrzymywanych wyników doświadczalnych układów magnetycznie nieuporządkowanych nie posiadających tekstury krystalicznej wymagał nowego podejścia do analizy wyników. W pracach [50, 54, 61] przedstawiona została metoda tzw. „niezmienników” bardzo istotna w przypadkach gdy w badanych materiałach mamy do czynienia z jednocześnie występującymi oddziaływaniami dipolowymi magnetycznymi i kwadrupolowymi elektrycznymi, uznawanymi za najtrudniejsze do interpretacji. Problem niejednoznaczności rozwiązań pojawia się wówczas wskutek braku kompletnej informacji o układzie. Metoda niezmienników polega na konstrukcji odpowiedniej bazy funkcji, której zastosowanie umożliwia jednoznaczny opis widm mössbauerowskich. Dzięki tej metodzie udało się zaobserwować różne zachowanie się lokalnych momentów magnetycznych związanych z czterema różnymi lokalnymi pozycjami atomów Fe w stopie UFe_5Sn . Okazało się, że obserwowane dla tego związku dwa przejścia magnetyczne w pomiarach

D. Satała

namagnesowania w funkcji temperatury związane są z pojawieniem się uporządkowania ferromagnetycznego momentów magnetycznych na atomach Fe, oraz z reorientacją momentu magnetycznego jednej z pozycji krystalograficznej atomów Fe względem osi głównych tensora gradientu pola elektrycznego.

W przypadkach analizy układów charakteryzujących się istnieniem rozkładów pól nadsubtelnych, w dostępnej literaturze istnieje wiele metod matematycznych rekonstrukcji rozkładów pól nadsubtelnych. W znakomitej większości dotyczą one jednowymiarowych rozkładów magnetycznych pól nadsubtelnych $P(B)$. Zwykle metody te opierają się na analizie rozkładu χ^2 . Oryginalną metodą opartą na analizie bayesowskiej, która jest bardzo użyteczna do opisu danych doświadczalnych jest tzw. *METODA MAKSYMALNEJ ENTROPII (MEM)*. W literaturze dotyczącej spektroskopii mössbauerowskiej metodę *MEM* stosowano bardzo rzadko i jedynie do otrzymywania rozkładów jednowymiarowych $P(B)$. W pracach [37, 43, 58, 60, 62] rozwinęliśmy i przetestowaliśmy tę metodę do rekonstrukcji dwuwymiarowych rozkładów pól nadsubtelnych $P(B, IS)$ i $P(B, QS)$, a następnie trójwymiarowych rozkładów $P(B, IS, QS)$, gdzie QS jest rozszczepieniem kwadrupolowym. Kolejnym rozwinięciem metody *MEM*, użytecznym w układach magnetycznie nieuporządkowanych, jest możliwość rekonstrukcji rozkładów $P(B, IS, z)$ (z parametr tekstury magnetycznej). Dzięki temu podejściu pokazałem brak istnienia różnych rozkładów kątowych magnetycznych pól nadsubtelnych w stopach inwarowych Fe-Ni bez odwoływania się do założeń dotyczących rozkładów pól nadsubtelnych.

Bardzo często w przypadku analizy pomiarów mössbauerowskich stosowane jest przybliżenie cienkiego absorbenta. W tym przybliżeniu ze względu na nieliniowy wpływ parametru grubości, względne natężenia linii jak i względne natężenia widm składowych są zaburzone. W pracy [60] opisaliśmy nową metodę otrzymywania przekroju czynnego i zastosowaliśmy ją do analizy widm stopu inwarowego Fe-Ni. Nowością jest tu zastosowanie *MEM* do dekonwolucji widma ze względu na zdolność rozdzielczą spektrometru i następnie zastosowanie opracowanego algorytmu do otrzymywania przekroju czynnego na absorpcję.

Rozwinięte przeze mnie nowe metody analizy danych mössbauerowskich, metoda niezmienników, metoda maksymalnej entropii i metoda otrzymywania przekroju czynnego, stanowią element metodologiczny, który razem z polarymetrią mössbauerowską stanowią nowy wkład do rozwoju spektroskopii mössbauerowskiej. Metody te okazały się niezbędne w możliwie ścisłej analizie stopów magnetycznie nieuporządkowanych i zaowocowały serią prac będących podstawą prezentowanej rozprawy habilitacyjnej.

Wybrane publikacje razem z przewodnikiem pod tytułem „**Spektroskopia mössbauerowska układów magnetycznie nieuporządkowanych – polarymetria mössbauerowska oraz nowe metody analizy danych**” stanowią materiał rozprawy habilitacyjnej.

D. Sutiła

*Spektroskopia mössbauerowska układów magnetycznie
nieuporządkowanych – polarymetria mössbauerowska oraz
nowe metody analizy danych*

Dr Dariusz Maciej Satuła
Wydział Fizyki
Uniwersytet w Białymstoku

Przewodnik do rozprawy habilitacyjnej
Białystok 2012

Spis treści

1. Wstęp.....	15
1.1. Zasadnicze elementy rozprawy habilitacyjnej.....	15
2. Polarymetria mössbauerowska.....	20
2.1. Polarymetria z użyciem promieniowania spolaryzowanego liniowo.....	24
3. Nowe metody analizy danych doświadczalnych.....	29
3.1. Metoda maksymalnej entropii w spektroskopii mössbauerowskiej.....	29
3.2. Metoda niezmienników.....	35
3.3. Metoda otrzymywania przekroju czynnego.....	39
4. Zastosowanie polarymetrii mössbauerowskiej oraz nowych metod analizy danych.....	44
4.1. Materiały lite.....	44
4.1.1. Układ Cr-Fe-Mn	
4.1.2. Stop Fe-Ni	
4.1.3. Związek międzymetaliczny UFe ₅ Sn	
4.2. Materiały nanometrowe.....	52
4.2.1. Stop Fe-Al	
4.2.2. Nanocząstki magnetytu	
5. Podsumowanie.....	59
6. Literatura.....	61

**Lista publikacji obejmująca jednotematyczny cykl prac autora
przedkładającego rozprawę habilitacyjną**

- P1.** D. Satuła, K. Szymański, J. Waliszewski, L. Dobrzyński and B. Prus, „Mössbauer and X-ray diffraction study of Cr-Fe-Mn alloys”, *Mol. Phys. Rep.* **30** (2000) 151-8.
- P2.** K. Szymański, D. Satuła, L. Dobrzyński, K. Perzyńska M. Biernacka, P. Zaleski, “Spin alignment and related properties of bcc Cr-Fe-Mn system”, *JMMM* **263** (2001) 56-70. Impact Factor 1.329
- P3.** K. Szymański, D. Satuła, L. Dobrzyński M. Biernacka K. Perzyńska and P. Zaleski, “Iron atoms in Cr-Mn antiferromagnetic matrix”, *Hyp. Int.* **141/142** (2002) 231-5. Impact Factor 0.533
- P4.** D. Satuła, K. Szymański, L. Dobrzyński, K. Rećko, J. Waliszewski, "Mössbauer study of the $Fe_{1-x}Ni_x$ invar alloys by monochromatic circularly polarized source", *Nukleonika* **40** (2003) S71-74. Impact Factor 0.231
- P5.** K. Szymański, D. Satuła and L. Dobrzyński, “Angular Distribution of Hyperfine Magnetic Field in Fe_3O_4 and $Fe_{66}Ni_{34}$ from Mössbauer Polarimetry”, *Hyp. Int.* **156/157** (2004) 21-24. Impact Factor 0.358
- P6.** L. Dobrzyński, K. Szymański, D. Satuła, “The Maximum entropy method in the analysis of the Mössbauer spectra”, *Nukleonika* **49** (2004) S89-S93. Impact Factor 0.167
- P7.** K. Szymański, D. Satuła, L. Dobrzyński and B. Kalska, “Nuclear Resonance Scattering of circularly polarized SR”, *Acta Physica Polonica B* **35** (2004) 2313-2325. Impact Factor 0.495
- P8.** K. Szymański, D. Satuła, L. Dobrzyński, E. Voronina and E. P. Yelsukov, “Hyperfine fields in nanocrystalline $Fe_{0.48}Al_{0.52}$ ”, *Hyperfine Interactions* **159** (2005) 75-80. Impact Factor 0.254
- P9.** K. Szymański, D. Satuła, L. Dobrzyński, E. Voronina, E. P. Yelsukov and T. Miyanaga "Arrangements of magnetic moments in nanocrystalline $Fe_{48}Al_{52}$ " *Phys. Rev. B* **72** (2005) 104409-1-12. Impact Factor 3.185
- P10.** K. Szymański, L. Dobrzyński and D. Satuła E. Voronina and E. P. Yelsukov, “Magnetization distribution in nanocrystalline $Fe_{0.48}Al_{0.52}$ ”, *Materials Science-Poland* **24**, (2006), 753-759. Impact Factor 0.333
- P11.** L. Dobrzyński, A. Holas, D. Satuła and K. Szymański “Interpretation of the Mössbauer Spectroscopy Data by the Maximum Entropy Method”, *Book Series: AIP CONFERENCE PROCEEDINGS* 872 (2006). Twenty sixth International Workshop on Bayesian Inference and Maximum Entropy Methods in Science and Engineering CNRS, Paris, France, July 8-13, 2006.

- P12.** D. Satuła, K. Szymański, V. H. Tran, L. Dobrzyński, “Hyperfine Fields in UFe_5Sn Compound”, *Nukleonika* **52** (2007) 63-65. Impact Factor 0.18
- P13.** D. Satuła, B. Kalska-Szostko, K. Szymański, L. Dobrzyński, J. Kozubowski, “Microstructure and Magnetic Properties of Iron Oxide Nanoparticles Prepared by Wet Chemical Method”, *Acta Physica Polonica A* **114**, (2008) 1615-1621. Impact Factor 0.321
- P14.** D. Satuła, K. Szymański, L. Dobrzyński, V.H. Tran, R. Troć, “Mössbauer data analysis based on invariants and application to UFe_5Sn ”, *Physical Review B* **78**, (2008) 0.14411 Impact Factor 3.322
- P15.** K. Szymański, D. Satuła, L. Dobrzyński, “The method of invariants applied to the analysis of ^{57}Fe Mössbauer spectra”, *Hyp. Int.* **192** (2009) 77-83.
- P16.** D. Satuła, K. Szymański, L. Dobrzyński, “Determination of the Mössbauer absorption cross section and reconstruction of the hyperfine field distribution by the maximum entropy method”, *J.Phys.:Condens Matter* **22** (2010) 296005 Impact Factor 1.964
- P17.** K. Szymański, D. Satuła, L. Dobrzyński, K. Rećko, W. Olszewski, K. Brzózka, J. Jankowska-Kisielińska, “The method of invariants in ^{57}Fe Mössbauer spectroscopy on selected examples”, *J.Phys.: Conference Series* **217** (2010) 012010
- P18.** D. Satuła, K. Szymański, L. Dobrzyński, “Maximum entropy method in Mössbauer spectroscopy – arrangements of the iron magnetic moments”, *Acta Physica Polonica A* **119** (2011) 78 Impact Factor 0.433
- P19.** D. Satuła, K. Szymański, L. Dobrzyński, „A single line linearly polarised source for Mössbauer spectroscopy”, *Nuclear Instruments and Methods in Physics Research B* **269** (2011) 2504-2508 Impact Factor 1.042

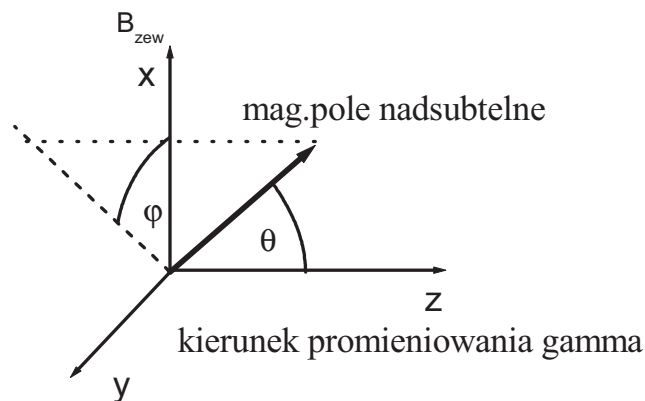
1. Wstęp

Minęło już ponad pół wieku od odkrycia przez R. Mössbauera (1958 r.) bezdrutowej emisji i absorpcji promieniowania gamma i opartej na tym efekcie metody badawczej zwanej spektroskopią mössbauerowską. Przeżyła już ona okres swojego największego rozkwitu. Minęły czasy, gdy wiele renomowanych czasopism poświęconych fizyce zawierało artykuły, w których spektroskopia mössbauerowska była podstawową metodą badawczą. Spektroskopia mössbauerowska w chwili obecnej stała się instrumentem, który liczne laboratoria światowe wykorzystują jako jedną z wielu technik pozwalających na pełną charakteryzację badanego materiału. Jak każda, spektroskopia mössbauerowska posiada swoje ograniczenia, wśród których jednym z najważniejszych jest występujący problem niejednoznaczności interpretacyjnych mierzonych widm. Wymusza to tworzenie zarówno nowych technik badawczych jak i nowych metod analizy danych doświadczalnych.

1.1 Zasadnicze elementy rozprawy habilitacyjnej

Bardzo istotnym ograniczeniem klasycznej spektroskopii mössbauerowskiej, w której używane jest promieniowanie niespolaryzowane jest problem wyznaczania zwrotu lokalnych magnetycznych pól nadsubtelnych oraz opis istniejących w badanym materiale rozkładów tych pól, zwanych teksturą magnetyczną. Klasyczna spektroskopia mössbauerowska pozwala na wyznaczenie jedynie średniej wartości $\langle \cos^2 \theta \rangle$, gdzie θ – jest kątem pomiędzy lokalnym magnetycznym polem nadsubtelnym i kierunkiem wektora falowego promieniowania gamma. Informacje dotyczące znaku lokalnego pola nadsubtelnego oraz pełniejszy opis rozkładu kąтового magnetycznych pól nadsubtelnych w badanych materiałach można uzyskać przy użyciu promieniowania spolaryzowanego. W tym wypadku istnieje możliwość wyznaczenia następujących parametrów opisujących teksturę magnetyczną: $\langle \cos \theta \rangle$ w przypadku promieniowania spolaryzowanego kołowo i $\langle \sin^2 \theta \cos^2 \varphi \rangle$ w przypadku polaryzacji liniowej, gdzie θ i φ są kątami polarnym i azymutalnym wektora nadsubtelnego pola magnetycznego w układzie związanym z wektorem falowym promieniowania gamma i płaszczyzną próbki (rysunek 1.1.1). Jednoczesna analiza rezultatów otrzymanych zarówno klasyczną techniką spektroskopii mössbauerowskiej jak i polarymetrii mössbauerowskiej pozwala na pełniejszą analizę uzyskanych rezultatów, w szczególności w odniesieniu do badań układów magnetycznie nieuporządkowanych. W pracy habilitacyjnej przedstawiam swój wkład

w rozwoju metodologii analizy widm mössbauerowskich otrzymywanych przy użyciu promieniowania gamma spolaryzowanego kołowo [P2, P3, P4, P5, P8, P9, P10] oraz pomiary na uruchomionym przez mnie nowym stanowisku korzystającym z monochromatycznej wiązki spolaryzowanej liniowo. W ramach rozprawy habilitacyjnej prezentowany jest opis konstrukcji takiego źródła, wyznaczanie stopnia polaryzacji liniowo spolaryzowanej wiązki oraz metody analizy otrzymywanych widm [P19]. Użycie w badaniach monochromatycznych wiązek spolaryzowanych kołowo i liniowo umożliwia pełniejszą analizę układów magnetycznie nieuporządkowanych. Ponadto, w ramach prac związanych z zastosowaniem polarymetrii mössbauerowskiej skonstruowano polaryzator kołowy dla wiązki synchrotronowej w technice rozpraszania rezonansowego do przodu [P7]. Umożliwia on pomiary polarymetryczne układów, w przypadku których niezbędne są silne źródła promieniowania. Określono parametry wiązki synchrotronowej, w szczególności określono rozbieżność wiązki dla której zaproponowany polaryzator kołowy pracowałby poprawnie.



Rys.1.1.1. Definicje kątów polarnego θ i azymutalnego φ pomiędzy wektorem nadsubtelnego pola magnetycznego, kierunkiem wektora falowego promieniowania gamma i płaszczyzną próbki x, y .

Niejednoznaczności interpretacyjne w spektroskopii mössbauerowskiej są dwójakiego rodzaju. Pierwszy rodzaj niejednoznaczności jest związany z nakładaniem na siebie składowych o niewiele różniących się oddziaływaniach nadsubtelnych, co prowadzi do poszerzeń linii absorpcyjnych i stopniowego zatarcia szczegółów w widmie. W istocie mamy do czynienia z rozkładami oddziaływań nadsubtelnych. Istnieje wiele różnorodnych metod wyznaczania powyższych rozkładów. W większości z nich stosowane są silne założenia dotyczące korelacji pomiędzy polami nadsubtelnymi B , IS i QS . Najczęściej spotykane w literaturze dotyczą liniowej relacji pomiędzy oddziaływaniami dipolowymi magnetycznymi

i monopolowymi elektrycznymi. Ponadto spotykane w literaturze rekonstrukcje dotyczą rozkładów jednowymiarowych $P(B)$ dla układów magnetycznych lub $P(QS)$ dla układów w stanie paramagnetycznym. Zgodnie z moją wiedzą nie istnieje procedura pozwalająca na rekonstrukcje rozkładów trójwymiarowych $P(B, IS, QS)$.

W ramach przedstawianej rozprawy habilitacyjnej opracowano i rozwinięto metodę analizy rozkładów pól nadsubtelnych opartą na metodzie maksymalnej entropii, która nie wymaga stosowania powyższych założeń [P6, P11, P16, P18]. W szczególności opracowano i przetestowano możliwość rekonstrukcji trójwymiarowych rozkładów pól nadsubtelnych $P(B, IS, QS)$ lub $P(B, IS, z)$ (z parametr tekstury magnetycznej) w przypadku układów regularnych ($QS = 0$ mm/s). Metoda maksymalnej entropii została również z powodzeniem zastosowana do dekonwolucji widm mössbauerowskich ze względu na zdolność rozdzielczą spektrometru.

Drugi aspekt niejednoznaczności interpretacyjnych widm mössbauerowskich dotyczy przejść jądrowych w układach ze spinem jądrowym większym niż $1/2$ w przypadku istnienia oddziaływań nadsubtelnych mieszanych, tzn. dipolowych magnetycznych i kwadrupolowych elektrycznych. Jeśli próbka nie posiada tekstury magnetycznej wówczas ten sam kształt widma absorpcyjnego można otrzymać dla kontinuum różnych wartości parametrów oddziaływań nadsubtelnych. Przyczyna takiego stanu rzeczy tkwi w tym, że mieszane oddziaływania nadsubtelne w przypadku spinu $3/2$ określone są przez dwie niezależne składowe tensora gradientu pola elektrycznego oraz przez pseudowektor nadsubtelnego pola magnetycznego (trzy składowe) co razem daje pięć niezależnych parametrów. Tymczasem prawdopodobieństwa przejść oraz położenia linii absorpcyjnych są całkowicie określone przez cztery mierzalne parametry. Prowadzi to w oczywisty sposób do niejednoznaczności interpretacyjnych mierzonych widm absorpcyjnych. W ramach przedstawianej rozprawy opracowano i zastosowano nową metodę tzw. metodę niezmienników, która pozwala na jednoznaczną parametryzację mierzonych widm mössbauerowskich [P14, P15, P17].

Kolejnym elementem dotyczącym metodologii spektroskopii mössbauerowskiej, jest wprowadzona w pracy [P16] metoda wyznaczania przekroju czynnego na absorpcję. Możliwość otrzymywania przekroju czynnego pozwala na analizę mierzonych widm dla dowolnej grubości efektywnej t użytych w eksperymencie absorbentów. Powszechnie stosowane w analizie widm mössbauerowskich przybliżenie cienkiego absorbenta prowadzi w przypadku grubych próbek do zaburzenia relacji natężeń mierzonych widm absorpcyjnych,

co może skutkować pojawianiem się artefaktów w rekonstruowanych rozkładach pól nadsubtelnych.

Wprowadzone przeze mnie nowe metody analizy danych jak i zastosowanie metod polarymetrycznych pozwoliło na ujawnienie istotnych cech fizycznych i weryfikację modeli opisujących materiały magnetycznie rozporządkowane, zarówno lite jak i nanokrystaliczne. W pracy habilitacyjnej przedstawione zostaną wyniki badań dotyczące:

- 1) układów litych Fe-Cr-Mn z konkurencyjnymi oddziaływaniami wymiennymi [**P1, P2, P3**],
- 2) układu Fe-Ni w obszarze koncentracji występowania zjawiska invaru wiązanego z postulowanym w teorii istnieniem dwóch stanów atomów Fe o różnych rozkładach kątowych momentów magnetycznych atomów żelaza [**P4, P5, P16**],
- 3) związku metalicznego UFe_5Sn , w którym obserwuje się występowanie magnetycznych przejść fazowych związanych z reorientacją lokalnych momentów magnetycznych atomów Fe [**P12, P14, P15**],
- 4) układów nanowymiarowych Fe-Al otrzymywanych metodą mielenia mechanicznego [**P8, P9, P10**],
- 5) nanocząstek magnetytu otrzymanych metodami chemicznymi [**P13**].

Krótkie streszczenia otrzymanych rezultatów przedstawione jest w rozdziale 4.

Reasumując, przedkładana rozprawa habilitacyjna dzieli się na dwie zasadnicze części:

1) **metodologiczną, obejmującą:**

- konstrukcję monochromatycznego źródła spolaryzowanego liniowo oraz sposobu analizy widm doświadczalnych mierzonych z użyciem takiego promieniowania,
- opracowanie i przetestowanie metody maksymalnej entropii w spektroskopii mössbauerowskiej w celu rekonstrukcji trójwymiarowych rozkładów pól nadsubtelnych $P(x, y, z)$, gdzie x, y, z – są dowolnymi polami nadsubtelnymi,
- opracowanie metody niezmienników, umożliwiającej jednoznaczny opis widm absorpcyjnych bez tekstury przy mieszanych oddziaływaniach nadsubtelnych dipolowych magnetycznych i kwadrupolowych elektrycznych,

- opracowanie metody otrzymywania przekroju czynnego z widm mössbauerowskich, w których parametr grubości efektywnej t ma dowolną wartość.

2) badawczą, obejmującą zastosowanie wyżej wymienionych metod do:

- badania litych układów Fe-Cr-Mn, Fe-Ni, UFe₅Sn nieuporządkowanych magnetycznie,

- badania układów nanometrowych Fe-Al oraz nanocząstek magnetytu.

2. Polarymetria mössbauerowska

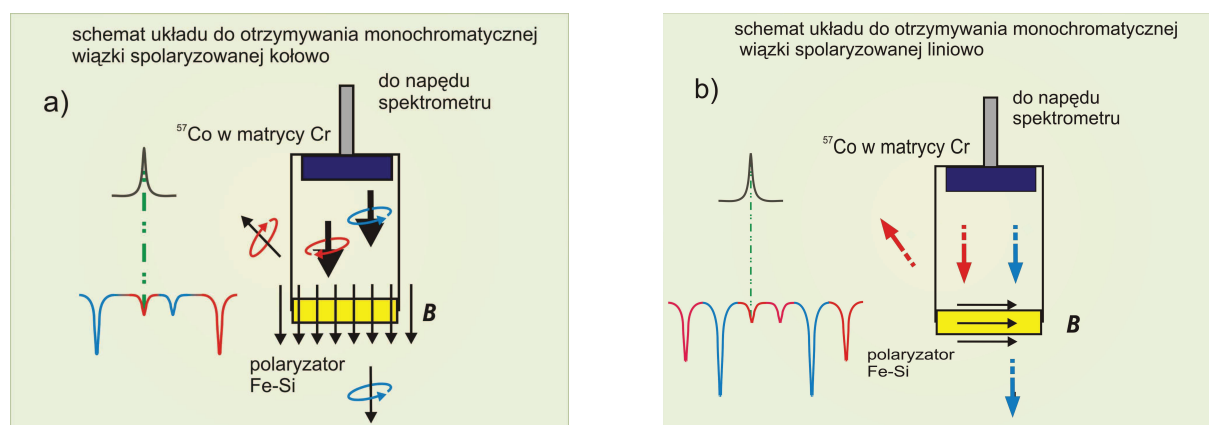
Względne natężenia linii w widmie mössbauerowskim niosą informację o kątowym rozkładzie wektorów magnetycznego pola nadsubtelnego tzw. teksturze magnetycznej. Wykorzystując promieniowanie niespolaryzowane możliwe jest otrzymanie pewnych użytecznych, lecz ograniczonych informacji o wielkościach średnich po rozkładzie, mianowicie $\langle \cos^2\theta \rangle$. Polarymetria mössbauerowska zasadniczo zwiększa dostępną informację. W przypadku stosowania wiązki spolaryzowanej kołowo otrzymujemy parametr $\langle \cos\theta \rangle$, który pozwala na określenie zwrotu wektora lokalnego magnetycznego pola nadsubtelnego. W przypadku polaryzacji liniowej mamy dodatkowy parametr opisujący teksturę magnetyczną, mianowicie $\langle \sin^2\theta \cos^2\varphi \rangle$. Wszystkie powyższe możliwości badawcze nadają się szczególnie do badań układów nieuporządkowanych magnetycznie. Ponadto, użycie monochromatycznej wiązki spolaryzowanej upraszcza widma absorpcyjne i możliwa jest separacja poszczególnych przejść jądrowych.

Korzyści płynące z wykorzystania wiązki spolaryzowanej w spektroskopii mössbauerowskiej zostały zauważone zaraz po odkryciu efektu Mössbauera [Han, Frau] i wykorzystane do pomiarów dotyczących gradientu pola elektrycznego [John], określania kierunku wektora magnetycznego pola nadsubtelnego [Blu] i struktury magnetycznej monokryształów [Gon]. Wiele różnych metod zostało zastosowanych w celu otrzymania wiązki spolaryzowanej. Większość z nich była jednak nieefektywna i zbyt skomplikowana do regularnych zastosowań. Z jednej strony otrzymywane źródła były polichromatyczne co bardzo komplikuje analizę mierzonych widm, z drugiej strony wymagały skomplikowanej aparatury utrzymującej linię emisyjną niespolaryzowanego źródła promieniowania gamma w rezonansie z odpowiednią spolaryzowaną linią filtra [Frau, Sht, Sta, Jäs]. W celu wyeliminowania powyższych trudności kluczową kwestią był dobór filtra, który pracuje z dostępnym komercyjnie źródłem promieniowania na standardowym układzie pomiarowym i jest w rezonansie z linią źródła przy zerowej prędkości.

W roku 1995 w Pracowni Metod Jądrowych Uniwersytetu w Białymstoku skonstruowano, w oparciu o metodę filtra, monochromatyczne źródło promieniowania spolaryzowanego kołowo pracujące z wykorzystaniem komercyjnego źródła ^{57}Co w matrycy chromowej z filtrem Fe-Si. Szczegółowy opis doboru filtra i metodologia analizy danych dostępne są w pracach [Szy1, Szy2, Szy3, Szy4]. Schemat układu użytego do otrzymywania

Wiązki spolaryzowanej kołowo przedstawiony jest na rysunku 2.1.a. Pomiary na próbkach proszkowych zazwyczaj przeprowadza się na absorbencji umieszczonej w zewnętrznym polu magnetycznym równoległym do kierunku propagacji promieniowania gamma. W ramach prezentowanej rozprawy habilitacyjnej pomiary i analiza wyników doświadczalnych, otrzymanych z zastosowaniem spektroskopii mössbauerowskiej z użyciem wiązki spolaryzowanej kołowo, zostały przedstawione w pracach [P2, P3, P4, P5, P8, P9, P10].

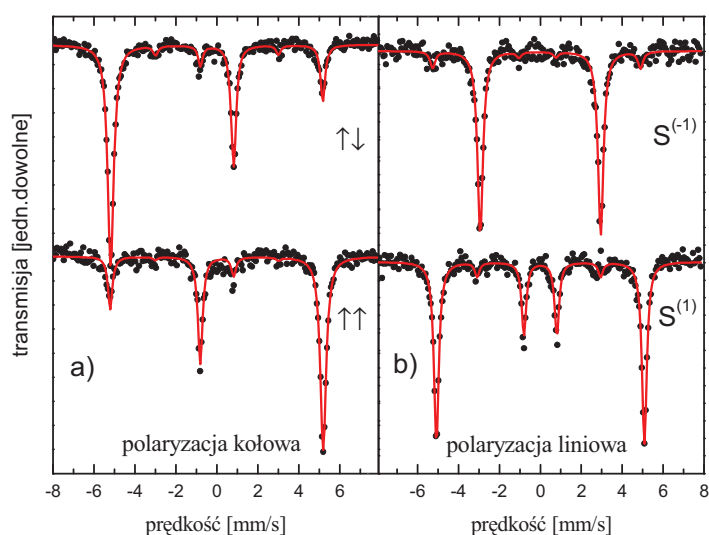
Naturalnym uzupełnieniem bazy badawczej pracowni było uruchomienie układu pracującego z monochromatyczną wiązką spolaryzowaną liniowo. Moje prace badawcze w latach 2010-2011 doprowadziły do uruchomienia takich pomiarów [P19]. Schemat budowy monochromatycznego źródła spolaryzowanego liniowo przedstawiony jest na rysunku 2.1.b. W tym przypadku zazwyczaj pomiary przeprowadza się na absorbencji umieszczonej w zewnętrznym polu magnetycznym prostopadłym do kierunku propagacji promieniowania gamma.



Rys. 2.1. Schemat konstrukcji źródła spolaryzowanego a) kołowo i b) liniowo.

Na rysunku 2.2. przedstawione są wyniki pomiarów $\alpha\text{-Fe}$ z użyciem monochromatycznego promieniowania spolaryzowanego kołowo (rysunek 2.2.a) i liniowo (rysunek 2.2.b). Charakterystyczną cechą pomiarów przeprowadzonych przy użyciu promieniowania spolaryzowanego kołowo, w przypadku momentów magnetycznych atomów Fe równoległych do kierunku promieniowania gamma, jest występowanie asymetrii widm mierzonych dla obu stanów polaryzacji wiązki, symbolicznie oznaczonych na rysunku $\uparrow\downarrow$, $\uparrow\uparrow$. W przypadku całkowitej polaryzacji wiązki i ustawieniu momentów magnetycznych równoległe do zewnętrznego pola magnetycznego równoległego do kierunku wiązki gamma widma powinny składać się jedynie z dwóch linii odpowiednio nr 1, 4 dla polaryzacji $\uparrow\downarrow$

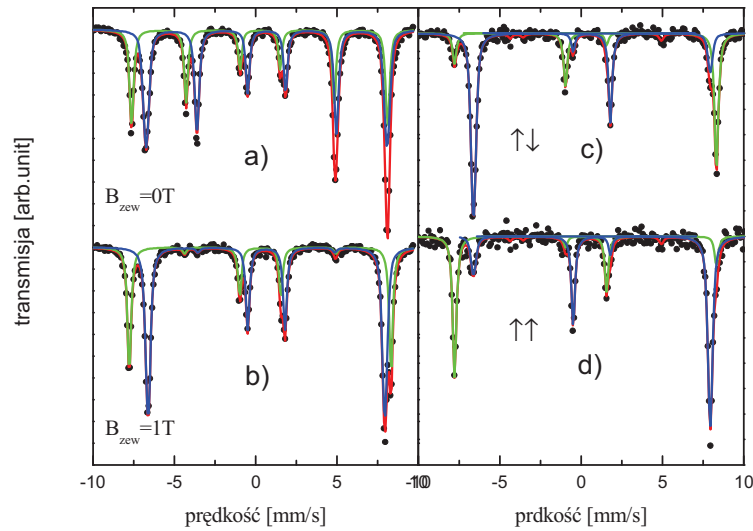
i 3, 6 dla polaryzacji $\uparrow\uparrow$. Szczątkowe występowanie linii nr. 2, 3, 5 i 6 dla polaryzacji $\uparrow\downarrow$ i nr. 1, 2, 4, 5 dla polaryzacji $\uparrow\uparrow$ jest związane z niecałkowitą polaryzacją wiązki (zmierzona wartość stopnia polaryzacji $p = 0.8 \pm 0.1$) oraz niecałkowitym uporządkowaniem momentów magnetycznych Fe w kierunku zewnętrznego pola magnetycznego $B = 1$ T. W szczególnym przypadku izotropowego rozkładu momentów magnetycznych, ewentualnie uporządkowania antyferromagnetycznego brak jest jakiegokolwiek asymetrii. W przypadku wiązki spolaryzowanej liniowo (rysunek 2.2.b) dla jednego stanu polaryzacji oznaczonej symbolicznie $S^{(-)}$ obserwowane są linie 2, 5, a w przypadku drugiej polaryzacji $S^{(+)}$ linie 1, 3, 4, 6. Podobnie jak w wypadku polaryzacji kołowej linie o bardzo małej intensywności nr. 1, 3, 4, 6 dla $S^{(-)}$ i 2, 5 dla $S^{(+)}$ związane są z niecałkowitą polaryzacją wiązki i niecałkowitym uporządkowaniem momentów magnetycznych Fe w kierunku zewnętrznego pola magnetycznego $B = 1$ T.



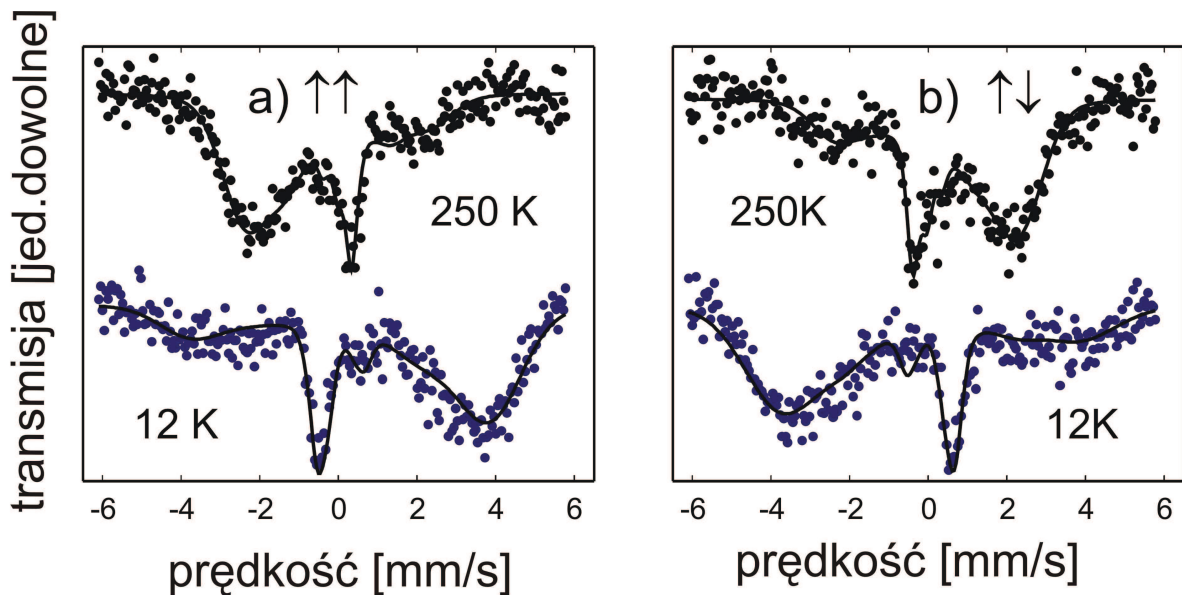
Rys.2.2. Widma α -Fe mierzone z użyciem wiązki spolaryzowanej w zewnętrznym polu magnetycznym 1 T równoległym i prostopadłym do wektora falowego promieniowania gamma odpowiednio dla polaryzacji, a) kołowej, b) liniowej.

Doskonałym przykładem użyteczności pomiarów z użyciem wiązki spolaryzowanej kołowo jest pomiar magnetytu Fe_3O_4 przedstawiony na rysunku 2.3. Magnetyt jest ferrimagnetykiem o dwóch nierównoważnych pozycjach chemicznych atomów Fe, tetraedrycznej Fe_A i oktaedrycznej Fe_B . Obserwowana asymetria na obu pozycjach żelaza jest przeciwna co świadczy, że momenty magnetyczne pozycji Fe_B są ustawiane równoległe do zewnętrznego pola magnetycznego (asymetrie takie same jak w przypadku α -Fe), natomiast

momenty magnetyczne Fe_A są ustawione antyrównolegle do zewnętrznego pola magnetycznego (obserwowane asymetrie przeciwne niż obserwowane w α -Fe). Drugim przykładem jest związek amorficzny $Fe_{0.66}Er_{0.19}B_{0.15}$ (rysunek 2.4.), w którym widać zmianę asymetrii wraz ze wzrostem temperatury, co świadczy o zmianie orientacji momentów magnetycznych Fe.



Rys.2.3. Widma mössbauerowskie magnetytu mierzone z użyciem promieniowania niespolaryzowanego, a) bez zewnętrznego pola magnetycznego, b) w B_{zew} równoległym do promieniowania gamma, c) i d) wiązki spolaryzowanej kołowo. Czerwona linia ciągła przedstawia najlepsze dopasowanie, zielona i niebieska odpowiednio składowe Fe_A i Fe_B .



Rys.2.4. Widma mössbauerowskie stopu amorficznego $Fe_{0.66}Er_{0.19}B_{0.15}$.

2.1. Polarymetria z użyciem promieniowania spolaryzowanego liniowo [P19]

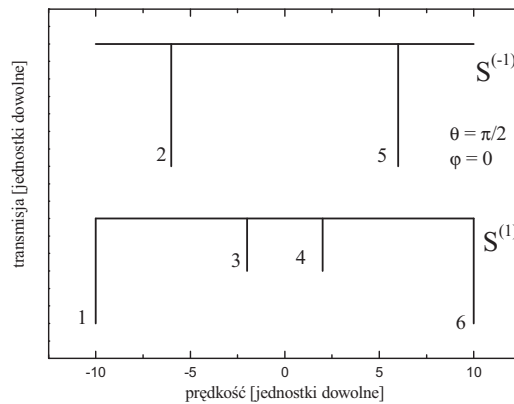
W przypadku użycia promieniowania spolaryzowanego liniowo możliwy jest dostęp do dodatkowej informacji o kątowym rozkładzie momentów magnetycznych, w postaci średniej wartości parametru $\langle \cos^2 \varphi \sin^2 \theta \rangle$ gdzie θ i φ są odpowiednio kątami polarnym i azymutalnym w układzie związanym z wektorem falowym \mathbf{k} promieniowania gamma i kierunkiem zewnętrznego pola magnetycznego prostopadłego do wektora \mathbf{k} . W szczególności, gdy $\theta = \pi/2$ otrzymujemy informację o kątowym rozkładzie wektorów pola nadsubtelnego w płaszczyźnie próbki. Ponadto widmo absorpcyjne staje się znacznie prostsze. Sytuacja, gdy $\theta = \pi/2$ i $\varphi = 0$ prezentowana jest schematycznie na rysunku 2.1.1.

W przypadku całkowicie spolaryzowanej liniowo monochromatycznej wiązki promieniowania i magnetycznego pola nadsubtelnego zorientowanego pod kątami θ i φ widmo mössbauerowskie składa się z sześciu linii o natężeniach $I^{(p)}_i$ ($i=1, 2, 3, 4, 5, 6$) wyrażonych relacjami [Bra]:

$$I_{1,6}^{(1)} : I_{2,5}^{(1)} : I_{3,4}^{(1)} = \left(\frac{3}{8}(1-ss) \right) : \left(\frac{ss}{2} \right) : \left(\frac{1}{8}(1-ss) \right) \quad (2.1.1)$$

$$I_{1,6}^{(-1)} : I_{2,5}^{(-1)} : I_{3,4}^{(-1)} = \left(\frac{3}{8}(1-cs) \right) : \left(\frac{cs}{2} \right) : \left(\frac{1}{8}(1-cs) \right) \quad (2.1.2)$$

gdzie $ss = \sin^2 \varphi \sin^2 \theta$ oraz $cs = \cos^2 \varphi \sin^2 \theta$, a wartości $p = -1$ i $p = 1$ oznaczają odpowiednio dwie ortogonalne polaryzacje wiązki.



Rys.2.1.1. Schematyczne przedstawienie widm mössbauerowskich monochromatycznej liniowo spolaryzowanej wiązki promieniowania gamma.

W przypadku niecałkowitej polaryzacji wiązki sytuacja się komplikuje. W pracy [P19] zostało pokazane, że w takim wypadku natężenia poszczególnych linii absorpcyjnych można wyrazić wzorami:

$$I_{1,6}^p : I_{2,5}^p : I_{3,4}^p = \left(\frac{3(p+1)}{16}(cs - ss) + \frac{3}{8}(1 - cs) \right) : \left(\frac{(p+1)}{4}(ss - cs) + \frac{cs}{2} \right) : \left(\frac{(p+1)}{16}(cs - ss) + \frac{1}{8}(1 - cs) \right) \quad (2.1.3)$$

W wypadku wiązki niespolaryzowanej ($p = 0$) otrzymujemy relację

$$I_{1,6}^0 : I_{2,5}^0 : I_{3,4}^0 = \left(\frac{3}{16}(1 + cc) \right) : \left(\frac{1}{4}(1 - cc) \right) : \left(\frac{1}{16}(1 + cc) \right) \quad (2.1.4)$$

gdzie $cc = \cos^2 \theta$.

W tym przypadku natężenia linii 2 i 5 wyrażają się następująco:

$$4I_{2,5}^0 = cs + ss \equiv 1 - cc \quad (2.1.5)$$

W rzeczywistości najczęściej mamy do czynienia z pewnymi rozkładami kątowymi magnetycznego pola nadsubtelnego, tzw. tekstury magnetycznej $P(\theta, \varphi)$. Liniowo spolaryzowane promieniowanie gamma o stopniu polaryzacji p pozwala na wyznaczenie parametru $\langle cs \rangle$. Relacje (2.1.3) i (2.1.5) prowadzą do wzoru :

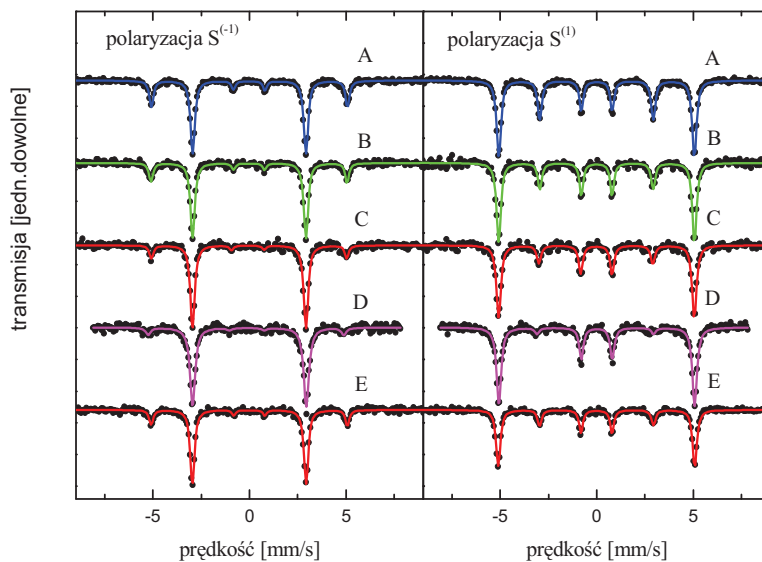
$$\langle cs \rangle = \frac{2(I_{2,5}^0(1+p) - I_{2,5}^p)}{p} \quad (2.1.6)$$

Opierając się na relacji 2.1.6 można oszacować stopień polaryzacji wiązki, który jest zależny od zastosowanego filtra. Niecałkowita polaryzacja wiązki może być spowodowana trzema efektami: 1) nieidealnym namagnesowaniem polaryzatora, 2) zbyt małą grubością materiału filtra, 3) brakiem homogeniczności polaryzatora. Brak idealnej homogeniczności filtra powoduje, że część niespolaryzowanej wiązki nie oddziałuje z polaryzującym materiałem. Przetestowano różne gęstości materiału zastosowanego w preparatyce filtra jak również różne sposoby preparatyki filtrów (tabela 1). Określone ilości materiału polaryzatora $^{57}\text{Fe}_{2.85}\text{Si}_{1.15}$ były mieszane z żywicą i poddawane polimeryzacji żywicy w różnych warunkach. Przykładane zewnętrzne pole magnetyczne podczas zastygania żywicy miało na celu orientację ziaren materiału polaryzatora. Wyniki pomiarów przeprowadzone w zewnętrznym

polu magnetycznym równoległym do płaszczyzny folii α -Fe otrzymane dla różnych filtrów prezentowane są na rysunku 2.1.2.

Tabla 2.1.1. Różne sposoby preparatyki polaryzatorów $^{57}\text{Fe}_{2.85}\text{Si}_{1.15}$.

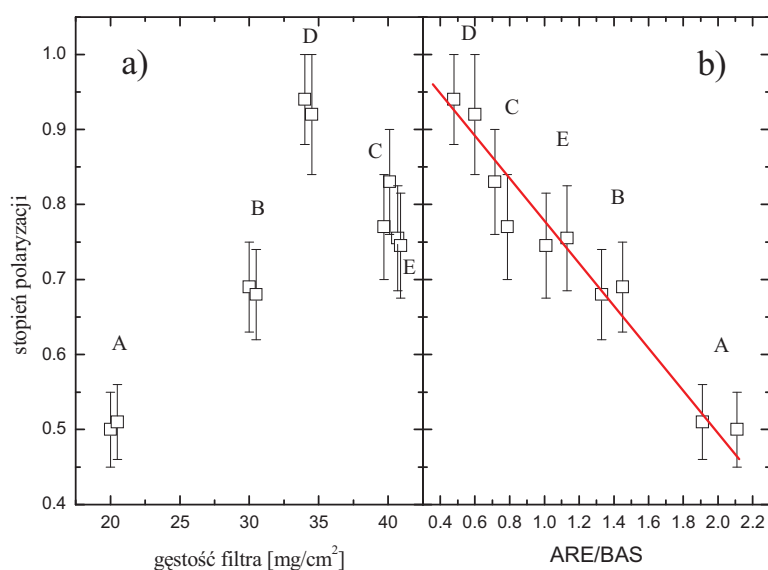
symbol	gęstość pow. materiału [mg/cm^2]	opis
A	20	Wiązanie w zewnętrznym polu magnetycznym równoległym do pow. polaryzatora
B	30	Wiązanie w zewnętrznym polu magnetycznym równoległym do pow. polaryzatora
C	40	Wiązanie w zewnętrznym polu magnetycznym równoległym do pow. polaryzatora
D	34	Wiązanie w zewnętrznym polu magnetycznym równoległym do pow. polaryzatora. Inna granulacja ziaren polaryzatora
E	40	Wiązanie bez zewnętrznego pola magnetycznego



Rys.2.1.2. Widma α -Fe otrzymane z zastosowaniem różnych sposobów preparatyki filtrów polaryzacyjnych.

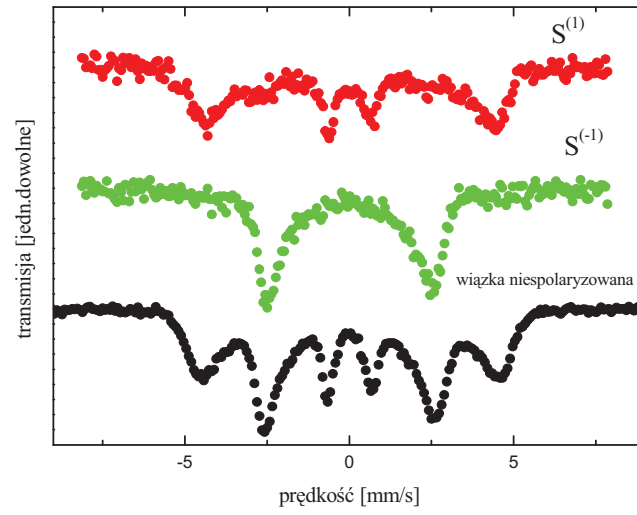
Jak widać, natężenie niepożądanych linii zmienia się w zależności od preparatyki filtrów. Występowanie tych linii absorpcyjnych związane jest z niecałkowitą polaryzacją

wiązki promieniowania gamma oraz brakiem nasycenia momentów magnetycznych atomów Fe w kierunku zewnętrznego pola magnetycznego. Oszacowane wartości stopnia polaryzacji w funkcji gęstości Fe-Si zastosowanego w polaryzatorze przedstawione są na rysunku 2.1.3.a. Obserwowany brak monotonicznej zależności stopnia polaryzacji wynika z efektów związanych z niehomogenicznością filtra. Inną reprezentacją jest przedstawienie stopnia polaryzacji w funkcji ilorazu pola powierzchni pod widmem i wielkości tła (ARE/BAS). Taka reprezentacja uwzględnia ewentualną niehomogeniczność polaryzatora rys.2.1.3.b. Jak widać, najbardziej efektywny polaryzator oznaczony jest symbolem D (patrz tabela 2.1.1). Jak pokazały badania jedną z kluczowych kwestii w przypadku preparatyki polaryzatorów jest ich homogeniczność - ta słabo zależy od zewnętrznych warunków preparatyki (wiązanie w zewnętrznym polu czy bez pola), a istotnie zależy od granulacji materiału polaryzującego (patrz rysunek 2.1.3 polaryzator D , C). W celu dokładniejszego zbadania występujących w tym problemie zjawisk planowane są dalsze badania.



Rys.2.1.3 Oszacowane stopnie polaryzacji dla testowanych polaryzatorów a) jako funkcja gęstości filtra, b) jak funkcja parametru ARE/BAS .

Na rysunku 2.1.4. przedstawione są pomiary $Fe_{65}Ni_{35}$ z wykorzystaniem źródła promieniowania spolaryzowanego liniowo. Analiza zestawu danych polarymetrii mössbauerowskiej i klasycznej spektroskopii mössbauerowskiej z wykorzystaniem promieniowania spolaryzowanego pozwoli na bardziej wiarygodną rekonstrukcję istniejącego rozkładu pola nadsubtelnego $P(B)$.



Rys.2.1.4. Widma mössbauerowskie stopu $Fe_{65}Ni_{35}$ mierzone z użyciem monochromatycznego promieniowania spolaryzowanego liniowo i niespolaryzowanego.

3. Nowe metody analizy danych doświadczalnych

W spektroskopii mössbauerowskiej znanych jest wiele algorytmów pozwalających na interpretację fizyczną mierzonych widm. Wiele nowych idei prowadzących do coraz lepszego opisu wyników doświadczalnych można było zastosować wraz z pojawieniem się dużych mocy obliczeniowych związanych z rozwojem techniki komputerowej. Pojawiające się w analizie danych trudności związane są między innymi z:

- rekonstrukcją rozkładów pól nadsubtelnych bez odwoływania się do założonego modelu,
- rekonstrukcją przekroju czynnego na absorpcję,
- interpretacją widm przy mieszanych oddziaływaniach dipolowych magnetycznych i kwadrupolowych elektrycznych.

W następnych podrozdziałach opiszę trzy nowe metody opracowania danych będące przedmiotem przedkładanej rozprawy habilitacyjnej.

3.1. Metoda maksymalnej entropii w spektroskopii mössbauerowskiej [P6, P11, P16, P18]

Jednym z ważniejszych problemów w spektroskopii mössbauerowskiej jest wyznaczanie rozkładów pól nadsubtelnych. W sytuacji braku efektów dynamicznych mierzone widmo absorpcyjne można opisać w następujący sposób:

$$M(V) = BG - S(V) = \int E(x, y, z, V)P(x, y, z)dx dy dz + N(V) \quad (3.1.1)$$

gdzie: BG – tło,

$S(V)$ – mierzone widmo absorpcyjne,

$E(x, y, z, V)$ – elementarny kształt linii dla danej wartości pola nadsubtelnego,

$P(x, y, z)$ – funkcja rozkładu dla danych pól nadsubtelnych,

$N(V)$ – szum eksperymentalny.

Powstało wiele algorytmów pozwalających na obliczanie rozkładów pól nadsubtelnych [Var, Hes, Win]. Metody te zazwyczaj pozwalają obliczyć funkcję rozkładu poprzez minimalizację statystycznego odchylenia, jak np. w teście χ^2 . Metoda Hesse - Rübartsch daje proste rozwiązanie tego problemu, opierające się na znalezieniu

macierzy odwrotnej. Wiadomo, iż poszukiwania macierzy odwrotnej w przypadku danych obarczonych statystycznym szumem dają wyniki numerycznie niestabilne. Nawet małe szумы mogą prowadzić do istotnie różniących się rezultatów. Problem ten staje się bardziej stabilny w przypadku, gdy włączone są pewne fizyczne założenia, które ograniczają przestrzeń rozwiązań np. często czynione założenie liniowej korelacji magnetycznego pola nadsubtelnego i przesunięcia izomerycznego itp. Takie założone korelacje były często stosowane do rekonstrukcji jednowymiarowych funkcji rozkładu, najczęściej magnetycznego pola nadsubtelnego, podczas gdy dla pozostałych parametrów (przesunięcie izomeryczne, rozszczepienie kwadrupolowe) przyjmowano najlepsze wartości średnie.

Inne podejście - znalezienia funkcji $P(B)$, B – jest magnetycznym polem nadsubtelnym, w spektroskopii mössbauerowskiej, opierające się na metodzie maksymalnej entropii zaproponowali Brandt i Le Caer [Bra]. Metoda ta bazuje na entropii informacyjnej i tzw. wnioskowaniu Bayesowskim [Jay]. Algorytm wnioskowania, na którym opiera się *MEM* wykorzystuje wyłącznie obiektywną wiedzę początkową (tzw. *prior*) dostępną eksperymentatorowi. Metoda ta była często z powodzeniem stosowana w przypadku analizy danych spektroskopowych [Dob, Ger, Buc], a bardzo rzadko w przypadku analizy danych mössbauerowskich.

Obecność rozkładów pól nadsubtelnych prowadzi do komplikacji mierzonych widm, których interpretacja staje się zależna od założeń poczynionych w celu rekonstrukcji szukanych funkcji rozkładu. Metoda *MEM*, jako niezależna od założeń powinna ułatwić interpretację widm mössbauerowskich, charakteryzujących się występowaniem rozkładów pól nadsubtelnych.

Jednym z osiągnięć przedstawianych w tej rozprawie habilitacyjnej jest rozwinięcie i zastosowanie metody maksymalnej entropii do poszukiwania rozkładów, w ogólności w trójwymiarowej przestrzeni pól nadsubtelnych $P(B, IS, QS)$.

W przypadku analizy widm mössbauerowskich z zastosowaniem metody maksymalnej entropii należy podzielić trójwymiarową przestrzeń pól nadsubtelnych na piksele i wprowadzić wektor ρ_j oznaczający prawdopodobieństwo wybranych trzech parametrów nadsubtelnych w j -tym pikselu. Ponieważ intensywności linii w widmie absorpcyjnym są liniową funkcją prawdopodobieństwa, mierzone intensywności T_k z niepewnościami statystycznymi σ_k w k -tym kanale widma są dane sumą:

$$T_k = \sum_{j=1}^{N_{pix}} r_{kj} \cdot \rho_j, \quad \text{gdzie } k=1,2,\dots,N \quad (3.1.2)$$

gdzie $r_{k,j}$ jest macierzą transformacji.

W metodzie zazwyczaj maksymalizuje się Lagrangian w postaci

$$L = \alpha S - \frac{1}{2} \chi^2 \quad (3.1.3)$$

gdzie S jest entropią informacyjną opisaną następującym wyrażeniem

$$S = - \sum_{j=1}^{N_{pix}} \rho_j \ln \left(\frac{\rho_j}{\rho_{oj}} \right) \quad (3.2.4)$$

gdzie ρ_j i ρ_{oj} są rekonstruowanym i początkowym rozkładem.

W celu rekonstrukcji żądanego rozkładu należy rozwiązać następujące równanie:

$$\rho_j = \frac{\rho_{oj} \exp \left(- \frac{1}{2\alpha} \frac{\partial \chi^2}{\partial \rho_j} \right)}{\sum_{j'=1}^{N_{pix}} \rho_{oj'} \exp \left(- \frac{1}{2\alpha} \frac{\partial \chi^2}{\partial \rho_{j'}} \right)} \quad (3.1.5)$$

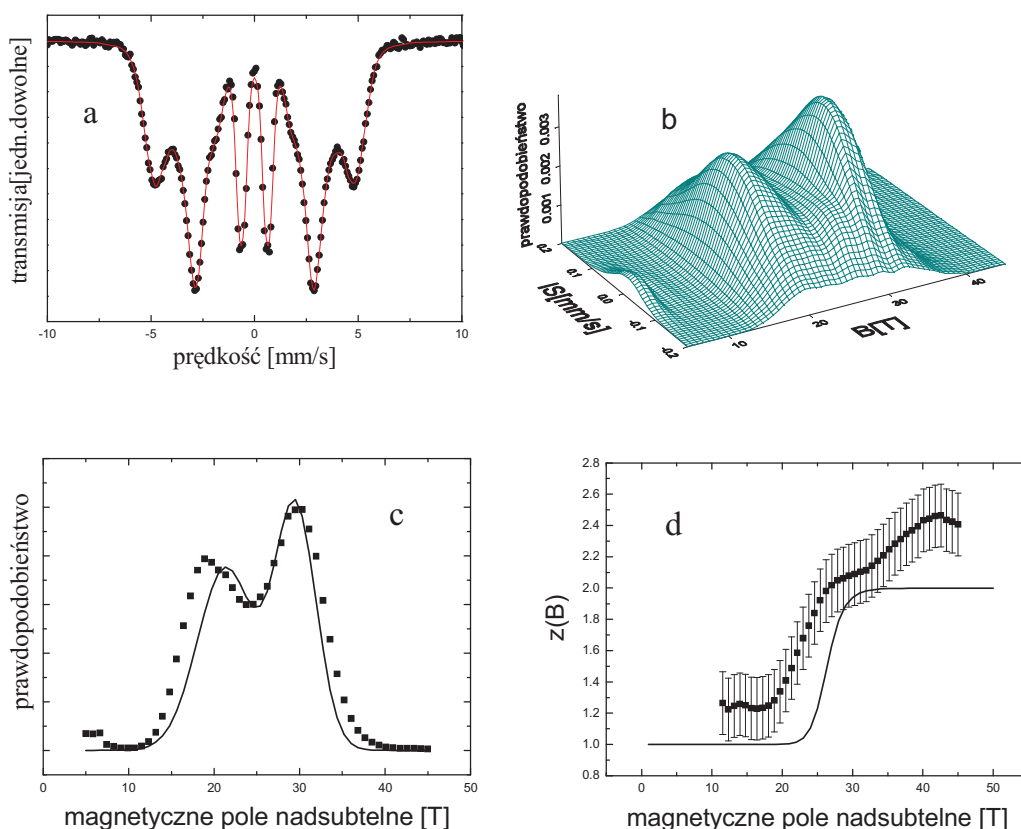
W praktyce istotnym problemem w zastosowaniu maksymalnej entropii jest wybór rozkładu początkowego, opartego na obiektywnej wiedzy o badanym układzie, który może wpływać na odpowiedź metody, a tym samym na rekonstruowane rozkłady pól nadsubtelnych.

W pracy [P6] wprowadziliśmy i przetestowaliśmy algorytm maksymalnej entropii w przypadku jednowymiarowego $P(B)$ i dwuwymiarowego $P(B, IS)$. Algorytm testowany był na symulowanych widmach. Otrzymane rezultaty pokazały bardzo dobrą zgodność symulowanych i rekonstruowanych rozkładów. Należy podkreślić, że w procedurze zastosowanej w tej pracy do rekonstrukcji rozkładów pól nadsubtelnych, jako wiedzę początkową o układzie, tzw. „*prior*”, zakładano płaski rozkład pól nadsubtelnych, co oznacza brak jakiegokolwiek wiedzy początkowej o badanym układzie. Pomimo tak prostego podejścia zgodność rekonstrukcji i symulacji były bardzo dobre.

W pracy [P11] analizowany był przypadek rozkładu $P(QS, IS)$ charakterystyczny dla próbek paramagnetycznych. Testowana była odpowiedź procedury *MEM* w przypadku, w którym można spodziewać się dużych trudności ze znanym w spektroskopii mössbauerowskim problemem niejednoznaczności rozwiązań tzw. *ambiguity problems* [Wil, Dab, Ito, LeC]. Testy wykazały, że w takim przypadku bardzo ważne jest zastosowanie wiedzy początkowej w miejsce płaskiego rozkładu parametrów początkowych. Wykazaliśmy również możliwość rekonstrukcji trójwymiarowego rozkładu pól nadsubtelnych $P(B, QS, IS)$. Istotne jest, że w przypadku skomplikowanego widma niezbędne jest stosowanie wiedzy

początkowej o układzie. Wiedza ta może pochodzić w najprostszym przypadku z oglądu charakterystycznych cech mierzonych widm.

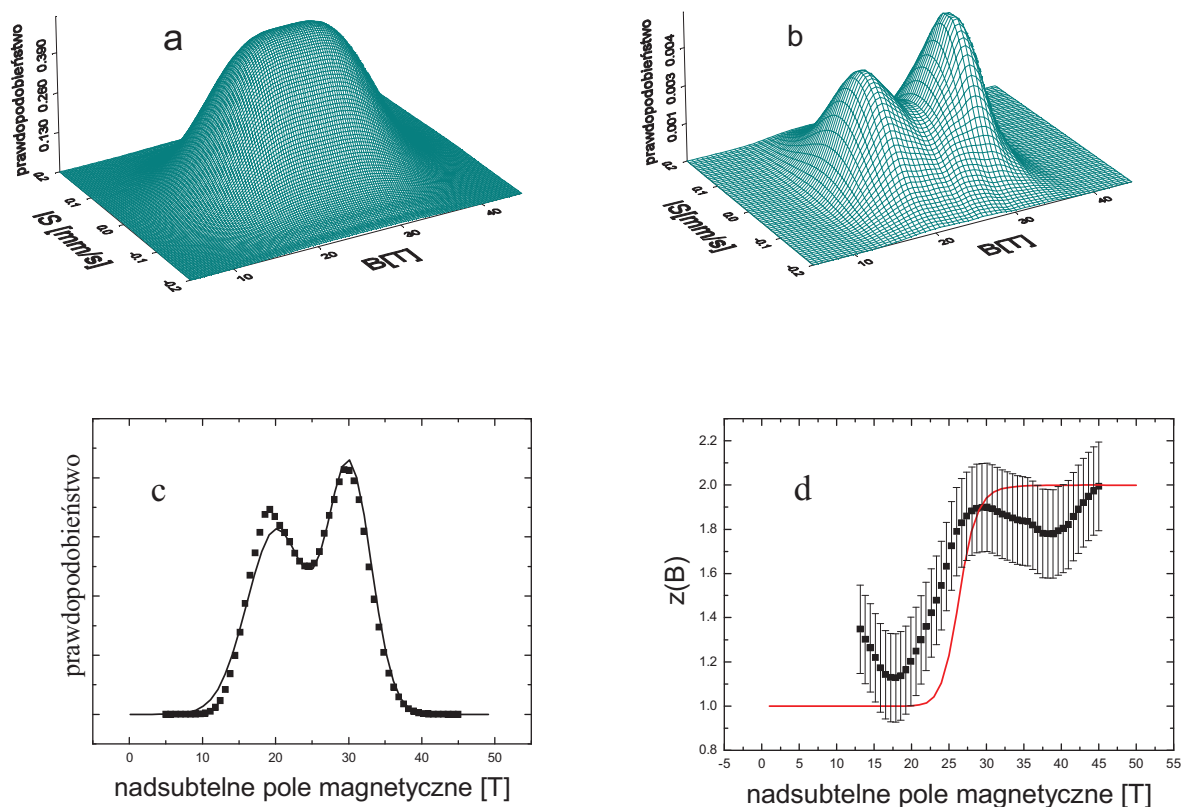
Praca [P16, P18] opisuje kolejne rozszerzenie zakresu stosowalności *MEM* do analizy widm mössbauerowskich, mianowicie poszukiwanie rozkładu $P(B, IS, z)$, gdzie z – jest parametrem tekstury magnetycznej. Testy przeprowadzono na bardzo skomplikowanym, symulowanym widmie, w którym założono istnienie tekstury magnetycznej zależnej od wartości nadsubtelnego pola magnetycznego. Na rysunku 3.1.1 (płaski *prior*) i 3.1.2 (*prior* w kształcie Gaussa) przedstawiono zasadnicze wyniki otrzymane w tej pracy, które pokazują zarówno zalety jak i problemy w rekonstrukcji rozkładów pól nadsubtelnych metodą *MEM*.



Rys.3.1.1. Rezultaty *MEM* otrzymane przy zastosowaniu płaskiego rozkładu początkowego a) symulowane widmo (punkty) z najlepszą rekonstrukcją (linia ciągła), b) zrekonstruowany rozkład $P(B, IS)$, c) symulowany (linia ciągła) i zrekonstruowany (punkty) rozkład $P(B)$ d) symulowana zależność $z(B)$ (linia ciągła) i zrekonstruowana $z(B)$ (punkty).

Jak widać, zastosowanie płaskiego rozkładu (zupełny brak wiedzy początkowej o układzie) do skomplikowanego widma (linie bardzo mocno nachodzą na siebie (rysunek 3.1.1.a)) odtwarza poprawnie rekonstruowany rozkład $P(B)$, chociaż widać wyraźną rozbieżność w szczególności dla pików o mniejszym polu nadsubtelnym. Otrzymane $z(B)$

pokazuje wyraźną zależność parametru z od wartości magnetycznego pola nadsubtelnego, jednak symulowany kształt nie jest odtwarzany w sposób doskonały. W przypadku $P(B, IS)$ rozkład w parametrze IS jest znacznie poszerzony. W symulacji założono dyskretną wartość przesunięcia izomerycznego. Niemniej jednak, jeśli weźmie się pod uwagę, że dane eksperymentalne to tylko jednowymiarowy rozkład składający się z zaledwie 256 punktów oraz przyjęty w analizie zupełny brak wiedzy początkowej o układzie, rekonstrukcja jest wręcz znakomita. Zastosowanie rozkładu Gaussa jako wiedzy początkowej (najprostsze założenie wynikające z kształtu widma) o układzie dają znacznie lepsze rezultaty. Jednakże, szerokość w parametrze IS jest w dalszym ciągu widoczna (rysunek 3.1.2).

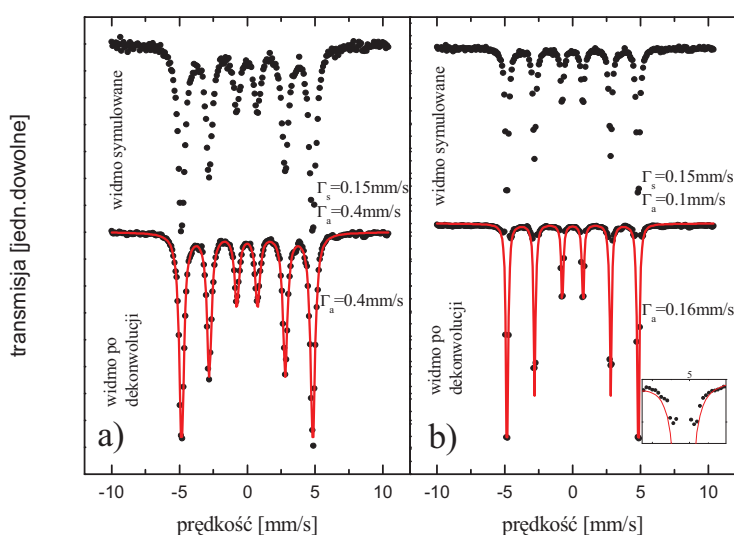


Rys.3.1.2. Rezultaty MEM otrzymane przy zastosowaniu gaussowskiego rozkładu początkowego a) zastosowany prior, b) rozkład zrekonstruowany, c) $P(B)$ założony (linia ciągła) i zrekonstruowany (punkty) d) zależność $z(B)$ symulowana (linia ciągła) i zrekonstruowana (punkty).

W pracy [P16], w której wprowadziłem procedurę otrzymywania przekroju czynnego na absorpcję $\sigma(E)$ niezbędnym elementem jest procedura dekonwolucji widma mössbauerowskiego z szumem eksperymentalnym ze względu na zdolność rozdzielczą

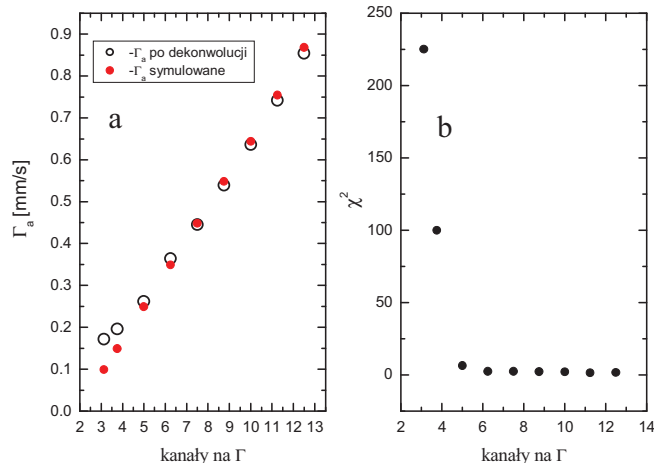
aparatury. W procesie tym doskonałym narzędziem okazuje się ponownie metoda maksymalnej entropii.

W celu przetestowania przydatności *MEM* w procesie dekonwolucji metoda ta została przetestowana na symulowanych widmach z narzuconym gaussowskim rozkładem szumu. Kształt symulowanych widm był splotem funkcji Lorentza i sekstetu z różnymi szerokościami połówekowymi, $\Gamma_s = 0.15$ mm/s (wielkości typowej dla źródła ^{57}Co) traktowany jako funkcja aparaturowa i Γ_a zmieniającej się w zakresie 0.1 mm/s do 0.85 mm/s. Γ_a w tym wypadku odpowiada możliwemu poszerzeniu linii absorpcyjnych. Wielkość $\Gamma_a = 0.1$ mm/s odpowiada widmu folii Fe używanemu najczęściej do kalibracji spektrometru. Rezultaty przykładowej dekonwolucji dla $\Gamma_a = 0.4$ mm/s i $\Gamma_a = 0.1$ mm/s są przedstawione na rysunku 3.1.3. Jak widać dla większej szerokości widma $\Gamma_a = 0.4$ mm/s dekonwolucja przebiega prawidłowo, podczas gdy dla $\Gamma_a = 0.1$ mm/s dekonwolucja nie odwzorowuje kształtu Lorentza. Jest to przedstawione na wstawce rysunek 3.1.3.b.



Rys.3.1.3. Przykład dekonwolucji dla symulowanych widm z parametrami $\Gamma_s = 0.15$ mm/s i a) $\Gamma_a = 0.4$ mm/s b) $\Gamma_a = 0.1$ mm/s. Linia ciągła reprezentuje najlepsze dopasowanie otrzymane w przybliżeniu cienkiego absorbenta.

Porównanie symulowanych Γ_a i szerokości połówekowych otrzymanych z analizy widm po procesie dekonwolucji w przybliżeniu cienkiego absorbenta prezentowane są na rysunku 3.1.4.



Rys.3.1.4. Zależność a) Γ_a użytego w symulacjach i uzyskanego po dekonwoluji, b) parametru χ^2 otrzymanego z dopasowania, w funkcji liczby kanałów przypadających na szerokość połówkową.

Istotnym parametrem, od którego zależy jakość przeprowadzanych dekonwoluji jest liczba kanałów przypadająca na szerokość połówkową. Podstawowym wnioskiem wynikającym z powyższej analizy jest to, że procedura dekonwoluji przeprowadzona na dyskretnym, symulowanym widmie z narzuconym szumem, poprawnie reprodukuje kształt w przypadku, gdy $\Gamma = \Gamma_a + \Gamma_s$ jest około 2.5 razy większa niż szerokość Γ_s . W przypadku naszej symulacji wynika, że procedura pracuje poprawnie gdy na szerokość połówkową widma przypada co najmniej pięć kanałów. Oznacza to, że procedura MEM pracuje właściwie dla próbek ze względnie szerokimi rozkładami pól nadsubtelnych.

3.2. Metoda niezmienników [P14, P15, P17]

Już w pierwszych latach spektroskopii mössbauerowskiej stwierdzono, iż szczegóły struktury nadsubtelnej nie mogą być jednoznacznie określone na podstawie widm mössbauerowskich próbek nie posiadających tekstury krystalicznej [Kar]. Niejednoznaczność istnieje nawet w najprostszym przypadku widma z pojedynczą pozycją krystalograficzną biorącą udział w efekcie Mössbauera [Wil, Dab1, Dab2, Don]. Do wyznaczenia oddziaływań nadsubtelnych pomocne są pomiary w zewnętrznych polach magnetycznych [Spi], wykorzystanie monokryształów [Wer], ewentualnie metod polarymetrycznych [Bar, Szy5]. Jeszcze większe problemy pojawiają się, gdy mamy do czynienia z rozkładami pól

nadsubtelnych powodującymi nakładanie się linii absorpcyjnych [Cae]. Nie ma do tej pory opublikowanych sposobów umożliwiających opracowanie w ścisły sposób wyników takich eksperymentów mössbauerowskich. W celu jednoznacznej analizy wyników otrzymywanych z pomiarów mössbauerowskich opracowana została w naszym zakładzie tzw. metoda niezmienników. Metoda ta polega na konstrukcji odpowiedniej bazy funkcji, której zastosowanie umożliwia jednoznaczne opracowanie wyników takiego eksperymentu mössbauerowskiego.

Pozycje linii absorpcyjnych widma mössbauerowskiego są obliczane poprzez diagonalizację Hamiltonianu spinowego, podczas gdy amplitudy są dane poprzez wartości własne [Gib]. Jak zostało pokazane w pracy [Szy6] koncepcja tensora natężeń [Zor, Ing, Zim, Zim1] prowadzi do opisu natężeń linii poprzez następujące niezmienniki skonstruowane z tensora gradientu pola elektrycznego V i pseudowektora magnetycznego pola nadsubtelnego \vec{B} :

$$\begin{aligned} S_0 &= a\sqrt{\text{Tr}V^2} \\ S_1 &= am^T \cdot V \cdot m \\ S_2 &= a\sqrt{m^T \cdot V^2 \cdot m} \end{aligned} \quad (3.2.1)$$

gdzie

$$a = eQc / E_\gamma \quad (3.2.2)$$

jest stałą proporcjonalności pomiędzy gradientem pola elektrycznego i powyższymi niezmiennikami wyrażonymi w jednostkach mm/s, Q jest momentem kwadrupolowym, e ładunkiem elementarnym, c prędkością światła, E_γ energią pomiędzy stanem podstawowym i wzbudzonym, $\vec{m} = \vec{B} / B$ (B jest modulem \vec{B}) wektorem jednostkowym równoległym do \vec{B} .

Wprowadzone niezmienniki S_0 , S_1 , S_2 posiadają jasną interpretację fizyczną. Niezmiennik $6^{-1/2}S_0$ jest równy wyrażeniu:

$$aV_{zz}(1 + \eta^2 / 3) / 2 \quad (3.2.3)$$

i określa odległość pomiędzy poziomami jądrowymi $I_e = 3/2$ w przypadku, gdy magnetyczne pole nadsubtelne jest równe zero. Niezmiennik S_1 jest składową tensora V gradientu pola elektrycznego w kierunku magnetycznego pola nadsubtelnego. Znak tego niezmiennika może być zarówno dodatni jak i ujemny. Niezmiennik S_2 jest proporcjonalny do przesunięcia linii absorpcyjnych numer 2, 3, 4, 5 względem linii numer 1, 6 w sekstecie zeemanowskim. W przypadku gdy wektor \vec{m} jest przypadkowo zorientowany w układzie osi głównych tensora

V średnia wartość niezmiennika jest równa zero. Kwadrat niezmiennika S_2 jest składową tensora V^2 w kierunku nadsubtelnego pola magnetycznego.

Równanie własne na energie stanu wzbudzonego $I_e = 3/2$ ma postać:

$$\begin{aligned}\lambda^4 + p\lambda^2 + q\lambda + r &= 0 \\ \lambda &= 2E/v_B\end{aligned}\tag{3.2.4}$$

gdzie $v_B = g_{3/2}\mu_N B c / E_\gamma$ jest rozszczepieniem Zemana pomiędzy podpoziomami stanu $I_e = 3/2$ wyrażonymi w mm/s, μ_N magnetonem jądrowym, $g_{3/2}$ jest jądrowym czynnikiem g stanu wzbudzonego.

Współczynniki powyższego równania można przedstawić w zależności od wprowadzonych niezmienników następująco:

$$\begin{aligned}p &= -10 - \frac{1}{3}(S_0/v_B)^2, \\ q &= -8S_1/v_B, \\ r &= \frac{1}{4}(p+4)^2 - 4(S_2/v_B)^2.\end{aligned}\tag{3.2.5}$$

Natężenia linii absorpcyjnych dla przypadkowo zorientowanego absorbenta w przypadku magnetycznego dipolowego przejścia $3/2 \rightarrow 1/2$ jest proporcjonalne do śladu tensora natężeń co wyrażamy w postaci:

$$\text{Tr } \mathbf{I}_{\alpha\beta} = \frac{3}{8} + \beta \frac{40\lambda_\alpha^2 - 4q\lambda_\alpha + (p+4)(p+16) - 4r}{16(4\lambda_\alpha^3 + 2p\lambda_\alpha + q)}\tag{3.2.6}$$

Indeks $\beta = \pm 1$ odpowiada dwóm stanom podstawowym a cztery wartości własne λ_α są pierwiastkami równania własnego. Ostatecznie relacja na pozycje linii absorpcyjnych wyraża się wzorem:

$$v_{\alpha,\beta} = (\lambda_\alpha - \beta g_{1/2} / g_{3/2}) v_B / 2\tag{3.2.7}$$

Zależności (3.2.1), (3.2.6) i (3.2.7) w pełni określają pozycje linii absorpcyjnych oraz ich natężenia i zależą jedynie od czterech niezmienników: B , S_0 , S_1 i S_2 , podczas gdy niezależnych parametrów nadsubtelnych jest pięć: B , θ , φ , V_{zz} i η . Zatem tylko powyższe niezmienniki mogą jednoznacznie być wyznaczone z widm dla przypadkowo zorientowanych absorbentów.

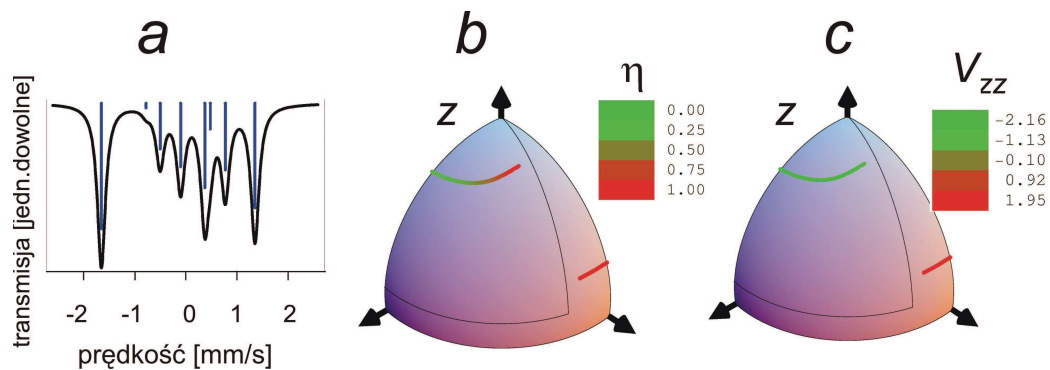
W praktyce procedura dopasowania polega na wykorzystaniu dowolnego pakietu oprogramowania posiadającego opcję liczenia pełnego Hamiltonianu, dopasowując następujące swobodne parametry B , θ , φ , V_{zz} , η z więzami: $\varphi = \pi/2$, lub $\varphi = 0$, lub $\theta = \pi/2$. Tak wybrane więzy są równoważne stwierdzeniu, że \vec{B} jest prostopadły do jednej z osi

głównych gradientu pola elektrycznego. Parametry θ , φ , V_{zz} , η stosujemy do obliczenia niezmienników wyrażonych równaniami (3.2.1) wyrażonymi w bezpośredniej formie następująco:

$$\begin{aligned}
 S_0 &= \frac{a|V_{zz}|}{\sqrt{6}} \sqrt{1 + \frac{1}{3}\eta^2}, \\
 S_1 &= \frac{aV_{zz}}{2} (3 \cos^2 \theta - 1 + \eta \cos 2\varphi \sin^2 \theta), \\
 S_3 &= \frac{a|V_{zz}|}{2} \sqrt{4 - (3 - 2\eta \cos 2\varphi + \eta^2) \sin^2 \theta}
 \end{aligned}
 \tag{3.2.8}$$

Powyższe trzy niezmienniki oraz nadsubtelne pole magnetyczne mogą być wyznaczone z widm mössbauerowskich bez tekstury magnetycznej.

W celu ilustracji problemu niejednoznaczności na rysunku 3.2.1 a przedstawione jest widmo symulowane na podstawie określonych wartości niezmienników B , S_0 , S_1 i S_2 . Na rysunkach 3.2.1 b, c w postaci ciągłych linii przedstawione są wartości parametrów V_{zz} , η , θ , φ , dla których niezmienniki, a zatem i widmo nie zmieniają się.



Rys.3.2.1. a) Symulowane widmo mössbauerowskie dla magnetycznego pola nadsubtelnego $B = |eQV_{zz}| / (4g3/2\mu_N)$ ($=7.3641$ T), i niezmienników S_0 , S_1 , S_2 równych $(57/8)1/2$, $-5/4$, $(217/64)1/2$ (wszystkie w jednostkach mm/s). Kolorowe linie na wycinku sfery pokazują możliwe wartości kątów polarnego θ i azymutalnego φ wektora B w układzie osi głównych tensora gradientu pola elektrycznego V . Należy zwrócić uwagę, że linie zmieniają kolory zgodnie ze zmianą b) parametru asymetrii η i c) głównej składowej tensora gradientu pola elektrycznego V_{zz} , podczas gdy wartości niezmienników nie zmieniają się. Oznacza to, że widmo mössbauerowskie pokazane w części a) pozostaje niezmienione.

Powyżej opisana procedura zastosowana została do opracowania pomiarów dla stopu UFe_5Sn , UFe_4Al_8 oraz γ -FeMn. Szczegółowe wyniki uzyskane tą metodą dla związku

międzymetalicznego UFe_5Sn wykazującego reorientację lokalnych momentów magnetycznych w funkcji temperatury przedstawione są w paragrafie 4.1.3.

3.3. Metoda otrzymywania przekroju czynnego [P16]

Najczęściej stosowanym sposobem analizy widm mössbauerowskich jest ich opis jako superpozycji lorentzowskich linii absorpcyjnych lub zbioru sekstetów. Większość stosowanych metod pracuje w tzw. przybliżeniu cienkiego absorbenta i dobrze pracuje w przypadku gdy interesujemy się informacjami związanymi ze skalą prędkości. Informacje o natężeniach składowych opisujących widmo absorpcyjne są obciążone systematycznymi błędami jeśli grubość efektywna absorbenta przekracza $t > 1$. Jest to spowodowane nieliniową zależnością obserwowanych natężeń składowych od efektywnego parametru grubości t . Stosowanie zatem przybliżenia cienkiego absorbenta będzie prowadziło do systematycznych błędów rekonstruowanych pól nadsubtelnych i ewentualnie pojawiania się niefizycznych rozwiązań. Z tych powodów wygodniej byłoby pracować na przekroju czynnym na absorpcję $\sigma(E)$, który wolny jest od wpływu skończonej grubości absorbenta jak i wpływu funkcji aparaturowej na mierzone widma.

Metodę obliczania przekroju czynnego na podstawie mierzonych widm absorpcyjnych opublikowałem w pracy [P16]. Widma mössbauerowskie mierzone w geometrii transmisyjnej przy założeniu cienkiego źródła można przedstawić w postaci [Mar]:

$$S(V) = C \left(1 - f_s + f_s \frac{\Gamma_s}{2\pi} \int_{-\infty}^{\infty} \frac{1}{(E - V)^2 + \Gamma_s^2 / 4} e^{-t\sigma(E)} dE \right) \quad (3.3.1)$$

gdzie

C	stała zależna od geometrii eksperymentu, absorpcji elektronowej próbki, aktywności użytego źródła,
f_s	współczynnik emisji bezodrzutowej źródła,
Γ_s	szerokość połowkowa źródła,
V	przesunięcie Dopplera pomiędzy źródłem i absorbentem,
$\sigma(E)$	przekrój czynny na rozpraszanie,
t	efektywny parametr grubości absorbenta:

$$t = \sigma_0 f_s n, \quad (3.3.2)$$

gdzie

σ_0	przekrój czynny na absorpcję,
f_a	współczynnik emisji bezodrzutowej ^{57}Fe w absorbencie,
n	liczba atomów ^{57}Fe na jednostkę powierzchni absorbenta.

Przekrój czynny na rozpraszanie jest proporcjonalny do sumy linii Lorenzowskich z warunkiem normalizacji natężeń w postaci:

$$\sigma(E) = \sum_{i=1}^n \frac{a_i \Gamma_a \Gamma_0 / 4}{(E - E_i)^2 + \Gamma_a^2 / 4}, \quad \sum_{i=1}^n a_i = 1 \quad (3.3.3)$$

W przypadku ciągłych rozkładów pól nadsubtelnych powyższe wzory wyraża się przez całki

$$\sigma(E) = \int_{-\infty}^{\infty} \frac{a(x) \Gamma_a \Gamma_0 / 4}{(E - x)^2 + \Gamma_a^2 / 4} dx, \quad \int_{-\infty}^{\infty} a(x) dx = 1 \quad (3.3.4)$$

gdzie Γ_0 – szerokość naturalna linii równa 0.097 mm/s,

Γ_a - szerokość połówkowa linii absorpcyjnych, która zawiera ewentualne poszerzenia linii.

Ze względu na warunek normalizacji amplitud linii, normalizacja na przekrój czynny przedstawia się w postaci

$$\int_{-\infty}^{\infty} \sigma(E) dE = -\frac{\pi \Gamma_0}{2} \quad (3.3.5)$$

Celem całej procedury jest obliczenie przekroju czynnego $\sigma(E)$ z mierzonego widma absorpcyjnego $S(V)$ wyrażonego równaniem 3.3.1. Efektywną grubość użytego absorbenta można obliczyć ze składu próbki i ilości atomów Fe przypadających na jednostkę powierzchni próbki. Wielkość C wyznaczamy z widma absorpcyjnego daleko od rezonansu. Parametr f_s występujący w równaniu 3.3.1 z powodów skończonej zdolności rozdzielczej detektora jak i istnienia nierezonansowego tła jest mniejszy niż czynnik Lamba-Mössbauera. W praktyce zatem f_s zależy od warunków eksperymentu i musi być wyznaczony dla każdego pomiaru.

Zdefiniujmy funkcję $Y^*(x, \Gamma)$ jako dekonwolucję $Y(V)$ z funkcją Lorentza

$$Y(V) = \frac{\Gamma}{2\pi} \int_{-\infty}^{\infty} \frac{1}{(V - x)^2 + \Gamma^2 / 4} Y^*(x, \Gamma) dx, \quad (3.3.7)$$

Funkcję $Y^*(x, \Gamma)$ uzyskuje się poprzez dekonwolucję $Y(v)$ i można wyrazić w postaci operatora F_Γ działającego na Y :

$$Y^*(x, \Gamma) = F_\Gamma[Y](x) \quad (3.3.8)$$

Zdefiniujmy znormalizowane widmo absorpcyjne $s(V)$ jako:

$$s(V) = 1 - \frac{S(V)}{C} \quad (3.3.9)$$

Tak opisane widmo jest dodatnio określone i może być przedstawione w postaci:

$$s(V) = f_s \frac{\Gamma_s}{2\pi} \int_{-\infty}^{\infty} \frac{1}{(E-V)^2 + \Gamma_s^2/4} (1 - e^{-t\sigma(E)}) dE \quad (3.3.10)$$

Na takim widmie można przeprowadzić procedurę dekonwolucji otrzymując równanie:

$$1 - e^{-t\sigma(E)} = \frac{1}{f_s} F_{\Gamma_s} [s](E) \quad (3.3.11)$$

Zatem przekrój czynny wyraża się wzorem:

$$\sigma(E) = \frac{-1}{t} \ln \left(1 - \frac{1}{f_s} F_{\Gamma_s} [s](E) \right) \quad (3.3.12)$$

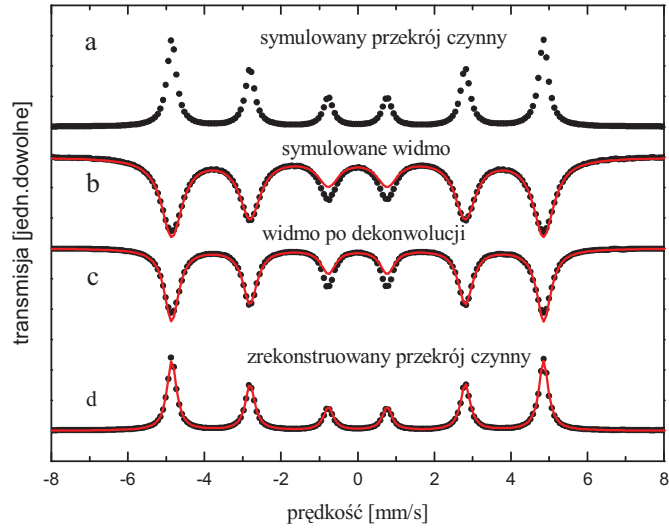
Korzystając z warunku normalizacyjnego na przekrój czynny otrzymujemy równanie w postaci:

$$\int_{-\infty}^{\infty} \ln \left(1 - \frac{1}{x} F_{\Gamma_s} [s](E) \right) dE = -\frac{\pi \Gamma_o t}{2} \quad (3.3.13)$$

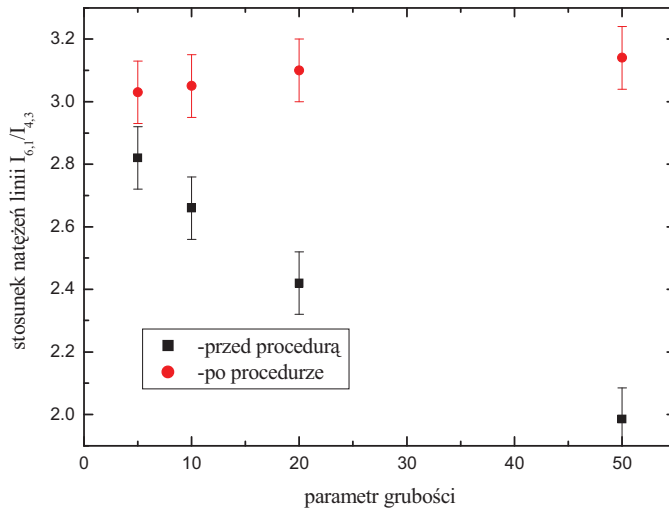
W celu otrzymania przekroju czynnego należy:

- wyznaczyć wartość Γ_s z niezależnego eksperymentu kalibracji α -Fe. Analizę kalibracji przeprowadzamy stosując całkę transmisji przy założeniu, że $\Gamma_a = \Gamma_o$. Otrzymywane wartości Γ_s są zwykle większe niż Γ_o z powodu poszerzeń występujących w źródle,
- przeprowadzić dekonwolucję funkcji aparaturowej na mierzonym widmie absorpcyjnym,
- uzyskać $f_s = x$ poprzez rozwiązanie numeryczne równania (3.3.13),
- obliczyć przekrój czynny na podstawie równania (3.3.12).

W pracy [P16] zastosowano i przetestowano metodę otrzymywania przekroju czynnego dla symulowanych widm o parametrze grubości t w granicach 5 do 50. Na rysunku 3.3.1. przedstawiono wynik całej analizy dla założonych parametrów $t = 10$, $\Gamma_a = 0.30$ mm/s, $\Gamma_s = 0.15$ mm/s. Linia ciągła oznacza najlepsze dopasowanie w przybliżeniu cienkiego absorbenta. Jak widać istnieją wyraźne niedopasowania na liniach 3, 4 dla widma symulowanego jak i po dekonwolucji (rysunek 3.3.1.b, c). Jest to widoczny wpływ parametru grubości na względne natężenia linii. Po zastosowaniu procedury otrzymywania przekroju czynnego ten efekt jest niewidoczny. Świadczy to o poprawności zastosowanej procedury. Na rysunku 3.3.2. przedstawione są względne stosunki natężeń $I_{6,1}/I_{4,3}$ w funkcji parametru grubości otrzymane przy zastosowaniu przybliżenia cienkiego absorbenta dla symulowanych widm i analizy rekonstruowanych przekrojów czynnych. Widać, że efekty związane z parametrem grubości są bardzo istotne dla widm symulowanych z $t > 5$ podczas gdy dla wszystkich rekonstruowanych $\sigma(E)$ stosunek $I_{6,1}/I_{4,3}$ jest w granicach błędu równy 3, jak przewiduje teoria.

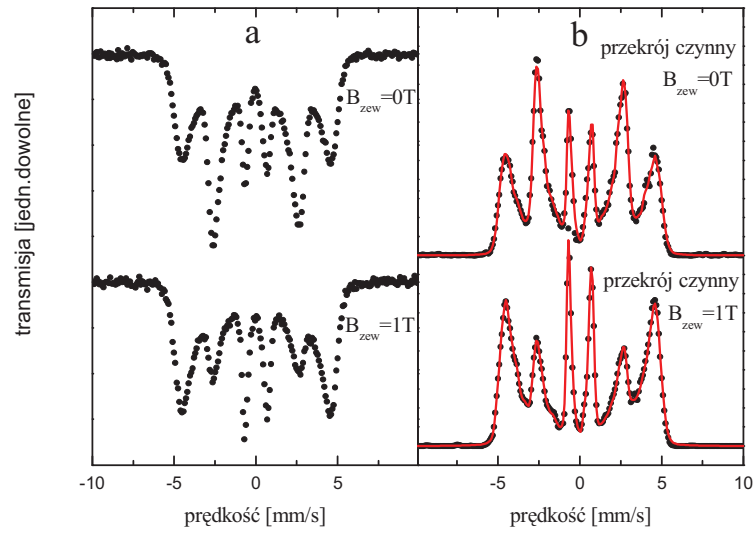


Rys.3.3.1. a) Symulowany przekrój czynny, b) widmo mössbauerowskie, c) jego dekonwolucja i d) wynik rekonstrukcji. Linia ciągła reprezentuje najlepsze dopasowanie w przybliżeniu cienkiego absorbenta.



Rys.3.3.2. Względne natężenia $I_{1,6}/I_{3/4}$ przed i po procedurze otrzymywania przekroju czynnego.

Wyżej opisana procedura zastosowana została do rekonstrukcji $\sigma(E)$ z widm stopów inwarowych Fe-Ni mierzonych bez zewnętrznego pola magnetycznego jak i mierzonych w zewnętrznym polu magnetycznym równoległym do kierunku propagacji promieniowania gamma (rysunek 3.3.3.). Tak otrzymane $\sigma(E)$ zostały następnie użyte do rekonstrukcji rozkładu $P(B, IS, z)$. Wyniki przeprowadzonej rekonstrukcji przedstawione są w paragrafie 4.1.2.



Rys.3.3.3. a) Widma mössbauerowskie, b) przekroje czynne stopu Fe-Ni mierzonego bez zewnętrznego pola i w zewnętrznym polu magnetycznym równoległym do kierunku promieniowania gamma.

4. Zastosowanie polarymetrii mössbauerowskiej oraz nowych metod analizy danych

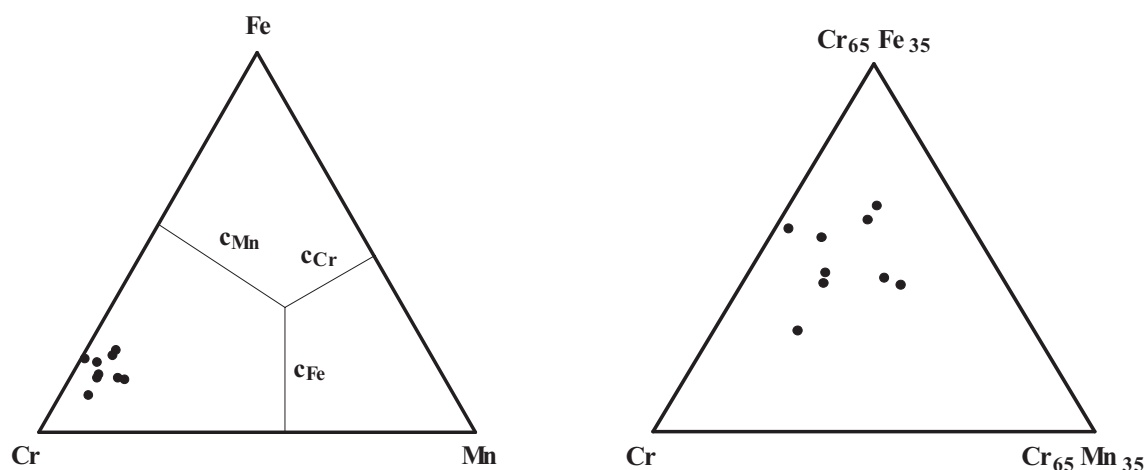
Wszystkie wyżej opisane metody analizy danych jak i polarymetria mössbauerowska zostały wykorzystane do opisu układów nieuporządkowanych magnetycznie. Ze względu na ogólność wprowadzonych metod zostały one zastosowane zarówno do układów litych jak i nanomateriałów.

4.1. Materiały lite

4.1.1. Układ Cr-Fe-Mn [P1, P2, P3]

Układy trójskładnikowe Cr-Fe-Mn ze względu na własności elektronowe występujących pierwiastków powinny charakteryzować się występowaniem konkurencyjnych oddziaływań wymiennych [Das], a tym samym współistnieniem różnych faz uporządkowania magnetycznego oraz dużym magnetooporem [Xu, Wu]. Materiały wykazujące duży magnetoopór stanowią interesujący przedmiot badań z uwagi na ich potencjalne wykorzystanie w dziedzinie zapisu informacji. Trójskładnikowe stopy Cr-Fe-Mn wykazują bardzo skomplikowane własności magnetyczne, które nie są do końca poznane [Ace, Ace1, Xu1, Tsu].

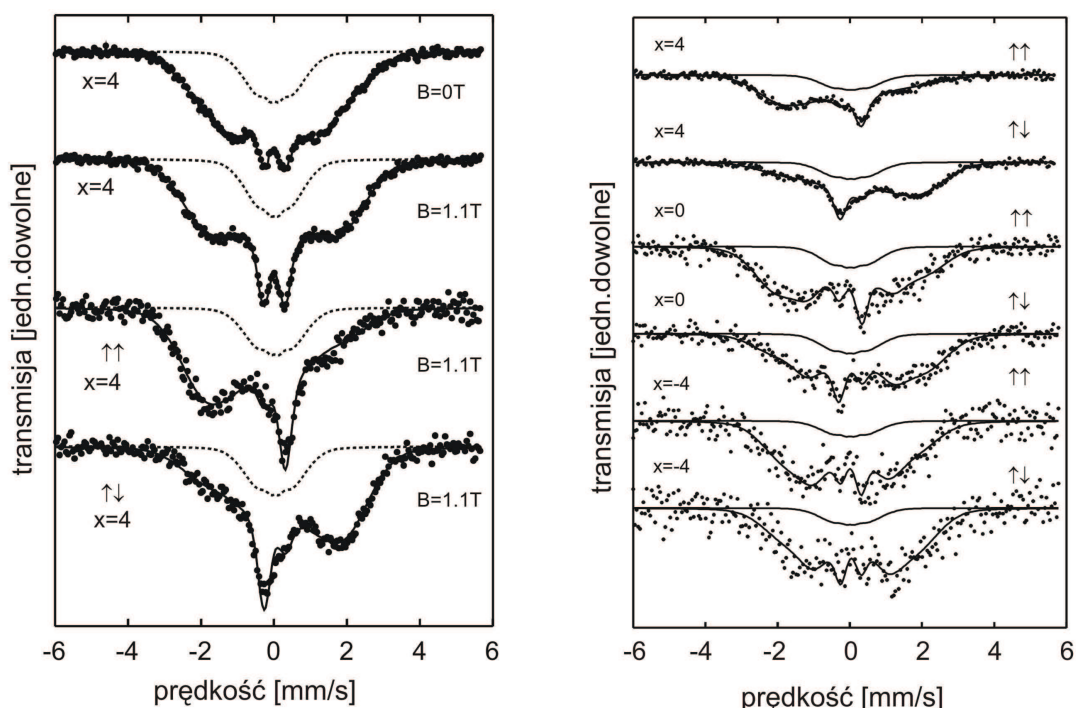
Wykonano dwie serie próbek: $\text{Cr}_{75+x}\text{Fe}_{16+x}\text{Mn}_{9-2x}$ oraz $\text{Cr}_{75+y}\text{Fe}_{16-y}\text{Mn}_9$. Pierwsza seria obejmuje próbki o stałej koncentracji elektronów $3d+4s$ (6.41 elektronów/atom), przy której zaobserwowano zjawisko gigantycznego magnetooporu w stopach $\text{Cr}_{75}(\text{Fe}_x\text{Mn}_{1-x})_{75}$. Druga seria charakteryzuje się maksymalną, w ramach układu trójskładnikowego Cr-Fe-Mn, zmianą koncentracji elektronów $3d+4s$: $dn_{3d+4s}/dy = -0.02$. W pierwszej serii próbek zmiany koncentracji Mn skorelowane są ze zmianą koncentracji elektronów, natomiast druga seria próbek charakteryzuje się stałą koncentracją Mn. Celem badań układów Cr-Fe-Mn było zbadanie czy niejednorodności namagnesowania związane są ze strukturą elektronową i oddziaływaniami wymiennymi, czy też raczej z niejednorodnościami składu lub efektami bliskiego zasięgu. Na rysunku 4.1.1.1 prezentowane są położenia wybranych do badań koncentracji stopów na trójskładnikowym diagramie Fe, Cr, Mn.



Rys.4.1.1.1. Koncentracje trójskładnikowych próbek $Cr_{75+x}Fe_{16+x}Mn_{9-2x}$ i $Cr_{75+y}Fe_{16-y}Mn_9$ na trójskładnikowym diagramie.

Wyniki badań przedstawione są w publikacjach [P1, P2, P3], będących częścią prezentowanej rozprawy habilitacyjnej. Badania mössbauerowskie wykonane w temperaturze pokojowej wykazały istnienie w widmach poszerzonej pojedynczej linii absorpcyjnej. Analiza wyników pokazała, iż omawiane poszerzenie da się ilościowo wyjaśnić dla wszystkich badanych składów przy założeniu, że atomy Cr i Mn są źródłem stałego, niezależnego od koncentracji wkładu do zmiany przesunięcia izomerycznego jak i rozszczepienia kwadropolowego. Badania z użyciem zewnętrznego pola magnetycznego pokazały, że próbki z najmniejszą koncentracją żelaza ($y = 6, x = -4$) wykazują dodatkowe poszerzenie będące wynikiem stanu antyferromagnetycznego, charakterystycznego dla stopów o strukturze *bcc* bogatych w Cr.

Najistotniejszą odpowiedź na temat uporządkowania magnetycznego i wpływu atomów Fe i Mn w zaburzeniu antyferromagnetycznego uporządkowania Cr dały pomiary mössbauerowskie przeprowadzone w niskich temperaturach oraz badania z użyciem promieniowania spolaryzowanego kołowo. Badania te wykazały, że w temperaturze 12 K (poniżej T_c lub T_f) na części atomów Fe tworzy się lokalny moment magnetyczny o wielkości $1 \mu_B$. Moment ten wykazuje wyraźną reakcję na przyłożone zewnętrzne pole magnetyczne. Wyznaczono ilościowy wkład momentów magnetycznych Fe do namagnesowania. W próbkach o niskiej koncentracji Fe rozkład kątowy zbliżony jest do rozkładu izotropowego. Efekt ten widoczny jest na rysunku 4.1.1.2.



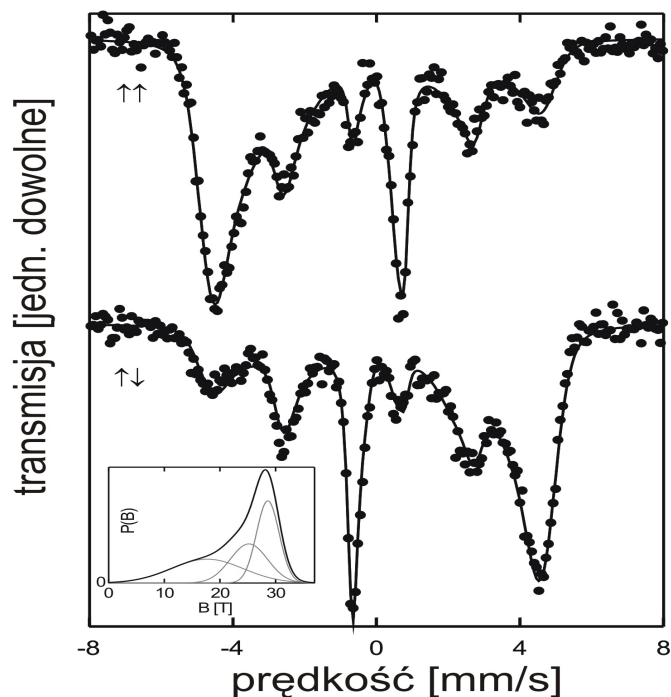
Rys.4.1.1.2. Wybrane widma mössbauerowskie stopów Cr-Fe-Mn mierzone w $T=12\text{ K}$ w zewnętrznym polu magnetycznym równoległym do kierunku promieniowania gamma dla wiązki niespolaryzowanej i spolaryzowanej kołowo.

W miarę zbliżania się do próbek o dużej koncentracji Fe obserwowany jest coraz większy wpływ zewnętrznego pola magnetycznego na uporządkowanie momentów Fe, a więc ich większy wkład do namagnesowania. Pomiar z użyciem promieniowania spolaryzowanego kołowo wykazały istnienie około 10% Fe z małym momentem magnetycznym ($0.1\ \mu_B$ - $0.3\ \mu_B$). Widma mössbauerowskie otrzymane z użyciem promieniowania spolaryzowanego kołowo odpowiadające tym atomom, wykazują brak asymetrii charakterystycznej dla pomiarów Fe uporządkowanych ferromagnetycznie. Oznacza to, że momenty te są albo rozłożone izotropowo albo tworzą strukturę antyferromagnetyczną i tym samym nie dają wkładu do namagnesowania. Zostało pokazane, że atomy Fe niosące mały moment magnetyczny zawierają w swoim otoczeniu jedynie atomy chromu. Pojawienie się w najbliższym otoczeniu innego atomu Fe lub Mn prowadzi do powstania dużego lokalnego momentu magnetycznego. Ten bardzo ważny wniosek wskazuje na istotne różnice we wpływie Mn i Cr na tworzenie się momentu magnetycznego na żelazie. Kolejnym wnioskiem wynikającym z pomiarów mössbauerowskich i namagnesowania jest fakt, iż w niskich temperaturach i w zewnętrznym polu magnetycznym 1 T atomy Cr i Mn dają wkład do namagnesowania wielkości około 0.3 do $0.2\ \mu_B$. Prawdopodobnie jest to spowodowane tym, że atomy Fe polaryzują elektrony przewodnictwa najbliższego otoczenia – czyli antyferromagnetyczną matrycę.

4.1.2. Stop Fe-Ni [P4, P5, P16]

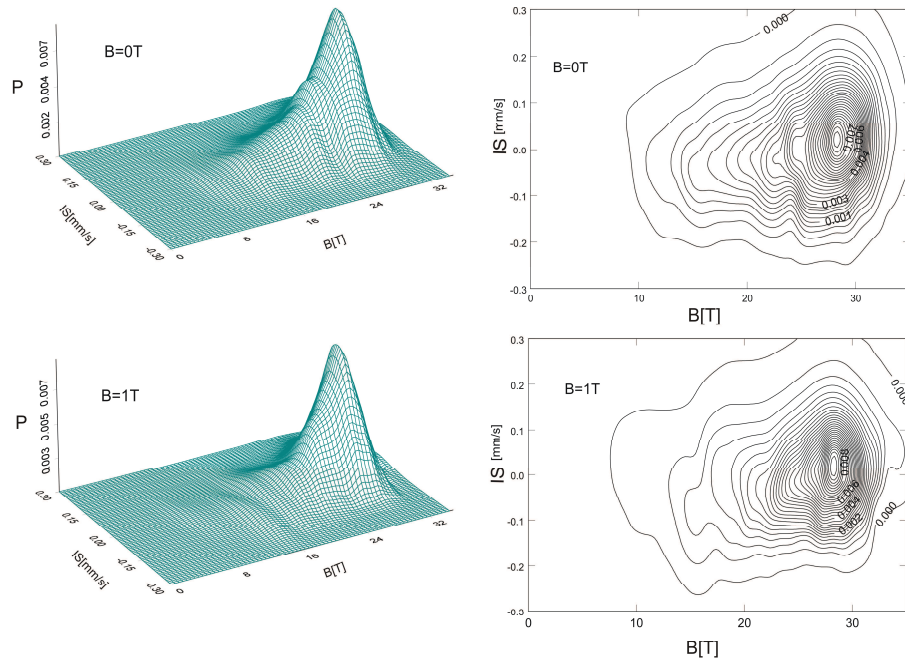
Problem zjawiska inwaru, występującego między innymi w stopach Fe-Ni dla koncentracji w pobliżu przejścia strukturalnego $fcc \leftrightarrow bcc$ ma już bardzo długą historię lecz w dalszym ciągu brak jest pełnego zrozumienia tego zjawiska. Istnieją w literaturze wyniki badań Fe-Ni przeprowadzone w wysokich ciśnieniach [Ruf] potwierdzające najbardziej popularny model przewidujący istnienie dwóch stanów atomów Fe w stopach Fe-Ni ($2-\gamma$ state model) zaproponowany przez Weissa [Wei]. Z drugiej strony, można znaleźć wyniki [Dub] potwierdzające istnienie nisko spinowego, niekolinearnego uporządkowania momentów magnetycznych atomów Fe zaproponowanego w pracy [Sch]. Badania neutronowe prezentowane w pracy [Bro] pokazały z kolei silne sprzężenie pomiędzy siecią krystaliczną i magnetycznymi własnościami stopów Fe-Ni w obszarze inwaru.

W pracach [P4, P5] zastosowana została polarymetria mössbauerowska z użyciem promieniowania spolaryzowanego kołowo w celu zbadania istnienia nisko spinowej niekolinearnej struktury magnetycznej związanej z atomami Fe w stopach Fe-Ni w obszarze występowania zjawisk inwarowych. Zmierzone widma stopu $Fe_{66}Ni_{34}$ w temperaturze pokojowej w zewnętrznym polu magnetycznym równoległym do kierunku promieniowania gamma przedstawione są na rysunku 4.1.2.1. Dopasowania uzyskano zakładając trzy gaussowskie rozkłady pola (patrz wstawka na rysunku 4.1.2.1). Linia ciągła oznacza najlepsze dopasowanie. Najistotniejszym rezultatem otrzymanym z opracowania jest fakt, że najlepsze dopasowanie uzyskano dla tych samych wartości parametrów tekstury magnetycznej $\langle \cos^2 \theta \rangle$ i nieznacznie różniących się wartości parametru $\langle \cos \theta \rangle$. Najmniejszą wartość parametru $\langle \cos \theta \rangle$ uzyskano dla składowej o najmniejszym polu nadsubtelnym. Analiza wyników pokazała, że składowa związana z najmniejszymi wartościami pól nadsubtelnych nie jest uporządkowana antyferromagnetycznie, jak postuluje model Weissa, ani nie wykazała przypadkowego rozporządkowania momentów magnetycznych atomów Fe jak postulowano w pracy [Sch].

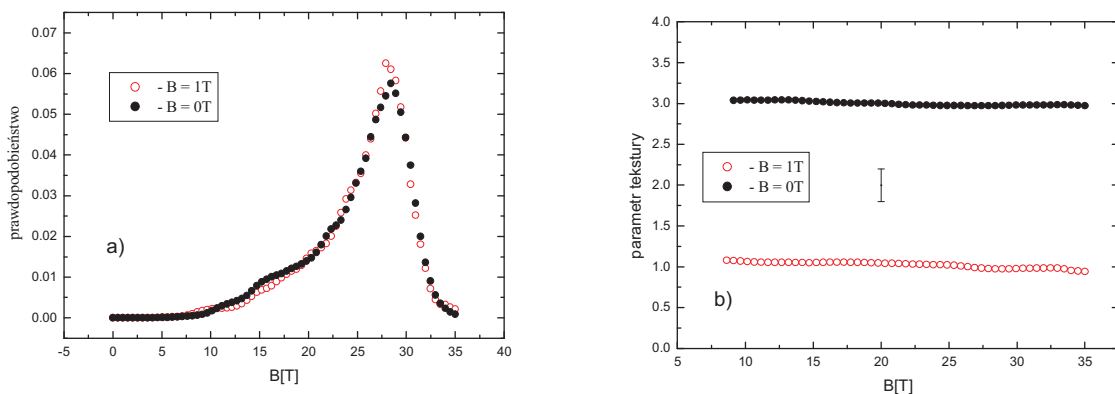


Rys.4.1.2.1. Widma mössbauerowskie stopu inwarowego $Fe_{66}Ni_{34}$ mierzone przy użyciu spolaryzowanego kołowo promieniowania gamma.

W omawianej analizie rozkład pola nadsubtelnego stopu Fe-Ni modelowany był jako superpozycja trzech rozkładów Gaussowskich co mogło mieć wpływ na otrzymane rezultaty. W pracy [P16] analiza stopu Fe-Ni polegała na zastosowaniu metody maksymalnej entropii do rekonstrukcji rozkładu $P(B, IS, z)$, metody niezależnej od zastosowanego modelu. W celu wyeliminowania ewentualnego wpływu parametru grubości na rekonstruowane rozkłady, do analizy wykorzystano przekroje czynne otrzymane metodą opisaną w paragrafie 3.3. Wyniki rekonstrukcji $P(B, IS)$ otrzymane dla $\sigma(E)$ w zewnętrznym polu magnetycznym $B=1 T$ równoległym do kierunku promieniowania gamma jak i pomiarów bez zastosowania zewnętrznego pola magnetycznego oraz zależności parametru tekstury magnetycznej prezentowane są na rysunkach 4.1.2.2 i 4.1.2.3.



Rys.4.1.2.2. Rozkłady prawdopodobieństwa $P(B, IS)$ i ich rzuty na płaszczyznę B, IS otrzymane metodą MEM dla pomiarów Fe-Ni w zewnętrznym polu magnetycznym i bez wewnętrznego pola magnetycznego.



Rys.4.1.2.3.a) Rozkłady prawdopodobieństwa $P(B)$ uzyskane metodą MEM dla pomiarów w polu i bez pola magnetycznego, b) zależności $z(B)$.

Otrzymana zależność $z(B)$ nie wykazała istotnych zmian parametru tekstury od wartości magnetycznego pola nadsubtelnego. Oznacza to, że nie obserwujemy różnych kątowych rozkładów momentów magnetycznych w stopach inwarowych Fe-Ni.

4.1.3. Związek międzymetaliczny UFe_5Sn [P12, P14, P15]

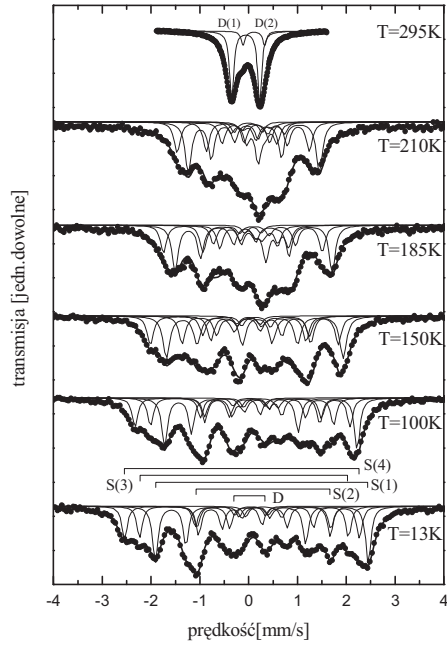
Związek międzymetaliczny UFe_5Sn krystalizuje w strukturze ortorombowej typu $CeCu_5Au$ (grupa przestrzenna $Pnma$) [Gon]. Komórka elementarna zawiera 4 atomy U w pozycjach $4c$, 4 atomy Sn w pozycjach $4c$, 8 atomów Fe (Fe1) w pozycjach $8d$ i 12 atomów

Fe w pozycjach $4c$ (Fe₂, Fe₃, Fe₄). Badania namagnesowania przeprowadzone na próbce proszkowej pokazały, że związek ten jest słabym ferromagnetykiem w temperaturze pokojowej i wykazuje dwa przejścia odpowiednio w temperaturach 248 K i 180 K. Pomiarów wykonanych na monokryształach pokazały, że przejście obserwowane w 248K związane jest z ferromagnetycznym uporządkowaniem momentów magnetycznych atomów Fe wzdłuż osi c , podczas gdy przejście obserwowane w temperaturze 180K prawdopodobnie związane jest z reorientacją momentów magnetycznych Fe w kierunku osi b . Badania mössbauerowskie tego związku przedstawione w pracy [Gon1] wykonane były na próbce proszkowej, a przeprowadzona analiza polegała na zastosowaniu rachunku zaburzeń pierwszego rzędu. Ponieważ w badanym związku oddziaływania kwadrupolowe nie są małe w stosunku do oddziaływań dipolowych magnetycznych konieczne jest w tym wypadku użycie pełnego Hamiltonianu jako właściwego podejścia do opisu mierzonych widm. Jak już wspomniałem w paragrafie 3.2 nie jest możliwe jednoznaczne wyznaczenie pól nadsubtelnych. Z tego powodu widma analizowaliśmy przy użyciu metody niezmienników opisanej w paragrafie 3.2 dającej jednoznaczny opis widm mössbauerowskich.

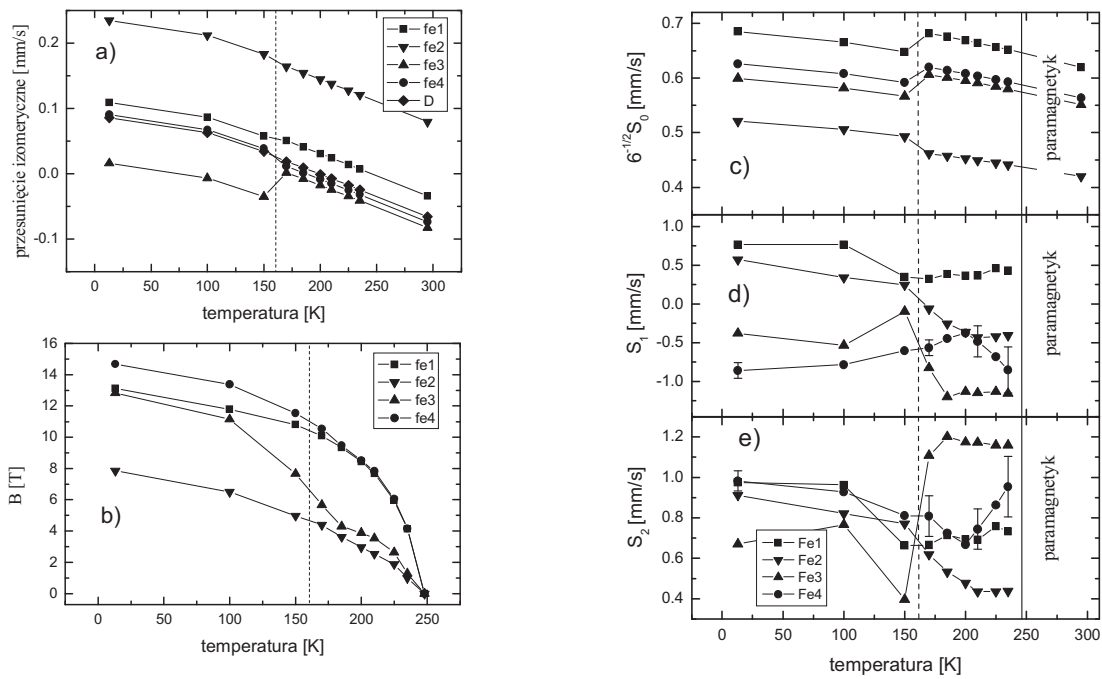
Pomiary temperaturowe przeprowadzone na próbce proszkowej przedstawione są na rysunku 4.1.3.1. Zastosowana metoda niezmienników pozwoliła na dobry opis mierzonych widm. Procedura dopasowania polegała na jednoczesnym dopasowaniu wszystkich widm przy następujących założeniach:

- względne natężenia sekstetów składowych trzymane były takie same dla wszystkich mierzonych widm,
- przesunięcie izomeryczne drugiego rzędu było przybliżone przy założeniu modelu Debye'a sieci krystalicznej przy tej samej charakterystycznej temperaturze dla wszystkich pozycji żelaza,
- założono zależność temperaturową gradientu pola elektrycznego zgodną z prawem $T^{3/2}$.

Ponieważ w temperaturze około 180 K możliwe jest przejście fazowe i związana z tym zmiana struktury magnetycznej, podczas dopasowania dopuszczona została możliwość skokowej zmiany przesunięcia izomerycznego jak i wartości rozszczepienia kwadrupolowego. Otrzymane wyniki parametrów nadsubtelnych jak i niezmienników przedstawione są na rysunku 4.1.3.2.



Rys.4.1.3.1. Widma mössbauerowskie UFe_5Sn mierzone w różnych temperaturach. Linia ciągła przedstawia najlepsze dopasowanie za pomocą niezmienników.



Rys.4.1.3.2. Rezultaty otrzymane z analizy metodą niezmienników wyników otrzymanych dla stopów UFe_5Sn a) przesunięcia izomerycznego, b) magnetycznego pola nadsubtelnego, c) d) e) odpowiednio niezmienników S_0 , S_1 i S_2 .

Wyniki analizy pokazały, że:

- nadsubtelne pole magnetyczne związane z pozycją Fe³⁺ maleje ze wzrostem temperatury znacznie szybciej niż pole dla pozostałych atomów Fe. Największe zmiany obserwowane są w temperaturach około 170 K,
- obserwowany jest brak ciągłości zmian niezmienników S_1 i S_2 w funkcji temperatury dla atomów Fe³⁺. Oznacza to zmiany orientacji momentu magnetycznego Fe³⁺ w stosunku do osi głównych tensora gradientu pola elektrycznego,
- niezmiennik S_0 wykazuje wyraźną nieciągłość w pobliżu temperatury 170K co można wiązać ze zmianą struktury elektronowej badanego związku.

4.2. Materiały nanometrowe

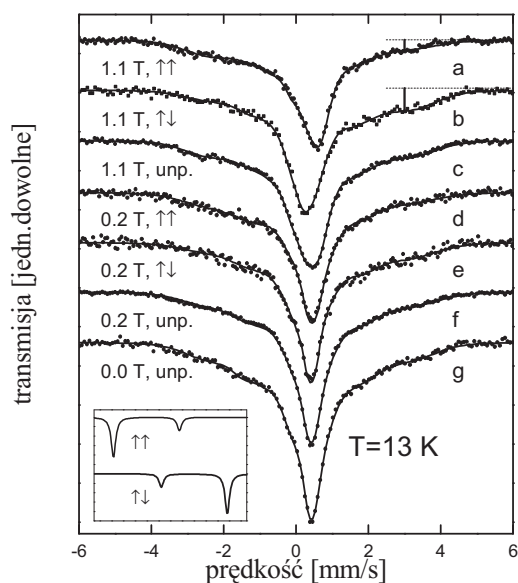
4.2.1. Stop Fe-Al [P8, P9, P10]

Stopy międzymetaliczne Fe-Al są w dalszym ciągu bardzo interesującym obiektem badań z punktu widzenia podstawowych badań magnetyzmu. Dostępna literatura dotycząca tych stopów jest pełna kontrowersji dotyczących uporządkowania magnetycznego, lokalnych momentów magnetycznych i dynamiki spinów, w szczególności dla koncentracji Al w okolicach Fe_{0.5}Al_{0.5} [Shi]. W przypadku Fe-Al średni moment magnetyczny stopu gwałtownie maleje dla koncentracji Al większych od 20% at., a ekstrapolowana wartość osiąga zero w okolicach 34% at. W obszarze 35% at. do 43% at. stop wykazuje stan antyferromagnetyczny [Sat, Huf]. Inne prace pokazują, że dla składu w okolicach Fe_{0.5}Al_{0.5} w dalszym ciągu stop wykazuje zachowanie ferromagnetyczne. W przypadku stopów rozporządkowanych stan ferromagnetyczny obserwowany jest do koncentracji 70% at. Al [Bes, Shi1, Kul]. Pomiary dyfrakcji neutronów pokazały dla koncentracji 50% at. Al istnienie niewspółmiernych z siecią fal gęstości spinowych [Noa]. W pracach [Arz, Arz1] autorzy pokazali, że momenty magnetyczne atomów Fe otoczonych przez dużą liczbę atomów Al (sześć i więcej) mogą wykazywać frustrację.

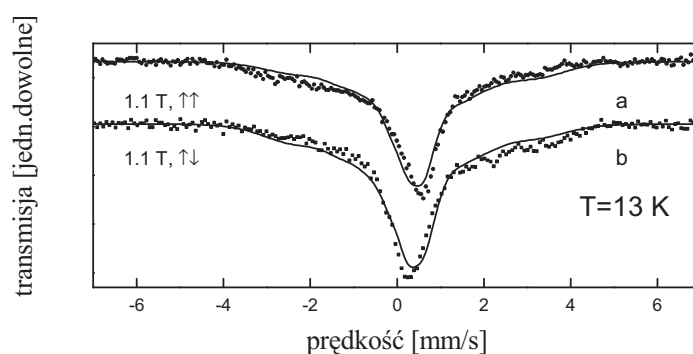
Kontrowersje występujące w literaturze oraz wyraźny wpływ uporządkowania jak i homogeniczności stopów Fe-Al na makroskopowe jak i lokalne własności magnetyczne skłoniły nas do badań nanokrystalicznego stopu Fe₄₈Al₅₂. Doskonałą metodą z punktu widzenia lokalnego magnetyzmu badanych stopów jest polarymetria mössbauerowska. Jest

ona czuła na znak nadsubtelnego pola magnetycznego atomów Fe i pozwala na określenie rozkładu momentów magnetycznych oraz obliczenie wkładu lokalnego momentu magnetycznego do namagnesowania.

W pracach [P8, P9, P10] przedstawione zostały wyniki pomiarów nanokrystalicznego stopu $\text{Fe}_{48}\text{Al}_{52}$. Widma mössbauerowskie mierzone w temperaturze 13 K z użyciem wiązki promieniowania gamma spolaryzowanej i niespolaryzowanej dla dwóch wartości zastosowanego zewnętrznego pola magnetycznego 1.1 T i 0.2 T przedstawione są na rysunku 4.2.1.1.



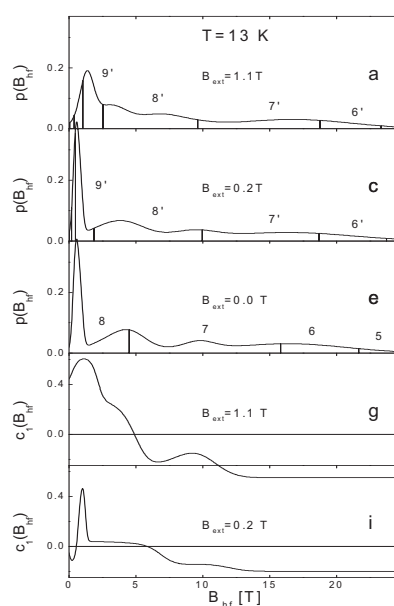
Rys.4.2.1.1. Widma mössbauerowskie uzyskane przy użyciu spolaryzowanego i niespolaryzowanego promieniowania gamma w osiowym zewnętrznym polu magnetycznym. Linia ciągła oznacza najlepsze jednoczesne dopasowanie przy tych samych wartościach IS , QS .



Rys.4.2.1.2. Widma mössbauerowskie mierzone z użyciem promieniowania spolaryzowanego kołowo. Linia ciągła oznacza najlepsze dopasowanie przy założeniu, że kątowy rozkład wektora B nie zależy od jego wartości.

Jak pokazała przeprowadzona analiza nie można poprawnie dopasować widm przy założeniu, że $c_1 = \langle \cos \theta \rangle$ i $c_2 = \langle \cos^2 \theta \rangle$ mają te same wartości dla całego rozkładu pola $P(B)$. Na rysunku 4.2.1.2. przedstawione są widma z dopasowaniem przy powyższym założeniu. Jak widać linia najlepszego dopasowania nie pasuje do wyników doświadczalnych. Dopuszczenie zależności $c_1(B)$ pozwoliło na dobre dopasowanie. Otrzymane rozkłady $P(B)$ i $c_1(B)$ przedstawione są na rysunku 4.2.1.3. Kluczowym wnioskiem wynikającym z przeprowadzonej analizy danych widm mierzonych z użyciem wiązki promieniowania gamma spolaryzowanej kołowo jest otrzymana zależność $c_1(B)$ czyli wyraźna zależność kątowych rozkładów magnetycznych pól nadsubtelnych od ich wartości a więc i składu najbliższego otoczenia. Należy podkreślić, że wynik ten bardzo trudno byłoby otrzymać innymi metodami. Parametr $c_1(B)$ odpowiadający polom nadsubtelnym większym od 5 T ma wartości ujemne (tak jak w przypadku α -Fe) podczas gdy dla pól mniejszych od 5 T przyjmuje wartości dodatnie, co oznacza lokalnie różny rozkład momentów magnetycznych atomów Fe.

Otrzymane rozkłady pól nadsubtelnych opisane zostały w języku modelu lokalnego otoczenia. Przyporządkowanie najbliższego otoczenia jest względnie proste, gdy atomy Fe otoczone przez $(n-k)$ atomów Fe i k innych atomów charakteryzuje dobra separacja rozkładów ich pól $P(B)$. Niestety nie jest to reguła i tak w przypadku stopów Fe-Al dobrze rozdzielone piki w $P(B)$ odpowiadające lokalnym otoczeniom nie są widoczne.

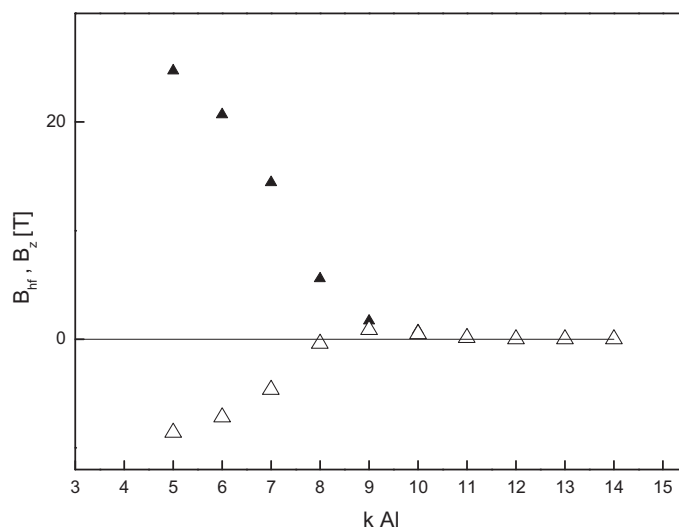


Rys.4.2.1.3. Rozkłady pól nadsubtelnych otrzymanych z widm mierzonych dla różnych zewnętrznych pól magnetycznych.

W celu podziału $P(B)$ na wkłady związane z najbliższym otoczeniem założyliśmy, że pole nadsubtelne rośnie ze wzrostem liczby Fe w pierwszych dwóch strefach koordynacyjnych. Jak pokazały wyniki EXAFS prawdopodobieństwa znalezienia atomu Fe w pierwszej i drugiej strefie koordynacyjnej jest określone przez $x_I = 0.8/8$ i $x_{II} = 5.3/6$. Zakładając przypadkowy rozkład Fe w strefach koordynacyjnych, prawdopodobieństwo $P(k)$, że atom Fe jest otoczony przez $(14 - k)$ atomów Fe i k atomów Al w dwóch pierwszych strefach jest opisane równaniem:

$$P(k) = \sum_{i,j,i+j=k} \binom{8}{j} \binom{6}{i} x_I^{8-j} (1-x_I)^j x_{II}^{6-i} (1-x_{II})^i \quad (4.2.1.1)$$

Założenie to pozwoliło rozdzielić $P(B)$ na kilka sekcji, każda o polu powierzchni proporcjonalnym do prawdopodobieństwa $P(k)$. Tak określone sekcje są przedstawione na rysunku 4.2.1.3 przez pionowe linie dla odpowiednich ilości atomów Al będących w obu strefach. Zrobiony podział pozwala na wyznaczenie średnich wartości pola nadsubtelnego $B_{hf}(k)$ jak i średnich wartości składowych pola nadsubtelnego $B_z(k)$ w kierunku zastosowanego zewnętrznego pola magnetycznego. Wyniki przedstawione są na rysunku 4.2.1.4.



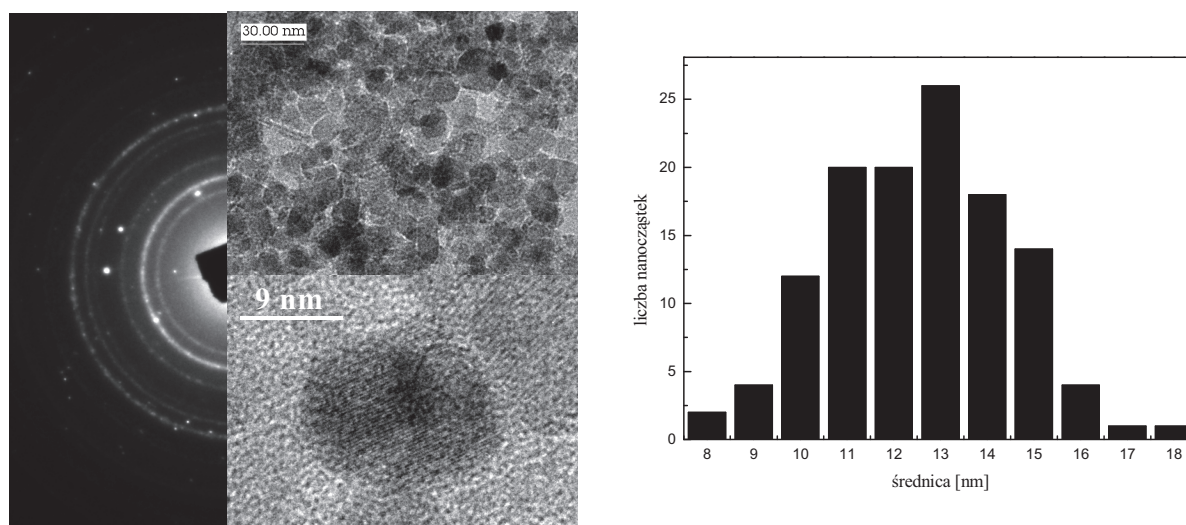
Rys.4.2.1.4. Zależność średniego magnetycznego pola nadsubtelnego (symbole pełne) i składowej na kierunek magnetyzacji (symbole puste) w funkcji liczby atomów Al w pierwszych dwóch strefach koordynacyjnych.

4.2.2. Nanocząstki magnetytu [P13]

Magnetyczne nanocząstki cieszą się dużym zainteresowaniem ze względu na niespotykane wcześniej własności, różne od obserwowanych w ciałach litych [Dor]. W przypadku obiektów o nanometrowych rozmiarach istotne stają się efekty powierzchniowe, które bardzo silnie zmieniają ich własności magnetyczne. Fundamentalne mechanizmy, które rządzą zachowaniem się nanocząstek są związane z własnościami samych nanocząstek, takimi jak defekty i mikrostruktura oraz kolektywnymi oddziaływaniami pomiędzy zespołami nanocząstek. Bardzo często prowadzi to do rozporządkowania momentów magnetycznych na powierzchni nanocząstek [Coe, Mor]. Oddziaływania obecne w zespole nanocząstek prowadzą z kolei do wygaszania relaksacji superparamagnetycznych i mogą prowadzić do uporządkowania typu szkła spinowego w niskich temperaturach [Mor1, Sun].

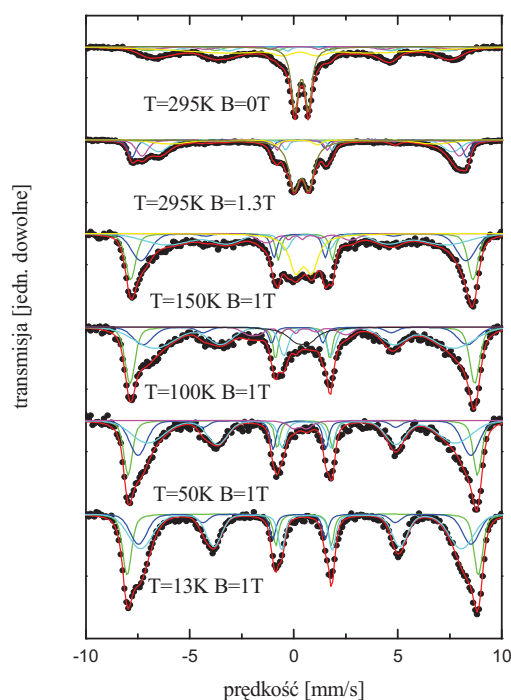
W pracy [P13] badany był wpływ mikrostruktury na własności magnetyczne nanocząstek magnetytu od temperatury $T=13$ K do temperatury pokojowej oraz wpływ na własności magnetyczne i mikrostrukturę wygrzewania nanocząstek w powietrzu. Wygrzewanie nanocząstek magnetytu prowadzone w powietrzu powinno prowadzić do transformacji magnetyt-maghemit-hematyt, co prowadzi do stopniowej zmiany mikrostruktury badanych nanocząstek, a tym samym zmiany ich własności magnetycznych. Badane nanocząstki magnetytu syntetyzowane były chemicznie w oparciu o metodę Massarta [Mas].

Na rysunku 4.2.2.1 przedstawione są wyniki otrzymane przy użyciu transmisyjnego mikroskopu elektronowego (*TEM*). Oszacowana średnia wartość rozmiaru nanocząstek wynosiła (12.8 ± 1.5) nm.



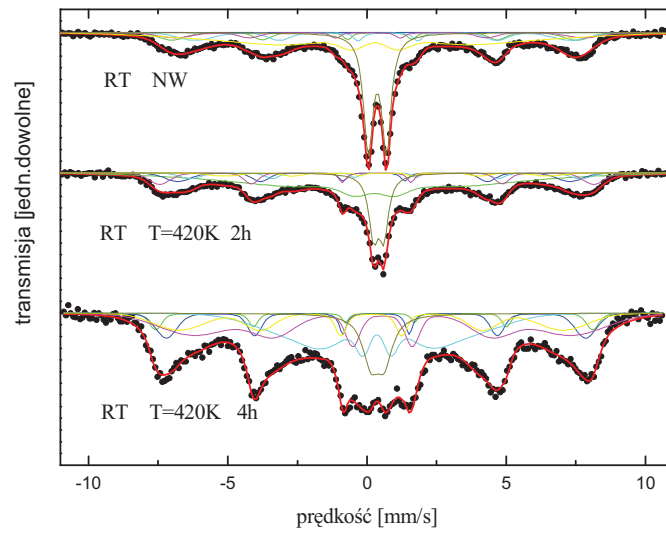
Rys.4.2.2.1 Obraz TEM badanych nanocząstek i rozkład ich rozmiarów.

Na rysunku 4.2.2.2 przedstawione są widma Mössbauera nanocząstek magnetytu mierzone w funkcji temperatury i w zewnętrznym polu magnetycznym równoległym do kierunku promieniowania gamma. Analiza widm mierzonych w pokojowej temperaturze pokazała istnienie szerokiej składowej magnetycznej i dubletu kwadrupolowego. Pomiar w zewnętrznym polu magnetycznym powoduje wyostrenie linii w składowej magnetycznej. Możliwe staje się identyfikacja lokalnych otoczeń atomów Fe. Dublet kwadrupolowy praktycznie nie uległ zmianie. Wraz ze zmniejszaniem się temperatury wkład dubletu kwadrupolowego stopniowo zmniejsza się, a w składowej magnetycznej pojawiają się wyraźne linie 2, 5 świadczące o istnieniu rozporządkowanych momentów magnetycznych Fe. Zachowanie takie interpretujemy jako stopniowe tłumienie relaksacji superparamagnetycznych i jednocześnie formowanie się rozporządkowanej struktury magnetycznej.



Rys.4.2.2.2. Widma Mössbauera nanocząstek magnetytu w funkcji temperatury mierzone w zewnętrznym polu magnetycznym równoległym do kierunku promieniowania gamma.

Na rysunku 4.2.2.3 przedstawione są widma nanocząstek magnetytu mierzone po zastosowaniu różnych procedur wygrzewania w powietrzu. Rezultaty pokazują zmniejszanie się wkładu związanego z dubletem co świadczy o zmianie mikrostruktury nanocząstek jak i o zmianie oddziaływań pomiędzy nanocząstkami.



Rys.4.2.2.3. Widma mössbauerowskie mierzone w temperaturze pokojowej dla różnych procedur wygrzewania przeprowadzonych w powietrzu.

5. Podsumowanie

W niniejszej pracy przedstawione zostały moje podstawowe osiągnięcia w obszarze metodologii związanej z rozwojem nowych metod analizy danych doświadczalnych w spektroskopii mössbauerowskiej jak i rozwoju polarymetrii mössbauerowskiej. Wprowadzone nowe metody analizy danych i metoda polarymetrii mössbauerowskiej zostały z powodzeniem zastosowane do układów magnetycznie nieuporządkowanych.

W pracy pokazana została użyteczność polarymetrii mössbauerowskiej, dzięki której zbadaliśmy wiele aspektów związanych z lokalnymi własnościami magnetycznymi badanych układów. Wymagało to bardzo rzetelnej analizy danych i zastosowania algorytmów, w których zmierzone widma analizowane były jednocześnie. Taka analiza danych otrzymywanych z wykorzystaniem polarymetrii mössbauerowskiej, klasycznej spektroskopii mössbauerowskiej, pomiarów w zewnętrznym polu magnetycznym i pomiarów temperaturowych pozwoliła na możliwie jednoznaczną interpretację wyników.

Wprowadzona przeze mnie metoda niezmienników pozwala na interpretację wyników otrzymanych dla układów, w których występują mieszane oddziaływania kwadrupolowe elektryczne i dipolowe magnetyczne uznawane za bardzo trudne do interpretacji. Ponadto, ogólność metody niezmienników pozwala na ewentualne porównywanie wyników eksperymentalnych i tych wynikających z obliczeń teoretycznych.

Kolejnym bardzo ważnym elementem metodologicznym wprowadzonym przeze mnie jest zastosowanie metody maksymalnej entropii w spektroskopii mössbauerowskiej do bezmodelowej rekonstrukcji rozkładów pól nadsubtelnych. W szczególności, możliwa stała się rekonstrukcja dwuwymiarowych i trójwymiarowych rozkładów pól nadsubtelnych $P(x, y, z)$ gdzie x, y, z – dowolne pola nadsubtelne. Testy *MEM* pokazały, że w celu otrzymania poprawnej odpowiedzi metody, bardzo istotną kwestią jest wykorzystanie wiedzy początkowej o badanym układzie.

Kolejnym ważnym moim wkładem w rozwój metodologii spektroskopii mössbauerowskiej jest wprowadzona i przetestowana przeze mnie metoda otrzymywania przekrojów czynnych na absorpcję pozwalająca na analizę wyników dla próbek o dużym efektywnym parametrze grubości t . Pozwala ona uniknąć ewentualnych niefizycznych rozwiązań, które pojawiać się mogą przy zastosowaniu przybliżenia cienkiego absorbenta.

Innym bardzo ważnym moim osiągnięciem jest zbudowanie, przetestowanie i przeprowadzenie pierwszych pomiarów z zastosowaniem monochromatycznego spolaryzowanego liniowo źródła promieniowania gamma. Istotne jest wprowadzenie przeze mnie metodologii opracowywania tak mierzonych widm. Możliwość korzystania z wyników pomiarów z użyciem wiązki spolaryzowanej kołowo jak i liniowo oraz pomiarów na wiązce niespolaryzowanej stanowi kompletny zestaw wyników umożliwiający analizę układów charakteryzujących się skomplikowanymi widmami absorpcyjnymi.

Bardzo ważnym wynikiem prowadzonych przez mnie prac metodologicznych jest to, że wszystkie nowe metody analizy danych zostały z powodzeniem zastosowane do badań układów magnetycznie nieuporządkowanych.

6. Literatura

- [Ace] M.Acet, Ch.Somsen, G.Nepecks, E.F.Wassermann, *J.Magn.Magn.Mater.* **208** (2000) 191
- [Ace1] M.Acet, T.Schneider, H.Zahres, W.Stamm, E.F.Wassermann, W.Pepperhoff, *Physica B* **161** (1989) 63
- [Arz] A.K.Arzhnikov, L.V.Dobysheva, *J.Magn.Magn.Mater.* **117** (1992) 87
- [Arz1] A.K.Arzhnikov, L.V.Dobysheva, *Phys.Lett. A* **195** (2000) 176
- [Bar] D.Barb, D.Tarina, A.Ito, S.Morimoto, *J.Phys.C* **14** (1981) 497
- [Bes] M.J.Besnus, A.Herr, A.J.P.Meyer, *J.Phys.F* **5** (1975) 2138
- [Blu] N.Blum, L.Grodzins, *Phys. Rev.* **136** (1964) A133
- [Bra] R.A.Brand, G.Le Caer, *Nucl. Instr. Meth. Phys. Res B* (1988) 272
- [Bra] R.A.Brand, *Nucl.Inst. and Meth.B* **28** (1987) 417
- [Bro] P.J.Brown, T.Kanomata, M.Matsumoto, K.-U.Neumann, K.R.A.Ziebeck, *J.Magn. Mater.* **242-245** (2002) 781
- [Buc] B.Buck, V.A.Macaulary, *Maximum entropy in action*. Clarendon Press, Oxford 1991
- [Cae] G.Le Caer, R.A.Brand, *J.Phys.: Condens. Matter* **10**, (1998) 10715
- [Coe] J.M.D.Coey, *Phys.Rev.Lett.* **27**, (1971) 1140
- [Dab1] L.J.Dąbrowski, J.Piekoszewski, J.Suwalski, *Nucl. Instr. Meth.* **91**, (1971) 93
- [Dab2] L.J.Dąbrowski, J.Piekoszewski, J.Suwalski, *Nucl. Instr. Meth.* **103**, (1972) 545
- [Das] A.Das, S.K.Paranjpe, S.Honda, S.Murayama, Y.Tsuchiya, *J.Phys.: Condens.Matter* **11** (1999) 5209
- [Dob] L.Dobrzyński, *X-ray Compton scattering*, Oxford University Press, (2004) 188
- [Don] J.Dongen, Torman, R.Jagannathan, J.M.Trooster, *Hyperfine Interact.* **1** (1975) 135
- [Dor] J.L.Dormann, D.Fiorani, E.Tronc, *Adv.Chem. Phys.* **98**, (1997) 283
- [Dub] L.Dubrovinsky, N.Dubrovinska, I.A.Abrikosov, M.Vennstrom, F.Westman, S.Carlson, M. van Schilfgaarde, B.Johansson, *PRL* **86** (2001) 4851
- [Frau] H.Fraunfelder, D.E.Nagle, R.D.Taylor, D.R.F.Cochran, W.M.Visscher, *Phys. Rev.* **126** (1962) 1065
- [Ger] U.Gerhard, S.Marquardt, N.Schroeder, S.Weiss, *Phys. Rev. B* (1998) 6877
- [Gib] T.C.Gibb, N.N.Greenwood, *Mössbauer spectroscopy* (Chapman and Hall,

- London, UK), (1971) 63-72
- [Gon] A.P.Goncalves, M.Godinho, H.Noel, *J.Solid State Chem.* **154** (2000) 551
- [Gon] U.Gonser, R.W.Grant, H.Wiederseich, S.Geller, *Apel. Phys. Letters* **9** (1966) 18
- [Gon1] A.P.Goncalves, J.C.Waerenborgh, M.Almeida, M.Godinho, I.Catarino, G.Bonfait, H.Noel, *J.Magn.Magn.Mater.* **260** (2003) 473
- [Han] S.S.Hanna, J.Heberle, C.Littlejohn, G.J.Perlow, R.S.Preston, D.H.Vincent, *Phys. Rev. Letters* **4** (1960) 177
- [Hes] J.Hesse, A.Rübartsch, *J.Phys.E: Sci. Instrum.* **7** (1974) 526
- [Huf] G.P.Huffman, *J.Appl.Phys.* **42** (1971) 1606
- [Ing] R.Inglls, K.Ono, L.Chandler, *Phys.Rev.* **172**, (1968) 295
- [Ito] A.Ito, M.Tanaka, S.Morimoto, T.Tokoro, *Nat.Sc. Rep. Ochanomizu Univ.* **27** (1976) 149
- [Jay] E.T.Jaynes, *Probability Theory. The Logic of Science.* Cambridge University Press, 2003
- [John] C.E.Johnson, W.Marshall, G.J.Perlow, *Phys. Rev.* **126** (1962) 1503
- [Kar] S.W.Karyagin, *Fiz.Tverd.Tela* (Leningrad) **8**, (1966) 493
- [Kul] N.I.Kulikov, A.V.Postnikov, G.Borstel, J.Braun, *Phys.Rev.B* **59** (1999) 6824
- [Lec] G.Le Caer, J.M.Dubois, *J.Phys.E: Scientific Instruments*, **12** (1979) 1083
- [Mar] S.Margulies, J.R.Ehrman, *Nucl. Instrum. Methods* **12** (1961) 131
- [Mas] R.Massart, V.Cabuil, *J.Chim.Phys.* **84**
- [Mor] S.Morup, *J.Magn.Magn.Mater.* **266** (2003) 110
- [Mor1] S.Morup, F.Bodker, P.V.Hendriksen, S.Linderorth, *Phys.Rev.B* **52**, (1995) 287
- [Noa] D.R.Noakes, A.S.Arott, M.G.Belk, S.C.Deevi, Q.Z.Huang, J.W.Lynn, RD.Shull, D.Wu, *Phys.Rev.Lett.* **91** (2003) 217201
- [Rue] J.P.Rueff, A.Shukla, A.Kaprolat, M.Krisch, M.Lorenzen, F.Sette, R.Verbeni, *Phys. Rev.B* **63** (2001) 132409
- [Sat] H.Sato, A.Arrott, *Phys.Rev.* **114** (1959) 1427
- [Sch] M. van Schilfgaarde, I.A.Abrikosov, B.Johansson, *Nature* **400** (1999) 46
- [Shi] M.Shiga, Y.Nakamura, *J.Phys.Soc.Japan*, **40** (1976) 1295
- [Shi1] M.Shiga, T.Kikawa, K.Sumiyama, Y.Nakamura, *J.Magn.Soc.Japan* **9** (1985) 187
- [Sht] S.Shtrikman, S.Somekh, *Rev. Sci. Instr.* **40**, 9 (1969) 1151
- [Spi] H.Spiering, *Nucl. Instrum.Methods*, **154**, (1978) 295
- [Sta] J.P.Stampfel, P.A.Flinn, in: *Mössbauer Effect Methodology*, Vol 6, ed.

- I.J.Gruverman (New York, 1971) 95-107
- [Sun] Y.Sun, M.B.Salamon, K.Garnier, R.S.Averback, *Phys.Rev.Lett.* **91** (2003) 167206
- [Szy1] K.Szymański, *Proc. Conf. Of ICAME 95*, **50** (1995) 891
- [Szy2] K.Szymański, *Hyp. Inter.* **97/98** (1996) 573
- [Szy3] K.Szymański, L.Dobrzyński, B.Prus, M.J.Cooper, *Nucl. Inst. and Meth. B* **119** (1996) 438
- [Szy4] K.szymański, *Nucl. Inst. and Meth. B* **168**, (2000) 125
- [Szy5] K.Szymański, *Phys.Rep.* **423**, (2006) 295
- [Szy6] K.Szymański, *J.Phys.:Condens. Master* **12**, (2000) 7495
- [Tsu] Y.Tsuchiya, T.Bitoh, S.Marayama, S.Chikazawa, Y.Hamaguchi, *J.Phys.Soc.Jpn.* **65** (1996) 3289
- [Var] F.Varet, A.Gerard, P.Imbert, *Phys. Status Solidi B* **43**, (1971) 723
- [Wei] J.Weiss, *Proc.R.Soc. London A* **82** (1963) 281
- [Wer] G.K.Wertheim, *Phys.Rev.* **121**, (1961) 63
- [Wil] P.G.L.Williams, G.M.Bancroft, *Mössb. Effect Meth.* **7**, (1971) 39
- [Win] B.Window, *J.Phys. E: Sci. Instrum.* **4** (1971) 401
- [Wu] B.M.Wu, D.S.Yang, S.Sheng, Y.L.Du, W.M.Xu, , *J.Magn.Magn.Mater.* **202** (1999) 426
- [Xu] W.M.Xu, P.Zheng, Z.J.Chen, B.G.Shen, *J.Magn.Magn.Mater.* **172** (1997)
- [Xu1] W.M.Xu, W.Steiner, M.Reissner, A.Posinger, M.Acet, W.Pepperhoff, *J.Magn. Mater.* **104-107** (1992) 2023
- [Zim] R.Zimmerman, *Nucl.Instrum.Methods*, **128**, (1975) 537
- [Zim1] R.Zimmerman, *Chem.Phys.Lett.* **34**,(1975) 416

Dariusz Maciej Satuła



**TEKSTY PUBLIKACJI OBEJMUJĄCYCH
JEDNOTEMATYCZNY CYKL PRAC
ROZPRAWY HABILITACYJNEJ**

P1

MÖSSBAUER AND X-RAY DIFFRACTION STUDY OF Cr-Fe-Mn ALLOYS

D. SATULA¹, K. SZYMAŃSKI¹, J. WALISZEWSKI¹, L. DOBRZYŃSKI^{1,2}, B. PRUS¹

¹*Institute of Experimental Physics, University of Białystok, 15-424 Białystok, Lipowa 41, Poland*

²*Soltan Institute for Nuclear Studies, 05-400 Otwock-Świerk, Poland*

Abstract: Mössbauer and X-ray diffraction measurements were carried out on two series of $\text{Cr}_{75+x}\text{Fe}_{16+x}\text{Mn}_{9-2x}$ ($-4 \leq x \leq 4$) and $\text{Cr}_{75+y}\text{Fe}_{16-y}\text{Mn}_9$ ($-6 \leq y \leq 6$) disordered alloys at room temperature. The concentration dependence of lattice parameter is compared with the Vegard law. Room temperature Mössbauer spectra consist of a single, symmetric, broadened line only. The isomer shift distribution and its influence on spectra broadening was explained in the framework of a model of the nearest neighbor, Cr or Mn, contributions to the parameters of interest. The contribution of the quadrupole splitting to the spectra broadening was estimated. Measurements in homogeneous external magnetic field show splitting of the spectra due to a hyperfine magnetic field distribution whose origin is discussed.

1. INTRODUCTION

Magnetic and transport properties of *bcc*, Cr-rich, ternary Cr-Mn-Fe alloys were published in [1-6]. The system exhibits a complex magnetic phase diagram. The chemical short-range order plays an important role in magnetic properties of these alloys since miscibility gap of the ternary Fe-Cr-Mn alloys with low Mn concentration is similar to those of binary Fe-Cr [7]. The alloys exhibit giant magnetoresistance, which is important for technological reasons. It was recently shown that conditions necessary for occurrence of maximum magnetoresistance are correlated with temperature T_c [8]. Ternary Cr-Fe-Mn alloys offer possibility of changing magnetic and transport properties within the same *bcc* crystal structure. The goal of present studies was to investigate the Mössbauer effect and concentration dependence of the lattice parameter of two series of alloys: in one of them the electron concentration is kept constant, $\text{Cr}_{75+x}\text{Fe}_{16+x}\text{Mn}_{9-2x}$ ($-4 \leq x \leq 4$), while in the second one, $\text{Cr}_{75+y}\text{Fe}_{16-y}\text{Mn}_9$ ($-6 \leq y \leq 6$), the electron concentration is maximally varied. Note that the samples for $x = 0$ and $y = 0$ correspond to the same composition.

2. SAMPLE PREPARATION AND X-RAY MEASUREMENTS

The samples were prepared by mixing of the Cr, Fe and Mn powders. Because of expected vaporation of Mn and Cr during arc melting, 3% wt. of Cr and 3% wt. of Mn were added to the nominal composition. Next the samples were pressed into discs, melted and remelted a few times under an argon atmosphere. After powdering, the X-ray diffraction measurements with K_{α} radiation of Mo showed that the samples contain two *bcc* phases with a slightly different lattice parameters. Subsequent pressing and melting of the samples resulted in arriving at a single phase alloys with the *bcc* structure. Some of the samples were annealed (900°C, 2 h, cooled with furnace) for easier detection of eventual second crystallographical phase. As expected, diffraction peaks became narrower in comparison with non-annealed samples but only single phase was

found. The measured lattice parameters are listed in Table 1. All further measurements were performed on non-annealed samples.

Part of each sample was used for chemical analysis by optical emission spectroscopy (OES-ICP, ARL 3520 spectrometer). Resulting compositions are listed in the Table 1. Because sample preparation involved complex technological process, the upper limits of the concentration of impurities have been measured. We found the following concentrations: C 0.04, Ni 0.02, Si 0.02 wt. %. In spite of the heavy loss of manganese (on the average 27 at.%), the compositions obtained, see Fig. 1, form systems fulfilling our basic intentions: x -series corresponds to the largest variations of the electron concentration while the y -series corresponds to a constant electron concentration.

Table 1. Composition and lattice parameter of the $\text{Cr}_{75+x}\text{Fe}_{16+x}\text{Mn}_{9-2x}$ and $\text{Cr}_{75+y}\text{Fe}_{16-y}\text{Mn}_9$ alloys

nominal, x or y	measured concentrations [%]			lattice parameter [Å]	
	Cr	Fe	Mn	non-ann.	annealed
$x = -4$	74.68	13.27	12.05	2.880	-
$x = -2$	75.62	13.92	10.46	2.880	-
$x = y = 0$	78.75	15.35	5.90	2.879	2.882
$x = 2$	78.67	17.60	3.73	2.879	-
$x = 4$	80.73	18.37	0.9	2.880	-
$y = -6$	73.00	20.47	6.53	2.878	2.880
$y = -3$	74.17	19.23	6.60	2.879	-
$y = 3$	80.47	13.46	6.06	2.880	-
$y = 6$	84.15	9.24	6.61	2.881	2.883

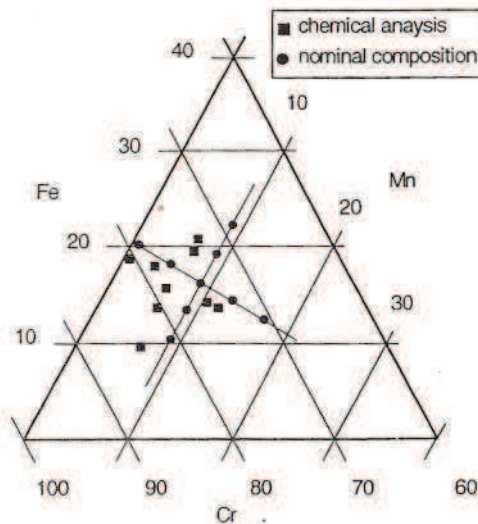


Fig. 1. Nominal and measured concentrations of the $\text{Cr}_{75+x}\text{Fe}_{16+x}\text{Mn}_{9-2x}$ and $\text{Cr}_{75+y}\text{Fe}_{16-y}\text{Mn}_9$ series

3. MÖSSBAUER MEASUREMENTS

Mössbauer measurements were carried out in transmission geometry, in constant acceleration mode. ^{57}Co in Cr matrix was used as a source, width of calibration lines was 0.235(5) mm/s. An external magnetic field of 1 T, parallel to the beam direction, was produced by a permanent magnet. Spectra were analysed using commercially available "Normos" package. Because absorbers were thin, dimensionless thickness parameter $t = 0.70 \div 1.5$ depending on concentration, the thickness effects cause only small Lorentzian broadening, ranging from 0.017 to 0.038 mm/s [9], and were neglected.

Mössbauer spectra measured at room temperature and in zero applied field consist of single, symmetric, broadened peak, see examples in Fig. 2 a, b. Its FWHM is constant in certain concentration region where it is equal to 0.32(1) mm/s. However, the FWHM increases strongly with decreasing x for $x < 0$ and with increasing y for $y > 3$, see Fig. 3.

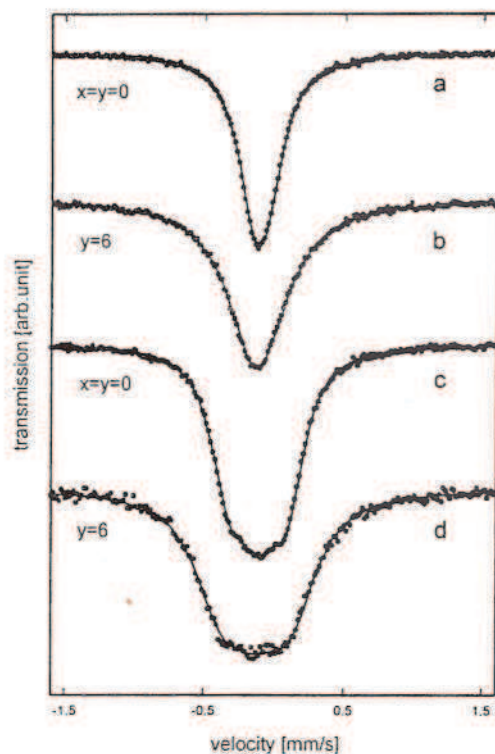


Fig. 2. Representative examples of the spectra measured in zero (a, b) and in external field of 1 T (c, d).

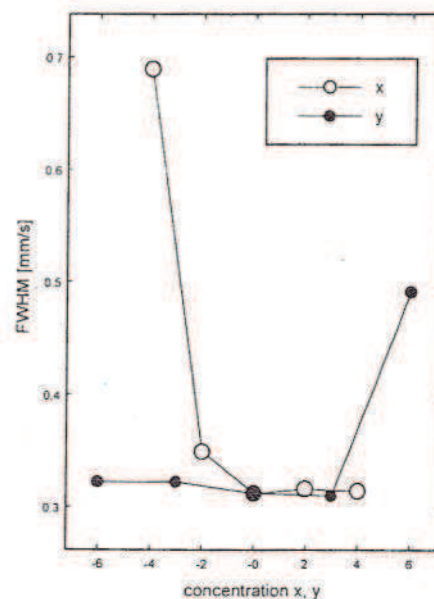


Fig. 3. FWHM of the spectra

Three mechanisms should be considered as responsible for the broadening: (i) distribution of the isomer shift connected with the existence of different local surroundings of iron atoms, (ii) non-zero quadrupole interaction due to breaking of cubic symmetry of iron atoms and (iii) small hyperfine magnetic field (static and (or) dynamic).

In order to select the samples for which a small magnetic contribution to the broadening can be expected, we note that when Mn is added to Cr, the Neel temperature of the *bcc* alloy [10] increases at the rate $dT_N/dc_{Mn} = 4.6 \cdot 10^3$ K. When iron is added, T_N decreases at the rate $dT_N/dc_{Fe} = -1.5 \cdot 10^3$ K [11]. Assuming additivity of the effects, which may be rather poor assumption, we can roughly expect $dT_N/dx = -11$ K for the *x*-series and $dT_N/dy = +15$ K for the *y*-series. Thus one expect low T_N at large *x* and at small *y*. Indeed, within these range of concentrations, the FWHMs of the spectra exhibit pleateau and no apparent broadening is observed.

The closer look into the spectra measured with the magnetic field applied to the samples shows that these spectra become asymmetric, see Figs. 2c, d. We tried to perform simultaneous fits to the in-field and zero-field spectra by adopting the simplest models widely used in literature. Thus, the presence of hyperfine magnetic field and quadrupole splitting only, or the presence of correlations in *h. m. f.* and isomer shift distributions were considered. However, these models did not lead to satisfactory fits: the obtained width of the *IS* distribution or the value of the quadrupole splitting were inconsistent (too large) with those observed in zero-field measurements. We conclude that both effects must simultaneously be present.

Let us estimate the effects of the isomer shift distribution and apply quite popular model in which a change of the local isomer shift ΔIS depends only on the chemical composition of the first coordination sphere:

$$\Delta IS = n\Delta_{Cr} + m\Delta_{Mn}, \quad (1)$$

where *n* and *m* are number of Cr and Mn atoms, respectively, and Δ_{Cr} and Δ_{Mn} denote changes of the isomer shifts due to one given atom in the first coordination shell. Next, we assume that atoms are distributed randomly, so the probability of finding Fe atom surrounded by *n* Cr and *m* Mn atoms is equal to:

$$p(n, m, K) = \frac{K!}{n!m!(K-n-m)!} c_{Cr}^n c_{Mn}^m (1 - c_{Cr} - c_{Mn})^{K-n-m}, \quad (2)$$

where c_{Cr} and c_{Mn} are concentrations of the elements and *K* is the coordination number equal to 8 in our case. Calculating the first and second moments of (1) with the probability (2), one obtains the following formulas for the average value of the isomer shift $\langle \Delta IS \rangle$ and its standard deviation σ_{IS} :

$$\langle \Delta IS \rangle = K(c_{Cr}\Delta_{Cr} + c_{Mn}\Delta_{Mn}), \quad (3)$$

$$\sigma_{IS}^2 = \langle \Delta IS^2 \rangle - \langle \Delta IS \rangle^2 = K(c_{Cr}\Delta_{Cr}^2 + c_{Mn}\Delta_{Mn}^2) - K(c_{Cr}\Delta_{Cr} + c_{Mn}\Delta_{Mn})^2. \quad (4)$$

Assuming that Δ_{Cr} and Δ_{Mn} are constant within the whole concentration range of c_{Cr} and c_{Mn} covered by our experiment, the measured isomer shift (see Fig. 4) could be fitted by Eq. (4) with

$$\Delta_{Cr} = -0.017 \text{ mm/s}, \quad \Delta_{Mn} = -0.008 \text{ mm/s}. \quad (5)$$

Next we performed fitting of the spectra in which broadening resulting from *h. m. f.* may be expected to be small ($x = -2, 0, 2, 4$, $y = -6, -3, 3$). We fitted a doublet with a quadrupole splitting and Lorentzian line width being free parameters, and with the distribution of the isomer shift as given by Eqs. (4) and (5). The results of the fit, shown in the Table 2 and in Fig. 2, lead

to the conclusion that a small quadrupole splitting, on the average equal to 0.08 ± 0.01 mm/s, must be present in our samples.

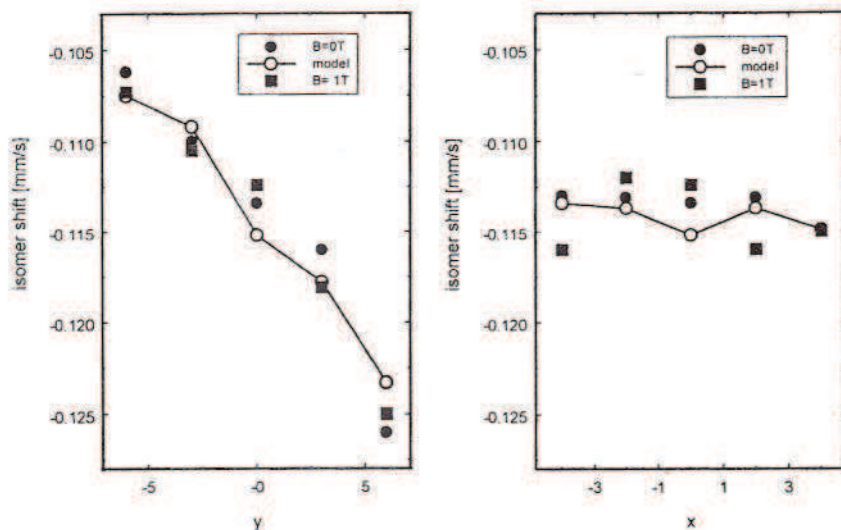


Fig. 4. Measured isomer shift (full symbols) and values obtained in the model, see text

Table 2. The Mössbauer parameters obtained from fitting procedures. Γ^B and IS^B are obtained from the measurements in an external magnetic field while * indicates parameters which were taken as averages from other measurements

		Γ	Γ^B	IS	IS^B	$ Qs $	B	σ_B
		[mm/s]	[mm/s]	[mm/s]	[mm/s]	[mm/s]	[T]	
x	-4	0.69	0.66	-0.113	-0.116	0.09*	1.5	0.35
	-2	0.34	0.31	-0.113	-0.112	0.09*	1.2	0.45
	0	0.29	0.26	-0.113	-0.112	0.086	1.1	0.50
	2	0.28	0.24	-0.113	-0.116	0.094	1.1	0.65
	4	0.28	0.26	-0.115	-0.115	0.084	1.1	0.60
y	-6	0.28	0.28	-0.106	-0.107	0.098	1.5	0.35
	-3	0.29	0.27	-0.110	-0.111	0.084	1.2	0.65
	3	0.27	0.24	-0.116	-0.118	0.084	1.1	0.65
	6	0.49	0.42	-0.126	-0.125	0.09*	1.1	0.65

The spectra measured in external magnetic field were analysed using Blaes et al. procedure [12]. Because a single value of the hyperfine magnetic field turned out to be insufficient for description of the measured spectra, it was assumed that *h. m. f.* is described by a Gaussian distribution with certain variance σ_B . Respective fitted values can be found in the Table 2. The best fits were obtained when correlation between *h. m. f.* and isomer shift was introduced. The correlation coefficient was found to be equal to -30 ± 15 T · s/mm. It has been checked that when the opposite sign of the dB/dIS is assumed, the observed spectra asymmetries cannot be explained. The shape of the spectra was insensitive to the change of sign of the electric field

gradient, so this parameter was not determined. The fitted parameters for all measured spectra, with and without the applied magnetic field, are given in the Table 2. The quality of fits can be inferred from examples presented in Fig. 2.

4. DISCUSSION

Within accuracy of our data, the lattice parameters depend linearly on concentration of Mn and Cr, which calls for the Vegard's law. Following this law one expects that the lattice parameter a should depend linearly on the atomic fraction c_i of the elements:

$$a = \sum_i c_i A_i, \quad (6)$$

where A_i are constants characteristic for an i -th element. Both, iron and chromium, form bcc type of structure with lattice parameters, A_{Cr} and A_{Fe} , equal at room temperature to 2.885 Å and 2.866 Å, respectively. These two values describe correctly the lattice parameter variation of Fe-Cr bcc alloys in the concentration range 30-100% at Cr [13]. Since there is no stable bcc Mn phase at room temperature, A_{Mn} can be estimated from the lattice parameter measurements for bcc Cr-rich Cr-Mn alloys [10, 13] as $A_{Mn} = 2.896$ Å. The lattice parameters expected from Eq. (6) are compared with the measured ones in Fig. 5.

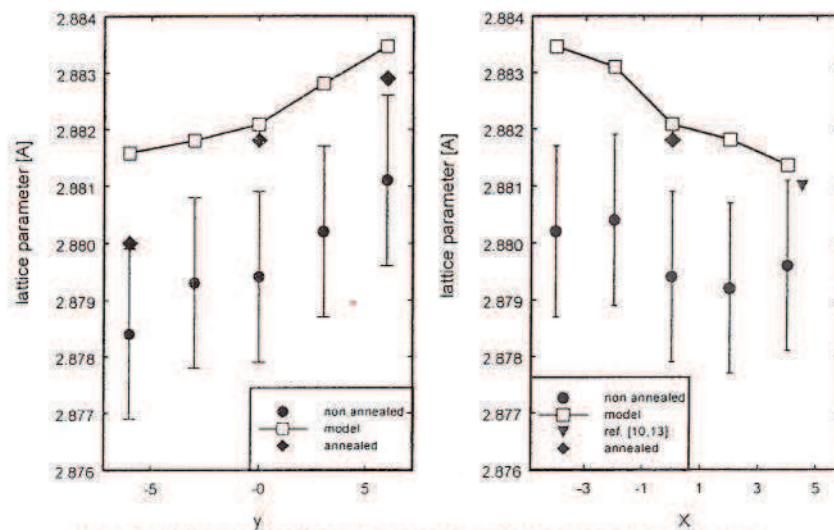


Fig. 5. Lattice parameter and comparison with the Vegard law, see text

The estimated changes of the isomer shift per atom given by Eq. (5) are slightly smaller in absolute value from the ones reported previously in different systems: -0.02 [14], -0.020(2) [15], -0.024 [16], -0.03(1) [17] for Cr and -0.016(2) [15], -0.02 [16] for Mn, (all values in mm/s, rel. to α -Fe). The experimental errors are not permitting for drawing definite conclusions, nevertheless if our values were truly smaller than the respective ones in other quoted systems, this could indicate some chemical segregation of elements.

We have shown that in order to explain the shape of the in-field measured spectra, the *h.m.f.* distribution has to be introduced. There are two mechanisms responsible for existence of *h.m.f.d.* The first is the sensitivity of iron magnetic moment to its chemical environment. When external homogeneous field is applied, an induced hyperfine field appears and its value depends on the local environment. The second mechanism can be thought of being the result of antiferromagnetic correlations present in this class of alloys. If two magnetic moments are oriented antiparallel and placed in an external field, one expects, basing on the vector model [18], that hyperfine fields acting on atoms will differ both in the value and the direction. This will result in creation of a *h.m.f.* distribution. Obtained correlation between the hyperfine magnetic field and the isomer shift is smaller than reported for ferromagnets. For example, the coefficient of interest is -64 for Fe-Al [19] and $-2.1 \cdot 10^2$ for amorphous Fe-Ni-Si-B [20] (in T·s/mm). This effect is due to the fact that in the present studies the system is investigated in the vicinity of transition temperature.

The width of the Lorentzian line was fitted as a free parameter. Its value, see Table 2, is (i) systematically larger than the width of the calibration line, and (ii) correlated with FWHM of the spectra, see Fig. 3. This indicates that Lorentzian broadening is observed in all the spectra. It is particularly large in the samples with highest temperatures T_N ($x = -4$ and $y = 6$). Lorentzian line broadening can be explained in the limit of fast relaxation [20] by dynamic behaviour of the hyperfine magnetic field. The effects of fluctuations are expected to be particularly important in the vicinity of the transition temperature and are consistent with reported magnetic inhomogeneity [8] in the Cr-Fe-Mn system.

In summary, concentration dependence of the lattice parameters of investigated alloys follow the Vegard law within the experimental accuracy. The isomer shift and its contribution to the line broadening (in the range $0.01 \div 0.02$ mm/s) was explained quantitatively by a simple model. The quadrupole splitting of 0.08 mm/s was found. The spectra measured in the field of 1 T indicate the presence of *h.m.f.* distribution with the width ranging from 0.3 to 0.6 T. The spectra asymmetry measured in magnetic field has been explained quantitatively as resulting from quadrupole splitting and correlation between the isomer shift and *h.m.f.* distribution.

Acknowledgements

The work was sponsored by the State Council of Science through grant 2P03B11516.

References

- [1] W. M. Xu, W. Steiner, M. Reissner, A. Pösinger, M. Acet, W. Pepperhoff, *JMMM* **104**, 2023 (1992).
- [2] W. M. Xu, P. Zheng, Z. J. Chen, B. G. Shen, *J. Magn. Magn. Mater.* **172**, 183 (1997).
- [3] M. Acet, T. Schneider, H. Zähres, W. Stamm, E. F. Wassermann, W. Pepperhoff, *Physica B* **161**, 63 (1989).
- [4] Y. Tsuchiya, H. Takita, S. Murayama, Y. Hamaguchi, *J. Phys. Soc. Jpn.* **62**, 3764 (1993).
- [5] Y. Tsuchiya, H. Nakamura, S. Murayama, K. Hoshi, Y. Shimojyo, Y. Morii, Y. Hamaguchi, *JMMM* **177**, 1447 (1998).
- [6] Y. Tsuchiya, T. Bitoh, S. Murayama, S. Chikazawa, Y. Hamaguchi, *J. Phys. Soc. Japan* **65**, 3289 (1996).
- [7] T. Schneider, Thesis, Universität Duisburg, Germany (1990).
- [8] Ch. Somsen, M. Acet, G. Nepecks, E. F. Wassermann, *JMMM* **208**, 191 (2000).
- [9] S. Margulies and J. R. Ehrman, *NIM* **12**, 131 (1961).

-
- [10] Y. Hamaguchi and N. Kunitomi, *J. Phys. Soc. Jpn.* **19**, 1849 (1964).
 - [11] S. K. Burke, R. Cywinski, J. R. Davis, B. D. Rainford, *J. Phys. F: Met. Phys.* **13**, 451 (1983).
 - [12] N. Blaes, H. Fischer, U. Gonser, *NIM B9*, 201 (1985).
 - [13] W. B. Pearson, in: *A handbook of lattice spacings and structures of metals and alloys*, Pergamon Press, London (1958).
 - [14] R. Ingals, H. G. Drickamer, G. De Pasquali, *Phys. Rev.* **155**, 165 (1964).
 - [15] Vincze and A. Campbell, *J. Phys. F: Metal. Phys.* **3**, 647 (1973).
 - [16] H. Akai, S. Blügel, R. Zeller, P. H. Dederichs, *Phys. Rev. Letters* **56**, 2407 (1986).
 - [17] D. Satula, K. Szymański, L. Dobrzyński, J. Waliszewski, *JMMM* **119**, 309 (1993).
 - [18] V. A. Niculescu, T. J. Burch, J. I. Budnick, *JMMM* **39**, 223 (1983).
 - [19] G. Athassiadis, G. Le Caer, J. Foct, L. Rimlinger, *phys. stat. sol. (a)* **40**, 425 (1977).
 - [20] G. Le Caer and J. M. Dubois, *J. Phys E: Sci. Instrum* **12**, 1083 (1979).
 - [21] L. Cianchi, P. Moretti, M. Mancini, G. Spina, *Rep. Prog. Phys.* **49**, 1243 (1986).

P2



ELSEVIER

Journal of Magnetism and Magnetic Materials 236 (2001) 56–70



www.elsevier.com/locate/jmmm

Spin alignment and related properties of BCC Cr–Fe–Mn system

K. Szymański^{a,*}, D. Satuła^a, L. Dobrzyński^{a,b}, M. Biernacka^a, K. Perzyńska^a,
P. Zaleski^a

^a *Institute of Experimental Physics, University of Białystok, Lipowa 41, 15-424 Białystok, Poland*

^b *The Soltan Institute for Nuclear Studies, 05-400 Otwock-Świerk, Poland*

Received 5 March 2001; received in revised form 8 June 2001

Abstract

Magnetic properties of the Cr-rich BCC Cr–Mn–Fe system are reported. Mössbauer spectroscopy with circularly polarised source allowed one to determine the Fe magnetic moment's component parallel to the applied field. These measurements combined with magnetisation measurements and standard Mössbauer spectroscopy reveal that the main contribution to the magnetisation at low temperature is due to the Fe moments. Their values vary from about $0.7 \mu_B$ to about $1 \mu_B$. The directions of iron moments also vary in space even in an external field of 1 T. The angular disordering of Fe magnetic moments increases with decreasing Fe concentration. A part of the Fe atoms, namely the ones surrounded by eight Cr atoms as a nearest neighbours, exhibits a low magnetic moment. These moments are completely disordered and do not contribute to the measured magnetisation. Cr and Mn atoms contribute to the net magnetisation (in the applied field of 1 T). This contribution amounts to 0.03 to $0.20 \mu_B$ per atom. The value of the Cr and Mn total contribution to the magnetisation depends linearly on the Fe concentration and is clearly uncorrelated with the concentration of Mn, which shows that Cr and Mn give similar contributions to the magnetisation. © 2001 Elsevier Science B.V. All rights reserved.

PACS: 76.80; 75.25; 75.50.B; 75.50.L

Keywords: Chromium alloys; Reentrant spin glass; Mössbauer polarimetry; Ferromagnetism; Antiferromagnetism; Alloys

1. Introduction

The behaviour of impurities in the AF matrix of Cr was a subject of numerous investigations [1 and references therein]. In particular, when Fe is added to Cr, a transition from incommensurate to commensurate spin density wave (SDW) takes

place and the Néel temperature decreases at the rate $dT_N/dc_{Fe} = -1.5 \times 10^3$ K [2,3]. With increasing iron concentration, the antiferromagnetism disappears at the critical concentration $c_{Fe} = 0.160 \pm 0.005$ [2]. Although the value of the magnetic moment of an isolated Fe atom in the Cr matrix was studied by many investigators, the situation is still far from being well understood. Magnetic susceptibility measurements indicated that the localised moment is about $2 \mu_B$ [4,5]. In

*Corresponding author. Fax: +48-85-745-7223.

E-mail address: kszym@alpha.uwb.edu.pl (K. Szymański).

accordance with the band structure calculations [6], if an iron atom is surrounded by eight Cr atoms, its magnetic moment should be reduced by 46% and its hyperfine field by 67% as compared to the values known for pure Fe. Kulikov [7] showed by means of self-consistent spin polarised KKR-CPA calculations that for 10% Fe in Cr, the iron has a moment of about $2\mu_B$. The author pointed out, however, that more precise calculations are necessary for a discussion on AF Cr with iron impurities. On the experimental side, the hyperfine magnetic field (h.m.f.) identified as due to an isolated iron atom in the Cr matrix ($B = 5\text{ T}$ at $T = 5\text{ K}$ [8], 3 T at 0.1 K [9]), turned out to be weakly dependent on concentration and interpreted as representing a small or zero moment. Thus, the quoted experiments disproved the theoretical findings. Determination of the sign of the h.m.f. of Fe in Cr [10] showed on the conduction and not the core origin of h.m.f.

At Fe concentrations larger than $c_{\text{Fe}} = 0.190 \pm 0.005$ [2] FM order sets in. The average iron moment rises from about $1.8\mu_B$ (at $c_{\text{Fe}} = 0.25$) to a small maximum $\mu_{\text{Fe}} = 2.3\mu_B$ (around $c_{\text{Fe}} = 0.85$) and then decreases to $2.2\mu_B$ for pure iron [11].

In contrast to iron, when chromium is substituted by manganese, the Néel temperature and the magnetic moment per atom increase with increasing Mn concentration. Both values approach a saturation above 20% Mn and reach about 750 K and $0.8\mu_B$, respectively [12]. One can say that Mn enhances the effective antiferromagnetic exchange interaction in the system. In this situation, it is clear that the magnetism of chromium alloyed simultaneously with iron and manganese may show interesting properties due to mixed interactions in the alloys.

Cr-rich Cr–Fe–Mn ternary BCC alloys exhibit the interesting property of giant magnetoresistance [13] in the vicinity of concentrations where ferro- and antiferromagnetic [14] ordering coexist. It was recently shown that the most favourable conditions for a large magnetoresistance occur at temperatures close to the Curie temperature [15]. In general, the ternary Cr–Fe–Mn system shows complex magnetic behaviour [14–20] which is not fully understood yet.

It is well known that the hyperfine magnetic field depends strongly on the 3d magnetic moment [21–23]. In the case of magnetically saturated ordered ferromagnets, the hyperfine field intensity and the saturation magnetisation, both values easily accessible experimentally, are strongly correlated. The situation is more complicated in disordered systems in which spin misalignment is present. In systems in which the directions of magnetic moments are somehow distributed, the macroscopic magnetisation is determined by two factors: the values of the individual magnetic moments and their average z -component, where z denotes the direction along the magnetisation. In some systems as, e.g., Fe–Au [24], the transverse spin component may become frozen below a certain temperature. Such freezing can be seen in the Mössbauer spectrum through the behaviour of the intensity of lines 2 and 5. Systems in which magnetic disorder is present exhibit hyperfine field distributions which complicates the analysis of the spectra. Le Caer et al. [25] showed that in order to determine unambiguously the hyperfine field parameters in standard Mössbauer spectroscopy, the ratio of the width of the distribution and to the average hyperfine field intensity should not be too large.

Mössbauer polarimetry with circularly polarised radiation proved to be a useful tool in the investigation of magnetic structures of disordered materials, since it is sensitive to the sign of the h.m.f. In particular, it was demonstrated that monochromatic circularly polarised Mössbauer spectroscopy (MCPMS) [26] gives important information concerning h.m.f. distributions in the case of poorly resolved spectra [27], and allows one to determine the h.m.f. direction [26,28], the magnetic remanence of iron [29] and the iron moment contribution to the net magnetisation [30].

In order to investigate the ternary Cr–Fe–Mn system characterised by two independent parameters (for example, concentrations c_{Fe} and c_{Mn}), two series, $\text{Cr}_{75+x}\text{Fe}_{16+x}\text{Mn}_{9-2x}$ and $\text{Cr}_{75+y}\text{Fe}_{16-y}\text{Mn}_9$, called here as x - and y -series, respectively, have been prepared. The x -series is characterised by a constant electron density while the electron concentration within the y -series is

maximally varied. The compositions of these two series form, on the so called Gibbs ternary diagram, two straight lines which cross at the point corresponding to $\text{Cr}_{75}\text{Fe}_{16}\text{Mn}_9$, the composition for which complex magnetic behaviour was already observed [14–20].

We report here the results of measurements performed on aforementioned BCC Cr–Fe–Mn alloys. Investigation of the iron contribution to the magnetisation using MCPMS is presented. The spectroscopic results appear to be strongly correlated with macroscopic magnetisation. There is also clear evidence that the Cr and Mn atoms contribute to the magnetisation.

2. Samples

The samples with nominal compositions $\text{Cr}_{75+x}\text{Fe}_{16+x}\text{Mn}_{9-2x}$ ($-4 \leq x \leq 4$) and $\text{Cr}_{75+y}\text{Fe}_{16-y}\text{Mn}_9$ ($-6 \leq y \leq 6$) were prepared first by mixing Cr, Fe and Mn powders. The samples were next pressed into discs, melted and remelted a few times under argon atmosphere. After powdering, the X-ray diffraction measurements with K_α radiation of Mo showed that the samples contained two BCC phases with slightly different lattice parameters. Subsequent pressing and melting of the samples resulted in arriving at a single phase with the BCC structure. A part of each sample was used for chemical analysis by optical emission spectroscopy. The first results on X-ray diffraction, chemical analysis and room temperature Mössbauer examination were published in Ref. [31].

3. Magnetisation measurements

The magnetisation measurements were carried out by means of a vibrating sample magnetometer on spherical bulk samples between 12 and 300 K in magnetic fields up to ± 1.2 T. The magnetic field dependence of the magnetisation for both x - and y -series at 12 K is shown in Fig. 1. The values of the spontaneous magnetisation σ_0 were derived by

fitting the relation

$$\sigma = \sigma_0 \left(1 - \frac{a}{H} - \frac{b}{H^2} \right) + \chi H \quad (1)$$

to the data. Here χ describes the paramagnetic contribution, while parameters a and b , characterise the non-linear magnetic field dependence of the ferromagnetic part of magnetisation. The values of the spontaneous magnetisation for all our samples at 12 K are collected in Table 1, together with the magnetisation measured in an external field of 1 T. All samples exhibit a small coercive field, H_c listed in the Table 1. It is seen that the samples which saturate easily have the smaller values of H_c .

The magnetisation curves of all samples measured at room temperature consist of a linear, paramagnetic-like contribution and a small amount of contribution exhibiting a hysteresis loop. The parameters of hysteresis loops do not depend on the sample composition: the saturation magnetisation amounts to 0.001–0.0025 μ_B per average atom of the sample and the coercive field is 0.01–0.02 T. These values of the coercive field are apparently larger than the ones measured at 12 K for samples with large magnetisation (x positive and y negative). One cannot exclude that the samples are not completely homogeneous and may contain small amount of soft FM Fe-rich BCC phase. Assuming arbitrarily that the magnetic moment of the Fe atom in this phase is 2.2 μ_B , one can estimate that 0.04–0.09% of all atoms should form the Fe-rich BCC phase. Such a small amount of the extra phase can hardly be detected by diffraction methods. We have attempted to measure Mössbauer spectra in the velocity range appropriate for the detection of the α -Fe phase, however, the attained accuracy of the measurements permits to determine 0.2% of FM phase at best.

The Curie temperatures T_C were attempted to be obtained from Arrot plots (after correction for the aforementioned presence of small amount of ferromagnetic phase), seen in Fig. 2. Doubtlessly, the isotherms have non-linear shape. Similar behaviour was observed in the $\text{Cr}_{75}(\text{Fe}_x\text{Mn}_{1-x})_{25}$ system [17]. Nevertheless, one can find samples for which the high field part of appropriate isotherms

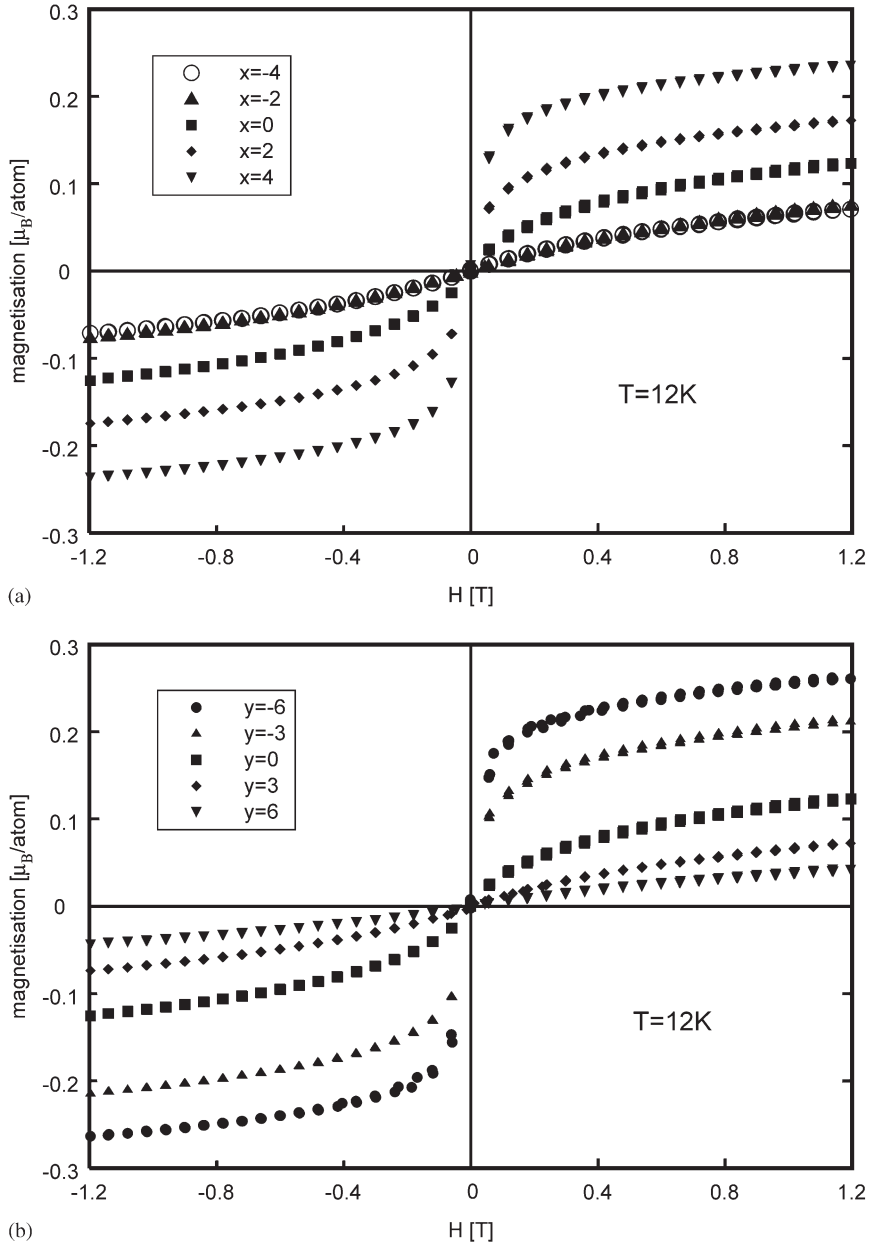


Fig. 1. Magnetisation per average atom at $T = 12\text{ K}$ vs. intensity of the external magnetic field for x -series (a) and y -series (b).

extrapolate to the axes origin. These are the samples with $y = -6$, $y = -3$, $x = 4$ and $x = 2$ (see the example in Fig. 2a). For all other samples, the Arrot plots indicate lack of the transition to

FM phase, even at the lowest measured temperatures (see the examples in Figs. 2b and 3).

Because of the non-linearity of isotherms in Arrot plots, the estimation of the transition

Table 1
Properties of $\text{Cr}_{75+x}\text{Fe}_{16+x}\text{Mn}_{9-2x}$ and $\text{Cr}_{75+y}\text{Fe}_{16-y}\text{Mn}_9$ ^a

	B, T	$x = -4$	$x = -2$	$x = y = 0$	$x = 2$	$x = 4$	$y = -6$	$y = -3$	$y = 3$	$y = 6$	
n_+	1	0 T, 12 K	0.88 (3)	0.89 (3)	0.84 (3)	0.83 (3)	0.77 (3)	0.89 (3)	0.89 (3)	0.83 (3)	0.75 (4)
n_-	2	0 T, 12 K	0.12 (3)	0.11 (3)	0.16 (3)	0.17 (3)	0.23 (3)	0.11 (3)	0.11 (3)	0.17 (3)	0.25 (4)
B_+ (T)	3	0 T, 12 K	11.2 (3)	11.8 (3)	12.2 (3)	12.2 (3)	11.7 (3)	14.2 (3)	13.2 (3)	9.8 (5)	9.5 (5)
B_- (T)	4	0 T, 12 K	4.2 ^b	4.2 ^b	4.2 (3)	4.5 (3)	4.2 (3)	4.25 (3)	4.2 ^b	4.6 (5)	4.2 (5)
n_+	5	1 T, 12 K	0.89 (3)	0.88 (3)	0.86 (3)	0.82 (3)	0.81 (3)	0.90 (3)		0.83 (3)	0.75 (4)
n_-	6	1 T, 12 K	0.11 (3)	0.12 (3)	0.14 (3)	0.18 (3)	0.19 (3)	0.10 (3)		0.17 (3)	0.25 (4)
B_+ (T)	7	1 T, 12 K	10.9 (3)	11.6 (3)	12.0 (3)	12.3 (3)	11.1 (3)	13.7 (3)		11.3 (3)	9.5 (5)
B_- (T)	8	1 T, 12 K	4.4 ^b	4.2 ^b	4.2 (3)	4.6 (3)	4.2 (3)	4.6 (3)		4.6 ^b	4.2 (5)
av. \cos^2	9	1 T, 12 K	0.35 (5)	0.36 (5)	0.42 (5)	0.51 (6)	0.77 (8)	0.61 (10)	0.53 (2)	0.37 (7)	0.35 (7)
av. \cos	10	1 T, 12 K	0.13 (2)		0.30 (3)		0.57 (6)	0.47 (4)			0.15 (12)
T' (K)	11	0.01 T, –	40 (5)	35 (5)	55 (5)	68 (15)	90 (15)	125 (15)	103 (5)	30 (5)	30 (5)
T_{Arrot} (K)	12	–, –				78 (15)	95 (15)	155 (15)	115 (15)		
T_g (K)	13	0.01 T, –		40 (10)				100 (10)	80 (10)		30 (10)
H_c (T)	14	–, 12 K	0.013 (1)	0.008 (1)	0.001 (1)	0.001 (1)	0.001 (1)	0.003 (1)	0.001 (1)	0.009 (1)	0.008 (1)
σ_0 (μ_B/atom)	15	0 T, 12 K	0.031 (6)	0.035 (6)	0.087 (8)	0.144 (12)	0.213 (11)	0.237 (7)	0.188 (9)	0.036 (5)	0.013 (2)
σ (μ_B/atom)	16	1 T, 12 K	0.066 (10)	0.068 (10)	0.116 (17)	0.166 (12)	0.228 (11)	0.255 (8)	0.187 (9)	0.066 (9)	0.037 (6)
μ_{Fe} (μ_B/atom)	17	1 T, 12 K	0.84 (2)	0.89 (2)	0.96 (2)	0.95 (2)	0.85 (2)	1.05 (2)		0.87 (2)	0.69 (4)
μ (CrMn) (μ_B/atom)	18	1 T, 12 K	0.06 (1)		0.09 (1)		0.18 (1)	0.20 (1)			0.032 (5)

^aThe external magnetic field and temperature in the measurement is given in column 3. Rows 1–5 and 6–11 correspond to zero and in-field Mössbauer measurement, while rows 12–17 correspond to magnetic measurements. n_{\pm} and B_{\pm} correspond to the fraction of Fe and the intensity of the average field of high and low field components of iron in the Mössbauer spectra, respectively.

^bIndicates that the parameter was fixed during the fitting procedure. Experimental uncertainties are given in parenthesis.

temperatures cannot be done with great precision. Therefore, we also estimated complementary temperatures T' at which $d^2\sigma/dT^2 = 0$ at a low field of 0.01 T. These temperatures, displayed in Table 1, seem systematically to be slightly smaller than the ones determined from the Arrot plots for FM phase (see Fig. 4a).

Part of the samples exhibit magnetisation depending on the scenario of measurements. The T_g temperatures at which zero field cooled and field cooled magnetisation curves (in field of 0.01 T) start to differ are given in Table 1.

4. h.m.f. Distribution

Mössbauer measurements were performed at 12 K in zero field and in a $B = 1$ T axially applied external field (see Fig. 5). Because of a broad distribution of h.m.f., the absorption peaks are poorly resolved. In our previous report [31], we have shown that the distributions in the isomer shift and the quadrupole splitting are not larger than 0.08 mm/s, so these interactions were

neglected in actual treatment. We tried first to fit the spectra with a single Zeeman component having a Gaussian distribution of the h.m.f. The fits were of insufficient quality indicating at least a two peak structure of the h.m.f. This result is in agreement with those of Refs. [17,20]. Then, all the spectra were satisfactorily fitted with two Zeeman components having Gaussian distribution of the h.m.f. The widths of the Gaussian distributions for dominating and low field components are 3.9 ± 0.3 T and 2.1 ± 0.2 T, respectively, and are independent of the sample compositions under study. Results of the fits are given in Table 1 and can be summarised as follows. The average h.m.f. can be expressed as a linear function of iron and manganese concentrations. By the least square fit it was found that the average h.m.f. $B/[T] = (2.11 \pm 0.02) + (68.7 \pm 0.4)\xi$, where $\xi = (0.647c_{\text{Fe}} + 0.353c_{\text{Mn}})$ (see Fig. 6). Certain fraction of Fe atoms (n_- , given in Table 1), exhibits low field with the average value equal to 4.5 ± 0.4 T, independent of the sample composition. Within the experimental accuracy the shapes of the h.m.f. distributions measured with and without the field

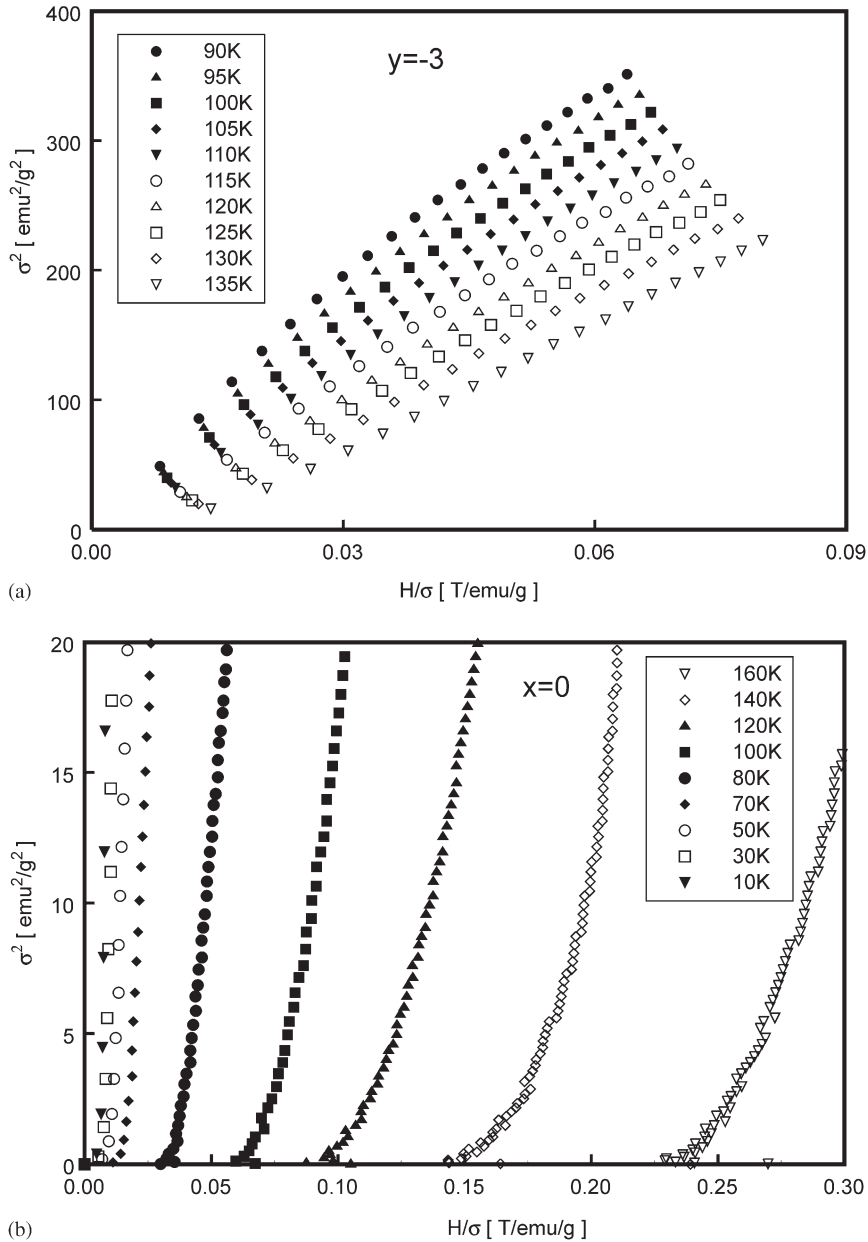
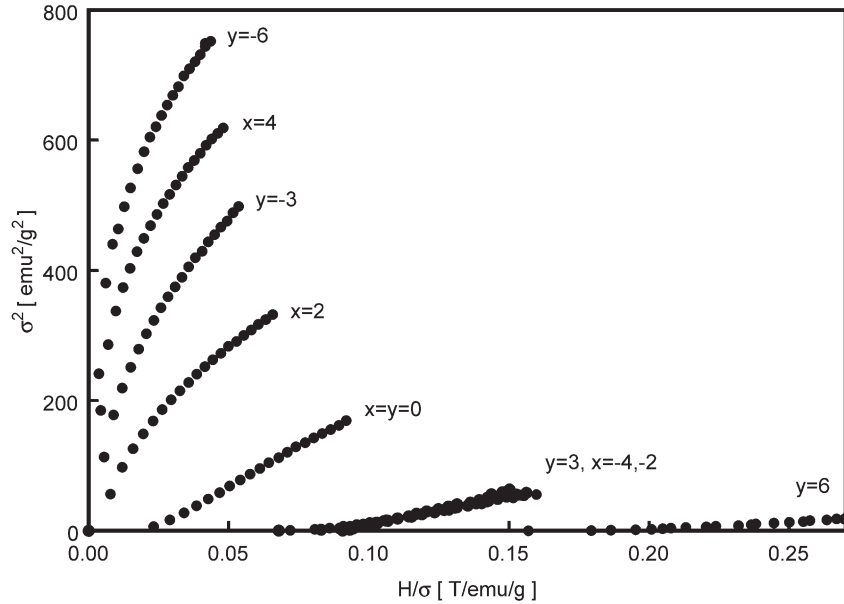


Fig. 2. An example of the Arrot plots for $y = -3$ (a) and $x = 0$ (b).

are the same, and only the relative line intensities in the spectra depend on the applied magnetic field. The latter conclusion is confirmed by model-independent data treatment [32]. The exemplary difference spectra are shown in Fig. 7. The difference spectrum for $x = +4$ and $y = -6$ has a

two peak shape. The peak amplitudes decrease continuously to zero with x and y varying to $x = -4$ and $y = +6$, respectively. The observed two peaks are due to lines 2 and 5 only. The zero difference for $x = -4$ and $y = +6$ indicates that the spin structure in the considered samples is not

Fig. 3. Isotherms at $T = 12$ K of Arrot plots.

sensitive to the applied field of 1 T, in which the samples were cooled from room temperature. This behaviour is studied quantitatively with the polarised source.

5. MCPMS measurements

MCPMS measurements were performed at 12 K in axially applied field of 1 T on the samples with $x = -4, 0, +4$ and $y = -6, +6$ (see Fig. 8). Details of the experimental set-up and the methodology used in the data analysis are given elsewhere [26–30]. The magnetic texture in a sample can be extracted from the relative line intensities in a standard Mössbauer spectrum: $i_1 : i_2 : i_3 : i_4 : i_5 : i_6 = 3 : z : 1 : 1 : z : 3$, where the z value allows one to estimate $\langle(\gamma\mathbf{m}_{\text{Fe}})^2\rangle$ —the average square of the cosine between the direction of the photon γ and the direction of the Fe hyperfine magnetic field \mathbf{m}_{Fe} :

$$\langle(\gamma\mathbf{m}_{\text{Fe}})^2\rangle = \frac{4-z}{4+z}. \quad (2)$$

The brackets denote an average over the hyperfine field orientations in the sample, and γ and \mathbf{m}_{Fe} are

unit vectors. For a fully isotropic orientation of the Fe moments, $z = 2$. MCPMS spectra exhibit characteristic asymmetry (see Figs. 6 and 3 of Ref. [26]). Defining the asymmetry in intensities for lines 3 and 4 (or 1 and 6) as

$$A = \frac{|i_3 - i_4|}{i_3 + i_4} = \frac{|i_1 - i_6|}{i_1 + i_6}, \quad (3)$$

one can express an average cosine $\langle\gamma\mathbf{m}_{\text{Fe}}\rangle$ (projection of the iron moment on the field direction) by

$$\langle\gamma\mathbf{m}_{\text{Fe}}\rangle = \frac{4A}{(4+z)p}, \quad (4)$$

where p is the degree of circular polarisation of the beam. The spectra measured with the MCPMS were fitted simultaneously with the spectra measured with the unpolarised source. The overall shape of the spectra is preserved and only the line intensities change, in comparison with the in-field, unpolarised beam measurements. Correcting for the degree of polarisation, $\langle\gamma\mathbf{m}_{\text{Fe}}\rangle$ were determined from MCPMS measurements. The average cosine multiplied by the average magnetic moment of iron is equal to the iron contribution to the magnetisation. The magnetic moment of iron itself was estimated from the average value of the

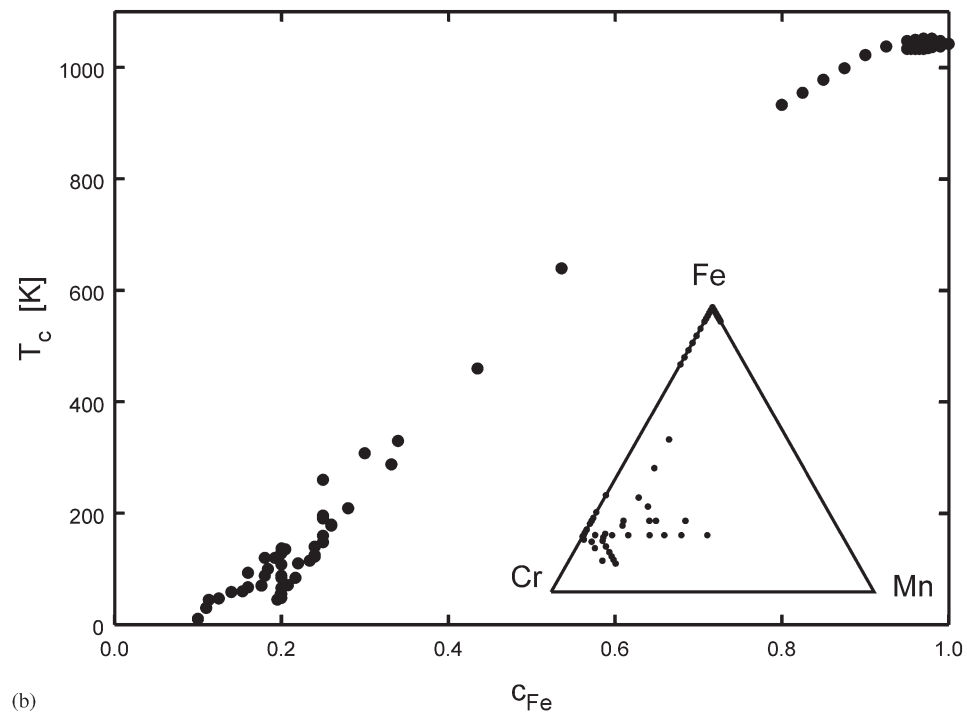
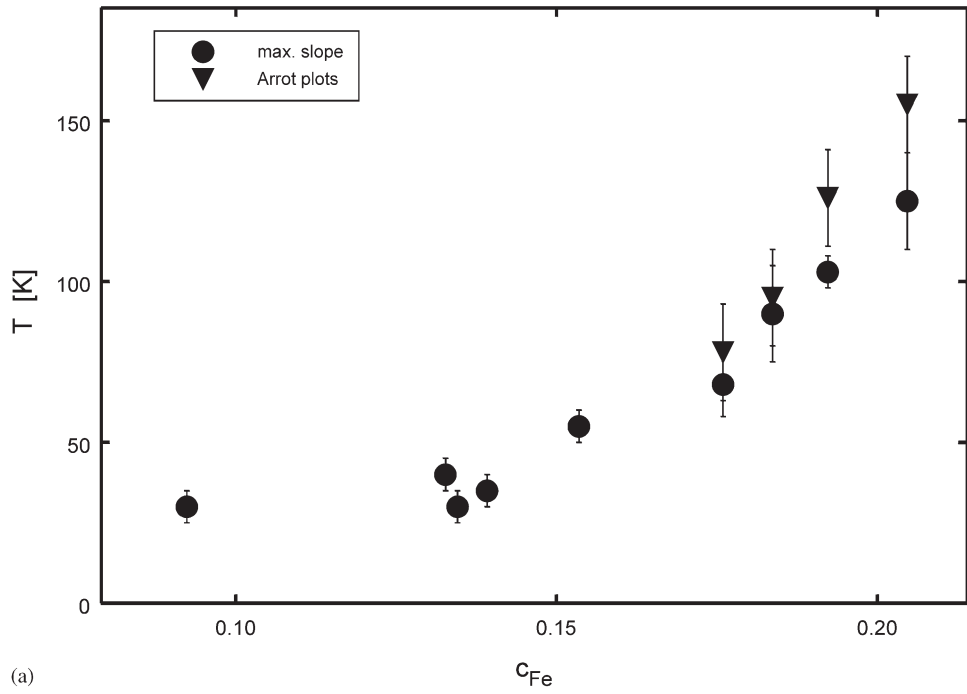


Fig. 4. Correlation of T_c and Fe concentration for (a) investigated alloys and (b) reported data (inset shows the concentrations of the reported data).

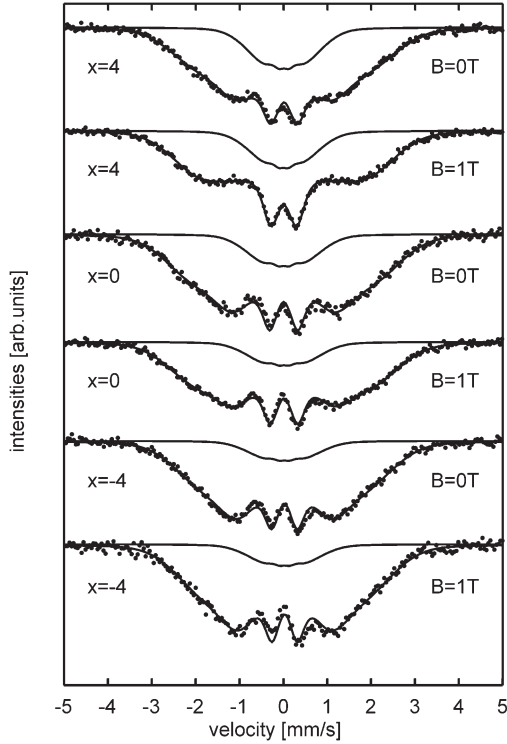


Fig. 5. Mössbauer spectra measured at $T = 12\text{ K}$ and in external axial field of 1 T.

hyperfine field assuming the hyperfine constant $13\text{ T}/\mu_{\text{B}}$ [33].

The important result is that the observed asymmetry A is non-zero for the high field component only. The estimated average cosine of the angle between the applied field and the large component of the hyperfine magnetic field is given in Table 1. Within an experimental accuracy, zero asymmetry for the low field component is observed (see fitted lines in Fig. 8). This indicates that the iron moments exhibiting this field component do not contribute to the magnetisation measured in our experiment.

6. Discussion

As mentioned in the introduction, the average h.m.f. of collinear ferromagnets is usually correlated with the magnetisation. In Fig. 9, the spontaneous magnetisation and the average h.m.f. of iron are shown by squares. The interrelation between these two values becomes more clear when the hyperfine field is multiplied by the average cosine. Fig. 9 shows that the average z -component of the h.m.f. is proportional to the

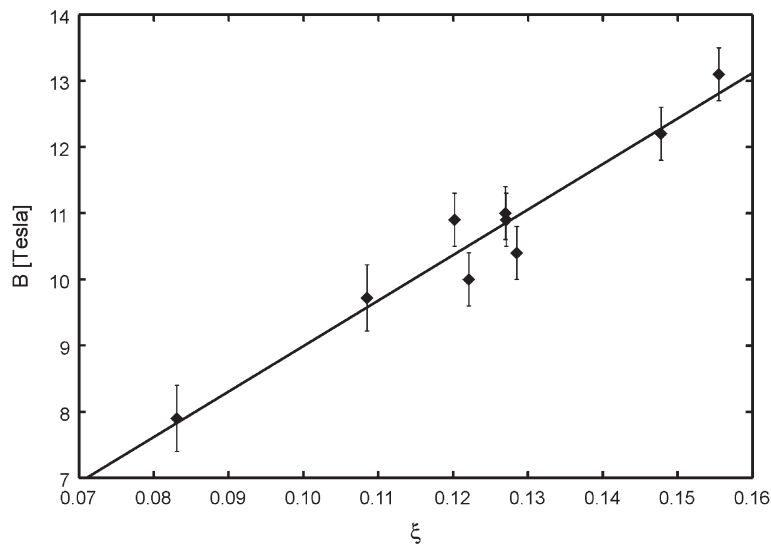


Fig. 6. Average hyperfine field vs. ξ , where $\xi = (0.647c_{\text{Fe}} + 0.353c_{\text{Mn}})$. The straight line is given by the relation $B/[T] = 2.11 + 68.7 \cdot \xi$.

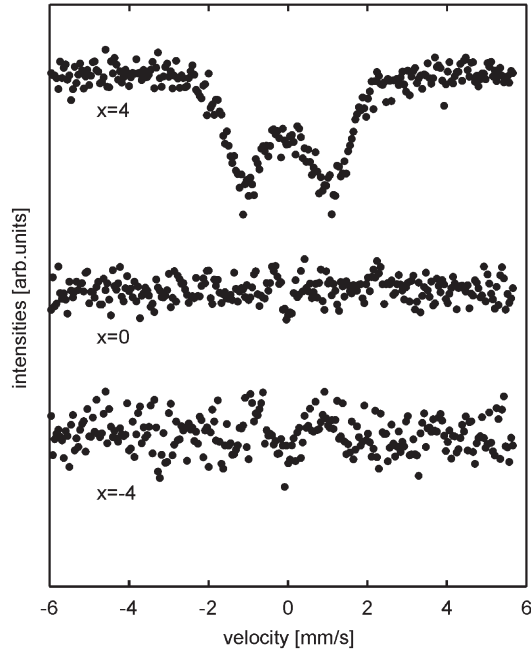


Fig. 7. Difference between the spectra measured in external field and without field at $T = 12$ K.

average magnetic moment. This indicates to what extent the spin misalignment in the 3d disordered system under study reduces the average magnetisation. Certainly, such a conclusion could not be inferred from the magnetisation and conventional Mössbauer spectroscopy alone.

The transition temperatures to FM phase depend smoothly on the Fe concentration (see Fig. 4a). This result is in agreement with the general trend observed in BCC Fe–Cr–Mn, deduced from published results [2,3,13–18,20,34–44] (Fig. 4b). The slope dT_c/dc_{Fe} in Fig. 4a is close to the slope in Fig. 4b and it seems that the formation of FM phase is ruled by the Fe concentration only. Our observation thus agrees with the suggestion of Ref. [19] that “ferromagnetism and re-entrant spin glass are mainly due to Fe atoms”. In other words, Cr and Mn atoms have, within given range of concentration, little influence, if any, on formation of FM phase. It is believed that small hysteresis loops observed at room temperature originate from sample inhomogeneities. Fe-rich FM particles or

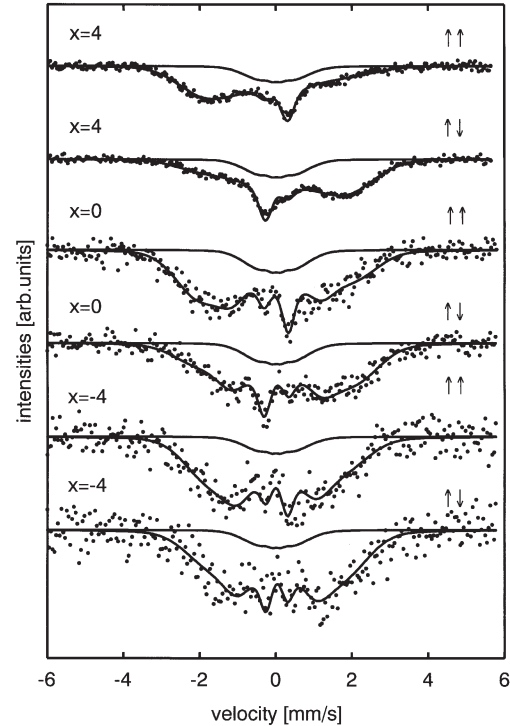


Fig. 8. Mössbauer spectra measured at $T = 12$ K using polarised radiation. For each spectrum the low field component and total fitted spectrum are shown by solid lines.

clusters in AF or PM matrices exhibit a coercive field of the order of 0.01 T, most probably because of shape and crystalline anisotropy. At low temperatures when a FM or a SG state develops, they interact with the magnetically ordered framework. Consequently, this results in a decrease of the coercive field due to the inhomogeneities and thus of the overall coercivity.

Extrapolation of high field isotherms in Fig. 3 permits one to estimate that the onset of ferromagnetism takes place at points ($c_{Cr} = 0.79$, $c_{Fe} = 0.17$, $c_{Mn} = 0.04$) and ($c_{Cr} = 0.76$, $c_{Fe} = 0.18$, $c_{Mn} = 0.06$). These two points, together with the iron concentration $c_{Fe} = 0.19$ determined by Burke [2] for the onset of ferromagnetism in Fe–Cr, indicate that the presence of Mn only slightly shifts the onset of ferromagnetism, and the shift is towards smaller Fe concentrations.

Magnetisation and Mössbauer measurements indicate that not only Fe moments contribute to

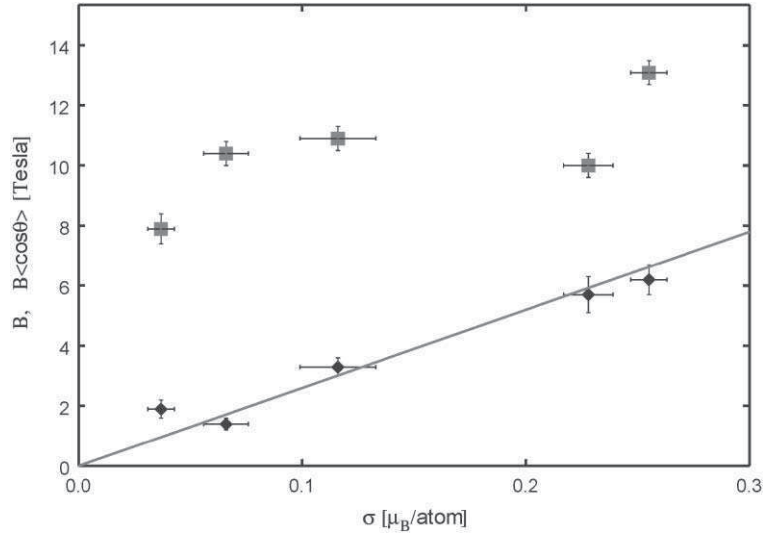


Fig. 9. Correlation between magnetisation and h.m.f. (squares) and h.m.f. projected on magnetisation direction (diamonds), respectively. Both measurements in external field of 1 T and $T = 12$ K.

the magnetisation. Indeed, from the measured intensity of h.m.f. and the already cited hyperfine constant, one could estimate the magnetic moments of Fe corresponding to the high field fraction. These moments are listed in Table 1. Next, from measured average cosines, the iron contribution to the magnetisation could be deduced. This contribution is definitely smaller than the measured total magnetisation. We thus conclude, that Cr and Mn atoms must contribute to the magnetisation; the respective values per atom are given in Table 1 and shown in Fig. 10. One sees a lack of direct correlation between Cr and Mn contribution to magnetisation and Mn concentration. On the other hand, a smooth increase of Cr, Mn contribution with increasing Fe concentration is observed. This can be interpreted in terms of the commonly used model of additive influence of high iron moment, located in the nearest neighbourhood, on the moment formation. One can deduce that a single Fe atom induces in its nearest (Cr, Mn) vicinity a magnetic moment of $0.06 \mu_B$ for $c_{Fe} \approx 0.1$ to $0.12 \mu_B$ for $c_{Fe} \approx 0.2$, oriented parallel to the iron magnetic moment.

The magnetic moment of the Cr–Mn matrix estimated above depends sensitively on the value

of the phenomenological hyperfine constant. It was considered in Ref. [19] that only the Fe magnetic moment contributes to the magnetisation in $Cr_{65}Fe_{20}Mn_{15}$. If we assume that this is the case, then using the measured value of average cosines for fraction n_+ of Fe with high moment and taking into account that $1-n_+$ fraction of Fe with low moment does not contribute to the magnetisation, the magnetic moment of the former Fe atoms must be

$$\mu_{Fe} = \frac{\sigma}{\langle \gamma \mathbf{m}_{Fe} \rangle c_{Fe} n_+}, \quad (5)$$

where σ is the magnetisation per average atom and c_{Fe} the total iron concentration. Using expression (5) one obtains the average magnetic moment at $T = 12$ K and in an external field of 1 T to be more than $3 \mu_B$. Such a high value is hard to reconcile with h.m.f. in the range of 10 T (see Table 1), which supports our conclusion that Cr, Mn atoms also contribute to the magnetisation, or at least, they are significantly polarized by Fe atoms.

Quantitative results obtained for the hyperfine magnetic field for both x and y series show different influence of Cr and Mn on the Fe moment formation. An iron atom embedded in

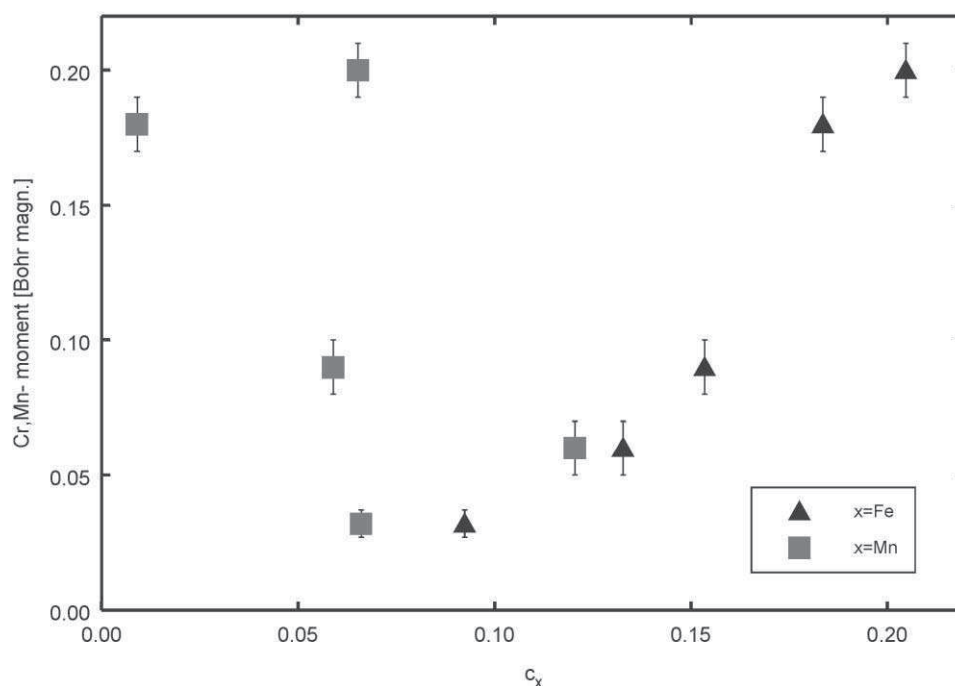


Fig. 10. Cr and Mn atomic moment contribution to the magnetisation vs. Fe concentration (triangles) and Mn concentration (squares), respectively.

the Cr matrix is surrounded by eight Cr atoms and, according to our results, exhibits a low magnetic moment. Fig. 11a shows that the fraction of Fe possessing a low field is directly correlated with the Cr concentration. The solid line shows calculated probabilities of finding Fe surrounded by eight Cr in the first coordination shell. This proves that Fe with low field must be connected with Cr surrounding. Our result agrees well with the result of Ref. [9] when the intensity of the h.m.f. is concerned, however, it is still unclear whether the Fe atoms in question have low or zero magnetic moments. The zero asymmetry of the low field part measured by MCPMS suggests that only the directions of low fields are strongly disordered. We thus conclude that irrespective of whether the Fe surrounded by Cr has or has not zero magnetic moment, such Fe atoms do not contribute to the average magnetisation.

When one or more Fe or Mn atoms appear as nearest neighbours of Fe, the latter atom acquires a large magnetic moment, which contributes to the

average magnetisation. We tried to find the most important mechanism responsible for a high iron moment formation. The experiment demonstrates that the average h.m.f. is correlated with ζ , see Fig. 6. The linear correlation between average field and ζ can be interpreted in terms of a simple model of additivity of hyperfine fields caused by nearest neighbouring atoms. Indeed, the data shown in Fig. 6 can be explained by the assumption that one Mn atom substituting for one Cr in the first coordination shell increases the h.m.f. of the iron atom by 3 T, while one Fe atom replacing Cr increases the h.m.f. in question by 5.5 T. Thus, in contrast to Cr atoms, the Fe and Mn atoms enhance the formation of the large Fe moment. The field extrapolated to $\zeta = 0$ is about 2 T and may be interpreted as that of an isolated Fe in the Cr matrix. This value corresponds well to the measured low field component recognised as Fe surrounded by eight Cr, equal on average 4.5 T (see 4th and 8th row of Table 1). Our result that Mn acts similarly to Fe and in an opposite way

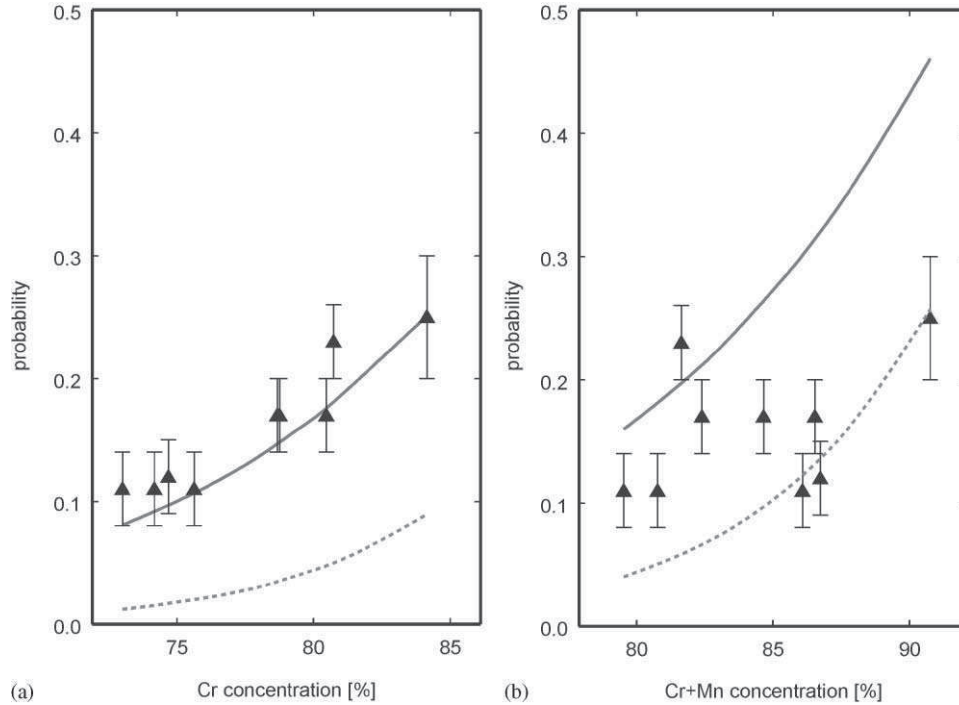


Fig. 11. (a) Fraction of Fe possessing low field vs. Cr concentration. Calculated probability of iron having eight Cr as first n.n. (solid line) and 14 Cr as both first and second n.n. (dashed line). (b) Fraction of Fe possessing low field vs. Cr + Mn concentration. Calculated probability of Fe having eight Cr or 7Cr + 1Mn n.n. (solid line) and 14 Cr or 13Cr + 1Mn (dashed line) in both first and second n.n., respectively.

than Cr is consistent with the results of Ref. [18]. They observed an increase of magnetisation when Cr was replaced by Mn in $\text{Cr}_{80-x}\text{Fe}_{20}\text{Mn}_x$ and $\text{Cr}_{75-x}\text{Fe}_{25}\text{Mn}_x$ in the range of not very large Mn concentrations ($x < 30$).

The iron moments responsible for the formation of the FM phase can be considered as being embedded in AF Cr–Mn matrix. It is likely that such moments (or clusters—we do not intend to speculate on their size) interact with the nearest surrounding via exchange interaction, and interactions can effectively be described by an exchange anisotropy term [45–47]. The energy of the Fe moments in the AF matrix at $T = 0$ may be postulated to be described by the following Hamiltonian:

$$H = \sum_i J s_i m_i - K (r_i m_i)^2 - \mu B m_i, \quad (6)$$

where m_i is a unit vector along the direction of the Fe moment μ , B the magnetic induction resulting from the external magnetic field, magnetisation and demagnetising field. It is assumed, for simplicity, that the average exchange interaction, J , with the surroundings (or molecular field) is described by a single exchange integral (molecular field intensity), while the direction of the molecular field may vary from site to site. Thus, in the first term the unit vectors s_i intend to denote the anisotropy of the distribution of effective exchange interaction with local surroundings. The next term intends to describe the consequences of variation of local crystal fields. Unit vectors r_i indicate easy directions of the magnetic moments in their local crystalline fields. Also, only one uniaxial anisotropy K is assumed. It is reasonable to assume that the external field does not modify the magnetic structure of the AF phase and that the unit vectors

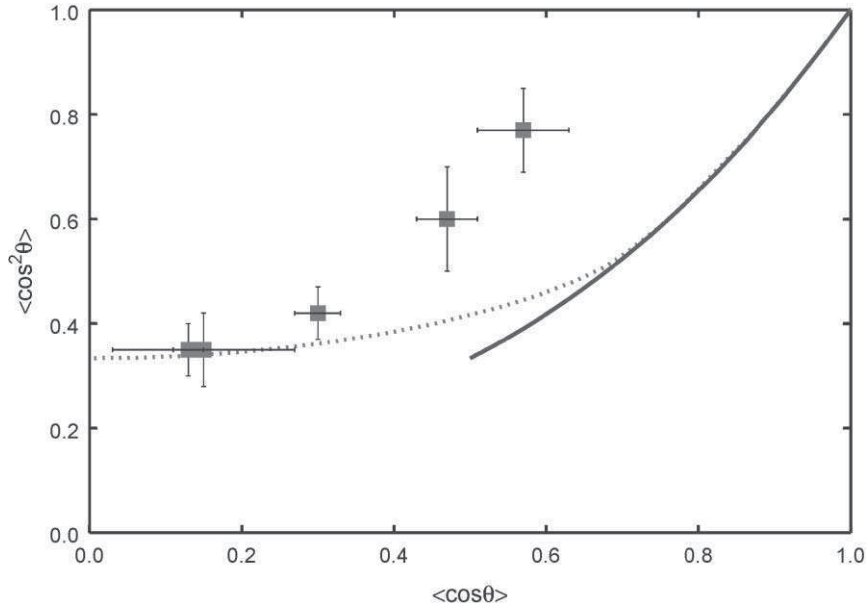


Fig. 12. Correlation between $\langle (\gamma m_{\text{Fe}})^2 \rangle$ and $\langle \gamma m_{\text{Fe}}^2 \rangle$ when the intensity of the external field is varied with respect to the uniaxial anisotropy (solid line) and exchange anisotropy (dotted line) energy, respectively.

r_i and s_i are randomly oriented in a polycrystalline sample. Minimising Eq. (6) with respect to the m_i directions one can find dependencies between $\langle (\gamma m_{\text{Fe}})^2 \rangle$ and cosine $\langle \gamma m_{\text{Fe}} \rangle$ when the intensity of the external field interaction \mathbf{B} is varied with respect to J and K . Vectors \mathbf{B} and γ are parallel in the considered case. In Fig. 12 two lines illustrate two limiting cases of $J = 0$ and $K = 0$, respectively. The experimental data shows that the exchange anisotropy term plays an important role in the ordering of Fe moments. The deviations observed can most easily be interpreted as due to the presence of some Fe moments oriented on the average antiparallel to the resultant magnetisation.

7. Conclusions

The formation of the FM phase in Cr-rich ternary Cr–Fe–Mn alloys depends mainly on the iron atoms. If they are surrounded by at least one Fe or Mn atom, they acquire a magnetic moment of about $1 \mu_{\text{B}}$. Fe surrounded by eight Cr atoms possesses zero or a very low magnetic moment.

However, even in this latter case, the directions of low hyperfine magnetic field are strongly spatially misaligned with respect to the direction of net magnetisation, indicating that Fe surrounded by Cr does not contribute to the magnetisation. The Cr–Mn atoms form a matrix which in applied field of 1 T contributes from 0.03 to $0.20 \mu_{\text{B}}$ per atom to the average magnetisation. Our results do not contradict the presence of AF order in Cr–Mn matrix observed in neutron diffraction [14] and resistivity measurements [16,48]. The transition temperature to the ferromagnetic phase as well as the onset of ferromagnetism depend mainly on the iron concentration. MCPMS measurements reveal that the net magnetisation is strongly influenced by the misalignment of the 3d magnetic moments. The mechanism responsible for strong misalignment seems to be predominately an exchange anisotropy.

Acknowledgements

The work was sponsored by the State Council of Science through grant 2P03B11516.

References

- [1] E. Fawcett, V. Yu Galkin, *J. Phys. Condens. Matter* 3 (1991) 7167.
- [2] S.K. Burke, R. Cywinski, J.R. Davis, B.D. Rainford, *J. Phys. F: Met. Phys.* 13 (1983) 451.
- [3] B. Loegel, *J. Phys. F5* (1975) 497.
- [4] Y. Ishikawa, R. Tournier, J. Filippi, *J. Phys. Chem. Solids* 26 (1965) 1727.
- [5] V. Yu Galkin, P.C. De Camargo, N. Ali, J. Schaf, E. Facett, *J. Magn. Magn. Mater.* 159 (1996) L23.
- [6] Zhiqiang Li, Helie Luo, *J. Phys. Condens. Matter* 3 (1991) 9141.
- [7] N.I. Kulikov, C. Demangeat, *Phys. Rev. B* (1997) 3533.
- [8] M. Shiga, Y. Nakamura, *J. Phys. Soc. Jpn.* 49 (1980) 528.
- [9] T. Shinjo, K. Okada, T. Takada, Y. Ishikawa, *J. Phys. Soc. Jpn.* 37 (1974) 877.
- [10] N. Blume, L. Grodzins, *Phys. Rev.* 136 (1964) A133.
- [11] A.T. Aldred, B.D. Rainford, J.S. Kouvel, T.J. Hicks, *Phys. Rev. B.* 14 (1976) 228.
- [12] Y. Hamaguchi, N. Kunitomi, *J. Phys. Soc. Jpn.* 19 (1964) 1849.
- [13] W.M. Xu, P. Zheng, Z.J. Chen, B.G. Shen, *J. Magn. Magn. Mater.* 172 (1997).
- [14] A. Das, S.K. Paranjpe, S. Honda, S. Murayama, Y. Tsuchiya, *J. Phys. Condens. Matter* 11 (1999) 5209.
- [15] M. Acet, Ch Somsen, G. Nepecks, E.F. Wassermann, *J. Magn. Magn. Mater.* 208 (2000) 191.
- [16] M. Acet, T. Schneider, H. Zähres, W. Stamm, E.F. Wassermann, W. Pepperhoff, *Physica B* 161 (1989) 63.
- [17] W.M. Xu, W. Steiner, M. Reissner, A. Pösinger, M. Acet, W. Pepperhoff, *J. Magn. Magn. Mater.* 104–107 (1992) 2023.
- [18] Y. Tsuchiya, T. Bitoh, S. Murayama, S. Chikazawa, Y. Hamaguchi, *J. Phys. Soc. Jpn.* 65 (1996) 3289.
- [19] Y. Tsuchiya, H. Nakamura, S. Murayama, K. Hoshi, Y. Shimojyo, Y. Morii, Y. Hamaguchi, *Physica B* 237–238 (1997) 446.
- [20] Y. Tsuchiya, H. Nakamura, S. Murayama, K. Hoshi, Y. Shimojyo, Y. Morii, Y. Hamaguchi, *J. Magn. Magn. Mater.* 177–181 (1998) 1447.
- [21] Y. Muraoka, M. Shiga, H. Yasuoka, Y. Nakamura, *J. Phys. Soc. Jpn.* 402 (1976) 414.
- [22] J.P. Eymery, S.B. Raju, P. Moine, *Phys. Lett.* 68A (1978) 260.
- [23] H. Ebert, H. Winter, D.D. Johnson, F.J. Pinski, *J. Phys. Condens. Matter* 2 (1990) 443.
- [24] J. Lauer, W. Keune, *Phys. Rev. Lett.* 48 (1982) 1850.
- [25] G. Le Caer, J.M. Dubois, H. Fischer, I.U. Gonser, H.G. Wagner, *Nucl. Instrum. Meth. B5* (1984) 25.
- [26] K. Szymański, L. Dobrzyński, B. Prus, M.J. Cooper, *Nucl. Instrum. Meth. B119* (1996) 438.
- [27] K. Szymański, D. Satula, L. Dobrzyński, *J. Phys. Condens. Matter* 11 (1999) 881.
- [28] K. Szymański, *J. Phys. Condens. Matter* 12 (2000) 7495.
- [29] K. Szymański, *Nucl. Instrum. Meth. B134* (1998) 405.
- [30] K. Szymański, K. Rečko, L. Dobrzyński, D. Satula, *J. Phys. Condens. Matter* 11 (1999) 6451.
- [31] D. Satula, K. Szymański, J. Waliszewski, L. Dobrzyński, B. Prus, *Mol. Phys. Rep.* 30 (2000) 151.
- [32] J. Balogh, I. Vincze, *Sol. State Commun.* 25 (1978) 695.
- [33] P. Panissod, J. Durand, J.I. Budnick, *Nucl. Instrum. Meth.* 199 (1982) 99.
- [34] S. Aarj, *Phys. Stat. Sol.* 121 (1965) 121.
- [35] Y. Ishikawa, Y. Endoh, *J. Phys. Soc. Jpn.* 23 (1967) 205.
- [36] M.V. Nevitt, A.T. Aldred, *J. Appl. Phys.* 34 (1965) 463.
- [37] R.D. Shull, P.A. Beck, *AIP Conf. Proc.* 24 (1975) 95.
- [38] A.T. Aldred, J.S. Kouvel, *Physica B* 86–88 (1977) 326.
- [39] O. Kubashewski, in: *Iron Binary Phase Diagrams*, ed. Springer, Berlin, 1982.
- [40] N.W. Ashcroft, N.D. Mermin, in: *Solid State Physics*, ed. Holt, Rein hard and Winston 1976.
- [41] S.M. Shapiro, C.R. Fincher Jr., A.C. Palumbo, R.D. Parks, *Phys. Rev. B* 24 (1981) 6661.
- [42] C. Paduani, J.A. Plascak, E. Galvao da Silva *Phys. Rev. B* 44 (1991) 9715.
- [43] O. Kubashewski, in: *Iron alloys*, 1981.
- [44] Y. Ishikawa, Y. Endoh, *J. Phys. Soc. Jpn.* 23 (1967) 205.
- [45] W.H. Miklejohn, C.P. Bean, *Phys. Rev.* 102 (1956) 1413.
- [46] W.H. Miklejohn, C.P. Bean, *Phys. Rev.* 105 (1956) 904.
- [47] E. Berkowitz, Kentaro Takano, *JMMM* 200 (1999) 552.
- [48] Y. Tsuchiya, H. Takita, S. Murayama, Y. Hamaguchi, *J. Phys. Soc. Jpn.* 62 (1993) 3764.

P3



Iron Atoms in Cr–Mn Antiferromagnetic Matrix

K. SZYMAŃSKI¹, D. SATUŁA¹, L. DOBRZYŃSKI^{1,2}, M. BIERNACKA¹,
K. PERZYŃSKA¹ and P. ZALESKI¹

¹*Institute of Experimental Physics, University of Białystok, 15-424 Białystok, Lipowa 41, Poland*

²*The Soltan Institute for Nuclear Studies, 05-400 Otwock-Świerk, Poland*

Abstract. The results of the Mössbauer effect measurements on bcc Cr rich Cr–Fe–Mn alloys in temperature range 12–296 K in zero- and in applied magnetic fields are reported. Monochromatic, circularly polarized radiation was used for investigation of iron moments alignment. Strong enhancement of internal hyperfine magnetic field induced by the applied magnetic field was detected and explained as due to dynamical effects. At high temperatures alignment of iron moments in antiferromagnetic phase is weakly magnetic field-dependent. At low temperatures the average hyperfine magnetic field is antiparallel to the net magnetization showing that iron moments are partly ordered by the applied field.

1. Introduction

Ternary Cr-rich Cr–Fe–Mn alloys with bcc structure exhibit complex magnetic behaviour [1, 2]. At certain composition ferro- and antiferromagnetic orders were found to coexist [3, 4]. A giant magnetoresistance of these alloys [5, 6] make them also attractive for applications.

We report investigations of the temperature dependence of magnetic hyperfine field (hf) and reaction of the system to the applied external magnetic field. In particular, the angular distribution of iron magnetic moments is studied by Mössbauer polarimetry with ⁵⁷Fe as a probe. Determination of the sign of the magnetic hf with monochromatic circularly polarized resonant radiation is very straightforward. I.e., in the case of pure Zeeman interactions, when direction of the magnetic hf is parallel to the direction of radiation, one observes that outer line No 1 has large intensity in comparison with the line intensity No 6. Reversing the hyperfine field by π results in the reversal of intensities as well, i.e., intensities of lines 1 and 6 are small and large, respectively [7].

In the case of disordered systems, broad distributions of hyperfine parameters are usually present. Wide hyperfine field distributions make it difficult to determine the transitions uniquely as one cannot resolve the absorption lines whose intensities have to be analysed.

Within the scope of the intensity tensor formalism we have presented analytical expressions for the absorption line intensities for $I = 3/2 \rightarrow I = 1/2$ nuclear transitions [8]. These results allows one to define so-called n th velocity moment:

$$W_{\zeta}^n = \sum_{\alpha\beta} v_{\alpha\beta}^n A_{\alpha\beta\zeta} / \sum_{\alpha\beta} A_{\alpha\beta\zeta}, \quad (1)$$

where $v_{\alpha\beta}$ is the Doppler velocity, $A_{\alpha\beta\zeta}$ is the area under absorption line for transition $\alpha\beta$ and ζ is polarization of the photon. The explicit formula for the first velocity moment reads:

$$W_{\zeta}^1 = \delta + \frac{1}{4}\gamma_{3/2}B\vec{\gamma} \cdot \hat{\Phi} \cdot \vec{\gamma} - \zeta\frac{1}{4}(\gamma_{1/2} - 5\gamma_{3/2})\vec{B} \cdot \vec{\gamma}, \quad (2)$$

where $\hat{\Phi}$ is dimensionless EFG tensor [8], $B = (\vec{B} \cdot \vec{B})^{1/2}$ is the magnetic hf, δ is the isomer shift, $\gamma_{3/2}$, $\gamma_{1/2}$ are nuclear g -factors of the excited and ground nuclear states, respectively and $\vec{\gamma}$ is the unit vector indicating direction of the photon.

The result (2) depends explicitly on the hyperfine fields sensed by the nucleus. Moreover, Equation (3) is valid irrespective of the strength of the quadrupole interaction. The quantities defined by (1) are directly available in experiment: one needs to sum up absorption line intensities multiplied by a power of the velocity. Particularly useful is the difference of the first moments measured with two opposite polarization, which is proportional to the product $\vec{B} \cdot \vec{\gamma}$, or z component of the magnetic hf:

$$W_{\zeta}^1 - W_{-\zeta}^1 = -\zeta\frac{1}{2}(\gamma_{1/2} - 5\gamma_{3/2})\vec{B} \cdot \vec{\gamma}. \quad (3)$$

2. Experiment and discussion

Two series, $\text{Cr}_{75+x}\text{Fe}_{16+x}\text{Mn}_{9-2x}$ and $\text{Cr}_{75+y}\text{Fe}_{16-y}\text{Mn}_9$, called here x - and y -, respectively, were prepared [9]. Results of low temperature studies were reported in [10]. We detected two kinds of Fe moments, large and small ones. The large moments can be aligned by an external magnetic field while the small ones can hardly be aligned and thus do not contribute to the net magnetization. Samples with $x = 4$ and $y = -6$ exhibit ferromagnetic properties.

For $x = -4$ and $y = 6$ samples, characterised by low iron concentration, magnetization measurements indicate moment per average atom smaller than $0.07 \mu_B$ at $T = 12$ K and $B = 1.1$ T. An inverse of DC susceptibility, measured at $B = 10$ mT, extrapolated to zero value, crosses the temperature axis at negative temperatures, which indicate presence of an antiferromagnetic ordering.

Results of a typical temperature scan of Mössbauer measurements for sample with $x = 4$ are shown in Figure 1a. A sharp transition at T about 50 K to a state at which magnetic hf is zero is observed, see the average field intensity in Figure 2a.

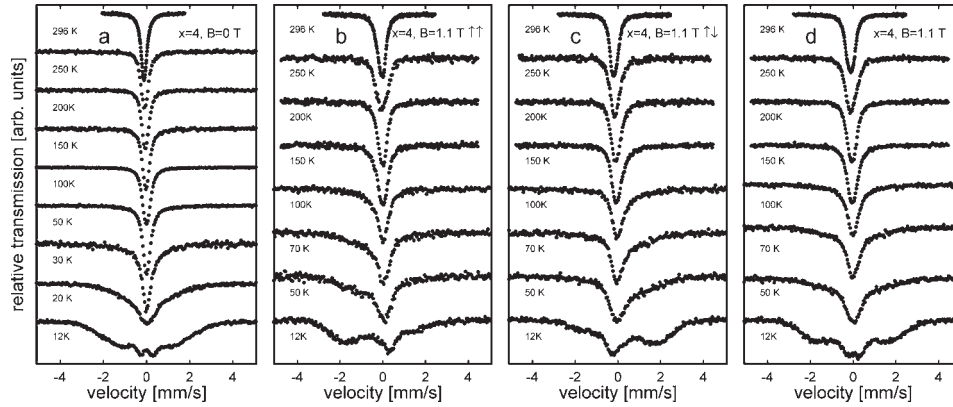


Figure 1. Spectra of the $x = 4$ sample measured in zero applied field with unpolarized beam (a), and in an applied field with two opposite circular polarizations (b), (c). Arrows $\uparrow\uparrow$ and $\uparrow\downarrow$ correspond to two opposite polarizations (ζ and $-\zeta$). Sum of the normalized spectra corresponding to two polarizations is equivalent to the measurement in the applied magnetic field of 1.1 T with unpolarized radiation (d).

Similarly, FWHMs of the Lorentzian line obtained from fits at high temperatures, indicate also sharp transition (Figure 2b).

Measurements with monochromatic, circularly polarized radiation were performed in external magnetic field $B = 1.1$ T parallel to the direction of gamma rays (Figures 1b,c). At $T = 12$ K the spectra show apparent asymmetries, namely line No 1, located at $v = -2$ mm/s, is much deeper than the line No 6, located at $v = 2$ mm/s in Figure 1b. The asymmetry is reversed in Figure 1c. The same type of asymmetry characterises α -Fe sample [7]. We thus observe for $x = 4$ magnetic hf which is, on average, directed antiparallel to the magnetization. When temperature increases, the spectra exhibit smaller asymmetry. At high temperature spectra consist of a single, slightly asymmetric peak. Average position of the peak measured at temperatures above 200 K for polarization shown in Figure 1b is larger than measured with the polarization shown in Figure 1c. This indicates that at high temperature ^{57}Fe nucleus detects external magnetic field only. To analyse measured spectra quantitatively, we determined W_{ζ}^1 , see Equation (1). The difference of the first velocity moments (3) increases nearly linearly with temperature (see Figure 2c) and attains zero at T close to 150 K, three times larger than the onset determined from zero-field experiment. Since the difference of the first velocity moments is proportional to the average z component of the magnetic hf, a strong enhancement of the internal field caused by applied magnetic field at $T > 50$ K is observed. It is known, that sum of the normalised spectra measured with two opposite polarizations is equivalent to the measurement with unpolarized radiation [7, 8], in our case in the applied field. In Figure 1d the sums of the spectra are shown, which were analysed (Figure 2a) in the same way as the zero field spectra. One clearly observes that the difference between zero field and in-field average

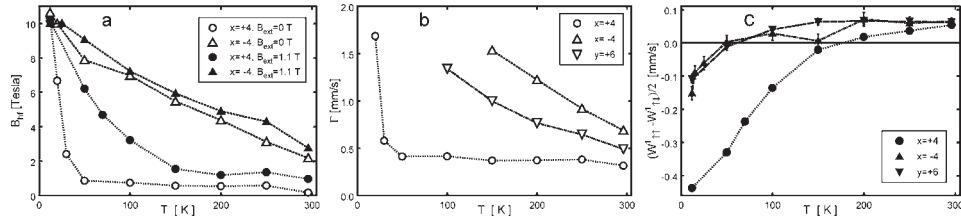


Figure 2. (a) Average value of magnetic hf intensity. (b) FWHM of the Lorentzian line fitted to zero-field spectra. (c) Experimentally determined difference $W_{\zeta}^1 - W_{-\zeta}^1$, see Equation (3), measured in external magnetic field $B = 1.1$ T.

magnetic hf at $T = 50$ K exceeds the applied field about 5 times. To our knowledge this is the first report of such an enhancement of magnetic hf in Cr-Fe-Mn system. A change of the shape of the spectra in temperature range between $T = 70$ K and 50 K, see Figure 1d, suggests that dynamical effects should be considered. Ferromagnetically coupled magnetic moments, forming clusters at these temperatures, fluctuate with characteristic time shorter than Larmor period of the nucleus in magnetic hf. A single line observed in zero-field experiment (Figure 1a) suggests that under applied external field an additional uniaxial anisotropy is introduced, which slows down the fluctuations and allows observation of magnetic hf splitting. Experiment with polarized radiation clearly demonstrate, that wings which appear at $T = 50$ and 70 K (Figures 1c,d) have the same type of asymmetry as spectra measured at the lowest temperature. Polarized experiment shows also that projection of the average magnetic hf is antiparallel to the direction of magnetization up to $T = 150$ K, Figure 2c. Thus the magnetic hf is likely to be of the core origin. Besides, it must be concluded that localised iron moments are still present at temperatures about three times larger than the temperature marking an onset of the magnetic hf in zero-field Mössbauer experiment. Nearly linear decrease of average magnetic hf (Figure 2a) with increasing temperature, accompanied by almost linear increase of the difference of first moments (Figure 2c), both for in-field experiments at $T < 150$ K, indicate, that the ratio of these values remains approximately constant within wide (compared to $0 \div T_c$) temperature range. This indicates that angular distribution of Fe magnetic moments does not change dramatically with temperature.

Average magnetic hf measured in zero- and nonzero magnetic fields is shown in Figure 2a for the $x = -4$ sample, containing AF phase. The temperature dependence of magnetic hf is similar in both series of measurements, indicating weak influence of external field on the iron moments. A characteristic feature of the $x = -4$ and $y = 6$ sample is that the shape of the zero field spectra can be described well by Lorentzian line in wide temperature range, see temperature dependence of the linewidth in Figure 2b. Measurements with polarized radiation show that at higher temperatures the average z component of the magnetic hf corresponds to the applied external magnetic field (Figure 2c), while the average magnetic hf (Figure 2a) definitely exceeds the applied field. This indicates that in

the AF phase and at high temperature the iron moments form a structure which can hardly be modified by application of external magnetic field. At low temperatures this component is directed antiparallel to the magnetization, and its absolute value is much smaller than that one in the ferromagnetic, $x = 4$, sample. However, Fe magnetic moments can be partly aligned at low temperatures, with a clearly antiparallel orientation of the z component of the magnetic hf.

Acknowledgement

The work was sponsored by the State Council of Science through grant 2P03B11 516.

References

1. Xu, W. M., Steiner, W., Reissner, M., Pösinger, A., Acet, M. and Pepperhoff, W., *J. Magn. Magn. Mater.* **104–107** (1992), 2023.
2. Acet, M., Schneider, T., Zähres, H., Stamm, W., Wassermann, E. F. and Pepperhoff, W., *Physica B* **161** (1989), 63.
3. Tsuchiya, Y., Nakamura, H., Murayama, S., Hoshi, K., Shimojyo, Y., Morii, Y. and Hamaguchi, Y., *Physica B* **237–238** (1997), 446.
4. Das, S., Paranjpe, K., Honda, S., Murayama, S. and Tsuchiya, Y., *J. Phys. Condens. Matter* **11** (1999), 5209.
5. Wu, B. M., Yang, D. S., Sheng, S., Du, Y. L. and Xu, W. M., *J. Magn. Magn. Mater.* **202** (1999), 426.
6. Somsen, Ch., Acet, M., Nepecks, G. and Wassermann, E. F., *J. Magn. Magn. Mater.* **208** (2000), 191.
7. Szymański, K., Dobrzyński, L., Prus, B. and Cooper, M. J., *Nucl. Instr. Meth. B* **119** (1996), 438.
8. Szymański, K., *J. Phys.: Condens. Matter* **12** (2000), 7495.
9. Satuła, D., Szymański, K., Waliszewski, J., Dobrzyński, L. and Prus, B., *Mol. Phys. Rep.* **30** (2000), 151.
10. Szymański, K., Satuła, D., Dobrzyński, L., Biernacka, M., Perzyńska, K. and Zaleski, P., *J. Magn. Magn. Mater.* **263** (2001), 56.

P4

Mössbauer study of the $\text{Fe}_{1-x}\text{Ni}_x$ Invar alloys by monochromatic circularly polarized source

Dariusz Satuła,
Krzysztof Szymański,
Ludwik Dobrzyński,
Katarzyna Rećko,
Janusz Waliszewski

Abstract X-ray diffraction measurements and Mössbauer spectroscopy with and without external magnetic field parallel to beam direction have been performed for $\text{Fe}_{1-x}\text{Ni}_x$ ($x = 0.25, 0.30, 0.35$) alloys. The compositions of the studied alloys were chosen in order to cover the concentration range where the fcc \leftrightarrow bcc structural transformation appears, as well as where single phase fcc Fe-Ni alloys exhibit the Invar phenomena. Spatial distribution of the iron magnetic moments is discussed. The hyperfine magnetic field (h.m.f.) distribution is analyzed within a scope of two models discussed in the literature. In the first model it is assumed that any hyperfine magnetic field vector have the same spatial distribution (the same values of $\langle \cos \theta \rangle$). In the second, the low field component of the hyperfine magnetic field is ordered antiferromagnetically (or disordered) while the high field component is aligned by an external magnetic field. In order to determine the mean values of cosine of the angle between γ -rays direction and hyperfine field vector of iron, $\langle \cos \theta \rangle$, a monochromatic circularly polarized Mössbauer source (MCPMS) was used. The analysis of the MCPMS results show that the shapes of the measured spectra can be explained by single values of $\langle \cos \theta \rangle$.

Key words Invar alloys • Mössbauer polarimetry • transition metal alloys

Introduction

The problem of the Invar effect in Fe-Ni alloys at the concentrations close to the fcc \leftrightarrow bcc transformation has a long story but the full understanding of the phenomena is still lacking. After discovery of the Invar effect in fcc Fe-Ni alloys, a number of experimental studies were done and theoretical models suggested. The most popular phenomenological model – so-called 2γ state model – was introduced by Weiss [9]. This model assumed the presence of two electronic states of Fe atoms: high spin and high volume (HS) ferromagnetic state and low spin and low volume (LS) state with an antiferromagnetic order. In papers [4, 5] the magnetic model proposed by the authors assumed localized magnetic moments of Fe and Ni with a mixed exchange coupling between them. This can lead to an antiparallel orientation of iron magnetic moments with respect to the net magnetization for a certain amount of Fe neighbours. The recent *ab initio* calculations of the volume dependences of magnetic properties, so-called classical Invar ($\text{Fe}_{0.65}\text{Ni}_{0.35}$), in which the non-collinear spin alignments were allowed, gives a new impulse to the studies of this intriguing phenomena [8]. In this calculations spins may be canted with respect to the average magnetization direction. The results show that the Invar properties could be explained by a continuous transition of Fe spins from nearly ferromagnetic ordering at the large volume to an approximately uniform spatial distribution of spins for small volume. The aim of the presented work is to explore the spatial distributions of the Fe magnetic hyperfine field vectors in fcc Fe-Ni alloys. Because a standard Mössbauer spectroscopy is not

D. Satuła✉, K. Szymański, K. Rećko, J. Waliszewski
Institute of Experimental Physics,
University of Białystok,
41 Lipowa Str., 15-424 Białystok, Poland,
Tel.: +48 85/ 745 72 15, Fax: +48 85/ 745 72 23,
e-mail: satula@alpha.uwb.edu.pl

L. Dobrzyński
Institute of Experimental Physics,
University of Białystok,
41 Lipowa Str., 15-424 Białystok, Poland
and The Andrzej Sołtan Institute for Nuclear Studies,
05-400 Otwock-Swierk, Poland

Received: 17 July 2002

sensitive to the sign of the hyperfine magnetic field, the measurements with MCPMS have been used to get information about the spatial distribution of the hyperfine field vectors.

Experimental

The $\text{Fe}_{1-x}\text{Ni}_x$ ($x = 0.25, 0.30, 0.35$) alloys were prepared by melting in an arc furnace stoichiometric amounts of iron and nickel elements under a protective argon atmosphere. The ingots were powdered, and then the samples were annealed at 600°C for 2 h and cooled at a rate of $300^\circ\text{C}/\text{h}$. X-ray diffraction measurements were used for the determination of the crystalline structure as well as of the lattice parameters. Standard ^{57}Fe Mössbauer measurements in constant acceleration mode with a commercial ^{57}Co source in the Cr matrix were performed. In the measurements, powder samples of about $12 \text{ mg}/\text{cm}^2$ with random grain orientation fixed by an epoxy glue were used. In order to determine the spatial distribution of hyperfine magnetic field of the sample in axial external field of 1.1 T, Mössbauer spectroscopy with monochromatic, circularly polarized radiation was used. Polarized beam was prepared by the filter technique: resonant photons with one polarization were absorbed by the filter. This technique is described in greater detail in [6].

Results and discussion

The X-ray diffraction measurements show that in the sample with $x = 0.25$ there are two cubic phases, bcc and fcc, while only the fcc structure is present for $x = 0.30$ and 0.35 . The measured lattices parameters are presented in Table 1.

Table 1. Lattices parameters of Fe-Ni alloys.

Lattice parameter (\AA)	$\text{Fe}_{0.75}\text{Ni}_{0.25}$	$\text{Fe}_{0.70}\text{Ni}_{0.30}$	$\text{Fe}_{0.65}\text{Ni}_{0.35}$
fcc	3.5839(7)	3.5876(6)	3.5955(5)
bcc	2.8691(6)		

It can be seen that the lattice parameter for the fcc phase increases with increasing Ni concentration. The measured value for $\text{Fe}_{0.65}\text{Ni}_{0.35}$ agrees well with the data published in [1].

The Mössbauer spectra measured in zero field and in the magnetic field of $B = 1.1 \text{ T}$ applied parallel to the gamma beam are presented in Figs. 1a and 1b, respectively. The spectra were fitted with a sum of sextets broadened by the Gaussian distribution of magnetic hyperfine field, and a single line, if necessary.

As can be inferred from Fig. 1, the measured shapes of the spectra change drastically with Ni concentration. The shape of the spectrum for $x = 0.25$ can be explained by one broadened sextet and one single line. The observed sextet comes from Fe in the bcc phase while the single line originates from the Fe atoms in fcc phase. We also note the presence of small amounts of Fe-O for $x = 0.25$, and 0.30 in all measured spectra. In addition, some slight amounts of Fe_3O_4 appeared after annealing for $x = 0.35$. Under the applied external magnetic field ($B = 1.1 \text{ T}$) the shape of the spectra changes, cf. Figs. 1a and 1b. The magnetic moments belonging to the ferromagnetic phase are aligned and in the axial field geometry this results in a decrease of the line intensities i_2 and i_5 of the Zeeman sextets:

$$(1) \quad i_1:i_2:i_3:i_4:i_5:i_6 = 3:z:1:1:z:3.$$

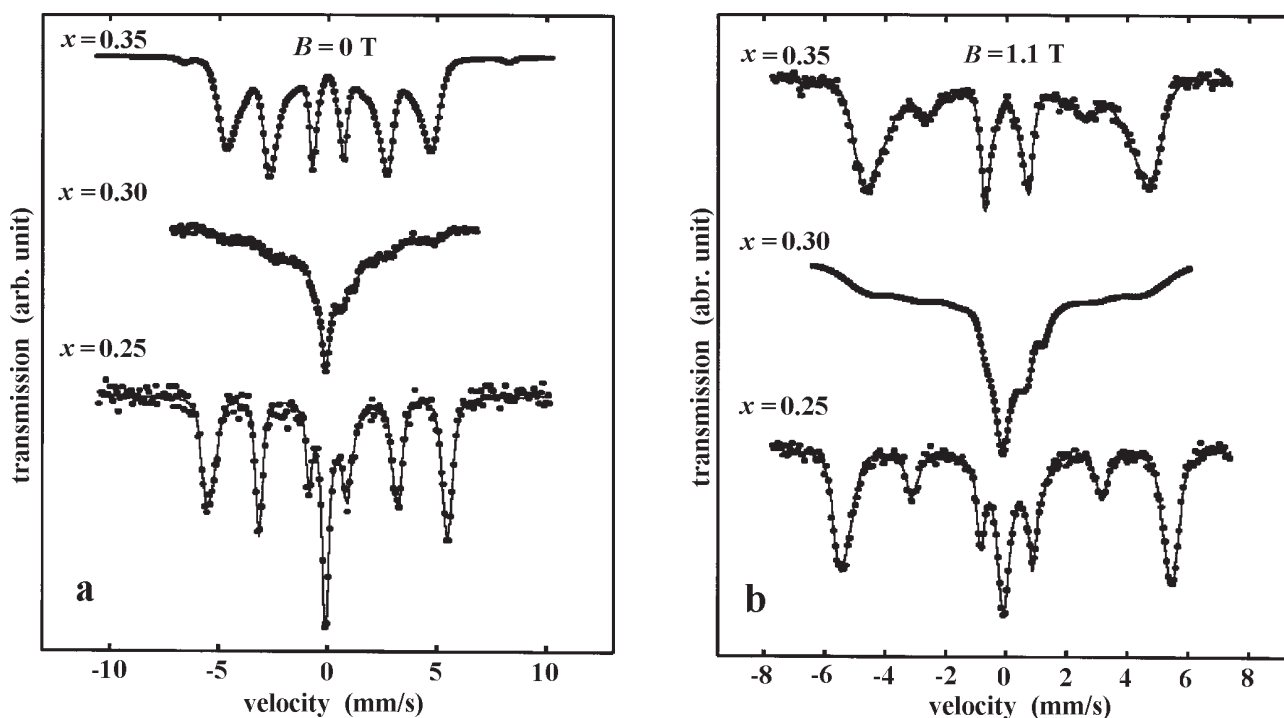


Fig. 1. Mössbauer spectra of $\text{Fe}_{1-x}\text{Ni}_x$ measured in (a) zero and (b) external applied magnetic field parallel to the direction of photons.

The z value corresponds to the average square of the cosine of an angle θ between the direction of the gamma beam and the direction of the magnetic hyperfine field:

$$(2) \quad \langle \cos^2 \theta \rangle = \frac{4-z}{4+z}.$$

We have found that the external field causes reorientation of magnetic moments only. Within the experimental accuracy the shape of the h.m.f. distribution remains unchanged. Therefore, we performed simultaneous fits to the spectra measured with (Fig. 1a) and without the field (Fig. 1b). The shapes of h.m.f. distributions are shown in Fig. 2. Their main features are the following. The shape for $x = 0.30$ reflects a very broad hyperfine field distribution and a paramagnetic line. The paramagnetic line is well separated from the broad magnetic component (see peak at $B = 0$ T in Fig. 2 for $x = 0.30$). Three weak peaks seen at $B = 9, 19$ and 26 T can be artefacts due to the use of three Zeeman components in the fitting procedure. The shape for $x = 0.35$ can be described by the two peak structure with a very broad low field component (see Fig. 2). This latter shape of hyperfine field distribution is typical for “classical Invar” concentration [2]. Average values of the h.m.f. fcc phase are equal to 0.0 T, 15 ± 2 T and 25 ± 1 T for $x = 0.25, 0.30$, and 0.35 , respectively, and agree well with the behavior of the mean magnetic hyperfine field as a function of Ni concentration for fcc phase in the range from 0.25 to 0.38 [3].

Because the standard Mössbauer spectroscopy is not sensitive to the magnetic hyperfine field direction, it is hard to get information about spatial distributions of Fe spins. Some interesting features of the spatial distribution of the hyperfine magnetic field vectors can be obtained from the spectra measured by polarized radiation (see Fig. 3a and 3b). The symbols $\uparrow\uparrow$ and $\uparrow\downarrow$ at the Fig. 3 refer to two opposite polarizations of the beam. The spectra exhibit characteristic asymmetry [6]. Defining the asymmetry parameters in the intensities between the lines number 1 and 6 or 4 and 3 as:

$$(3) \quad A = \frac{i_1 - i_6}{i_1 + i_6} = \frac{i_4 - i_3}{i_3 + i_4}$$

one can express an average $\langle \cos \theta \rangle$ (projection of the iron hyperfine field on the external field direction) by

$$(4) \quad \langle \cos \theta \rangle = \frac{4 \cdot A}{(4+z) \cdot p}$$

Table 2. The values of the parameters z , A , $\langle \cos^2 \theta \rangle$ and $\langle \cos \theta \rangle$ for the Fe_{1-x}Ni_x ($x = 0.25, 0.30, 0.35$).

	Fe _{0.75} Ni _{0.25}	Fe _{0.70} Ni _{0.30}	Fe _{0.65} Ni _{0.35}
z	0.81 ± 0.05	0.4 ± 0.30	0.27 ± 0.05
A	0.59 ± 0.15	0.4 ± 0.20	0.59 ± 0.15
$\cos^2 \theta$	0.66 ± 0.02	0.82 ± 0.12	0.87 ± 0.02
$\cos \theta$	0.61 ± 0.14	0.6 ± 0.30	0.69 ± 0.14

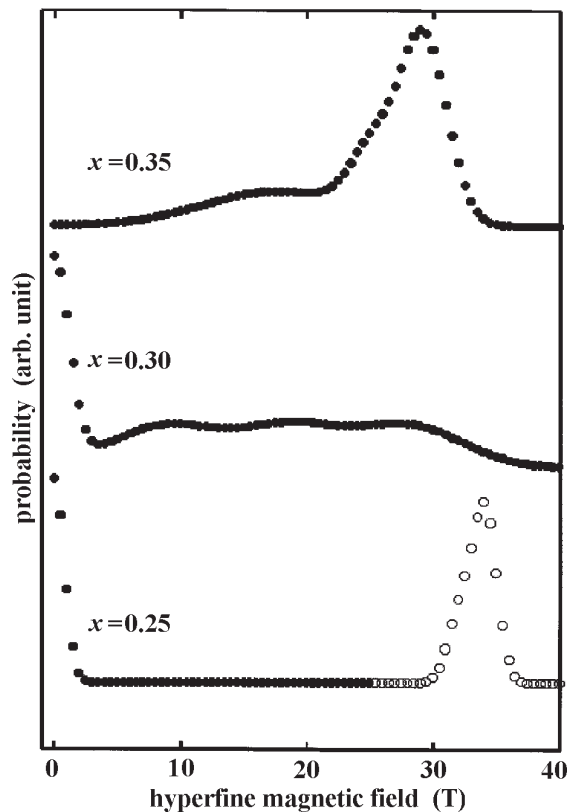


Fig. 2. Hyperfine magnetic field distributions. Full and empty symbols correspond to fcc and bcc phase, respectively.

where the parameter p denotes the polarization of the beam, in our case $p = (80 \pm 2)\%$.

As was already discussed in the literature [2, 9] and is also seen in the presented h.m.f. distributions (see Fig. 2) there are two kinds of iron magnetic moments in the fcc phase: large and small ones. We are interested in response of these moments to the applied field. As a first step, we assume that all the moments in the sample have the same angular distribution. This results in a single value of the $\langle \cos \theta \rangle$ (model I). The result of such an assumption is shown in Figs. 3a and 3b and in Table 2. Solid lines in Figs. 3a and 3b correspond to the fit with the same hyperfine parameters as in Fig. 1 (for the in-field experiment) except of the asymmetry between line intensities i_1 and i_6 (or i_4 and i_3). We see that the assumption is confirmed by the experiment.

In the second step we analyzed the spectrum for $x = 0.35$ in greater detail. We assumed that the low field component originates from antiferromagnetic or/and spin disordered phase. In this case the asymmetry parameter A for the low field component is zero. The results of the fitted model are presented in Figs. 3a and 3b (model II). We see that the ‘model II’ cannot explain the observed asymmetry in the spectra, while the ‘model I’ describes well the measured spectra.

Conclusions

The X-ray diffraction experiments show that the sample with $x = 0.25$ consists of two crystallographic phases (fcc

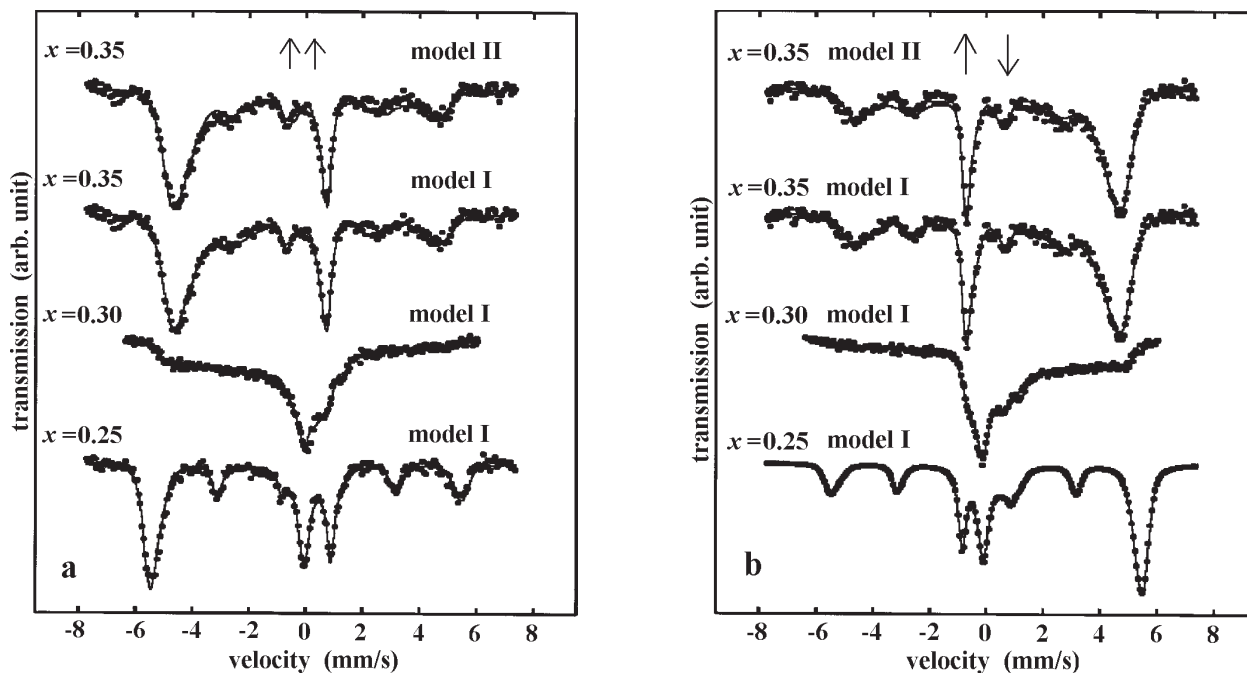


Fig. 3. Mössbauer spectra of Fe_{1-x}Ni_x measured using MCPMS source for both polarizations (a) and (b).

and bcc), while for $x = 0.30, 0.35$ only a single fcc phase was detected. The measured parameters of the lattices agree well with the data presented in [1].

The measured shapes of the Mössbauer spectra show remarkable changes with increasing nickel concentration. The mean values of magnetic hyperfine field for fcc phase are equal to 0.0 T , $15 \pm 2 \text{ T}$ and $25 \pm 1 \text{ T}$ for $x = 0.25, 0.30, 0.35$, respectively.

The monochromatic circularly polarized Mössbauer source has been used to measure spatial distributions of hyperfine field vectors of Fe atoms. The conclusion from the MCPMS measurements is that the average cosine between local iron magnetic moment and the average magnetization direction in the Invar Fe₆₅Ni₃₅ is the same for the whole sample. This conclusion is in contradiction with the Weiss 2γ state model where the LS antiferromagnetic state is postulated. Because of the relatively large uncertainty of the measured $\langle \cos \theta \rangle$ and $\langle \cos^2 \theta \rangle$, it is hard to say whether some minor part of iron hyperfine vectors are not antiparallel to the net magnetization as detected in [2, 7].

References

1. Dubrovinsky L, Dubrovinskaya N, Abrikosov IA (2001) Pressure-induced Invar effect in Fe-Ni alloys. *Phys Rev Lett* 86:4851–4854
2. Hesse J (1989) From FeNi-Invar to FeNiMn reentrant spin-glasses. *Hyperfine Interact* 47:357–378
3. Johnson CE, Ridout MS, Cranshaw TE (1963) The Mössbauer effect on iron alloys. *Proc Phys Soc* 81:1079–1090
4. Müller JB, Hesse J (1983) A model for magnetic abnormalities of FeNi Invar alloys. I. Macroscopic magnetic properties. *Z Phys B* 54:35–42
5. Müller JB, Hesse J (1983) A model for magnetic abnormalities of FeNi Invar alloys. II. Microscopic properties. *Z Phys B* 54:43–48
6. Szymański K, Dobrzyński L, Prus B, Cooper MJ (1996) A single line circularly polarised source of Mössbauer spectroscopy. *Nucl Instrum Meth Phys Res B* 119:438–441
7. Ullrich H, Hesse J (1984) Hyperfine field vectors and hyperfine field distributions in FeNi Invar alloys. *J Magn Mater* 45:315–327
8. Van Schilfgaarde M, Abrikosov IA, Johansson B (1999) Origin of the Invar effect in iron-nickel alloys. *Nature* 400:46–49
9. Weiss RJ (1963) The origin of the “Invar” effect. *Proc Phys Soc* 82:281–288

P5



Angular Distribution of Hyperfine Magnetic Field in Fe_3O_4 and $\text{Fe}_{66}\text{Ni}_{34}$ from Mössbauer Polarimetry

K. SZYMAŃSKI¹, D. SATUŁA¹ and L. DOBRZYŃSKI^{1,2}

¹*Institute of Experimental Physics, University of Białystok, 15-424 Białystok, Poland*

²*The Soltan Institute for Nuclear Studies, 05-400 Otwock-Świerk, Poland*

Abstract. Experimental determination of some angular averages of hyperfine field is demonstrated. The averages relates to magnetic structure. Exemplary results of the measurements for Fe_3O_4 and $\text{Fe}_{66}\text{Ni}_{34}$ show that it is possible to obtain valuable information about the field magnitudes and orientations even when distributions of fields are present in the system under study.

In disordered magnetic systems one encounters usually a distribution of both, the intensity and the orientation of hyperfine magnetic field (h.m.f.). Preferred orientation, $P(\Omega)$, of the hyperfine fields is of particular importance in the context of the contribution of selected elements to the magnetic texture [1, 2]. It is usually described in a certain set of basis functions, e.g., spherical harmonics Y_{lm} . Since only M1 dipolar transitions are measured in ^{57}Fe Mössbauer spectroscopy, unpolarized radiation delivers information on Y_{2m} only, while Y_{1m} harmonics can be known when circularly polarized radiation is used [3]. Knowing Y_{1m} and Y_{2m} in the texture function is equivalent to the knowledge of angular averages $\langle \gamma_r \cdot \mathbf{m} \rangle$ and $\langle (\gamma_r \cdot \mathbf{m})(\gamma_s \cdot \mathbf{m}) \rangle$ [4], where \mathbf{m} is an unit vector parallel to the local hyperfine field \mathbf{B} , γ_r is a Cartesian versor ($r = x, y, z$) and brackets $\langle \rangle$ denote angular averaging:

$$\langle f(\Omega) \rangle = \int_{4\pi} f(\Omega) P(\Omega) d\Omega. \quad (1)$$

In the case of a sample with axial symmetry it is convenient to choose one of the γ_r , denoted by γ , parallel to the \mathbf{k} vector of photon. Then the averages $\langle \gamma \cdot \mathbf{m} \rangle \equiv c_1$ and $\langle (\gamma \cdot \mathbf{m})^2 \rangle \equiv c_2$ can be measured with monochromatic, circularly polarized radiation [4, 5]. In disordered systems one can measure distribution of the intensity of h.m.f., $p(B)$, and for each intensity B , in principle, two averages c_1 and c_2 . This paper shows that one can finally get three distributions: $p(B)$, $c_1(B)$ and $c_2(B)$.

Normalized Mössbauer spectrum $S(v)$ consists of a linear combination of N subspectra $s(v, B_i)$:

$$S(v) = \sum_{j=1}^N p_j s(v, B_j), \quad (2)$$

where v is Doppler velocity, and p_j is a nonnegative coefficient for a field B_j . Subspectrum $s(v, B)$ is a Zeeman sextet:

$$s(v, B) = \sum_{n=1}^6 i_n L_n(v, B), \quad (3)$$

where $L_n(v, B)$ describes the shape of the absorption line corresponding to the n th nuclear transition and i_n is the line intensity dependent on the photon polarization and wave vector. For the case of single B and measurements with circularly polarized radiation, the coefficients i_n were given in [3]. One can show [4] that having a distribution of directions of vector B the expressions for i_n should contain already introduced averages, namely:

$$\begin{aligned} 16i_1 &= 48i_4 = 3(1 \pm 2c_1 + c_2), \\ 4i_2 &= 4i_5 = 1 - c_2, \\ 48i_3 &= 16i_6 = 3(1 \mp 2c_1 + c_2). \end{aligned} \quad (4)$$

Every subspectrum $s(v, B_j)$ is characterized by its relative area proportional to p_j and two averages c_1 and c_2 (the index j in c_1, c_2 as well as in p coefficients was dropped for simplicity reasons). Using the least squares fitting procedure and varying $3N$ coefficients p, c_1 and c_2 , one can find best fit of function $S(v)$, see Equation (2), to the experimental spectrum. Physically possible sets of p, c_1 and c_2 have to be considered only, namely:

$$p \geq 0, \quad -1 \leq c_1 \leq 1, \quad 0 \leq c_2 \leq 1, \quad c_1^2 \leq c_2. \quad (5)$$

The last inequality in (5) is the Buniakovsky–Schwartz relation. In order to make minimisation of χ^2 with conditions (5) effective, we introduce a set of $3N$ new variables, a, b, Δ , related to p, c_1 and c_2 through:

$$\begin{aligned} p[a, b, \Delta] &= \frac{(a^2 + b^2)^2 + 2\Delta^4}{4}, \\ c_1[a, b, \Delta] &= \frac{a^4 - b^4}{(a^2 + b^2)^2 + 2\Delta^4}, \\ c_2[a, b, \Delta] &= \frac{(a^2 - b^2)^2 + 2\Delta^4}{(a^2 + b^2)^2 + 2\Delta^4}. \end{aligned} \quad (6)$$

The square brackets were used in transformation functions (6) in order not to confuse them with the distribution functions $p(B), c_1(B)$ and $c_2(B)$. The functions (6) have following properties: (i) they are even, (ii) for a, b , and Δ positive there exist inverse functions $a[p, c_1, c_2], b[p, c_1, c_2], \Delta[p, c_1, c_2]$, (iii) the inequalities (5) hold for any real values of a, b , and Δ , (iv) χ^2 expressed in variables a, b , and Δ is a polynomial of 8th order. The two last properties make numerical process of searching of minimum of χ^2 very effective.

Two different distributions of hyperfine parameters may produce identical spectra. This leads to the ambiguity much discussed in literature [6–8]. One case of

Table I. Fitted probabilities p and magnetic texture coefficients. Two last columns contain average value of the h.m.f. and the width of its Gaussian distribution

	p	c_1	c_2	B [T]	ΔB [T]
Fe ₃ O ₄	0.38 ± 0.01	-0.78 ± 0.02	0.93 ± 0.01	49.92	0.18
	0.62 ± 0.01	0.80 ± 0.02	0.97 ± 0.01	45.13	0.53
Fe _{0.66} Ni _{0.34}	0.37 ± 0.02	0.57 ± 0.03	0.60 ± 0.02	28.6	2.04
	0.29 ± 0.02	0.62 ± 0.03	0.62 ± 0.02	25.2	3.36
	0.34 ± 0.02	0.44 ± 0.03	0.63 ± 0.02	17.7	6.45

ambiguity appears when multidimensional distribution is extracted from one dimensional data (i.e. Mössbauer spectrum). Additional independent experimental information usually reduces this ambiguity. We have demonstrated [9], as an example, that two different distributions of h.m.f. reproduce experimental spectra of Fe_{2.5}Cr_{0.5}Al alloy measured with unpolarized beam equally well. The measurements with monochromatic, circularly polarized radiation, showed which of the two is correct one. Continuing this direction we developed an algorithm for simultaneous fitting of the spectra measured with different photon polarization states (on the sample in the same conditions, like external magnetic field, temperature). Three distributions: $p(B)$, $c_1(B)$ and $c_2(B)$ are fitted simultaneously with the help of transformation (6).

In order to apply discussed algorithm to real cases, we have to take into account different isomer shift and quadrupole splitting for every subspectra (the latter is considered as small perturbation of the h.m.f.), and correction for polarization degree [4, 10].

The first example on which the algorithm was tested is Fe₃O₄ powdered absorber, prepared from stoichiometric single crystal of magnetite, with stoichiometry for which Verwey transition of the first kind is observed. The absorbers exposed to external field of 1.1 T were measured at room temperature and the spectra are shown in Figure 1. Fe₃O₄ is ferrimagnet and one expects that in an external magnetic field two hyperfine fields will be oriented antiparallel, resulting in c_1 parameters of opposite signs. This is observed indeed, see Table I. Results of simultaneous fit are shown by solid lines in Figure 1. Majority of the Fe moments, occupying octahedral positions with smaller h.m.f. are oriented parallel to the net magnetization, like in α -Fe (see the inset), and the c_1 parameter is positive. Minority of Fe with larger field (occupying tetrahedral positions) are oriented antiparallel to the net magnetization which is measured quantitatively by negative value of c_1 parameter. Absolute values of c_1 and c_2 parameters are slightly smaller than 1 indicating almost complete saturation of the sample in the applied external magnetic field.

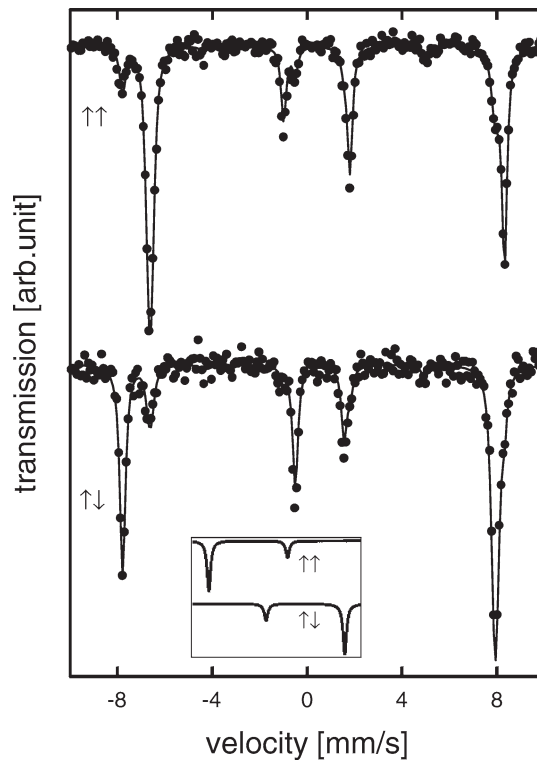


Figure 1. 1 Mössbauer spectra of Fe_3O_4 measured with two opposite circular polarizations of monochromatic radiation. Solid lines show the best simultaneous fit obtained from algorithm discussed in the text. The inset shows schematically the shape of $\alpha\text{-Fe}$ spectra measured with two opposite circular polarizations abbreviated by $\uparrow\uparrow$ and $\uparrow\downarrow$ arrows.

The second example is Invar Fe–Ni alloy, whose ground state magnetic structure is still under debate. There are recent experiments performed under high pressure, one of them [11] consistent with 2γ -state model proposed by Weiss [12], and other [13], consistent with low spin non-collinear structure proposed in [14]. Recent polarized neutron diffraction experiments indicated strong coupling of lattice and magnetic degrees of freedom [15]. Circularly polarized polychromatic radiation was used in investigation of Fe–Ni invar alloys [16], the spectra obtained were, however, complicated and difficult for interpretation.

In our experiment, $\text{Fe}_{66}\text{Ni}_{34}$ was prepared as a foil and measured in the magnetic field perpendicular to the foil at room temperature, see Figure 2. Three Gaussian components, displayed in the inset, describe full spectrum well. Results of the best fit are shown by solid lines in Figure 2; the fitted parameters are listed in the Table I. The most important result is, that the best fit is obtained for almost similar values of c_2 (quite similarly for c_1) for the three components. The smallest value of c_1 is related to the weakest h.m.f. This indicates that this component is more disordered than the remaining two. Our results leave no doubt that the lowest-field component

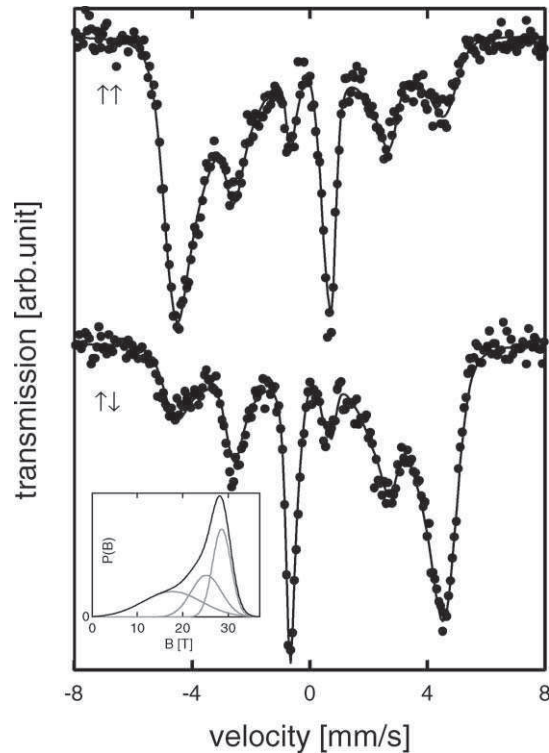


Figure 2. Same as Figure 1 for $\text{Fe}_{66}\text{Ni}_{34}$. The distribution of h.m.f. resulting from the components used is shown in the inset.

is neither due to the antiferromagnetic ordering postulated in 2γ -state model [12] nor to eventual random disorder. Were any of these two possibilities true, the c_1 should be close to 0.06, i.e. the ratio of the applied field and the mean value of the component (1.1/17.7), while c_2 would be close to 1/3. Moreover our results show that low field component does not have, in average, antiparallel orientation with respect to the net magnetization as interpreted in [16].

References

1. Pfannes, H.-D. and Fisher, H., *Appl. Phys.* **13** (1977), 317.
2. Pfannes, H.-D. and Paniago, R. M., *Hyp. Interact.* **71** (1992), 1499.
3. Frauenfelder, H., Nagle, D. E., Taylor, R. D., Cochran, D. R. F. and Visscher, W. M., *Phys. Rev.* **126** (1962), 1065.
4. Szymanski, K., *NIM B* **134** (1998), 405.
5. Szymanski, K., Dobrzynski, L., Prus, B. and Cooper, M. J., *NIM B* **119** (1996), 438.
6. Le Caer, G., Dubois, J. M., Fischer, H., Gonser, I. U. and Wagner, H. G., *NIM B* **5** (1984), 25.
7. Le Caer, G. and Brand, R. A., *J. Phys.: Condens. Matter* **10** (1998), 10715.
8. Rancourt, D. G., In: G. J. Long and F. Grandjean (eds), *Mössbauer Spectroscopy Applied to Magnetism and Materials Science*, Vol. 5, Plenum, New York, 1996, p. 105.
9. Szymanski, K., Satula, D. and Dobrzynski, L., *J. Phys.: Cond. Matter* **1** (1999), 881.

10. Szymanski, K., *J. Phys.: Cond. Matter* **12** (2000), 7495.
11. Rueff, J. P., Shukla, A., Kaprolat, A., Krisch, M., Lorenzen, M., Sette, F. and Verbeni, R., *Phys. Rev. B* **63** (2001), 132409.
12. Weiss, J., *Proc. R. Soc. London A* **82** (1963), 281.
13. Dubrovinsky, L., Dubrovinska, N., Abrikosov, I. A., Vennström, M., Westman, F., Carlson, S., van Schilfgaarde, M. and Johansson, B., *PRL* **86** (2001), 4851.
14. van Schilfgaarde, M., Abrikosov, I. A. and Johansson, B., *Nature* **400** (1999), 46.
15. Brown, P. J., Kanomata, T., Matsumoto, M., Neumann, K.-U. and Ziebeck, K. R. A., *JMMM* **242–245** (2002), 781.
16. Ulrich, H. and Hesse, J., *JMMM* **45** (1984), 315.

P6

The maximum entropy method in the analysis of the Mössbauer spectra

Ludwik Dobrzyński,
Krzysztof Szymański,
Dariusz Satuła

Abstract The paper shows the possibility of reconstruction of the distribution of hyperfine field parameters without prior assumptions concerning correlations between parameters. The method used is the maximum entropy method and the distributions considered concern the magnetic field and isomer shift. The results obtained are very encouraging and show the feasibility of the proposed method.

Key words Bayesian logic • maximum entropy method • Mössbauer spectra

Introduction

The maximum entropy method (MEM) stems from the so-called Bayesian logic [11]. It was used to analyze many spectroscopic data [2, 3, 7, 9]. However, this method was not as yet extensively applied to the analysis of Mössbauer spectra where presence of the distribution of hyperfine field parameters makes the spectra complicated and their interpretation becomes ambiguous because of the assumptions one makes in order to get the hyperfine field distributions.

In short, when the Zeeman interaction is dominating, the Mössbauer spectrum consists of lines measured as a function of the source velocity $V(i)$, where $i = 1, 2, \dots, N$ with N being usually 256. In a typical experiment with ^{57}Fe -based absorption, for a given hyperfine magnetic field B (in Tesla), isomer shift IS (in mm/s) and quadrupole splitting QS (in mm/s) the recoilless absorption should occur at the following six velocities (Zeeman sextet):

$$\begin{aligned}v_1 &= B^*(3g_{3/2} - g_{1/2})/2 + QS + IS \\v_2 &= B^*(g_{3/2} - g_{1/2})/2 - QS + IS \\v_3 &= B^*(-g_{3/2} - g_{1/2})/2 - QS + IS \\v_4 &= B^*(g_{3/2} + g_{1/2})/2 - QS + IS \\v_5 &= B^*(-g_{3/2} + g_{1/2})/2 - QS + IS \\v_6 &= B^*(-3g_{3/2} + g_{1/2})/2 + QS + IS,\end{aligned}$$

where the gyromagnetic factors for ^{57}Fe nucleus are:

$$g_{3/2} = -0.067897 \text{ mm/s/T}, \quad g_{1/2} = 0.118821 \text{ mm/s/T}.$$

In the case of infinitely thin absorber, the line intensities are:

Line number	Unpolarized radiation	Circularly polarized radiation
1	$I_1 = 3(1 + c_2)/16$	$I_1 = 3(1 + c_2 + 2c_1)/16$
2	$I_2 = (1 - c_2)/4$	$I_2 = (1 - c_2)/4$
3	$I_3 = (1 + c_2)/16 = I_1/3$	$I_3 = (1 + c_2 - 2c_1)/16$
4	$I_4 = I_3$	$I_4 = I_1/3$
5	$I_5 = I_2$	$I_5 = I_2$
6	$I_6 = I_1$	$I_6 = 3I_3$

L. Dobrzyński[✉]
Institute of Experimental Physics,
University of Białystok,
41 Lipowa Str., 15-424 Białystok, Poland
and The Andrzej Sołtan Institute for Nuclear Studies,
05-400 Otwock-Świerk, Poland,
Tel.: +48 22/ 718 06 12, Fax: +48 22/ 779 34 81,
e-mail: ludwik@ipj.gov.pl

K. Szymański, D. Satuła
Institute of Experimental Physics,
University of Białystok,
41 Lipowa Str., 15-424 Białystok, Poland

Received: 22 June 2004, Accepted: 6 August 2004

where

$$(1) \quad c_1 = \langle \cos\Theta \rangle, \quad c_2 = \langle \cos^2\Theta \rangle$$

with Θ being an angle between the direction of a photon and the direction of magnetization of a sample. The averaging runs over all possible grains and domains in the sample [14].

A given i th line contributes to the j th channel in the velocity spectrum, the intensity being proportional to

$$(2) \quad J_j = \frac{I_i}{(V(j) - v_i)^2 + (\Gamma/2)^2}$$

where the natural width, Γ , of the line from the Mössbauer source is 0.22–0.25 mm/s.

In the general case of dominating magnetic interaction, one deals with the distribution of all five parameters appearing in the above formulas i.e. B , IS, QS, c_1 and c_2 . There exist methods of reconstructing the hyperfine magnetic field distribution [4–6, 10, 12, 13, 15, 16] from measured spectra. However, in order to make such reconstruction one has usually to assume a certain correlation between, e.g., the hyperfine field B and the isomer shift IS. To the best knowledge of the authors, there is no code enabling one to get the distributions of B and IS independently of each other. Obviously, the situation becomes much more complex if the distributions of other parameters have to be taken into account. This paper shows that such task can be feasible when the analysis is carried out by means of the maximum entropy method. The first successful attempt to use this method for a single parameter distribution was published by Brand and Le Caer [1]. Dou *et al.* [8] were using the Bayesian inference theory to obtain the distribution of one parameter (B) assuming linear coupling of two other parameters (IS and QS) to B . Their approach, however, was not the MEM approach in strict sense.

Maximum Entropy Method

Assume that the whole space of parameters (five-dimensional in the most general case) was divided into pixels and the value ρ_j denotes the probability of having the values of these parameters corresponding to this particular pixel. Because the line intensities are linear in the densities, the intensities W_i measured at i th velocity channel will be given by:

$$(3) \quad W_i = \sum_{j=1}^{N_{pix}} r_{ij} \rho_j$$

where $i = 1, \dots, N$ and the transformation matrix $\{r_{ij}\}$ can easily be evaluated from the expressions given in the Introduction.

In accordance with the principles of the MEM, one has to maximize the information entropy:

$$(4) \quad S = - \sum_{j=1}^{N_{pix}} \left[\rho_j \ln(\rho_j / \rho_j^0) - \rho_j + \rho_j^0 \right]$$

under the constraint of minimum of the χ^2 misfit function and proper normalization of the spectra calculated from

the reconstructed distribution ρ . The simplest normalization condition is obtained from requiring that the sum of measured intensities W_i and the sum of intensities T_i corresponding to the distribution ρ be equal. The respective Lagrangian of the problem is

$$(5) \quad L = \alpha S - \frac{1}{2} \chi^2 - \alpha \gamma \sum_{j=1}^{N_{pix}} b_j \rho_j$$

where:

$$b_j = \sum_{i=1}^N r_{ij}, \quad \chi^2 = \sum_{l=1}^N \frac{1}{\sigma_l^2} (W_l - T_l)^2$$

where σ_l denotes the uncertainty of the W_l , while α and γ are the Lagrange multipliers. One can check that in the ideal case the values b_j should be independent of the index j , so one can set $b_j = b$, and the final equations to solve have the shape of

$$(6) \quad \rho_j = Z \cdot \frac{\rho_j^0 e^{-\frac{1}{2\alpha} \frac{\partial \chi^2}{\partial \rho_j}}}{\sum_{j=1}^{N_{pix}} \rho_j^0 e^{-\frac{1}{2\alpha} \frac{\partial \chi^2}{\partial \rho_j}}}$$

where

$$Z = \frac{\sum_{i=1}^N W_i}{b}$$

There are N_{pix} strongly non-linear eq. (6). To solve such a number of equations is a real problem. However, because the Mössbauer spectra are measured usually in 256 channels only, instead of solving N_{pix} equations one can solve $N = 256$ equations with respect to the “theoretical” intensities T_j :

$$(7) \quad T_j = \sum_{l=1}^{N_{pix}} r_{jl} \rho_l$$

Substituting eqs. (6) and (7) one can see that one gets the required equations with respect to the set of $\{T_j\}$. This set can be solved by the Newton-Raphson method.

In the practical case, we encounter the problem of finding an optimum parameter α . The parameter γ is obtained, if necessary, by a strict requirement of the spectrum normalization. The search for optimum α parameter is a tedious task, but our experience shows that once good χ^2 is obtained, the change in the optimum α value results in rather insignificant changes in the reconstructed distributions.

Results

Three cases were considered.

- (1) the distribution of hyperfine magnetic fields consisting of three Gaussian distributions,
- (2) the simultaneous Gaussian distributions of the field B and the isomer shift IS,
- (3) the case (1) with added Gaussian distributions of IS, non-correlated with the values of the magnetic field B .

For each simulated distributions, the Mössbauer spectrum was calculated and the noise corresponding to the assumed Poisson statistics was added to the simulated

spectrum. Next, by means of the MEM with ignorant prior ($\rho_j^0 = \text{const}$) the distribution $\{\rho_j\}$ was reconstructed. The

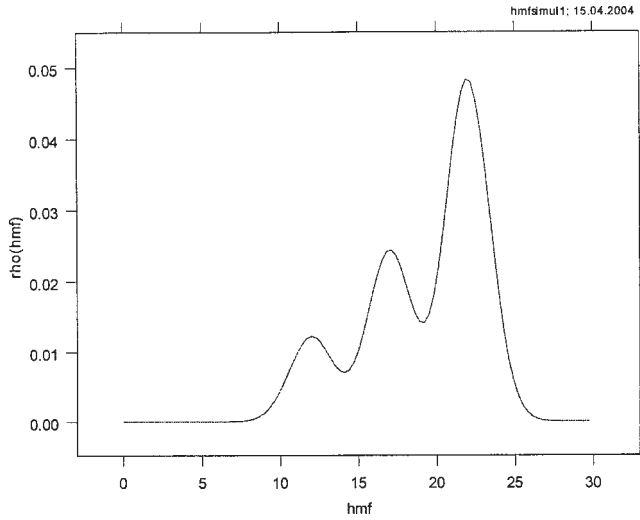


Fig. 1a. Simulated distribution of hyperfine magnetic fields.

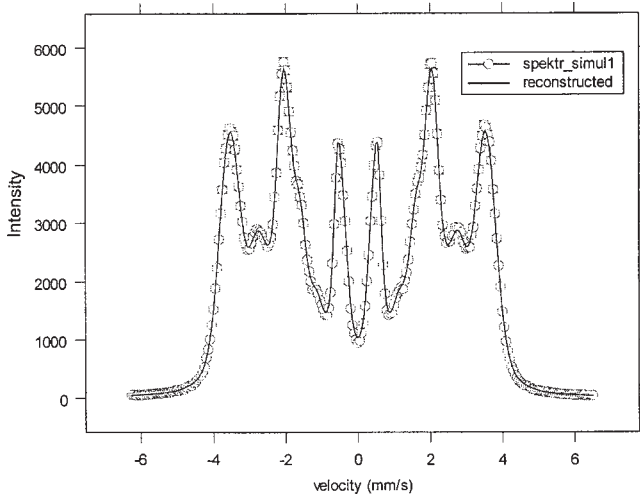


Fig. 1b. Spectrum obtained for the distribution shown in Fig. 1a. The solid line shows reconstructed spectrum.

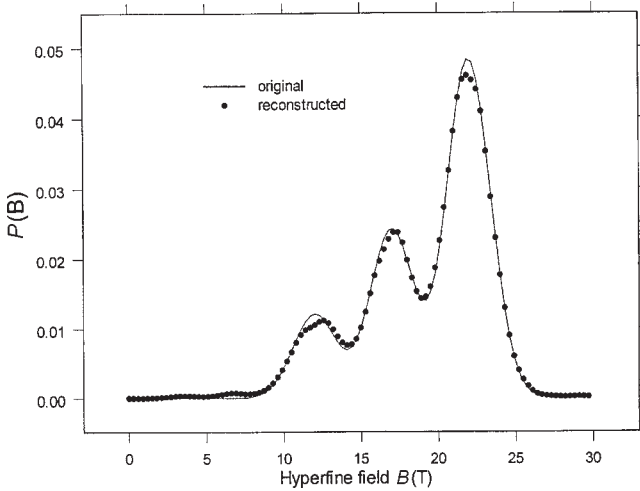


Fig. 1c. Reconstructed distribution of the hyperfine magnetic fields (dots) compared with the simulated original distribution (thick line).

parameter α was chosen so as to obtain χ^2 close to 1. The results are presented in Figs. 1–3.

In the first case, the reconstruction is almost perfect. There are some artifacts on the low-field side which show the tendency of splitting of the peak at the lowest field. This shows that one has to be careful with jumping to conclusions about such splitting. Happily, it is easy to make a check and see whether this kind of effect does not arise from the statistics or from the calculation method itself.

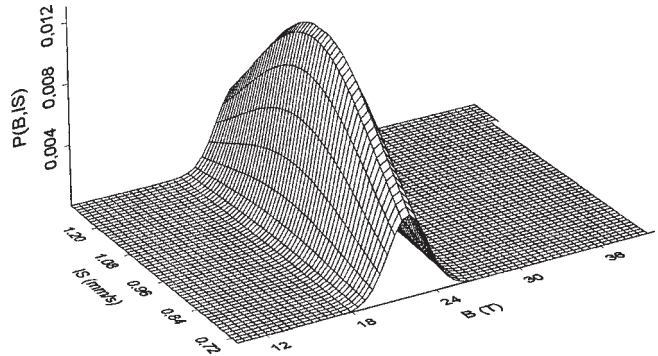


Fig. 2a. Simulated distribution of hyperfine parameters B and IS .

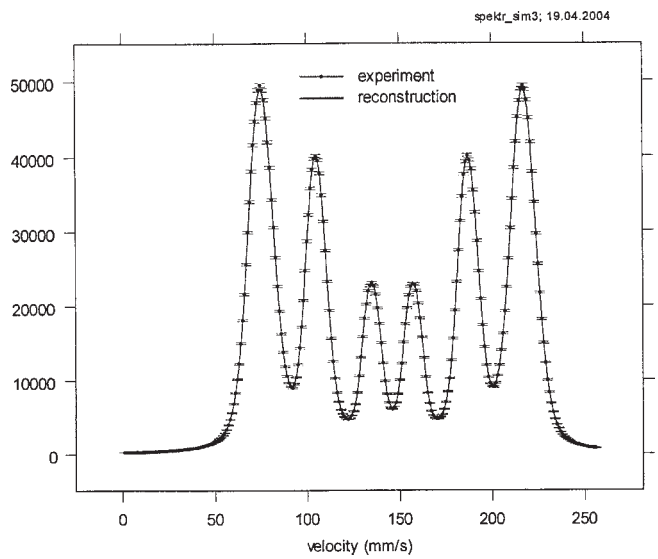


Fig. 2b. Simulated and reconstructed spectra for the distribution shown in Fig. 2a.

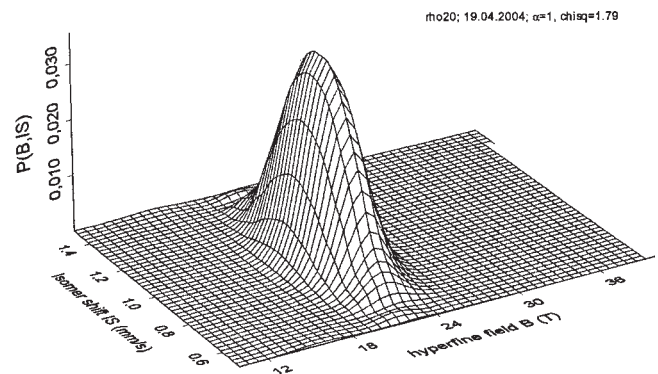


Fig. 2c. Reconstructed distribution in (B,IS) -plane. Note that the range of IS is broader than in Fig. 2a.

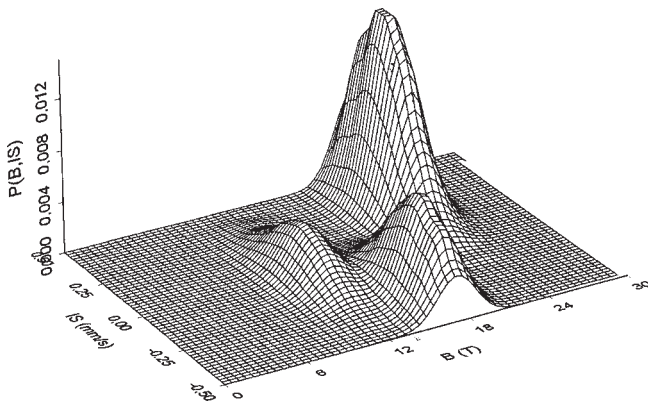


Fig. 3a. Simulated distribution of B and IS parameters.

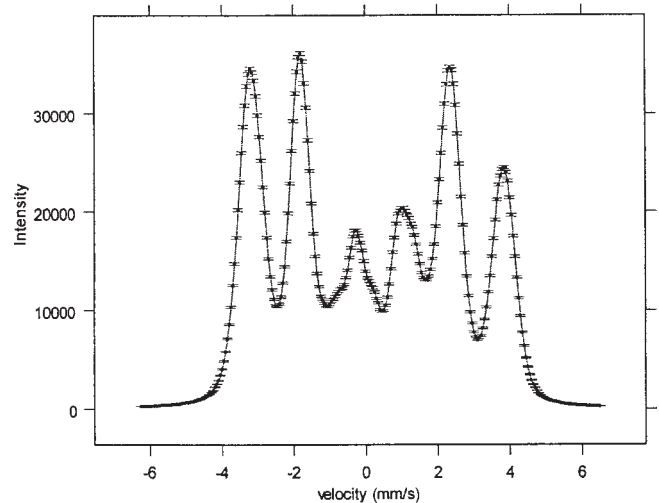


Fig. 3b. Simulated and reconstructed spectra for the distribution shown in Fig. 3a.

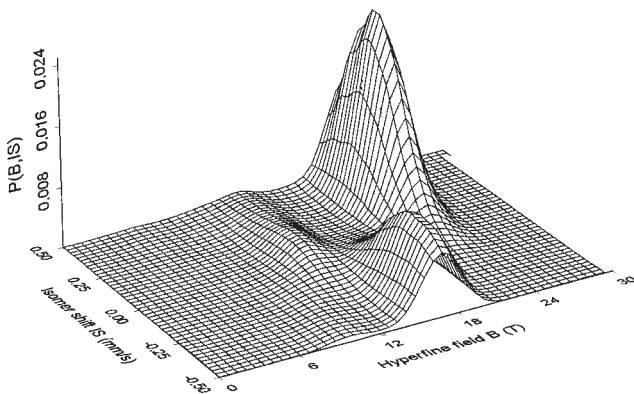


Fig. 3c. Reconstructed distribution from the spectrum shown in Fig. 3b.

There is no doubt that the field distribution with a single peak in two-dimensional space B - IS is very well reconstructed (Fig. 2) without any necessity of assuming, e.g., a linear relationship between the two parameters of interest. In the most difficult case studied in this paper, Fig. 3, it is seen that the positions of the peaks are well reproduced. However, the peaks with lower intensities are reproduced with decreasing accuracy: the lower the field, the broader the distribution, so the peak intensity becomes much lower than the originally simulated one. This is not strange in light that MEM is showing the distributions as close to the prior as possible, and the prior was taken homogeneous in all the space. When the statistics in the measured spectrum increases, the reconstruction becomes also better. This is shown in Fig. 3d, which displays the reconstruction from the spectrum with statistics 10 times better than shown in Fig. 3b.

Conclusions

We have checked the feasibility of the maximum entropy method in reconstruction of the hyperfine distribution of field parameters in the Mössbauer spectra. The results turn out to be very promising. The reconstructions made were of high quality, even if the reconstructed and simulated distributions were not identical. We believe that this kind of

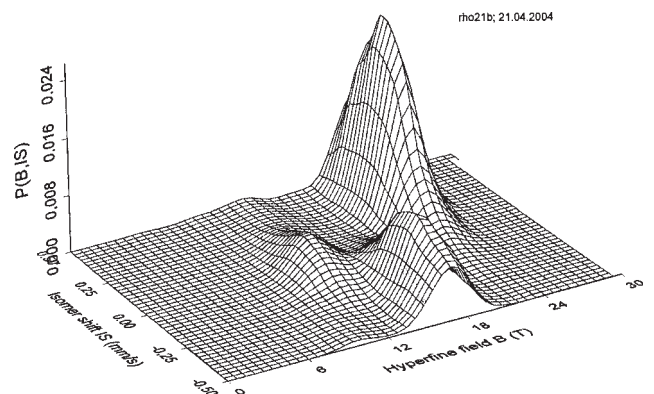


Fig. 3d. Reconstructed distribution from the spectrum with statistics 10 times better than in Fig. 3b.

reconstruction can become an excellent starting point to the interpretation of the measured spectra in physical terms.

References

- Brand RA, Le Caer G (1988) Improving the validity of Mössbauer hyperfine parameter distributions: the maximum entropy formalism and its applications. *Nucl Instrum Meth Phys Res B* 34:272–284
- Bretthorst GL (1988) Bayesian spectrum analysis and parameter estimation. *Lecture Notes in Statistics* 48. Springer Verlag, New York
- Buck B, Macaulay VA (eds) (1991) *Maximum entropy in action*. Clarendon Press, Oxford
- Campbell SJ, Whittle GJ, Stewart AM (1983) On the determination of the magnetic hyperfine field distribution in an amorphous alloy. *J Magn Magn Mater* 31/34:1521–1522
- Chuev MA, Hupe O, Bremers H, Hesse J, Afanas'ev AM (2000) A novel method for evaluation of complex Mössbauer spectra demonstrated on nanostructured ferromagnetic FeCuNbB alloys. *Hyperfine Interact* 126:407–410
- Cranshaw TE (1974) The deduction of the best values of the parameters from Mössbauer spectra. *J Phys E: Sci Instrum* 7:122–124
- Dobrzyński L (2004) Momentum density studies by the Maximum Entropy Method. In: Cooper MJ *et al.* (eds) *X-ray Compton scattering*. Oxford University Press, pp 188–209

8. Dou L, Hodgson RJW, Rancourt DG (1995) Bayesian inference theory applied to hyperfine parameter distribution extraction in Mössbauer spectroscopy. *Nucl Instrum Meth Phys Res B* 100:511–518
9. Gerhard U, Marquardt S, Schroeder N, Weiss S (1998) Bayesian deconvolution and analysis of photoelectron or any other spectra: Fermi-liquid vs. marginal Fermi-liquid behavior of the 3d electrons in Ni. *Phys Rev B* 58:6877–6891
10. Hesse J, Rübartsch A (1996) Model independent evaluation of overlapped Mössbauer spectra. *J Phys E: Sci Instrum* 7:526–532
11. Jaynes ET (2003) *Probability theory. The Logic of Science*, Cambridge
12. Le Caer G, Brand RA (1998) General methods for the distributions of electric field gradients in disordered solids. *J Phys: Condens Matter* 10:10715–10774
13. Le Caer G, Dubois JM (1979) Evaluation of hyperfine parameter distributions from overlapped Mössbauer spectra of amorphous alloys. *J Phys E: Sci Instrum* 12:1083–1090
14. Szymański K, Dobrzyński L, Satuła D, Kalska-Szostko B (2003) Trends in Mössbauer polarimetry with circularly polarised radiation. In: Mashlan M, Miglierini M, Schaaf P (eds) *Material research in atomic scale by Mössbauer spectroscopy*. NATO Science Series, II Mathematics, Physics and Chemistry. Vol 94. Kluwer Academic Publishers, Dordrecht, pp 317–328
15. Varret F, Gerard A, Imbert P (1971) Magnetic field distribution analysis of the broadened Mössbauer spectra of zinc ferrite. *Phys Status Solidi B* 43:723–730
16. Window B (1971) Hyperfine field distributions from Mössbauer spectra. *J Phys E: Sci Instrum* 14:401–402

P7

NUCLEAR RESONANCE SCATTERING OF
CIRCULARLY POLARIZED SRK. SZYMAŃSKI^a, D. SATUŁA^a, L. DOBRZYŃSKI^{a,b} AND B. KALSKA^{†c}^aInstitute of Experimental Physics, University of Białystok
Lipowa 41, 15-424 Białystok, Poland^bThe Sołtan Institute for Nuclear Studies
05-400 Otwock-Świerk, Poland^cFree University Berlin, Institute of Experimental Physics
Arnimalle 14, 114 195 Berlin, Germany*(Received April 7, 2004)*

Results of the experiments with nuclear resonance scattering of synchrotron radiation aiming at construction of the circularly polarized beam suitable for nuclear hyperfine studies are reported. Si(4 0 0) single crystal slab, 100 μm thick, was used as a quarter wave plate. Observed twofold reduction of the intensity in proposed geometry is due to the Si crystal itself. Hyperfine interactions are used to probe polarization state of the synchrotron beam. Too large angular beam divergence did not allow for achieving full circular polarization of photons. Consequently, further experiments are proposed to overcome beam divergence problems. A number of calculations presented in the paper show that cheap and easily available Si plate can serve as an effective desired polarizer.

PACS numbers: 76.80.+y, 07.85.Qe, 75.25.+z

1. Introduction

Nuclear Resonance Scattering (NRS) [1,2] proved to be powerful tool in investigation of hyperfine structure of the Mössbauer nuclei. High degree of polarization of the synchrotron radiation is a property that can be helpful in enriching information about the hyperfine structure under study. Because a change of the initial polarisation state of the beam results in a change of the amplitudes of the interfering components, experimental determination of the orientation of hyperfine fields is possible. Many experiments have been performed so far with linearly polarized incident beams [3–5]. Other

[†] Present address: University of Białystok, Institute of Chemistry, Hurtowa 1
15-399 Białystok, Poland.

polarization states, particularly the circular ones, may, however, also be useful because the circularly polarized radiation is sensitive to the sign of the hyperfine magnetic field. We are thus interested in a device, which would easily change linear to circular polarization of highly monochromatized radiation for NRS experiments. The circular polarization of the resonant beam can be generated by insertion of the ^{57}Fe foil, magnetized parallel to the \mathbf{k} vector of photon, as suggested in early paper of Frauenfelder [6]. However this leads to the beam polarization which is nonuniform across the useful energy range.

In order to transform linear to circular polarization one can use the Bragg scattering from a quarter plate. It was already demonstrated that single crystal Si plate, working in asymmetric Bragg geometry in the vicinity of Si(1 1 1) peak, serves as convenient quarter wave plate in transmission geometry [7,8]. The authors of the cited papers achieved circular polarization degree as high as 0.9. It was already noticed in [7] that the finite angular divergence of the incident beam causes smearing of the polarization states through the spread of the phase shift. Later on diamond (1 1 1) [9] and Si(3 3 3) [10] were used as a quarter wave plates.

The sophisticated monochromators dedicated for nuclear resonance studies monochromatize the 10^4 eV range synchrotron beam to 10^{-3} eV range [11]. However, in the typical stations horizontal beam divergence is much larger than the vertical one. As we will see this property makes some type of experiments not feasible. It is not clear how the polarization state of highly monochromatized resonant beam with relatively large horizontal divergence will be affected by transmission quarter wave plate, and whether the intensity reduction will not make NRS measurements impossible. This paper reports the results of using Si single crystals as the x-ray optical element causing a change of the linearly polarized beam of resonant radiation to the circularly polarized beam as indicated in [7–10]. The experiments with nuclear resonant scattering of circularly polarized radiation are not common and to our knowledge only the [12] report is published till now.

It follows from the Ref. [13], that the best condition for operation of the quarter wave plate is ensured when one maximizes the $\text{Re}(\chi_K \chi_{-K}) \sin 2\theta_B$, where θ_B is Bragg angle and χ_K is the Fourier transform of the susceptibility. We have found that for Si crystal and 14.4 keV energy maximum of the $\text{Re}(\chi_K \chi_{-K}) \sin 2\theta_B$ is achieved for Si(4 0 0) scattering planes. In order to determine polarization state of the beam, well-known hyperfine structure of the ^{57}Fe nucleus was used as a probe of the beam polarization. The experiment was performed in two steps: first, the ^{57}Fe foil was characterized with linearly polarized radiation. Then the quarter wave plate was inserted and the resonant scattering from the foil was used as a probe of the polarization state of the beam.

2. Idea of the experiment

The radiation used in the experiment is linearly polarized: \mathbf{E} and \mathbf{B} vectors of a photon with wavevector \mathbf{k} are directed as in Fig. 1. Polycrystalline ^{57}Fe iron foil with the surface of the foil oriented perpendicularly to the \mathbf{k} vector of photons is inserted into the beam. When the foil is fully

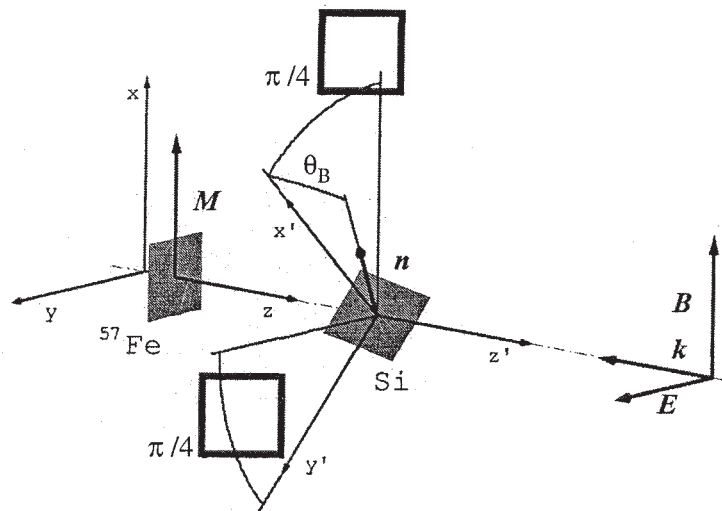


Fig. 1. Scheme of the experimental setup, and the coordination system used, see text.

magnetized perpendicular to the \mathbf{E} vector (Fig. 1), one observes quantum beating pattern with a single frequency, see Fig. 2(a). The spectrum corresponds to the lines 2 and 5 of the Zeeman sextet in the energy domain. After rotating direction of magnetization by $\pi/2$ (magnetization parallel to the \mathbf{E} vector) one expects to observe additional frequencies. The time beating corresponds to the lines 1,3,4,6 of the Zeeman sextet in energy domain [14], see Fig. 2(b). After insertion of ideal quarter wave plate, photons become circularly polarized and the time spectrum should not depend on the direction of magnetization in the plane. Simulated spectrum is shown in Fig. 2(c). For simplicity reasons all the spectra shown in Fig. 2 correspond to limiting case of thin absorber. In the case of thick absorber, shape of the spectrum is modulated by dynamical beats, predicted by theory of nuclear resonant scattering, see [15] for a review.

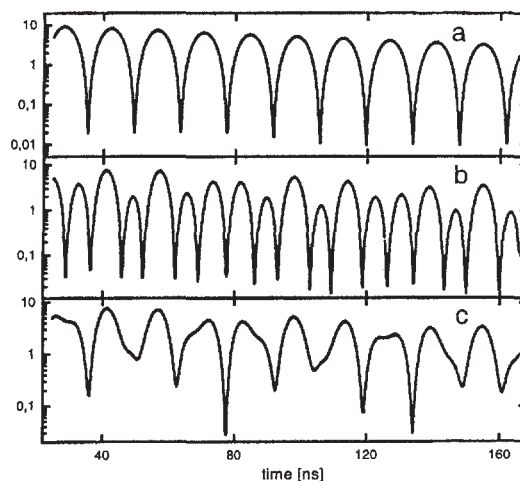


Fig. 2. Simulated spectra of the thin ^{57}Fe foil (a) magnetized perpendicularly to the \mathbf{k} and \mathbf{E} vectors of photon, measured with linearly polarized beam, (b) magnetized perpendicularly to the \mathbf{k} and parallel to the \mathbf{E} , measured with linearly polarized beam, (c) magnetized perpendicularly to the \mathbf{k} , measured with circularly polarized beam.

3. Results

Commercial Si single crystals grown by Czochralski method (producer: Institute of Electronic Materials Technology, ITME, Warsaw), with the thickness of $100\ \mu\text{m}$ were cut parallel to Si(1 0 0) planes and annealed for 1 h at 600°C to remove strains. Rocking curves of the Si plate were measured by neutron diffraction at MARIA reactor at Świerk, Poland, and compared with the rocking curves of almost perfect thick Si crystals. It was found that our crystal consists of mosaic blocks with relative orientation spread of the order of $100\ \mu\text{rad}$. Although this value is much larger than the Darwin width, one could hope that small linear size (about $0.5\ \text{mm}$) of the synchrotron beam used in our experiments will probe only a single block. Indeed, the width of the obtained transmission curves confirmed these expectations.

To insert the plate in the beam we used a holder having flat top surface at appropriate Bragg angle and a horizontal channel for $14.4\ \text{keV}$ X rays. The Si sample was put on the top surface of the holder. The radiation was passing through the Si crystal and the channel in the holder. By this holder, mounted on the goniometer, we were able to scan the Si sample in the vicinity of Bragg angle and also to rotate the sample by $\pi/4$ along the \mathbf{k} vector of radiation (see Fig. 1). ^{57}Fe foil was rolled and annealed for 2 h at

1173 K in order to recrystallize and remove strains. The thickness measured at different points of the foil varied from 10 to 14 μm . The foil was inserted between two poles of permanent Fe-Nd-B magnet. The cylindrical magnets produce field of about 0.203(1) T. The second derivative of the field along symmetry axis was measured to be 1.5(1) mT/mm².

The experiment was performed at BW4 station of DORIS ring at Hasy-lab, DESY. 2.7 m wiggler equipped with magnet of hybrid type produced X-ray radiation. Resonant photons were obtained after the scattering from the Si(4 2 2) \times Si(12 2 2) channel cut nested monochromator [16]. The beam was collimated by four pairs of slits. Horizontal and vertical pairs of primary slits were separated by 17.2 meters from vertical and horizontal pairs of slits located close to the sample. The maximum slits opening was about 1.5 mm and the beam size was much smaller than the source size. All measurements were done at room temperature. Within vertical divergence of the beam no linear polarization changes are expected.

Initially the time spectra from the magnetized iron foil were measured. The results, presented in Fig. 3, clearly show beatings corresponding to σ and π polarizations of the transitions. Next, the foil was removed and the Si plate

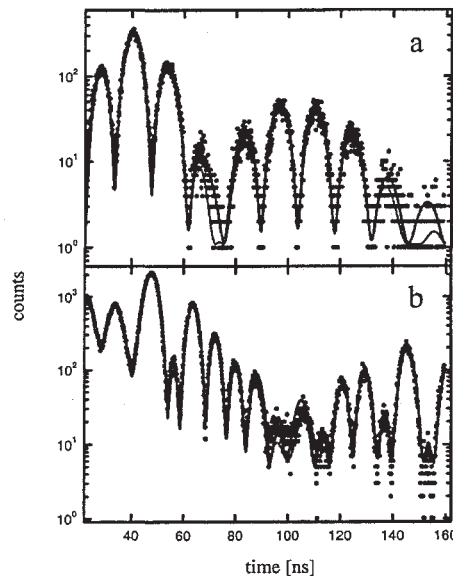


Fig. 3. NRS from ^{57}Fe foil in external magnetic field. The axis of the magnet is oriented (a) perpendicular (b) parallel to the \mathbf{E} vector of photons at linear polarization state. Surface of the foil is oriented perpendicularly to the \mathbf{k} vector of photons. Two solid lines on each graph correspond to the best fit. The thick lines correspond to the fit including distribution of the thickness parameter. Thin lines correspond to the single value of the thickness parameter.

was inserted at angle corresponding to Si(4 0 0) Bragg peak. The \mathbf{n} vector, normal to the scattering planes (and normal to Si plate), lies at the direction $\pm\pi/4$ with respect to \mathbf{E} and \mathbf{B} vectors, respectively (see Fig. 1). Measured transmitted intensity with all slits opened (about 1.5 mm each) is shown in Fig. 4. Since the Bragg angle was not measured with high precision, zero position in Fig. 4 was set at the minimum of the transmission curve. After selecting an angular position of the plate (see one of the seven bars in Fig. 4),

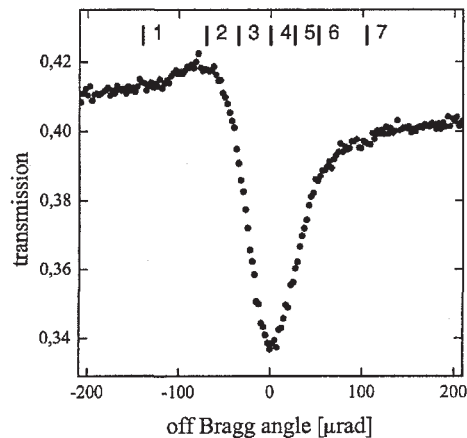


Fig. 4. Rocking curve of the transmitted intensity (Bragg geometry) in the vicinity of Si(4 0 0) Bragg peak. Horizontal scale was set to have 0 at the position of minimum. The vertical bars indicate positions at which time measurements were performed, see text.

so to obtain desired phase shift, the time measurements on the magnetized Fe foil with magnetization perpendicular to the \mathbf{E} vector of photon were carried out. Results are presented in Fig. 5(a). The results obtained for another direction of magnetization \mathbf{k} parallel to \mathbf{E} are shown in Fig. 5(b). We see that the spectra shown in Fig. 5, measured at small negative miss-setting Bragg angles (leftmost bar in Fig. 4), are similar to those shown in Fig. 3. Same similarity is observed for large positive miss-setting angles (rightmost bar in Fig. 4): the spectra in the bottom of Figs. 5(a) and (b) are similar to those in Figs. 3(a) and (b). This indicates, as expected, that at large (small) off-Bragg angles, the Si plate does not change the polarization state of photons.

The beam polarization is changed when the Si plate is set close to the Bragg peak. Then, the time spectra, shown in the middle of Fig. 5(a), become similar to those in Fig. 5(b). Simulated spectrum, corresponding to circularly polarized beam and in-plane magnetized foil with already determined parameters (see Fig. 3), is shown in Fig. 6. This spectrum is different

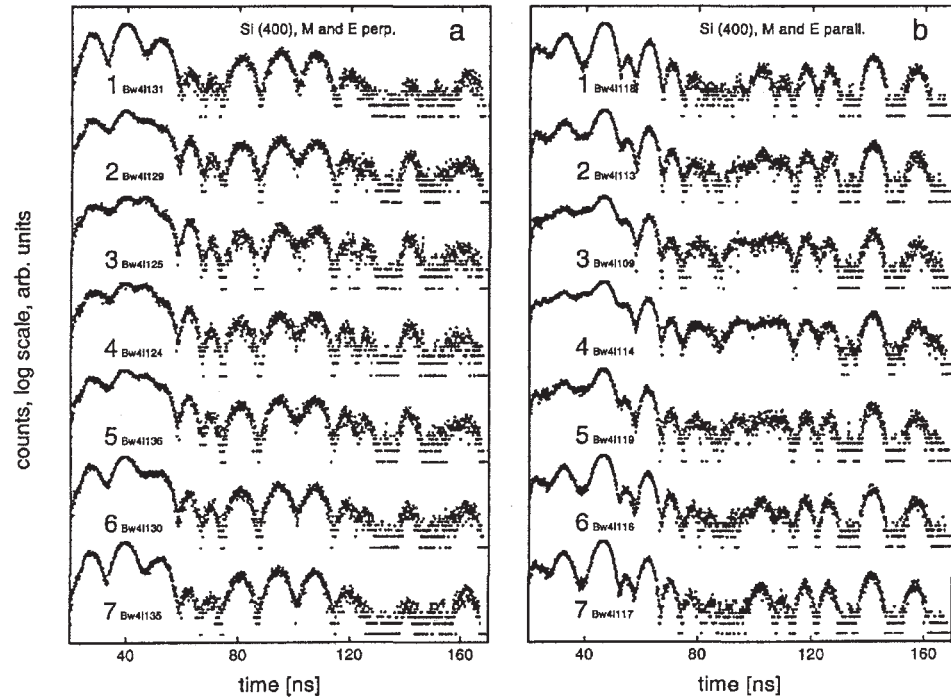


Fig. 5. Rocking curve of the transmitted intensity (Bragg geometry) in the vicinity of Si(4 0 0) Bragg peak. Horizontal scale was set to have 0 at the position of minimum. The vertical bars indicate positions at which time measurements were performed, see text.

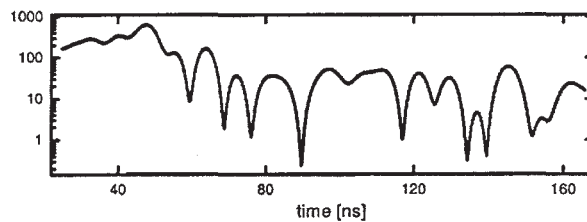


Fig. 6. Simulated NRS spectrum of the ^{57}Fe foil measured with circularly polarized beam.

from the ones presented in Fig. 5. This is due to the fact that the phase shift of photons is distributed in result of the too large angular beam divergence, and well defined polarization state could not be achieved. In order to demonstrate that beam divergence plays crucial role, set of transmission measurements in the vicinity of Si(4 0 0) Bragg peak was performed with

various vertical and horizontal slits sizes. The results, presented in Fig. 7 clearly show that a decrease of the beam divergence affects the angular shape of the transmitted intensity. One can estimate from the uppermost spectrum of Fig. 7 that the FWHM does not exceed $30 \mu\text{rad}$ and this value is the upper limit of the broadening caused by Si mosaicity, in agreement with our expectation.

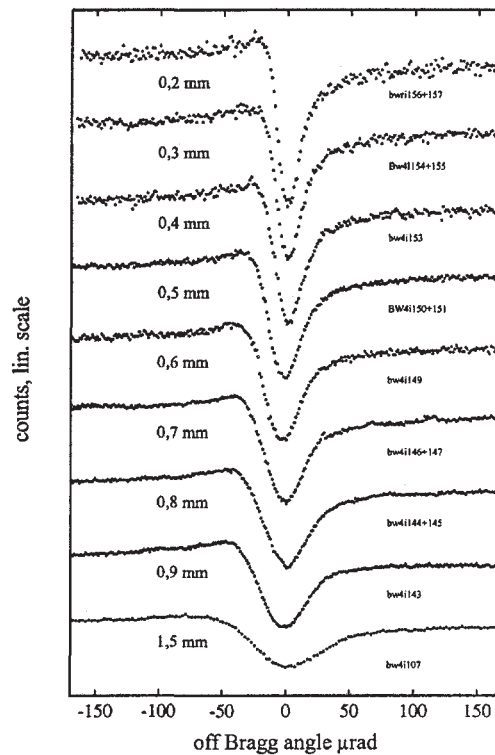


Fig. 7. Rocking curve of the transmitted intensity measured at the same geometry as in Fig. 4. The numbers indicate the slit size. Horizontal scale was set to have 0 at the position of minimum.

4. Discussion

Results of fitting (performed using MOTIF package [17]) theoretical to the two experimental spectra of ^{57}Fe magnetized foil, measured with two linear polarization states of the beam, is shown in Fig. 3. At first trial the only free parameters that depended on the sample, were hyperfine magnetic field B_{hf} , and effective thickness τ . We assumed that local magnetization

is perfectly aligned, horizontally (Fig. 3(a)) or vertically (Fig. 3(b)). There are some discrepancies between the experimental and predicted ideal spectra shown by the thin lines in Figs 3(a) and (b), respectively. Next, we assumed that the thickness parameter is nonuniform in the region probed by the beam. Using the Gaussian distribution of the thickness parameter we performed averaging assuming that components corresponding to different thickness add incoherently. The transverse coherence length of the SR in a forward nuclear resonant scattering experiment reported in [18] was about 30 nm. Since in our experiment the beam probe is measuring a few hundreds of μm , the condition for incoherent scattering is obviously fulfilled. Using the Gaussian distribution of the thickness parameter we found better agreement, particularly in the vicinity of the minima corresponding to the dynamical beats (see lines at $t = 70$ and 140 ns in Fig. 3(a), and at $t = 100$ ns in Fig. 3(b)). From the fits we got $B_{\text{hf}} = 32.9 \pm 0.1$ T, average effective thickness $\tau = 192 \pm 5$ and the width of the distribution of the effective thickness, $\sigma_\tau = 14$. Assuming the recoilless fraction to be 0.85 and isotopic abundance of ^{57}Fe $90 \pm 5\%$ (this value is not precisely known), one expects to obtain effective thickness ranging between 160 and 230, in good agreement with the value obtained from the fit.

Using the two wave fields approach of dynamical theory [19] we have simulated wave field in the Si plate with parallel surfaces. Rocking curves of the transmitted fields for two linear polarizations are shown in Fig. 8. It is seen, that for large miss-setting angles from the Bragg peak the transmitted intensity is reduced by approximately 50%, while in the vicinity of the Bragg peak, within $10 \mu\text{rad}$, all radiation is scattered (only small part absorbed) and no transmitted intensity is present. It follows from Fig. 8(b) that the $\pi/4$ phase difference for σ and π polarization states can be obtained at off-Bragg position of the plate equal to about -13.8 and $+22.5 \mu\text{rad}$.

The measured shape of the rocking curve (Fig. 4) is different from the one predicted by the theory. As it was aforementioned, the difference is due to too high angular beam divergence used in the experiment. Although high resolution $\text{Si}(4\ 2\ 2) \times \text{Si}(12\ 2\ 2)$ nested monochromator produces a vertical beam divergence of about $20 \mu\text{rad}$, horizontal divergence is few times larger. Vector \mathbf{n} normal to diffracted planes of our Si crystals was tilted by $\pi/4$ from the x direction (see Fig. 1). The angular divergence of the beam, controlled by pair of slits only, is quite poor. Indeed, for the slits opening and the distance given in paragraph 3, the maximum angular divergence in vertical or horizontal direction amounts to about $170 \mu\text{rad}$. This is, however estimation of the upper limit of the angular divergence. To have its better estimation we have performed convolution of the intensity curves presented in Fig. 8(a) with a triangular function of various width. The results are presented in Fig. 9. The obtained shapes can be easily compared with the

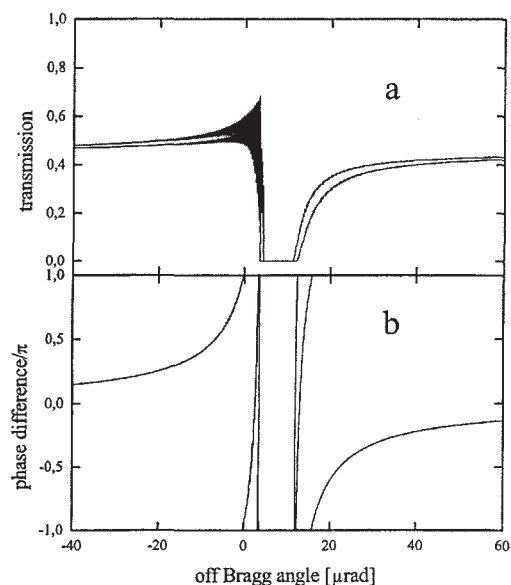


Fig. 8. (a) Simulated rocking curve for Si(4 0 0) transmitted intensity (symmetric Bragg geometry) simulated for 100 μm Si plate. Two lines correspond to σ and π linear polarizations. (b) difference of the phase shift for the transmitted fields with σ and π polarizations.

rocking curves obtained for various slit sizes. For given slit size one can find maximum and minimum of the intensity of the rocking curve, and define the ratio I_{\min}/I_{\max} . Then, using convoluted curves in Fig. 9, one can find the width φ of the triangular resolution function which produces identical ratio I_{\min}/I_{\max} . Results of the comparison are presented in Fig. 10 by squares. The characteristic width of the rocking curve can also be estimated from the distance between angular positions of the I_{\min} and I_{\max} . From the value of this distance one can similarly find the width φ of the triangular resolution function. The results are shown in Fig. 10 by circles. We see that both types of estimation of the width of the resolution function φ agree with each other and indicate proportionality between slit size and the φ . We also notice, that maximal beam divergence, defined by the ratio of the double slit size and the distance between the slits in our experiment, is larger than the required width φ of the resolution function by a factor of 1.3 ± 0.2 .

The discussion presented above explains why the measured rocking curve, shown in Fig. 4, is so broad and shallow with respect to the simulated one shown in Fig. 8. The slits used in this experiment correspond roughly to the triangular resolution function with the width of about 120 μrad . We have

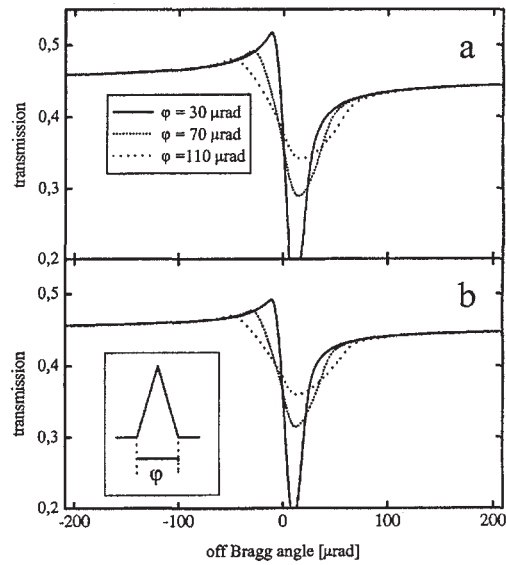


Fig. 9. Convolution of the rocking curve with triangular resolution function (see inset) of different width φ . (a) and (b) correspond to two polarizations indicated in Fig. 8. Note that vertical scales in Figs. 8 and 9 are different.

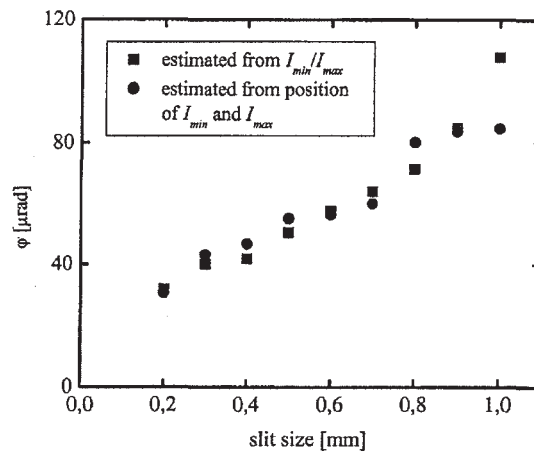


Fig. 10. Estimation of the width φ of the triangular resolution function performed by comparison of the experimental and theoretical relative intensity (squares) and the width (circles).

shown that the decrease of the angular spread of the beam (by varying the slit size) results in narrowing the shape of transmitted intensity. For the smallest slit size, 0.2 mm, at which the intensity was still reasonable, maximum beam divergence had an order of magnitude of the Darwin width. However, very low counting rate prevented us from carrying out time measurements. It is clear that better collimation is required. This can be achieved for example at ID18 or ID22 stations at ESRF, where beam divergence can be reduced below 10 μ rad [20]. One can also think about an enhancement of the angular acceptance range when highly asymmetric Bragg geometry is used. Our simulations indicate that for Si(4 0 0) Bragg reflection, at incidence above critical angle, equal to 0.002 rad, the Darwin width may increase by an order of magnitude.

Although the used beam station turned out to offer rather unsatisfactory conditions, remarkable change of the shape of time spectra was observed, see middle part of the Fig. 5. Quantitative analysis of the polarization degree is underway. In this report we have demonstrated that cheap and easily available Si plate can be used to obtain circularly polarized resonant radiation. We also presented simple way of checking whether polarization state of the beam was transformed from a linear to the circular one by using the hyperfine structure of ^{57}Fe nucleus.

This work was supported by the IHP-Contract HPRI-CT-2001-00140 of the EC. The authors thanks to D.L. Nagy, L. Bottyan, L. Deak and Y.V. Shvydk'o for valuable discussions, members of the "Hyperfine Interaction" group for technical help, and J. Milczarek for performing neutron check of the crystal quality.

REFERENCES

- [1] E. Gerdau, R. Ruffer, R. Hollatz, J.P. Hannon, *Phys. Rev. Lett.* **57**, 1141 (1986).
- [2] J.B. Hastings, D.P. Siddons, U. van Bürck, R. Hollatz, U. Bergmann, *Phys. Rev. Lett.* **66**, 770 (1991).
- [3] E. Gerdau, U. van Bürck, in: *Resonant Anomalous X-ray Scattering, Theory and Applications*, eds. G. Materlik, C.J. Sparks, K. Fischer, North-Holland, Amsterdam 1994, p. 589.
- [4] R. Ruffer, H.D. Rüter, E. Gerdau, *Hyp. Int.* **123/124**, 405 (1999).
- [5] Y.V. Shvyd'ko, *Hyp. Int.* **123/124**, 275 (1999).
- [6] H. Frauenfelder, D.E. Nagle, R.D. Taylor, D.R.F. Cochran, W.M. Visscher, *Phys. Rev.* **126**, 1065 (1962).
- [7] K. Hirano, K. Izumi, T. Ishikawa, S. Annaka, S. Kikuta, *Jpn. J. Appl. Phys.* **30**, L407 (1991).

- [8] T. Ishikawa, K. Hirano, S. Kikuta, *J. Appl. Cryst.* **24**, 982 (1991)
- [9] C. Giles, C. Malgrange, J. Goulon, F. de Bergevin, C. Vettier, A. Fontaine, E. Dartyge, S. Pizzini, *Nucl. Instrum. Methods Phys. Res.* **A349**, 622 (1994).
- [10] A. Kaprolat, K.-J. Gabriel, W. Schülke, P. Fischer, G. Schütz, *Nucl. Instrum. Methods Phys. Res.* **A361**, 358 (1995).
- [11] O. Leupold, J. Pollmann, E. Gerdau, H.D. Rüter, G. Faigel, M. Tegze, G. Bortel, R. Ruffer, A.I. Chumakov, A.Q.R. Baron, *Eruophys. Lett.* **35**, 671 (1996).
- [12] C.L. L'Abbé *et al.* APS Activity Report, ANL-02/06 December (2002).
- [13] V.A. Belyakov, V.E. Dmitrenko, *Sov. Phys. Usp.* **32**, 697 (1989).
- [14] G.V. Smirnov, *Hyp. Int.* **123/124**, 31 (1999).
- [15] U. van Bürck *Hyp. Int.* **123/124**, 483 (1999).
- [16] Yu. Shvyd'ko, Experience at Hasylab F4; October 1994/May (1995).
- [17] Yu. Shvyd'ko, *Hyp. Int.* **125**, 173 (2000).
- [18] A.Q.R. Baron *et al.*, *Phys. Rev. Lett.* **77**, 4808 (1996).
- [19] A. Authier, *Dynamical Theory of X-Ray Diffraction*, Oxford University Press, Oxford 2001.
- [20] O. Leupold, private information, also: www.esrf.fr/Accelerators/Performance

P8

Hyperfine Fields in Nanocrystalline Fe_{0.48}Al_{0.52}

K. SZYMAŃSKI^{1,*}, D. SATUŁA¹, L. DOBRZYŃSKI^{1,2}, E. VORONINA³
and E. P. YELSUKOV³

¹*Institute of Experimental Physics, University of Białystok, 15-424 Białystok, Poland;*
e-mail: kszym@alpha.uwb.edu.pl

²*The Soltan Institute for Nuclear Studies, 05-400 Otwock-Świerk, Poland*

³*Physical–Technical Institute of Ural Division of Russian Academy of Science, Izhevsk, Russia*

Abstract. Mössbauer measurements with circularly polarized radiation were performed on a nanocrystalline, disordered Fe₄₈Al₅₂ alloy. The analysis of the data for various polarization states resulted in the characterization of the hyperfine magnetic field distribution and the dependence of the average z-component of hyperfine field on the chemical environment. An increasing number of Al in the first coordination shell causes not only a decrease of magnetic moments but also introduces noncollinearity.

Key Words: circularly polarized radiation, Fe–Al alloys, nuclear resonant magnetometry.

1. Introduction

The magnetic ground state of Fe–Al alloys in the equiatomic concentration range depends strongly on the composition and structural order. Alloys of bcc-type structure were suspected to be antiferromagnets [1, 2], however, no antiferromagnetic ordering was detected in neutron scattering experiments. In many works noncollinear or antiparallel arrangements of magnetic moments were considered [3–5], but no experimental evidences was found. Directions of local Fe magnetic moments, including parallel or antiparallel configurations, can be investigated by Mössbauer polarimetry with circularly polarized radiation [6]. The present paper demonstrates how the magnetic moments of iron depend on the local environment in one selected Fe–Al alloy.

2. Sample

Because of the great sensitivity of magnetic properties on crystalline order, we aimed at the preparation of a homogeneous, disordered bcc state. Therefore melting, homogenization and grinding processes were applied as follows.

* Author for correspondence.

Fe–Al ingots were alloyed from high-purity components in an induction furnace in Ar atmosphere. They were homogenized in a vacuum furnace at 1400 K during 6 h. The chemical analysis showed that the Al concentration was (52.0 ± 0.5) at.%. At first, the ingots were milled in a mortar by hand. The powder with a particle size less than 300 μm was used for further mechanical grinding in a planetary ball mill with vials and balls made of tungsten carbide. The milling was performed in an inert gas atmosphere during 10 h, the time sufficient for creating disordered Fe–Al alloys [7]. X-ray studies showed a lattice parameter of 0.2918(4) nm, a mean grain size (4.0 ± 0.3) nm and microstrains $(0.5 \pm 0.1)\%$, the last values found from the broadening of the diffraction lines using harmonic analysis [8]. Magnetic measurements showed a Curie temperature $T_C = (110 \pm 10)$ K, the presence of a hysteresis, and lack of saturation at $T = 5$ K at fields up to 15 T. The powdered $\text{Fe}_{0.48}\text{Al}_{0.52}$ sample was mixed with Li_2CO_3 and epoxy glue in order to obtain texture free absorbers for Mössbauer measurements.

3. Principles of resonant polarimetric methods

For the case of measurements with circularly polarized radiation, the relative line intensity i_n of the n th nuclear transition in the Zeeman sextet depends on the average cosine square of the angle between k vector of photon and vector of B_{hf} , parameter which we call c_2 , and on the average cosine of the angle between k and B_{hf} , called c_1 [6, 9]:

$$\begin{aligned} 16i_1 &= 48i_4 = 3(1 \pm 2c_1 + c_2), \\ 4i_2 &= 4i_5 = 1 - c_2 \\ 48i_3 &= 16i_6 = 3(1 \pm 2c_1 + c_2). \end{aligned} \quad (1)$$

The upper and lower signs in (1) correspond to two opposite circular polarizations. In the case of a magnetic texture with axial symmetry, c_2 is a measure of the perpendicular component of the hyperfine field: when $c_2 = 0$ the perpendicular component achieves a maximum, while when $c_2 = 1$ this component is zero. The line intensities for unpolarized radiation can be obtained from (1) by setting $c_1 = 0$. The quantity $c_1 \times B_{hf}$ thus is an average component of the hyperfine field in the direction of the k vector and we will abbreviate it as a z-component of B_{hf} . It follows from equation (1) that polarized radiation allows to measure the average component of the hyperfine field along magnetization direction.

There are well established methods for evaluation of $p(B_{hf})$ distributions from Mössbauer spectra. We have developed an algorithm for evaluation of the $p(B_{hf})$, $c_1(B_{hf})$ and $c_2(B_{hf})$ from simultaneous fitting of set of a spectra measured for different polarization states [9]. Polarized, monochromatic radiation is obtained by resonant filter technique [6].

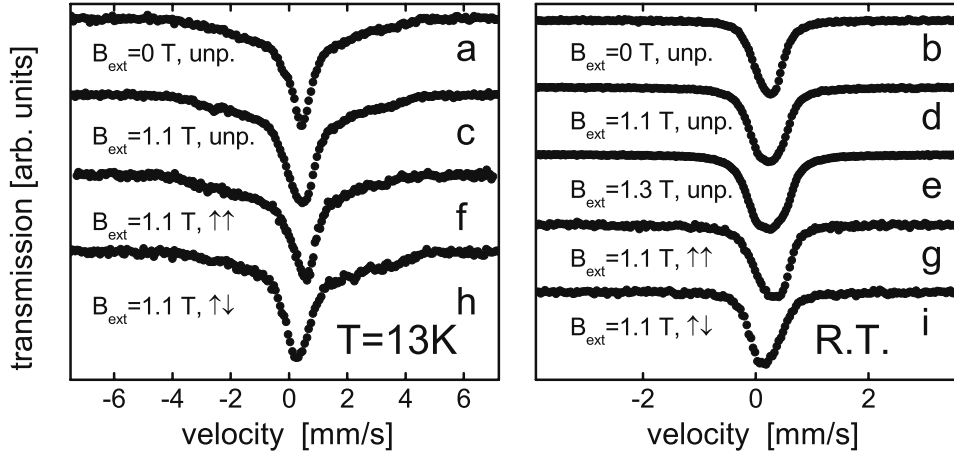


Figure 1. Mössbauer spectra measured with unpolarized radiation (a–e), circularly polarized radiation (f–i). Arrows $\uparrow\uparrow$ and $\uparrow\downarrow$ indicate two opposite circular polarizations. B_{ext} is applied magnetic field parallel to the photon k vector.

4. Measurements and results

The absorbers were placed inside the permanent magnet. Results of measurements which were performed at $T = 13$ K with two opposite circular polarizations and with unpolarized radiation in an external magnetic field of 1.1 T and in zero field, and spectra obtained at room temperature (well above Curie temperature) are presented in Figure 1.

A reversal of circular polarization state results in clear shift of the position of central absorption line (see Figure 1 f, h). There is also a change in the wide absorption area located at about -3 mm/s and $+3$ mm/s in Figure 1 f, h. This behaviour shows unambiguously that large Fe hyperfine fields (and related large magnetic moments) are parallel to the net magnetization as in Fe-based ferromagnets.

Detailed analysis based on the algorithm described in [9] allows one to get the distribution of hyperfine field shown in Figure 2a. The broad distribution of hyperfine field does not permit to make definite conclusions about transverse field component. In contrast, a clear-cut result is obtained for the c_1 parameter, see Figure 2b.

The hyperfine field in α -Fe is antiparallel to the direction of the magnetic moment of the iron atom [10] and to the magnetization. In Figure 2b the vertical axis corresponds to the $-c_1$ parameter. It is clear that iron magnetic moments with negative c_1 (large B_{hf}) are oriented parallel to the magnetization and those with positive c_1 (small B_{hf}) are oriented antiparallel.

The results presented in Figure 2a,b can be summarised as follows. Distribution $p(B_{\text{hf}})$ has a large value in the vicinity of $B_{\text{hf}} = 0$ and a tail ending at $B_{\text{hf}} \approx 30$ T. This result is in full agreement with earlier Mössbauer studies performed with unpolarized radiation [7].

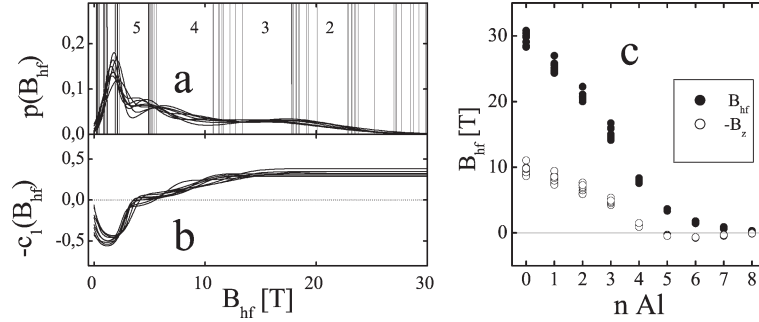


Figure 2. (a) Distribution of $p(B_{hf})$ and (b) dependence of c_1 on B_{hf} obtained from the data presented in Figure 1. Vertical lines in (a) show decomposition of the $p(B_{hf})$ distribution into sectors with area proportional to the probability given by binomial distribution $p(N, n, x)$. Numbers shown in rows correspond to n (number of Al atoms in the nearest coordination shell). (c) Average hyperfine field and average z -component of the hyperfine field related to sectors from (a) and (b). Note that there is a minus sign before c_1 in the vertical axis in (b) and before B_z in (c).

The most important result concerns the $c_1(B_{hf})$ dependence. The iron atoms with B_{hf} fields smaller than about 3.4 T develop a pronounced positive B_z component (Figure 2b). Next we observe that in the range of $B_{hf} = 5 \div 10$ T the c_1 parameter decreases and crosses zero. In that region the z -component of B_{hf} has a positive as well as a negative contribution to the hyperfine field, resulting in zero average value. The z -component saturates at B_{hf} larger than 15 T.

5. Discussion

The hyperfine magnetic field brings indirect information about the Fe magnetic moment. The positive values of c_1 seen in Figure 2b at $B_{hf} \approx 2$ T, could be interpreted assuming an antiparallel orientation of some fraction of the iron atoms, but could also be attributed to atoms with zero magnetic moment. To check what is the case we have to analyse the room temperature measurements, which are carried out in the paramagnetic state. They show a peak in the $c_1(B_{hf})$ parameter (not shown), the shape of which is similar to the one observed at $T = 13$ K. If the peak at $B_{hf} = 1 \div 2$ T in Figure 2b corresponded to iron atoms loosely bound to the rest of magnetic system, as is the case of a paramagnetic state, then one should expect to see the narrow peak precisely at 1.1 T. The most likely reason for seeing the broad peak at about 3 T is presence of small quadrupole interactions and a distribution of the isomer shift arising from variety of chemical environments [3]. Experimental confirmation of this interpretation is formed in the value of FWHM of the room temperature spectrum in zero applied field, equal to 0.62 ± 0.01 mm/s, see Figure 1b., while the FWHM for calibration spectra is 0.24 ± 0.01 mm/s only. We also see a clear asymmetry of the spectra measured at field $B_{ext} = 1.3$ T (Figure 1e). The asymmetry results from mixed magnetic dipole and electric quadrupole interactions. To obtain a correct description of the spectra one has to use a full Hamiltonian treatment, which is

beyond the scope of this paper. Small value of the parameter c_1 in the range of B_{hf} in range of 5 ÷ 10 T clearly shows either noncollinearity or antiparallel orientation of a fraction of Fe magnetic moments.

It is reasonable to assume that (1) the smaller B_{hf} values are observed, when there is a larger number n of Al which surround Fe atom, and that (2) the distribution of Fe and Al atoms is random. These two assumptions allow to divide the $p(B_{hf})$ distribution into a few sections, each one having the area proportional to the probability $p(N, n, x)$ given by binomial distribution:

$$p(N, n, x) = \binom{N}{n} (1-x)^n x^{N-n}. \quad (2)$$

Here $x = 0.48$, $N = 8$ and $n = 0 \dots N$. The sectioning is displayed in Figure 2a. For every section one can find an average $\bar{B}_{hf}(n)$. Similarly, using the same sectioning one can find from Figure 2b average z -component, which is displayed in Figure 2c. It is remarkable that the value $\bar{B}_{hf}(n)$ for $n = 0$ (Figure 2c), determined from the high field tail of the distribution (Figure 2a), coincides with the value for Fe surrounded by 0 Al in ordered Fe₃Al at low temperatures 31.8 T [11].

It follows from Figure 2b that $c_1(B_{hf})$ is constant for $B_{hf} > 15$ T, which strongly suggests (see Figure 2c) that Fe atoms surrounded by $n < 4$ Al exhibit the same type of magnetic structure. A reasonable assumption is that these moments are locally collinear.

Substantial changes are observed when n varies from $n = 3$ to $n = 4$. The hyperfine field is reduced to about 8 T, the value much smaller than 24.2 T found in ordered Fe₃Al [11]. Moreover, the c_1 (or B_z in Figure 2c for $n = 4$) is close to zero indicating that Fe moments become disordered. Fe atoms with $n = 5$ Al neighbours have small but nonzero total magnetic moments and the c_1 parameters indicate that, on the average, these moments are oriented antiparallel, see Figure 2b,c for $n = 5$.

When the number of Al nearest neighbors exceed $n = 5$ the Fe total magnetic moments are further reduced, see full points in Figure 2c. However, $n > 5$ is located in the region of B_{hf} equal or smaller than applied field 1.1T (see Figure 2a). Because the value of the applied field is comparable to the hyperfine field itself, and, as was already discussed, the quadrupole splitting and isomer shift interaction influence small magnetic interaction, information about the values and arrangements of these magnetic moments are not available at this stage of analysis.

In the presented analysis, random Fe distribution was assumed. If, however, short range order is present, sectioning shown in Figure 2a may not be valid. If the probabilities of the Al-rich environments are larger than given by 2, vertical lines with small n will shift towards higher B_{hf} values.

In summary, we present results of investigations of an magnetic moment arrangements in disordered Fe_{0.48}Al_{0.52} by Mössbauer polarimetric technique.

We have demonstrated that an increase of the number of Al in the first coordination shell causes a decrease of magnetic moments and introduces noncollinearity or antiparallel orientation when B_{hf} is in the range of $5 \div 10$ T. These noncollinear moments have positive as well as negative contributions to the net magnetization. The noncollinearity, present at low temperatures, explains the large coercivity, the lack of saturation and reduction of the ratio of magnetization and average hyperfine field.

References

1. Arrott A. and Sato H., *Phys. Rev.* **114** (1959), 1420.
2. Sato H. and Arrott A., *Phys. Rev.* **114** (1959), 1427.
3. Bogner J. *et al.*, *Phys. Rev. B* **58** (1998), 149922.
4. Jo T. and Akai H., *J. Phys. Soc. Jpn.* **50** (1981), 70.
5. Jo T., *J. Phys. Soc. Jpn.* **40** (1976), 715.
6. Szymański K., Dobrzyński L., Prus B. and Cooper M. J., *Nucl. Instrum. Methods B* **119** (1996), 438.
7. Yelsukov E. P., Voronina E. V. and Barinov V. A., *JMMM* **115** (1992), 271.
8. Warren B. E. and Averbach J., *J. Appl. Phys.* **21** (1950), 595.
9. Szymański K., *Nucl. Instrum. Methods B* **134** (1998), 405;
Szymański K., Satula D. and Dobrzyński L., *Hyperfine Interact.* **156/157** (2004), 21.
10. Hanna S. S. *et al.*, *Phys. Rev. Lett.* **4** (1960), 513.
11. Johnson C. E., Ridout M. S. and Cranshaw T. E., *Proc. Phys. Soc* **81** (1963), 1079.

P9

Arrangements of magnetic moments in nanocrystalline Fe₄₈Al₅₂

K. Szymański, D. Satuła, and L. Dobrzyński*

University of Białystok, Institute of Experimental Physics, Lipowa 41 15-424 Białystok, Poland

E. Voronina and E. P. Yelsukov

Physical-Technical Institute of Ural Division of Russian Academy of Sciences (Izhevsk)

T. Miyanaga

Department of Materials Science and Technology, Faculty of Science and Technology, Hirosaki University, Hirosaki, Aomori 036-8561, Japan

(Received 2 March 2005; revised manuscript received 20 June 2005; published 6 September 2005)

Combined techniques, EXAFS, magnetization, and Mössbauer polarimetry are used to investigate the orientation of Fe magnetic moments in a Fe₄₈Al₅₂ disordered alloy prepared by mechanical grinding. Local Fe magnetic moments and their contributions to the net magnetization at selected external fields and temperatures were estimated. It was found that components of the Fe magnetic moments parallel to the net magnetizations reduce their values much faster with an increasing number of neighboring Al atoms than the total iron moments. Data analysis indicates that magnetic moments of Fe atoms surrounded by (7Al+1Fe) in the first coordination shell and by (1Al+5Fe) in the second coordination shell possess nonzero magnetic moments that form a noncolinear structure.

DOI: 10.1103/PhysRevB.72.104409

PACS number(s): 76.80.+y

I. INTRODUCTION

The magnetism of the Fe-Al system has attracted and still attracts the attention of many scientists. The reason is simple: the scientific literature is full of controversy concerning magnetic ordering, individual magnetic moments, and spin dynamics, particularly in alloys with Al concentrations close to 50%. To recall, with aluminum concentrations exceeding 20 at. % the average magnetic moment decreases rapidly and—from extrapolation to zero—one can expect that the ferromagnetism should disappear at about 34 at. % of aluminum. However, around and above this concentration a truly interesting situation takes place.

A. Colinear versus noncolinear order and spin frustration

In Al-rich B2-type ordered alloys typically antiferromagnetic (AF) order is claimed. This order has been suggested for alloys with Al concentrations from above 35% to 43% and for equiatomic composition in papers.¹⁻⁵ At the same time it has been noticed that, close to FeAl composition, ferromagnetic order can exist,³ and supposedly antiferromagnetic or paramagnetic configurations can change into a ferromagnetic one upon simple filing.^{1,6-9} Ferromagnetism has been also detected in disordered alloys with an Al concentrations range 40–70 at. %.^{6,10-13}

For Fe concentrations close to 50 at. % a noncolinear ordering was considered by Bogner *et al.*¹⁴ It was found there that an Fe antisite atom surrounded by 8 Fe neighbors forms a cluster with mean moment of 0.4 μ_B . Band structure calculations show, however, that for ideally ordered FeAl an average magnetic Fe moment is much larger and amounts to 0.71 μ_B . The energy of the ferromagnetic ground state was found to be 0.7 mRy (per formula unit) lower than the energy of the nonmagnetic state. The observed difference of

magnetic moments was ascribed to possible noncolinear ordering. The authors of Ref. 14 found that the energy connected with a spin helix along the [100] direction is lower by 0.1 mRy/atom than the energy of a ferromagnetic state, if the spin direction is rotated from plane to plane by about 36 deg. Quite recent neutron diffraction data,¹⁵ taken on a bcc-ordered FeAl alloy, showed the presence of incommensurate spin density waves. The length of the wave vector of SDWs in FeAl is rather short $k=2\pi/(na)$ (n ranges from 11 to 6 and $a=0.290$ nm), which means nearly parallel orientation of the nearest neighbor Fe magnetic moments.

For systems with atomic and spin disorders—in particular for nonordered metal systems with RKKY interaction—Mattis¹⁶ considered a model in which spin-spin interactions were random in sign but did not result in frustrations. The spin system was considered as composed of two subsystems with randomly distributed antiparallel spins. The authors of Refs. 17 and 18 suggest that, in concentrated Fe-Al alloys, some iron atoms surrounded by a large number of aluminum atoms can flip their spins. It has also been shown¹⁸ that in a nonordered system containing magnetic moments m_+ and m_- parallel and antiparallel to the net magnetization, respectively, the magnetizations are characterized by different temperature dynamics: the average m_- vanishes at $T < T_C$ due to Stoner-type excitations. The magnetization behavior of the Fe-Al system and the ideas of Refs. 16–18 indicate that concentrated Fe-Al alloys could serve as candidates for alloys exhibiting the so-called Mattis phase; however, no experimental support to this expectation has been found so far.

Studies of Fe-Al alloys by Monte Carlo techniques¹⁹ in the Al concentrations range $0.25 < x < 0.50$ have showed that it is possible to account qualitatively for the transformation of a magnetic state from a ferromagnetic one to a certain spin glass state at about 34% Al. In these concentrated Fe-Al

alloys, RKKY interactions do not play an important role, unlike in the traditional diluted spin glass or cluster spin glass. The peculiar feature of this spin glass consists in the fact that frustrations arise from the positional disorder of Fe and Al atoms. The frustration is caused by n.n.n. Fe-Fe antiferromagnetic interactions. The authors¹⁹ conclude that Fe atoms with 6 and more n.n. Al atoms are found to be frustrated in an ordered ferromagnetic state.

B. Other findings and the motivation of the present work

The controversial findings and apparent impact of various defects and inhomogeneities on the magnetic structure of bulk and nanocrystalline alloys require a more detailed investigation that will elucidate the nature of magnetism in this system. In this paper we report studies of a nanocrystalline Fe-Al alloy in the concentration close to the onset of ferromagnetism. EXAFS measurements were used to characterize its chemical short-range order. Local magnetic properties were investigated by the Mössbauer technique with circularly polarized monochromatic radiation. Our observations strongly suggest that a noncolinear magnetic order must exist in the sample studied.

II. SAMPLE PREPARATION

An Fe-Al ingot was synthesized from high-purity components (99.99% Fe and 99.99% Al) in an induction furnace in an Ar atmosphere, then homogenized in a vacuum furnace at 1400 K for 6 h. Chemical analysis showed that the Al concentration was 52.0 ± 0.5 at. %. The carbon content in the alloys was not higher than 0.03 wt. %. The ingots were milled and a fraction with a particle size of less than 300 μm was used for further mechanical treatment in a planetary ball mill “Pulverisette” (Fritsch) with vials and balls made of tungsten carbide (WC). Mechanical grinding was performed in an inert gas atmosphere in an 80 cm³ volume vial filled with 4 g of powder and 25 balls with 10 mm diameter each. The supporting disk velocity was 450 rpm, with the vial velocity in relation to the supporting disk being 955 rpm. The milling of 10 h was enough to provide a disordered state in the Fe-Al alloys.¹³ According to the measurements on a laser analyzer “Analizette-22,” the particle size after milling ranged from 1 to 25 μm with an average of 6 μm .

III. X-RAY DIFFRACTION

X-ray diffraction studies were performed at room temperature using monochromatic Cu $K\alpha$ radiation. The lattice parameter was 0.2916(4) nm. The x-ray diffraction pattern consists of the broadened peaks (110), (200), (211), and (220) of the bcc structure. The shape of the diffraction lines was analyzed and mean grain size of 4.0(3) nm and microstrains $\langle e^2 \rangle^{1/2} = 0.5(1)\%$ were found by use of the harmonic analysis.²⁰ Additionally, the peaks of WC, that get into the milled powders due to the wear of the vials and balls, were revealed. A phase analysis of the x-ray diffraction data showed that the WC admixture in the milled powders was 2 wt. %. The position of the most intensive diffraction lines resulting from WC agrees with the position of those for the

milled WC powders under the same conditions of milling. We thus conclude that mechanical alloying of Fe-Al powder with WC does not occur.

IV. EXAFS MEASUREMENTS

The Fe K-edge EXAFS measurements were made at SPring-8 on the bending magnet beamline BL01B1 with a Si(111) fixed-exit double-crystal monochromator. The storage ring was operated at 8.0 GeV, and the ring current was 70–99 mA. Due to the double rhodium-coated mirror reflection, the higher harmonics were reduced to less than 10^{-5} . The spectra were taken at temperatures 10, 80, and 300 K in the transmission mode. Measurements were performed with two ionization chambers, filled with N₂ and mixture Ar + N₂ gases, registering incident intensity I_0 , and transmitted intensity I , respectively. The size of the output slit was 0.8 mm by 5 mm.

To perform the correct determination of the local atomic structure parameters from EXAFS spectra, a procedure for correcting the nonuniformity of sample thicknesses using measurements of the absorption at a different temperature was developed and tested on intermetallic compounds.²¹ The Debye temperature of the material was taken from Ref. 22. After correcting the experimental intensity ratio $I(E)/I_0(E)$ for sample thickness inhomogeneity, the absorption coefficient $\mu(E)$ was obtained. The procedure for calculating the normalized oscillatory part $\chi(k)$ consisted of standard steps—the subtraction of the pre-edge absorption function approximated by the Victoreen function, while a smooth atomlike background was approximated by a cubic spline function followed by normalization. To make the conversion of $\chi(E)$ from energy to momentum spaces, an ordered FeAl intermetallic compound was used as reference material. Then, the E_0 value was estimated by matching the experimental EXAFS spectrum of FeAl and theoretical EXAFS spectrum calculated by the FEFF7 code.²³ The backscattering phase and amplitude, the central atom phase shift, the mean-free path, and the reduction factor were calculated using this code for known intermetallic compounds FeAl and Fe₃Al.

The analysis of normalized oscillatory parts $\chi(k)$, shown in Fig. 1(a), was performed in a single-scattering approximation within Tikhonov’s regularization method.²⁴ The parameters of pair correlation functions (PCF): partial coordination numbers, $N_{\text{Fe-Fe}}$, $N_{\text{Fe-Al}}$, and the interatomic distances $R_{\text{Fe-Fe}}$, $R_{\text{Fe-Al}}$, were determined according to the scheme described in Refs. 25 and 26.

An analysis of the PCF parameters indicates the presence of a positional disorder induced by high-energy ball milling. This is in agreement with the EXAFS study of Ref. 27 on an implanted Fe₆₀Al₄₀ alloy. The disorder (atomic rearrangement) induced by irradiation or heavy plastic deformation was discussed in detail in Refs. 28 and 29. Our results show lower than expected (for a disordered alloy, deduced from stoichiometry) number of Fe atoms in the first coordination shell of Fe, and of Al atoms in the second shell of Fe, indicating a smaller disorder than reported in Refs. 28 and 29. This situation can be due to the fact that the concentration of the studied alloy is close to the stoichiometric composition.

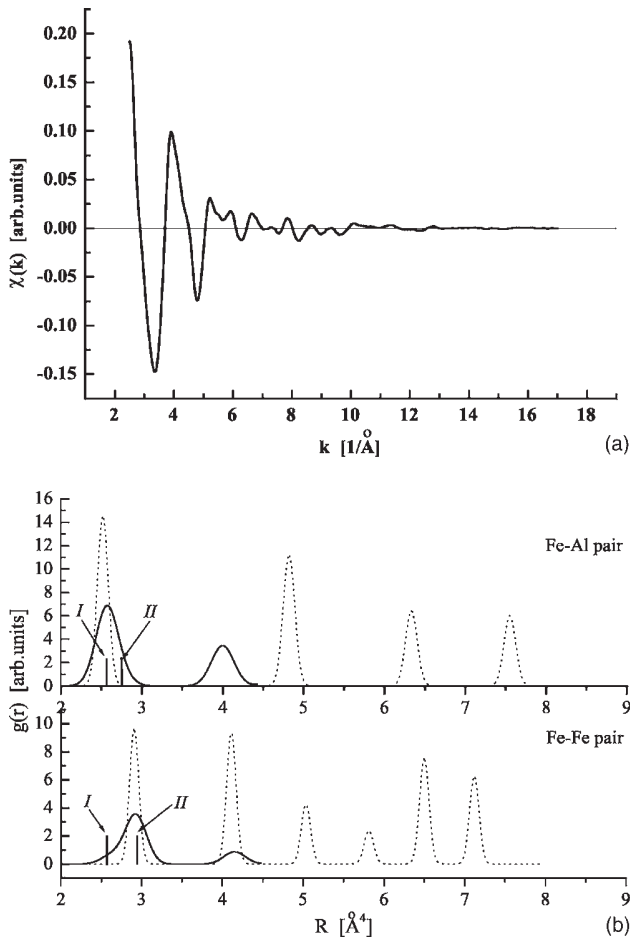


FIG. 1. (a) The EXAFS oscillatory part $\chi(k)$ taken at 10 K; (b) pair correlation functions for the disordered alloy (solid lines) in comparison with those of intermetallic compound FeAl (dashed lines). The interatomic distances for the pair correlation functions for the *I* and the *II* coordination shell are indicated by vertical bars.

The average values of interatomic distances $R_{\text{Fe-Fe}}$ for the nearest neighbors and $R_{\text{Fe-Al}}$ for the next nearest neighbors differ from the values deduced from the lattice parameter [see the vertical bars in Fig. 1(b)]. In a fully ordered alloy there are no Fe atoms in the first coordination shell of Fe and no Al atoms in the second coordination shell of Fe. In the investigated alloy with a distorted structure we observed a small number of Fe atoms in the first shell of Fe; their $R_{\text{Fe-Fe}}$ distance is 2.60 Å, larger than 2.526 Å deduced from the lattice parameter. For the Al atoms in the second shell of Fe we have found $R_{\text{Fe-Al}}=2.80$ Å, which is smaller than 2.916 Å. All these differences reflect the presence of local microdisplacements, and agree with the results of Ref. 22.

TABLE I. Partial coordination numbers for the first and second coordination shells, the interatomic distances, and mean square displacements determined from of EXAFS measurements.

Shell	$R_{\text{Fe-Fe}}$ (Å)	$N_{\text{Fe-Fe}}$	$\sigma_2 \times 10^2$ (Å ²)	$R_{\text{Fe-Al}}$ (Å)	$N_{\text{Fe-Al}}$	$\sigma_2 \times 10^2$ (Å ²)
<i>I</i>	2.60±0.03	0.8±0.5	1.70	2.56±0.02	7.2±0.5	1.86
<i>II</i>	2.92±0.01	5.3±0.5	1.73	2.80±0.05	0.7±0.5	1.91

The average EXAFS interatomic distance calculated from local parameters agrees to within 0.02 Å with our x ray diffraction data. Another peculiarity of the results obtained is the observed overlap of peaks in the PCF of the first and second coordination shells, which originates, first of all, from a static disorder. This cannot be caused by the poor quality of the algorithm used. Indeed, it is known that Tikhonov's regularization method, as compared to the standard Fourier transformation procedure, is of higher resolution.²⁵ Nevertheless, the peaks referring to the first and second distances for Fe-Fe and Fe-Al pairs in Fig. 1(b) are not resolved as well as in Fourier transformed data for FeAlMn alloys.³⁰

The obtained values of $N_{\text{Fe-Fe}}$ and $N_{\text{Fe-Al}}$ correspond in terms of Cowley short-range order parameters³¹ to the negative value for the first coordination shell and positive value for the second shell. The main conclusion from the EXAFS experiment is the detection of a pronounced short-range order with its quantitative characteristic $N_{\text{Fe-Fe}}$ and $N_{\text{Fe-Al}}$, presented in Table I, rather than the random distribution of atoms.

V. MAGNETIC MEASUREMENTS

Magnetic measurements were performed using a SQUID magnetometer MPMS-XL-5 (Quantum Design) in external magnetic fields up to 5 T at temperatures from 5 to 300 K. The magnetization curves and hysteresis loops were measured; FC and ZFC experiments were carried out. Magnetic measurements showed the presence of symmetric hysteresis, a lack of saturation at $T=5$ K and in fields up to 5 T (according to Ref. 6 even up to 15 T); see Figs 2 and 3. The closure of descending and ascending branches of the hysteresis loop, taking place at high B_{ext} values, $B_{\text{ext}} > 0.8$ T, also gives a rather high value of coercive force $B_c \approx 50$ mT at 5 K, which falls to ≈ 3 mT at 77 K.

The average magnetic moments per Fe atom, measured at external fields B_{ext} —the same as used in a Mössbauer experiment—are shown in Table II. The data were corrected for the fraction of WC present in the sample. The magnetic ordering temperature of the sample was (110 ± 10) K.

From an extrapolation of the high-field part of the magnetization curves to $B_{\text{ext}}=0$ we derived the value of specific magnetizations, from which the average magnetic moments per Fe atom were determined. In Fig. 4 they are presented together with the available magnetic data from literature,^{9,13} and compared with the average (hyperfine magnetic field) h.m.f. obtained from Mössbauer experiments.^{6,11,13} The ratio of the h.m.f. measured at a low temperature to the magnetic moments of iron inferred from magnetization measurements, is anomalously high -29.4 T/ μ_B , while it is about 12.0–13.5 T/ μ_B in ferromagnetic alloys with Al concentra-

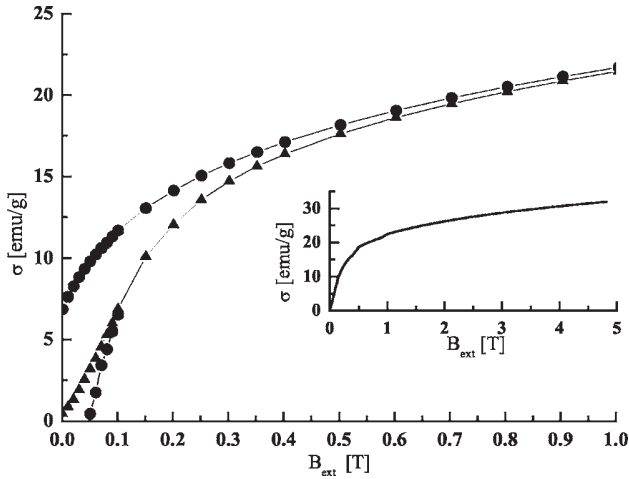


FIG. 2. The magnetization curve (triangles) and part of the hysteresis loop (circles) of the disordered $\text{Fe}_{48}\text{Al}_{52}$ measured at $T=5$ K. Inset—the magnetization curve measured in an external field up to 5 T.

tions less than 40 at. %. The temperature behavior of the magnetization measured at relatively low magnetic fields exhibits a pronounced maximum at about 40 K, Fig. 3.

VI. MÖSSBAUER SPECTROSCOPY

A. Principles of Mössbauer polarimetry

Since Mössbauer polarimetric techniques are not common, we briefly describe what physical information can be obtained from this type of measurement. ^{57}Fe h.m.f. is a vector quantity, related usually to the Fe magnetic moment. In disordered magnetic systems one encounters a distribution of both the length and the orientation of a h.m.f. vector \mathbf{B}_{hf} .

Preferred h.m.f. orientation, $P(\Omega)$, is usually described in a certain set of base functions, e.g., spherical harmonics Y_{lm} .^{32,33} Since only M1 dipolar transitions are measured in

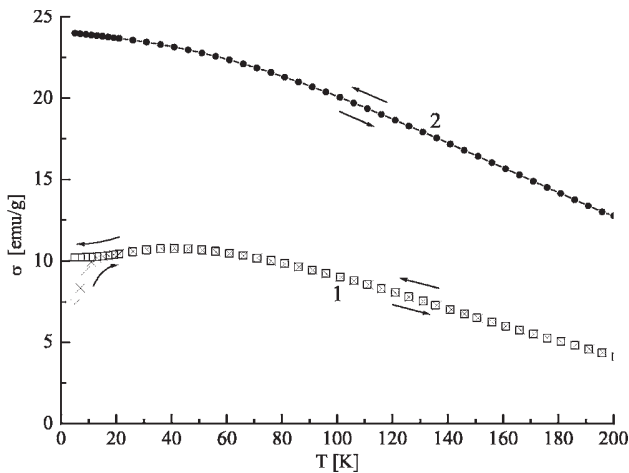


FIG. 3. ZFC (\square) and FC (\times) temperature dependences of the magnetization of the $\text{Fe}_{48}\text{Al}_{52}$ alloy at $B_{ext}=0.1$ T (curves 1) and $B_{ext}=1.6$ T (curves 2).

TABLE II. Magnetization, σ , and magnetic moment per Fe atom, μ_{Fe} , the average hyperfine magnetic field, \bar{B}_{hf} , its z component, \bar{B}_z , corrected for the external magnetic field, at selected temperatures and external magnetic fields.

B_{ext} (T)	T (K)	σ (emu/g)	μ_{Fe} (μ_B)	\bar{B}_{hf} (T)	$\bar{B}_z - B_{ext}$ (T)
0	13	0	0	7.9 ± 0.1	0
0	50	0	0	4.2 ± 0.2	0
0.2	13	12.0 ± 2.0	0.19 ± 0.03	7.9 ± 0.1	-1.4 ± 0.1
0.2	50	13.0 ± 2.0	0.20 ± 0.03	3.3 ± 0.2	-0.7 ± 0.2
1.1	13	21.4 ± 2.0	0.33 ± 0.03	8.2 ± 0.1	-2.9 ± 0.2
1.1	50	21.0 ± 2.0	0.30 ± 0.03	4.6 ± 0.2	-2.2 ± 0.2

^{57}Fe Mössbauer spectroscopy, unpolarized radiation delivers information on Y_{2m} only, while other Y_{1m} harmonics can be known when circularly polarized radiation is used. Knowledge of Y_{1m} and Y_{2m} in the texture function is equivalent to the knowledge of angular averages $\langle \boldsymbol{\gamma}_r \cdot \mathbf{m} \rangle$ and $\langle (\boldsymbol{\gamma}_r \cdot \mathbf{m})(\boldsymbol{\gamma}_s \cdot \mathbf{m}) \rangle$,³⁴ where \mathbf{m} is a unit vector parallel to the local hyperfine field \mathbf{B}_{hf} , $\boldsymbol{\gamma}_r$, $\boldsymbol{\gamma}_s$ are Cartesian vectors ($r, s = x, y, z$), and brackets $\langle \rangle$ denote angular averaging, for any function $g(\Omega)$,

$$\langle g(\Omega) \rangle = \int_{4\pi} g(\Omega) P(\Omega) d\Omega. \quad (1)$$

In the case of a sample with axial symmetry it is convenient to choose one of the $\boldsymbol{\gamma}_r$, denoted by $\boldsymbol{\gamma}$, parallel to the \mathbf{k} vector of the photon. Then the averages $\langle \boldsymbol{\gamma} \cdot \mathbf{m} \rangle \equiv c_1$ and $\langle (\boldsymbol{\gamma} \cdot \mathbf{m})^2 \rangle \equiv c_2$ can be measured with monochromatic, circularly polarized radiation.^{34,35} Parameter c_2 is the average cosine square of the angle between the h.m.f. and the given direction $\boldsymbol{\gamma}$. Mössbauer absorbers prepared from powder sample exposed to an external axial magnetic field exhibit axial sym-

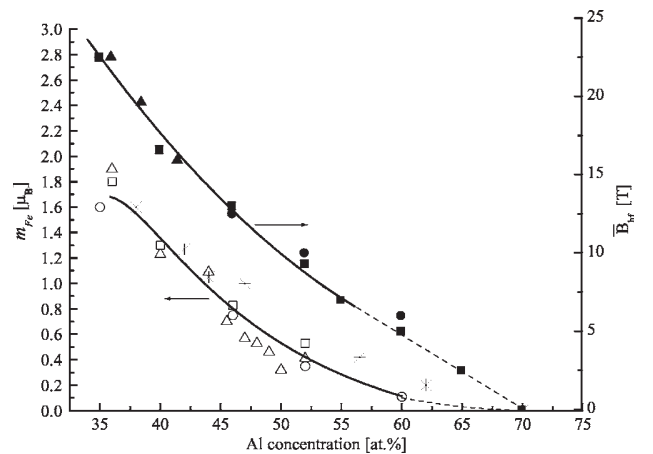


FIG. 4. The average magnetic moment per Fe atom obtained from extrapolation of high-field magnetization measurements and average hyperfine field from Mössbauer experiments \blacktriangle (Ref. 9), \triangle (Ref. 6); \square , \blacksquare (Ref. 13), (\times) (Ref. 11); \circ , \bullet the authors data published in Ref. 76.

metry. Thus, in the case of a texture with axial symmetry, c_2 is a measure of the perpendicular component of the h.m.f.: $c_2=0$ means that the perpendicular component has achieved its maximum, while this component is zero when $c_2=1$. It follows from Eq. (1) that $c_1 B_{hf}$ is the average component of the h.m.f. in the γ direction. If we assume that, to within reasonable accuracy the atomic magnetic moment is proportional to the h.m.f., the c_1 parameter gives element-selective information about the contribution of the element to total magnetization.³⁶ Recently this type of information was exploited in synchrotron experiments with nuclear scattering of circularly polarized radiation.³⁷

For the case of single \mathbf{B}_{hf} and measurements with circularly polarized radiation, the line intensity i_n of the n th nuclear transition in the Zeeman sextet was given in Ref. 38. One can show that, having a distribution of directions of vector \mathbf{B}_{hf} , the expressions for i_n should contain already introduced averages, namely,

$$\begin{aligned} 16i_1 &= 48i_4 = 3(1 \pm 2c_1 + c_2), \\ 4i_2 &= 4i_5 = 1 - c_2, \\ 48i_3 &= 16i_6 = 3(1 \mp 2c_1 + c_2). \end{aligned} \quad (2a)$$

We recall that, for unpolarized radiation, the line intensities are

$$\begin{aligned} 16i_1 &= 48i_3 = 48i_4 = 16i_6 = 3(1 - c_2), \\ 4i_2 &= 4i_5 = 1 - c_2. \end{aligned} \quad (2b)$$

Finally, the absorber can be measured in a way that the obtained spectrum will be equivalent to a measurement on a sample with no magnetic texture^{39,40} and the line intensities for such a texture-free mode are:

$$4i_1 = 6i_2 = 12i_3 = 12i_4 = 4i_6 = 1. \quad (2c)$$

B. Measurements

Texture-free absorbers for Mössbauer spectroscopy were prepared by mixing $\text{Fe}_{48}\text{Al}_{52}$ powder with Li_2CO_3 and epoxy. The measurements were performed on samples cooled in a closed cycle refrigerator equipped with an antivibration shroud. We have used absorbers containing 9.40 ± 0.23 and 13.16 ± 0.35 mg of $\text{Fe}_{48}\text{Al}_{52}/\text{cm}^2$. Since no available data on the temperature dependence of a recoilless fraction for disordered Fe-Al were known to us, we approximated $f_{\text{Fe-Al}}(T)$ by

$$f_{\text{Fe-Al}}(T) = f_{\alpha\text{-Fe}}(T) \frac{f_D(T, \theta_{\text{Fe-Al}})}{f_D(T, \theta_{\alpha\text{-Fe}})}, \quad (3)$$

where $f_D(T, \theta)$ is a recoilless fraction in harmonic approximation with Debye temperature θ , and $f_{\alpha\text{-Fe}}$ is a recoilless fraction of $\alpha\text{-Fe}$ determined in the precise experiment of Ref. 41. Debye temperatures for disordered $\text{Fe}_{48}\text{Al}_{52}$ and $\alpha\text{-Fe}$ were taken from Ref. 22. Finally, we estimated that the Mössbauer thickness τ (Ref. 42) of the measured absorbers were 2.60 ± 0.07 and 3.65 ± 0.10 at 298 K. Similarly, at

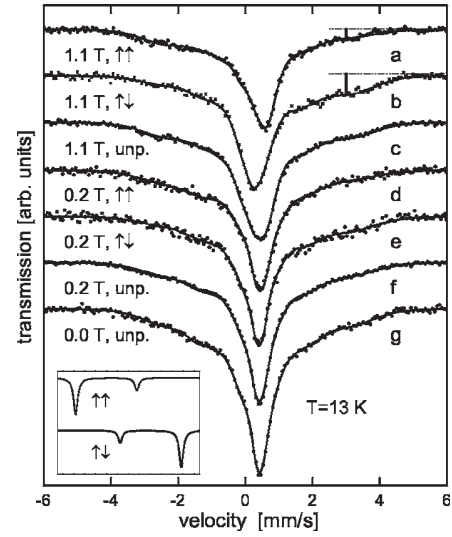


FIG. 5. Mössbauer spectra measured at $T=13$ K with polarized and unpolarized radiation in the axial applied magnetic field. Induction of the field is given on the left. Arrows $\uparrow\uparrow$ and $\downarrow\downarrow$ indicate two opposite circular polarizations. Solid lines represent a simultaneous fit with the same set of QS, IS, and intensities. Inset: schematic shape of the spectra of $\alpha\text{-Fe}$ absorber in an external magnetic field.

$T=13$ K the thicknesses τ were 3.16 ± 0.08 and 4.43 ± 0.11 , respectively.

The absorbers were placed inside one of the rare earth magnets, producing an axially symmetric field perpendicular to the absorber surface and parallel to gamma rays. The measurements were performed at temperatures $T=13, 50,$ and 298 K and external fields between 0 and 1.3 T; see Figs. 5–7.

The velocity scale of the spectra was calibrated with respect to $\alpha\text{-Fe}$ at room temperature. The source of unpolarized radiation was ^{57}Co in a Cr matrix. Circularly polarized monochromatic radiation was produced by the resonant filter technique.^{35,43–45} The polarization degree was estimated as in Ref. 35. Additionally, we have prepared a set of $\alpha\text{-Fe}$ absorbers with different thicknesses and different magnetic textures. The magnetization curves for all absorbers were mea-

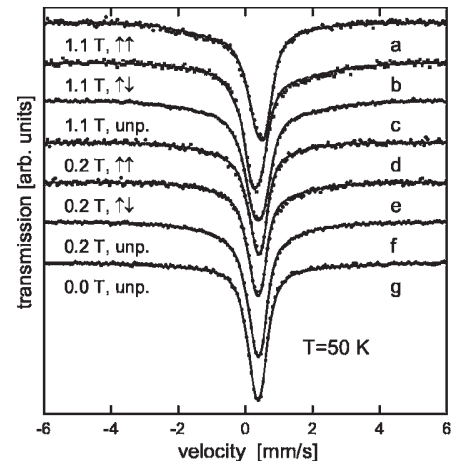


FIG. 6. The same as in Fig. 5 for $T=50$ K.

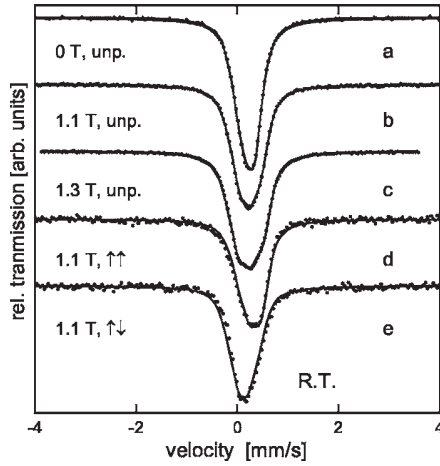


FIG. 7. Room temperature Mössbauer spectra measured with unpolarized (a)–(c) and polarized radiation (d), (e) in an external axial field. Induction of the field is given on the left. Arrows $\uparrow\uparrow$ and $\uparrow\downarrow$ indicate two opposite circular polarizations. Solid lines are results of a simultaneous fit with the same set of QS, IS and intensities for spectra shown in (a), (b), (c).

sured in external fields up to 3 T to obtain a fully saturated state. At a given B_{ext} the magnetization ratio $\sigma(B_{ext})/\sigma(\infty)$ is equal to the c_1 parameter. These measurements allow us to check whether nuclear polarimetry and magnetic measurements produce consistent results.

Usually the three measurements were performed at a given temperature and on an external magnetic field: with unpolarized radiation and with two opposite circular polarizations. An additional experiment in a zero applied field supplied magnetic texture-free results.

A quick inspection of these results shows that when a circular polarization state of radiation is changed to an opposite one, a clear shift of the position of the central absorption line is observed [see Figs. 5(a), 5(b), 6(a), 6(b), 7(d), and 7(e)]. It is also evident that the absorption in the region of +3 mm/s in Fig. 5(b) is larger than that one in Fig. 5(a) [see the vertical bar in Fig. 5(b), which is almost two times longer than the bar in Fig. 5(a)] while in the region of –3 mm/s the absorption in Fig. 5(a) is larger than in Fig. 5(b). From this behavior, one immediately concludes that large Fe magnetic moments (and related large hyperfine fields) are oriented as in Fe-based ferromagnets (see the inset in Fig. 5), i.e., parallel to the net magnetization. Because of the presence of a distribution of h.m.f. it is not obvious how the small hyperfine fields are spatially arranged.

C. Description of the data handling

A normalized Mössbauer spectrum $S(v)$ consists of a linear combination of N subspectra $s(v, B_j)$:

$$S(v) = \sum_{j=1}^N p_j s(v, B_j), \quad (4)$$

where v is Doppler velocity, and p_j is the non-negative coefficient for a field B_j . Subspectrum $s(v, B)$ is a Zeeman sextet,

$$S(v, B) = \sum_{n=1}^6 i_n L_n(v, B), \quad (5)$$

where $L_n(v, B)$ describes the shape of the absorption line corresponding to the n th nuclear transition. Every subspectrum $s(v, B_j)$ is characterized by its relative area proportional to p_j and the two already introduced averages c_{1j} and c_{2j} . In the algorithm used by us it is possible to decompose a set of spectra, measured with different polarization states of photons, into components that fulfill Eqs. (2). Physically possible sets of p_j , c_{1j} , and c_{2j} have to be considered only, namely,

$$0 \leq p_j, \quad -1 \leq c_{1j} \leq 1, \quad 0 \leq c_{2j} \leq 1, \quad c_{1j}^2 \leq c_{2j}. \quad (6)$$

The last inequality in (6) is the Buniakovsky-Schwartz relation applied to the distribution of cosine and cosine square; see Ref. 46 for details. Equations (2) show that four types of measurements—with an unpolarized beam, with two opposite circular polarizations, and in a texture-free mode—can be simultaneously fitted with a set of p_j , c_{1j} , and c_{2j} , ($j = 1, N$), fulfilling the conditions of inequalities (6).⁴⁷

Instead of using a discrete sum of Zeeman components, we have found that a better description can be obtained by using a sum of components with a Gaussian distribution of h.m.f. This set of functions is widely used in commercially available Mössbauer packages. In our case, the use of Gaussian components permits one to obtain a continuous distribution of the h.m.f. $p(B)$, and two functions: $c_1(B)$ and $c_2(B)$.

The treatment described so far can be applied to cases where pure magnetic interactions are present. The treatment of mixed dipole magnetic and quadrupole electric interactions coupled to circularly polarized radiation have been described in Ref. 34 Using intensity tensor formalism^{48–53} we have adopted expressions, Eqs. (2), to the case of mixed interactions under the assumption that the axes of the electric field gradient tensor are oriented randomly in space. In the special case of unpolarized radiation, Eqs. (2b) and (2c) and a single h.m.f. value, our algorithm is equivalent to the full Hamiltonian treatment described in Ref. 54.

Mössbauer transmission spectra are described quantitatively by the transmission integral.⁴² Thickness effects were included by the folding method:⁵⁵ the cross section for resonant scattering multiplied by the effective thickness τ enters as an argument of an exponential function and was convoluted with the Lorentzian function. In all presented fits (Figs. 5–7) thickness effects are included.

D. Results of the analysis

In the first step of analysis of the Mössbauer data we determined hyperfine interactions of the alloy at room temperature. As already discussed, it was assumed that the principal axes of the electric field gradients acting on ⁵⁷Fe nuclei are randomly oriented. Because the sample is in a paramagnetic state, the single value of the h.m.f. equal to the external magnetic field is acting on the system, like in Ref. 54. Successful simultaneous fits to the spectra measured in different external magnetic fields [Figs. 7(a) and 7(c)] were obtained assuming the presence of four components with isomer

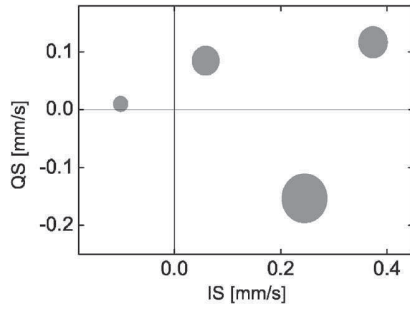


FIG. 8. Isomer shift and quadrupole splitting of four components obtained from simultaneous fits to room temperature data. The surface of the symbol is proportional to the intensity of the respective component.

shifts, quadrupole splittings, and the probabilities shown in Fig. 8. Quadrupole splitting, QS, is proportional to the main component of the electric field gradient V_{zz} ,

$$QS = \frac{e^2 Q V_{zz} c}{2E_\gamma} \sqrt{1 + \frac{\eta^2}{3}}, \quad (7)$$

where the right-hand side parameters have the usual textbook definition.⁵⁶ The asymmetry parameter η was assumed to be zero because the fitting procedure was insensitive to the value of η . We do not interpret components in Fig. 8 as resulting from well-defined chemical environments—such a two-dimensional distribution of quadrupole splitting and isomer shift represents the measured spectra relatively well.

To analyze low-temperature data, we assumed the same isomer shift and the electric field gradient, as well as their probabilities determined at room temperature. We allowed this only for the second-order Doppler shift⁵⁷ and for the appearance of the h.m.f. distribution.

In the first stage of the analysis it was assumed that hyperfine magnetic fields correspond to the colinear magnetic structure. Thus the c_1 (as well as c_2) parameter has the same value for all magnetic components. Under this assumption we were able to perform simultaneous fits (not shown) to the data measured at $T=13$ K with unpolarized radiation, while it was not possible to find a reasonable fit to data measured with polarized radiation; the best fit achieved is displayed in Fig. 9. Next, we allowed the c_1 and c_2 parameters to vary and the best results of simultaneous fits are presented in Fig. 5.

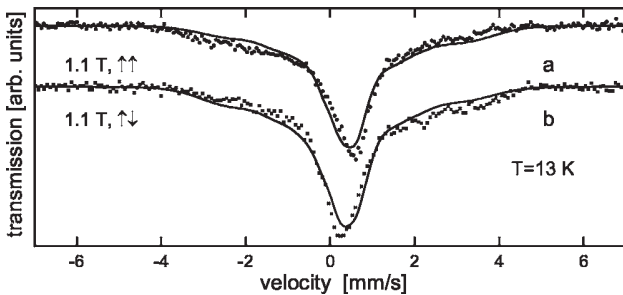


FIG. 9. Spectra measured with circularly polarized radiation and an example of the best fit under the condition that spatial orientation of the h.m.f. vector does not depend on the value of h.m.f.

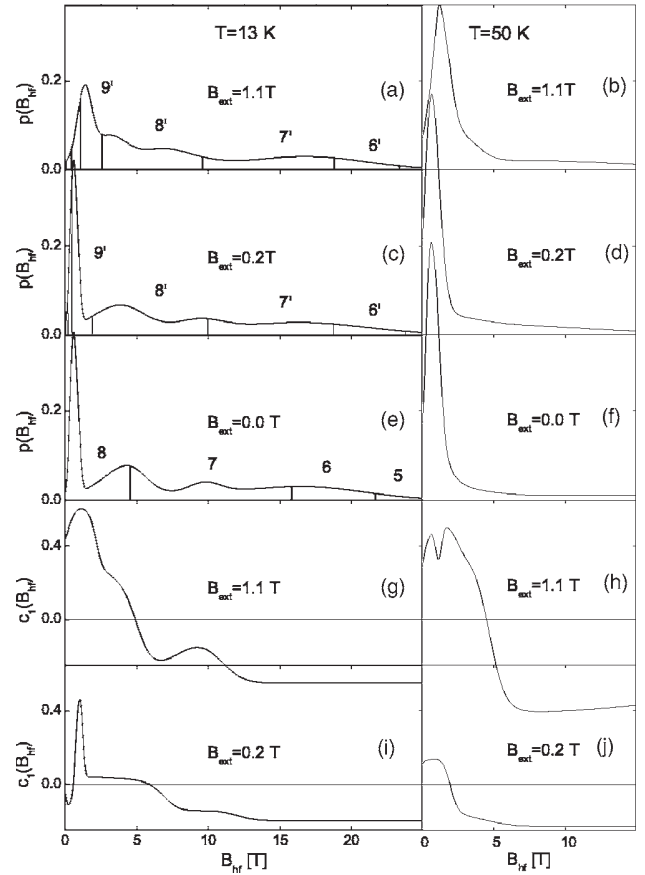


FIG. 10. Distributions of the hyperfine field measured at different values of an external magnetic field (a)–(f) and the hyperfine field dependence of the average cosine between the hyperfine field vector and magnetization (g)–(j). Vertical bars divide $p(B_{hf})$ distribution into the sectors numbered by integers $k=8, 7, 6, \dots, 9', 8', 7', \dots$ when the first (and the second) coordination shell is taken into account.

The distributions of the hyperfine fields $p(B_{hf})$ and the dependence of $c_1(B_{hf})$ are presented in Fig. 10. These dependences appeared to be almost insensitive to $c_2(B_{hf})$. Thus, the selection of $c_2(B_{hf})$ was not possible. The same treatment was used for $T=50$ K data and the results are shown in Figs. 6 and 10.

The results presented in Figs. 5, 6, and 10 can be summarized as follows. Distribution $p(B_{hf})$ has a large value in the vicinity of $B_{hf}=0$ and a tail ending at $B_{hf}=30$ T at $T=13$ K, and at about $B_{hf}=20$ T at $T=50$ K, which agrees with Refs. 13 and 10.

The most important result concerns $c_1(B_{hf})$ dependence. It is a known fact that the h.m.f. in the α -Fe is antiparallel to the direction of the magnetic moment of the iron atom:⁵⁸ the magnetization, i.e., the c_1 parameter, is negative. For our sample this behavior is observed only for hyperfine fields larger than about 5 T.

At $T=13$ K and a low external field, c_1 for B_{hf} smaller than approximately 5 T is small and positive. Its value decreases in the region of $B_{hf}=5-15$ T and for $B_{hf}>15$ T its value saturates. Our results indicate clearly that the average

c_1 parameter in the saturation region is larger for $T=50$ K than for $T=13$ K; compare Figs. 10(g) and 10(h).

Were the h.m.f. a monotonic function of the magnetic moment, the observed results could then be summarized as follows. The sharp peak in the $p(B_{hf})$ distribution observed close to $p(B_{hf})=0$ in the small external field and in the zero external field [Figs. 10(e) and 10(f)] corresponds to iron with a zero magnetic moment. When a larger external field is applied, we observe a shift of this peak to the B_{hf} value that is approximately equal to B_{ext} , i.e., 1.1 T [Figs. 10(a) and 10(b)], and the positive value of c_1 for the $B_{hf}=B_{ext}$ parameter [Figs. 10(g) and 10(h)] indicates that the directions of the h.m.f. and applied field coincide.

In the region close to $B_{hf}=4$ T, relatively large probability $p(B_{hf})$ is observed; see Figs. 10(a), 10(c), and 10(e). Because h.m.f. $B_{hf}=4$ T is much larger than the external field, it is reasonable to suppose that B_{hf} in this region corresponds to Fe atoms with nonzero magnetic moments. If this is so, the nearly zero value of the c_1 parameter in Fig. 10(i) indicates that these moments, on average, do not contribute to total magnetization. A similar situation is observed at $T=50$ K, $B_{ext}=1.1$ T, and B_{hf} approximately equal to 4 T [Fig. 10(b)]. One can note that the $|c_1|$ parameter for large fields [Fig. 10(h)] is larger at $T=50$ K than observed at $T=13$ K. This indicates that in the external applied field at $T=13$ K an iron subsystem with large magnetic moments is magnetically harder.

The data collected at $B_{ext}=0.2$ T should be treated more carefully. We think that the sharp peak in Fig. 10(i) and the dip in Fig. 10(h) are artefacts caused by the use of the approximated discrete hyperfine structure of QS, determined at room temperature. It is known that QS increases with decreasing temperature,⁵⁹ and the hyperfine structure in the vicinity of the zero field $p(B_{hf})$ should be interpreted with caution. However, such subtleties do not influence our main conclusions concerning the arrangements of magnetic moments.

Knowing the h.m.f. distribution, $p(B_{hf})$ and $c_1(B_{hf})$, one can calculate the average \bar{B}_{hf} and average z th component \bar{B}_z (to shorten notation we omit the hf subscript):

$$\begin{aligned}\bar{B}_{hf} &= \int_0^{\infty} p(B)B dB, \\ \bar{B}_z &= \int_0^{\infty} p(B)c_1(B)B dB.\end{aligned}\quad (8)$$

Both values are given in Table II and will be discussed in the next section.

As described earlier, in the fitting procedure the isomer shift distribution at low temperatures was constrained to coincide with room temperature data. The average shift of the whole spectra was a free parameter in the fit. This is shown in Fig. 11 and compared with the second-order Doppler shift in harmonic approximation.⁶⁰ The upper curve shown in Fig. 11 corresponds to the Debye temperature already used in EXAFS data evaluation. Figure 11 indicates that consistency of data evaluation has been achieved.

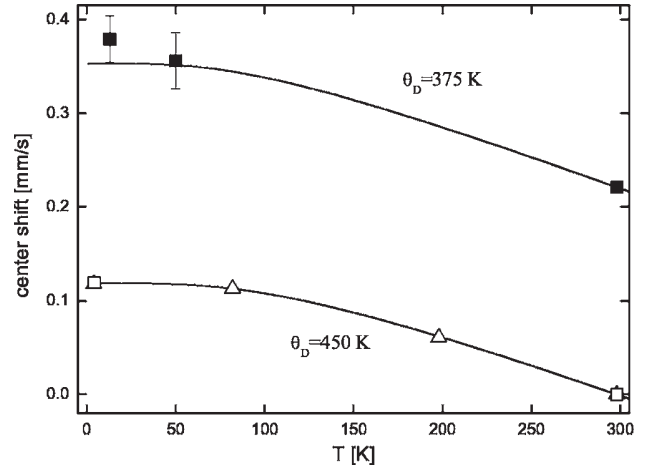


FIG. 11. Temperature dependence of the center shift. Data for α -Fe are given for a comparison. Solid lines correspond to the second-order Doppler shift in harmonic approximation with indicated Debye temperatures. \triangle (Ref. 77), \square (Ref. 78), \blacksquare (this work).

VII. DISCUSSION

It is well documented that hyperfine fields and magnetic moments (or magnetization) in many ferromagnetic systems are strongly correlated. For Fe-sp-element alloys, the ratio of these two quantities is distributed in the range 10.0–15.0 T/ μ_B . The data for disordered alloys of Fe with Al, Si, and P, summarized in Ref. 61, show that this factor is 12.0–13.0 T/ μ_B if concentrations of the sp element in alloys do not exceed 40 at. %. The value 12.5 T/ μ_B (Ref. 62) has been found in many ferromagnetic systems while it is equal to 15.2 T/ μ_B for α -Fe at $T=0$.

This correlation is supported by the proportionality of core electron polarization contribution B^{cep} (proportional to the integrated spin density of d electrons in MT sphere, M_d) to B_{hf} . First principles calculations⁶³ show that the proportionality coefficient B^{cep}/M_d is 12.3 T/ μ_B and does not depend either on a particular metalloid or on its concentration. Another contribution to B_{hf} comes from valence electrons and is denoted by B^{val} . In phenomenological models^{3,64} this contribution is proportional to the average magnetization. If B^{val} is not too large, the relative accuracy of localized moments calculated from the aforementioned proportionality is⁶⁵ $B^{val}/(B^{cep}+B^{val})$. As was shown in Ref. 65, the dependence of B^{val} on the distance of the Fe-sp element in disordered alloys resembles RKKY polarization damped by a factor proportional to $\exp(-r_{ij}/l_0)$, where r_{ij} is the distance between Fe and impurity atoms and l_0 denotes the mean-free path of electrons. The damping term comes from substantial localization of the valence electrons. In disordered concentrated alloys with a developed density of structural defects and microdistortions, the defects also reduce considerably the RKKY interaction. According to Ref. 65 the impurities located at n.n.'s distances creates a B^{val} value not greater than 0.7 T for the first and second coordination spheres. The small value of B^{val} allows one to use the hyperfine constant B_{hf}/μ_{Fe} for the estimation of magnetic moments from the B_{hf} data, and for the interpretation of the B_{hf} distributions in terms of localized magnetic moments.

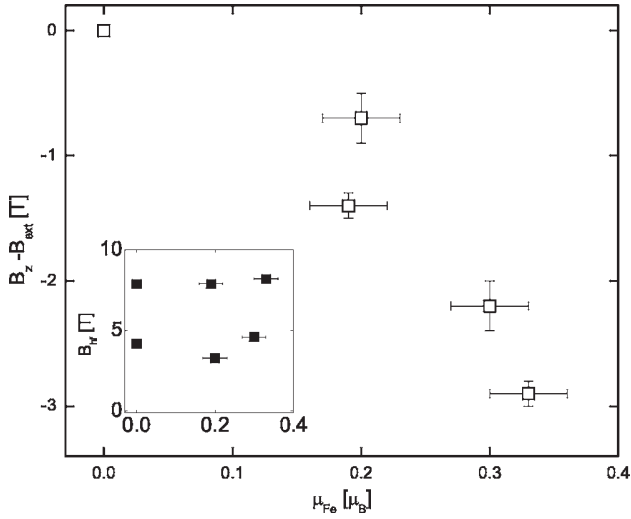


FIG. 12. The correlation between the average z component of a hyperfine field (corrected for an external field) and Fe magnetic moment (the inset shows a lack of correlation between the average h.m.f. and a magnetic moment). Open and full symbols correspond to the z component of the hyperfine field and the hyperfine field, respectively.

A considerable enhancement of the experimental value B_{hf}/μ_{Fe} (attaining values close to $30 \text{ T}/\mu_B$; see the end of Sec. V, in the Fe-Al system studied by us), can be explained as a signature of transformation from a ferromagnetic order to a nonferromagnetic one. Therefore one should expect that the magnetization should rather be correlated with the z component of the hyperfine field, B_z . This is indeed observed specifically in our alloy $\text{Fe}_{48}\text{Al}_{52}$; see Fig. 12.

The resonant polarimetric technique used in the present experiment allows one to gain some insight into the local magnetic moment arrangement. The shape of the $p(B_{hf})$ distribution can be discussed in terms of a local environment model. Such a model has been successfully used in many systems, including $\text{Fe}_{1-x}\text{Si}_x$, $\text{Fe}_{1-x}\text{Al}_x$, in the vicinity of $x = 0.25$ ^{9,66-70} and nonordered $\text{Fe}_{1-x}\text{V}_x$ alloys.⁷¹ In these systems the Fe atoms surrounded by $(n-k)$ Fe and k non-Fe atoms in the nearest coordination shell (consisting of n atoms) contribute to well-separated peaks in the $p(B_{hf})$ distribution.^{66-68,71} However, the existence of separated peaks related to well-defined local environments is not a rule, and non-Fe-rich Fe-Si and Fe-Al alloys serve as good examples of that.

It is reasonable to assume that the larger number of n.n. Fe atoms, the larger B_{hf} is observed. Next, from our EXAFS

TABLE III. Probabilities, local magnetic moment, μ , and its z component (both within $\pm 0.05 \mu_B$) in the external field of 0.2 and 1.1 T at $T = 13 \text{ K}$, for Fe surrounded by k Al and $(14-k)$ Fe atoms in the I and II coordination shells [see Eq. (9), $x_I = 0.8/8 = 0.1$, $x_{II} = 5.3/6$]. For an estimation of the total local magnetic moment, $12.5 \text{ T}/\mu_B$ was assumed.

k Al	0-4	5	6	7	8	9	10	11	12-14
$p(k)$	0.002	0.017	0.084	0.242	.368	0.213	0.062	0.010	0.001
μ (μ_B)	—	1.98	1.65	1.15	0.43	0.10	0.04	0.01	—
μ_z (μ_B) ($B_{ext} = 0.2 \text{ T}$)	—	0.73	0.61	0.40	0.06	0.00	0.03	0.03	—
μ_z (μ_B) ($B_{ext} = 1.1 \text{ T}$)	—	1.09	0.92	0.65	0.17	0.03	0.07	0.11	—

result it follows that the probabilities of finding Fe atom in the first and the second coordination shells are determined by $x_I = 0.8/8$ and $x_{II} = 5.3/6$, respectively. Assuming random distribution within the shells, the probability $P(k)$ that the iron atom is surrounded by $(14-k)$ Fe and k Al atoms in the two first coordination shells is

$$P(k) = \sum_{\substack{i,j \\ i+j=k}} \binom{8}{j} \binom{6}{i} x_I^{8-j} (1-x_I)^j x_{II}^{6-i} (1-x_{II})^i \quad (9)$$

see Table III. These assumptions allow one to divide the $p(B_{hf})$ into a few sections, each one having an area proportional to probability $P(k)$. The sectioning is displayed in Figs. 10(a) and 10(c) by vertical lines. By integration one can find the average field related to a given sector (or to the local environment),

$$\bar{B}(k) = \int_{B_k}^{B_{k+1}} p(B) B dB \left(\int_{B_k}^{B_{k+1}} p(B) dB \right)^{-1}, \quad (10)$$

where values of B_k can be found from

$$\int_0^{B_k} p(B) dB = \sum_{i=0}^k P(i). \quad (11)$$

The average fields estimated according to Eq. (10) are displayed in Fig. 13 by full symbols. In a similar way we can get the average value for the z component of the hyperfine field corresponding to the k th local environment,

$$\bar{B}_z(k) = \int_{B_k}^{B_{k+1}} p(B) B c_1(B) dB \left(\int_{B_k}^{B_{k+1}} p(B) dB \right)^{-1}. \quad (12)$$

The results are shown in Fig. 13 by empty symbols. Although from Eqs. (10) and (12) one gets formally 15 numerical values of $\bar{B}_z(k)$, those for $k = 0, 1, 2, 3$ and $12, 13, 14$ correspond to very small probability (9) and we do not regard them as reliable. As expected, the increase of the field from $B_{ext} = 0.2 \text{ T}$ to $B_{ext} = 1.1 \text{ T}$ results in an increase of the B_z and not the B_{hf} values; see the empty and the strongly overlapped full points in Fig. 13.

If the influence of the second coordination shell is neglected, the binomial distribution should be used instead of (9). The results of such treatment are shown in Fig. 10(e), Table IV, and Fig. 14.

Although the results presented in Figs. 13 and 14 suffer from a different kind of approximation, they are consistent with the following picture. Let (k_1, k_2) denote an Fe atom

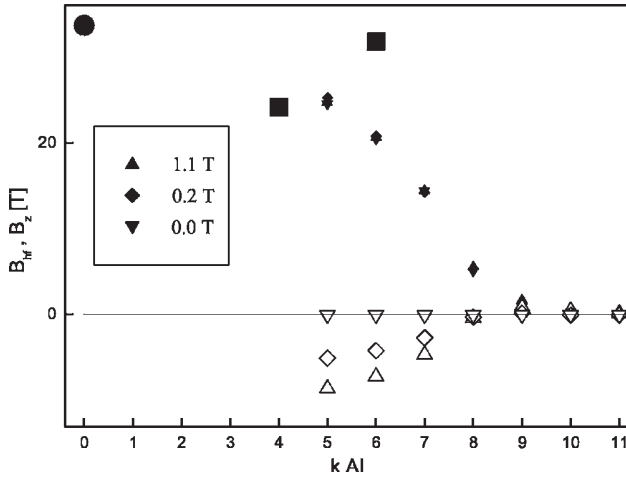


FIG. 13. Average h.m.f. and average z component of the field (not corrected for an external field) related to sectors from Fig. 10, assuming that contributions from the first and the second coordination shells to the hyperfine field are the same. Full symbols correspond to the hyperfine field; open ones to the z component of the hyperfine field. ● (Ref. 77), ■ (Ref. 64).

surrounded by k_1 Al atoms in the first coordination shell and k_2 Al atoms in the second coordination shell. Taking into account the most probable configurations, arbitrarily selected as those (k_1, k_2) for which the probability is greater than 5%, one observes for both models that (6,0) and (6,1) configurations have a clearly nonzero magnetic moment and a nonzero contribution to the magnetization. Configurations (8,1) and (8,2) have a clearly zero magnetic moment. Both models indicate that (7,1) has a nonzero magnetic moment and a very small contribution to the magnetization. The easiest explanation of this fact is that these configurations form a noncolinear arrangement of magnetic moments. Obviously, in Mössbauer polarimetry one measures the hyperfine field and its orientation. Thus, what can be concluded directly from our measurements is that we have evidence that the vector sum of the discussed nonzero fields is nearly zero. The noncolinear h.m.f. arrangement can be understood as a reflection of the noncolinearity of magnetic moments.

The (7,0) and (8,0) configurations could, in principle, be connected with noncolinearity. However, in light of rather poor evidence, one can also say that (7,0) configuration is connected with colinearly arranged nonzero magnetic moments, and (8,0) arrangement may have a zero magnetic moment.

TABLE IV. Probabilities, local magnetic moment, μ , and its z component (both within $\pm 0.05 \mu_B$) in the external field of 0.2 and 1.1 T at $T=13$ K, for Fe surrounded by k Al and $(8-k)$ Fe atoms in the first coordination shell. The binomial distribution of number of Fe, Al atoms with $x_F=0.8/8=0.1$ was assumed. The hyperfine constant $12.5 \text{ T}/\mu_B$ was used.

k Al	0–3	4	5	6	7	8
$p(k)$	4×10^{-4}	0.005	0.033	0.149	0.383	0.430
μ (μ_B)	—	2.19	1.88	1.48	0.74	0.14
μ_z (μ_B) ($B_{ext}=0.2$ T)	—	0.81	0.69	0.54	0.20	0.01
μ_z (μ_B) ($B_{ext}=1.1$ T)	—	1.18	1.04	0.85	0.38	0.04

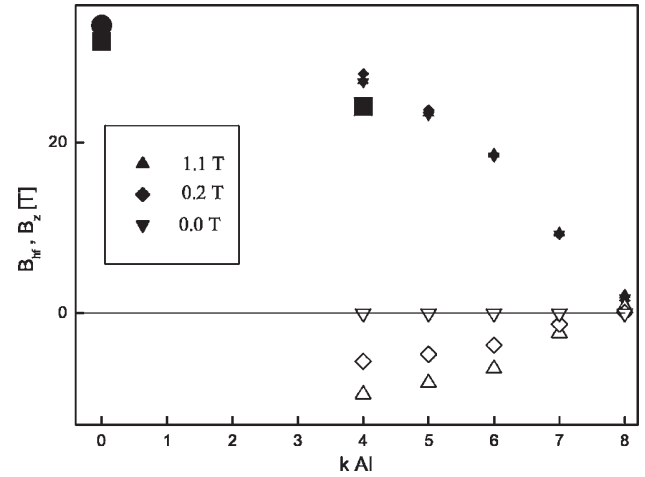


FIG. 14. The same as in Fig. 13, assuming that the contribution from the second coordination shell is neglected.

Our results are consistent with a picture in which Fe atoms with a large number of Al neighbors form a noncolinear local structure at low temperatures. Noncolinearity is probably caused by local anisotropy, which may be larger than the macroscopic anisotropy observed in a single crystal.⁴ Disordered moments cause large coercivity because of the interaction with a ferromagnetic matrix (neighboring magnetic moments). This is known as bias-type exchange anisotropy.⁷² Under an applied external field, a gradual metamagnetic type of reorientation occurs and magnetization slowly approaches saturation. At higher temperatures thermal excitations break the magnetic ordering in Al-rich surroundings and this results in the decrease of the coercivity. Indirectly, this is confirmed by a large (≈ 20 times) drop of coercive force as the temperature increases from 5 to 77 K, mentioned in Sec. V. One expects that the same external magnetic field will orient the ferromagnetic matrix more easily at higher (50 K) than at lower temperature ($T=13$ K). This is consistent with the larger value of the c_1 parameter that was obtained for $T=50$ K and with the maximum of magnetization observed during FC in the small magnetic field (see Fig. 3). A similar microscopic picture of the interaction was presented in Monte Carlo simulations of an Fe-Al system,¹⁹ where Fe atoms with six and more nearest neighbor Al atoms were found to be frustrated in an ordered ferromagnetic state and where chemical disorder introduced a spin-glass-like state in the region of critical concentration.

Two different distributions of hyperfine parameters may produce identical Mössbauer spectra. This leads to the ambi-

guity much discussed in the literature.^{73–75} Additional independent experimental information usually reduces this ambiguity. It has already been demonstrated that additional information received from the polarimetric method allows one to obtain the correct shape of the h.m.f. distribution.⁵³ In the described algorithm one should, in principle, estimate $c_2(B_{hf})$; see Eqs. (2a) and (2b). However, in the studied case we could not obtain reasonable information about the transverse component for such strongly overlapped spectra. One can show that fits of a similar quality can be obtained for a variety of c_2 values. Because information on transverse local magnetization is not available, we do not know whether we are dealing with an antiferromagnetic order (i.e., long-range order exists to some length scale), antiparallel arrangements of moments (some iron moments at random positions are oriented antiparallel to each other), or a disordered magnetic structure if all directions of magnetic moments are present. All three possibilities are consistent with the results of our measurements.

We hope that additional measurements in the field perpendicular to the \mathbf{k} vector or the use of linearly polarized radiation in which the intensity of lines 2 and 5 will be greatly enhanced, may reduce ambiguity.

The main conclusion that follows from the results presented in this report is that the arrangement of hyperfine magnetic fields is nonuniform. This kind of information could be obtained by the use of circularly polarized radiation only. The obtained result, that larger fields are better aligned in an externally applied magnetic field, is not strongly dependent on the details of data analysis. Indeed, some of the spectra were analyzed without using the transmission integral and under the assumption that the electric field gradient is zero. The main features of the $p(B_{hf})$ and $c_1(B_{hf})$ functions agree with those presented in Fig. 10.

Magnetization and Mössbauer data can be combined to obtain local magnetic moments of Fe. To estimate the z component of the magnetic moment in an external magnetic field we assume that it is proportional to $\bar{B}_z(k)$ and that the total contribution to magnetization of all Fe atoms is equal to the measured magnetization. The results are summarized in Tables III and IV.

VIII. RESUME

Combining magnetic, EXAFS, and Mössbauer polarimetric data, it was possible to get a consistent description of the arrangement of Fe magnetic moments in a $\text{Fe}_{48}\text{Al}_{52}$ alloy prepared in a structurally disordered state by mechanical grinding. The distribution of quadrupole splitting and isomer shift, determined in a RT experiment, was kept constant during low-temperature data evaluation, allowing only for the second-order Doppler shift. The Debye temperature used in EXAFS data evaluation and estimated in the diffraction experiment²² agrees with the second-order Doppler shift found in Mössbauer data evaluation. A full Hamiltonian was used for the exact treatment of a mixed magnetic dipole and electric quadrupole interaction. The transmission integral was used for treatment of the thickness effect, and the temperature dependence of the recoilless fraction was taken into account.

We have estimated the values of Fe magnetic moments as a function of the local environment. An increase of the number of Al in the two first coordination shells (bcc structure) causes a decrease of magnetic moments and a much faster decrease of the z component of the magnetic moment (the local contribution to the magnetization). Magnetic moments of iron in configurations (6,0) and (6,1), which can be considered as iron-rich clusters, form colinear arrangement. Configuration (7,1) was found as forming a noncolinear structure. Configurations (8,1) and (8,2) are so poor in iron that either no magnetic moment is formed on the central Fe atom, or the magnetic moment is below the detection limit of our technique. One should stress that such a detailed description of the magnetic moment arrangement would hardly be possible if an extensive combination of experimental methods had not been used in the present study.

The noncolinearity present at low temperatures explains the large coercivity, lack of saturation, and anomalously large ratio of the average h.m.f. to the magnetic moment in the range of critical concentration.

ACKNOWLEDGMENTS

The authors thank Dr. A. V. Korolyov for the magnetic measurements and the staff of SPring-8 for the maintenance of the facility of JASRI Grant No. 2002A0078NX-np.

*Also at The Sołtan Institute for Nuclear Studies, 05-400 Otwock-Świerk, Poland.

¹A. Arrott and H. Sato, Phys. Rev. **114**, 1420 (1959).

²H. Sato and A. Arrott, Phys. Rev. **114**, 1427 (1959).

³M. Shiga and Y. Nakamura, J. Phys. Soc. Jpn. **40**, 1295 (1976).

⁴H. Danan and H. Gengnagel, J. Appl. Phys. **39**, 678 (1968).

⁵G. P. Huffman, J. Appl. Phys. **42**, 1606 (1971).

⁶M. J. Besnus, A. Herr, and A. J. P. Meyer, J. Phys. F: Met. Phys. **F5**, 2138 (1975).

⁷A. Taylor and R. M. Jones, J. Phys. Chem. Solids **6**, 16 (1958).

⁸E. A. Friedman and W. J. Nicholson, J. Appl. Phys. **34**, 1048

(1963).

⁹G. P. Huffman and R. M. Fisher, J. Appl. Phys. **38**, 735 (1967).

¹⁰M. Shiga and Y. Nakamura, J. Physiol. Suppl. (Paris) **40**, C2 (1979).

¹¹M. Shiga, T. Kikawa, K. Sumiyama, and Y. Nakamura, J. Magn. Soc. Jpn. **9**, 187 (1985).

¹²N. I. Kulikov, A. V. Postnikov, G. Borstel, and J. Braun, Phys. Rev. B **59**, 6824 (1999).

¹³E. P. Yelsukov, E. V. Voronina, and V. A. Barinov, J. Magn. Mater. **115**, 271 (1992).

¹⁴J. Bogner, W. Steiner, M. Reissner, P. Mohn, P. Blaha, K.

- Schwarz, R. Krachler, H. Ipsier, and B. Sepiol, *Phys. Rev. B* **58**, 14922 (1998).
- ¹⁵D. R. Noakes, A. S. Arrott, M. G. Belk, S. C. Deevi, Q. Z. Huang, J. W. Lynn, R. D. Shull, and D. Wu, *Phys. Rev. Lett.* **91**, 217201 (2003).
- ¹⁶D. C. Mattis, *Phys. Lett.* **56A**, 421 (1976).
- ¹⁷A. K. Arzhnikov and L. V. Dobysheva, *J. Magn. Magn. Mater.* **117**, 87 (1992).
- ¹⁸A. K. Arzhnikov and L. V. Dobysheva, *Phys. Lett. A* **195**, 176 (2000).
- ¹⁹G. S. Grest, *Phys. Rev. B* **21**, 165 (1980).
- ²⁰B. E. Warren and B. L. Averbach, *J. Appl. Phys.* **21**, 595 (1950).
- ²¹E. Voronina, D. Guy, and T. Miyanaga, *Nucl. Instrum. Methods Phys. Res. B* **215**, 525 (2004).
- ²²H. W. Sheng, Y. H. Zhao, Z. Q. Hu, and K. Lu, *Phys. Rev. B* **56**, 2302 (1997).
- ²³S. I. Zabinsky, J. J. Rehr, A. Ankudinov, R. C. Albers, and M. J. Eller, *Phys. Rev. B* **52**, 2995 (1995).
- ²⁴Y. A. Babanov and V. R. Shvetsov, *Phys. Status Solidi B* **131**, K1 (1985).
- ²⁵Y. A. Babanov, V. V. Vasin, A. L. Ageev, and N. V. Ershov, *Phys. Status Solidi B* **105**, 747 (1981).
- ²⁶E. V. Voronina, V. Fomin, Y. Babanov, and E. P. Yelsukov, *Phys. Met. Metallogr.* **89**, 68 (2000).
- ²⁷T. Sikora, M. Jaouen, T. Girardeau, and J. Mimault, *Nucl. Instrum. Methods Phys. Res. B* **111**, 141 (1996).
- ²⁸H. Bakker, G. F. Zhou, and H. Yang, *Prog. Mater. Sci.* **159**, 39 (1995).
- ²⁹C. Suryanarayana, *Prog. Mater. Sci.* **46**, 1 (2001).
- ³⁰V. G. Harris, D. J. Fatemi, K. B. Hathaway, Q. Huang, A. Mohan, and G. J. Long, *J. Appl. Phys.* **85**, 5181 (1999).
- ³¹J. M. Cowley, *J. Appl. Phys.* **21**, 24 (1950).
- ³²H. D. Pfannes and H. Fischer, *Appl. Phys.* **13**, 317 (1977).
- ³³H. D. Pfannes and R. M. Paniago, *Hyperfine Interact.* **71**, 1499 (1992).
- ³⁴K. Szymański, *Nucl. Instrum. Methods Phys. Res. B* **134**, 405 (1998).
- ³⁵K. Szymański, L. Dobrzyński, B. Prus, and M. J. Cooper, *Nucl. Instrum. Methods Phys. Res. B* **119**, 438 (1996).
- ³⁶K. Szymański, D. Satuła, L. Dobrzyński, K. Perzyńska, M. Bieracka, and P. Zaleski, *J. Magn. Magn. Mater.* **236**, 56 (2001).
- ³⁷C. L'abbé, J. Meersschant, W. Sturhahn, J. S. Jiang, T. S. Toellner, E. E. Alp, and S. D. Bader, *Phys. Rev. Lett.* **93**, 037201 (2004).
- ³⁸H. Frauenfelder, D. E. Nagle, R. D. Taylor, D. R. F. Cochran, and W. M. Visscher, *Phys. Rev.* **126**, 1065 (1962).
- ³⁹J. M. Greneche and F. Varret, *J. Phys. (France) Lett.* **43**, L233 (1982).
- ⁴⁰J. M. Greneche and F. Varret, *J. Phys. C* **15**, 5333 (1982).
- ⁴¹U. Bergmann, S. D. Shastri, D. P. Siddons, B. W. Batterman, and J. B. Hastings, *Phys. Rev. B* **50**, 5957 (1994).
- ⁴²S. Margulies and J. R. Ehrman, *Nucl. Instrum. Methods* **12**, 131 (1961).
- ⁴³S. Shtrikman, *Solid State Commun.* **5**, 701 (1967).
- ⁴⁴J. P. Stampfel and P. A. Flinn, *Moessbauer Eff. Methodol.* **6**, 95 (1971).
- ⁴⁵F. Varret, P. Imbert, G. Jehanno, and R. Saint-James, *Phys. Status Solidi A* **27**, K99 (1975).
- ⁴⁶K. Szymański, D. Satuła, and L. Dobrzyński, *J. Phys.: Condens. Matter* **11**, 881 (1999).
- ⁴⁷K. Szymański, D. Satuła, and L. Dobrzyński, *Hyperfine Interact.* **156/157**, 21 (2004).
- ⁴⁸R. Zimmermann, *Chem. Phys. Lett.* **34**, 416 (1975).
- ⁴⁹U. Gonser and H. Fischer, in *Mössbauer Spectroscopy II* (Springer-Verlag, Berlin, 1981), p. 99.
- ⁵⁰R. Zimmermann, in *Advances in Mössbauer Spectroscopy Applications to Physics, Chemistry and Biology* (Elsevier, Amsterdam, 1983).
- ⁵¹H. Spiering, in *Mössbauer Spectroscopy Applied to Inorganic Chemistry* (Plenum, New York, 1984), Vol. 1, p. 77.
- ⁵²K. Szymański, *J. Phys.: Condens. Matter* **12**, 7495 (2000).
- ⁵³K. Szymański, *Nucl. Instrum. Methods Phys. Res. B* **171**, 515 (2000).
- ⁵⁴N. Blaes, H. Fischer, and U. Gonser, *Nucl. Instrum. Methods Phys. Res. B* **9**, 201 (1985).
- ⁵⁵T. M. Lin and R. S. Preston, *Moessbauer Eff. Methodol.* **9**, 25 (1974).
- ⁵⁶N. N. Greenwood and T. C. Gibb, *Mössbauer Spectroscopy* (Chapman and Hall Ltd., London, 1971).
- ⁵⁷B. D. Josephson, *Phys. Rev. Lett.* **4**, 341 (1960).
- ⁵⁸S. S. Hanna, J. Heberle, G. J. Perlow, R. S. Preston, and D. H. Vincent, *Phys. Rev. Lett.* **4**, 513 (1960).
- ⁵⁹B. Kolk, in *Studies of Dynamical properties of Solids with the Mössbauer Effect* (North-Holland, Amsterdam, 1984).
- ⁶⁰K. N. Shrivastava, *Phys. Rev. B* **1**, 955 (1970).
- ⁶¹E. P. Yelsukov, Y. N. Vorobyov, T. I. Arbusova, and I. B. Smolyak, *J. Magn. Magn. Mater.* **130**, 44 (1994).
- ⁶²P. Panissod, J. Durand, and J. I. Budnick, *Nucl. Instrum. Methods Phys. Res.* **199**, 99 (1982).
- ⁶³A. K. Arzhnikov and L. V. Dobysheva, *Phys. Rev. B* **62**, 5324 (2000).
- ⁶⁴C. E. Johnson, M. S. Ridout, and T. E. Cranshaw, *Proc. Phys. Soc. Jpn.* **81**, 1079 (1963).
- ⁶⁵A. K. Arzhnikov, L. V. Dobysheva, and F. Brouers, *Phys. Solid State* **42**, 89 (2000).
- ⁶⁶M. B. Stearns, *Phys. Rev.* **129**, 1136 (1963).
- ⁶⁷M. B. Stearns, *J. Appl. Phys.* **35**, 1095 (1964).
- ⁶⁸V. Niculescu, T. J. Burch, and J. I. Budnick, *J. Magn. Magn. Mater.* **39**, 223 (1983).
- ⁶⁹P. A. Beck, *Metall. Trans.* **2**, 2915 (1971).
- ⁷⁰B. Fultz, Z. Q. Gao, and H. H. Hamdeh, *Hyperfine Interact.* **54**, 521 (1990).
- ⁷¹J. C. Krause, J. Schaf, M. I. da Costa, Jr., and C. Paduani, *Phys. Rev. B* **61**, 6196 (2000).
- ⁷²A. E. Berkowitz and K. Takano, *J. Magn. Magn. Mater.* **200**, 552 (1999).
- ⁷³G. L. Caër, J. M. Dubois, H. Fischer, I. U. Gonser, and H. G. Wagner, *Nucl. Instrum. Methods Phys. Res. B* **5**, 25 (1984).
- ⁷⁴G. L. Caër and R. A. Brand, *J. Phys.: Condens. Matter* **10**, 10715 (1998).
- ⁷⁵D. G. Rancourt, in *Mössbauer Spectroscopy Applied to Magnetism and Materials Science* (Plenum, New York, 1996), Vol. 5, p. 105.
- ⁷⁶E. P. Yelsukov, E. V. Voronina, A. V. Korolyov, and G. N. Konygin, *NATO Sci. Ser. II Math. Phys. Chem.* **94**, 93 (2003).
- ⁷⁷C. E. Violet and D. N. Pipkorn, *J. Appl. Phys.* **42**, 4339 (1971).
- ⁷⁸R. S. Preston, S. S. Hanna, and J. Heberle, *Phys. Rev.* **128**, 2207 (1962).

P10

Magnetization distribution in nanocrystalline $\text{Fe}_{0.48}\text{Al}_{0.52}$

K. SZYMAŃSKI^{1*}, L. DOBRZYŃSKI^{1,2}, D. SATUŁA¹,
E. VORONINA³, E. P. YELSUKOV³

¹Institute of Experimental Physics, University of Białystok, 15-424 Białystok, Poland

²The Sołtan Institute for Nuclear Studies, 05-400 Otwock-Świerk, Poland

³Physical-Technical Institute of the Ural Division of Russian Academy of Sciences, Izhevsk 426000, Russia

Mössbauer polarimetry is used for investigating the orientation of Fe magnetic moments in the nanocrystalline $\text{Fe}_{0.48}\text{Al}_{0.52}$ disordered alloy prepared by mechanical grinding. Local Fe magnetic moments and their contributions to the net magnetization at selected external fields and temperatures were estimated. It was found that the components of the Fe magnetic moments parallel to the net magnetizations reduce their values much faster with an increasing number of neighbouring Al atoms than the total iron moments.

Key words: Mössbauer polarimetry; magnetic moment; nanocrystalline $\text{Fe}_{0.48}\text{Al}_{0.52}$

1. Introduction

Structurally ordered alloys with Al concentrations between 35% and 43% and with equiatomic composition have been suspected of the presence of antiferromagnetic order [1–5]. Quite recent neutron diffraction data for *bcc*-ordered Fe–Al with Al concentrations of 34–43 at. % [6] showed the presence of incommensurate spin density waves. It has been found earlier that ferromagnetic order can exist close to FeAl composition [7], and that supposedly antiferromagnetic or paramagnetic configurations can change to ferromagnetic upon simple filing [1, 8–11]. Ferromagnetism has also been detected in alloys with Al concentrations larger than 50 at. % [8, 12] and in the concentration range 40–60 at. % [13].

The ratio of hyperfine fields and magnetic moments (or magnetization) in many Fe-based ferromagnetic systems is in the range 10.0–15.0 T/ μ_B [14–16]. Magnetization data for disordered Fe–Al alloys [11, 17], can be compared with the average hyperfine magnetic field (h.m.f.) obtained from Mössbauer experiments [8, 12, 17]. The ratio is an-

*Corresponding author, e-mail: kszym@alpha.uwb.edu.pl

omalously high, about $30 \text{ T}/\mu_{\text{B}}$ for concentrations close to equiatomic, while it is about $12.0\text{--}13.5 \text{ T}/\mu_{\text{B}}$ in ferromagnetic alloys with Al concentrations less than 40 at. %.

For systems with atomic and spin disorders – in particular for non-ordered metal systems with RKKY interaction – Mattis has considered a model in which spin–spin interactions were random in sign but did not result in frustrations [18]. The spin system was considered to be composed of two subsystems with randomly distributed antiparallel spins, which form the so-called Mattis phase. The magnetisation behaviour of the Fe–Al system and the ideas found in Refs. [18–20] indicate that concentrated Fe–Al alloys could exhibit the Mattis phase, no experimental support, however, has been reported so far.

Studies of Fe–Al alloys by the Monte Carlo techniques [21] in the Al concentration range $0.25 < x < 0.50$ showed that it was possible to qualitatively account for the transformation of the magnetic state from a ferromagnetic one to a certain spin glass state at about 34% Al using the indirect exchange model [1]. A peculiar feature of this spin-glass is the fact that frustrations arise from the positional disorder of Fe and Al atoms.

These controversial findings, and the apparent impact of various defects and inhomogeneities on the magnetic structure of bulk and nanocrystalline alloys, require more detailed investigations that will elucidate the nature of magnetism in this system. This paper reports the studies of nanocrystalline Fe–Al alloys in the concentration range close to the onset of ferromagnetism by the Mössbauer technique with circularly polarized monochromatic radiation. Polarized radiation has been widely used in investigating magnetically ordered systems, for an extended review see Ref. [22]. Circularly polarized radiation has the advantage of being sensitive to the sign of the h.m.f. Our observations strongly suggest that a non-collinear magnetic order must exist in the sample studied.

2. Sample

Fe–Al ingot was synthesized from high-purity components (99.99 % Fe and 99.99% Al) in an induction furnace in Ar atmosphere, then homogenized in a vacuum furnace at 1400 K for 6 h. The chemical analysis showed that the Al concentration was 52.0 ± 0.5 at. %. The ingots were milled and a fraction with particle sizes lower than $300 \mu\text{m}$ was used for further mechanical treatment in a planetary ball mill with vials and balls made of tungsten carbide. Mechanical grinding was performed in an inert gas atmosphere. The milling time was adjusted to provide a disordered state in the Fe–Al alloys [17]. The obtained sample exhibited a single *bcc* phase with the lattice parameter $0.2918(4)$ nm. The X-ray diffraction pattern consists of the broadened peaks (110), (200), (211), and (220) of the *bcc* structure. The analysis of the shape of the diffraction lines using the harmonic analysis [23] lead to the conclusion that the mean grain size of the alloy is $4.0(3)$ nm.

3. Mössbauer polarimetric measurements

The absorbers were placed inside one of the rare earth magnets, producing an axially symmetric field perpendicular to the absorber surface and parallel to the gamma rays. The measurements were performed at temperatures of 13, 50, and 298 K and external fields between 0 and 1.1 T, see the example in Fig. 1.

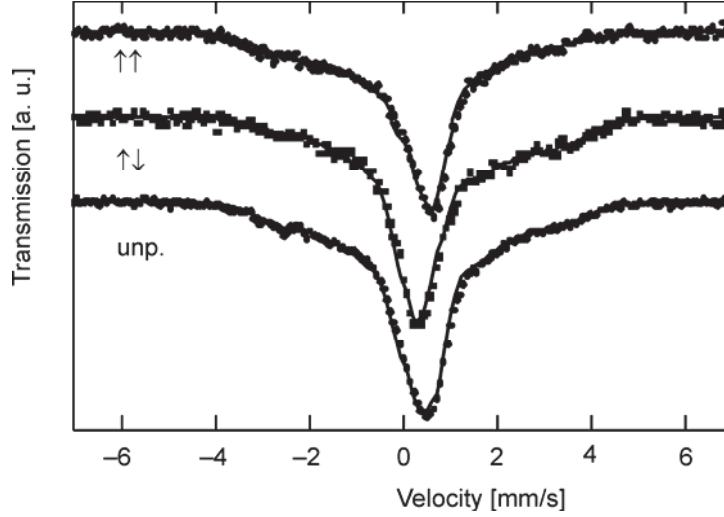


Fig. 1. An example of the Mössbauer spectra recorded at $T = 13$ K with polarized and unpolarized radiation in an axial, externally applied magnetic field of 1.1 T. The arrows $\uparrow\uparrow$ and $\uparrow\downarrow$ indicate two opposite circular polarizations. Solid lines represent the results of the simultaneous fitting the h.m.fs to all the recorded spectra

A full Hamiltonian was used for treating the mixed magnetic dipole and electric quadrupole interaction. The transmission integral was used to treat thickness effects, and the temperature dependence of the f -factor was taken into account. To analyse the low-temperature data, we assumed the same isomer shift and electric field gradient, as well as their probabilities determined at room temperature. We allowed only the second order Doppler shift and the appearance of the h.m.f. distribution. The principles of the adopted polarimetric method are given in Ref. [24], while details of the construction of the source of circularly polarized radiation in Refs. [25, 26].

An experiment with circularly polarized radiation is sensitive to the angular average $\langle \gamma_r \cdot \mathbf{m} \rangle$, where \mathbf{m} is a unit vector parallel to the local h.m.f., \mathbf{B}_{hf} , γ_r is the Cartesian vector ($r = x, y, z$) and the brackets $\langle \rangle$ denote angular averaging with the magnetic texture function $P(\Omega)$:

$$\langle \gamma_r \cdot \mathbf{m} \rangle = \int_{4\pi} \gamma_r \cdot \mathbf{m} P(\Omega) d\Omega \quad (1)$$

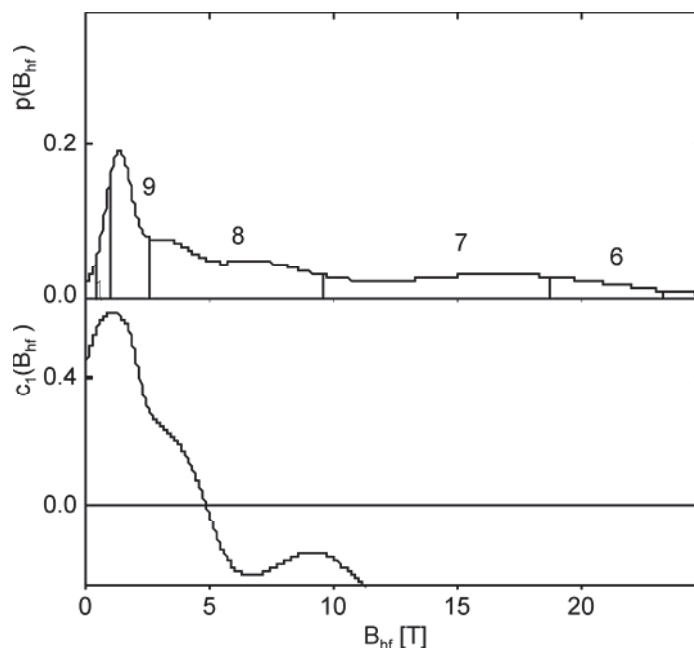


Fig. 2. An example of the distribution of h.m.f. obtained from experiment (up) and the h.m.f. dependence of the average cosine between the h.m.f. vector and magnetization (down) measured at $T = 13$ K and $B_{\text{ext}} = 1.1$ T. The vertical bars split the $p(B_{\text{hf}})$ distribution into sectors numbered by $k = \dots, 9, 8, 7 \dots$, for which the two first coordination shells are taken into account (cf. Eq. (2))

In particular, one can obtain the value of $c_1 B_{\text{hf}}$, which is an average component of the h.m.f. along photon directions. In the case of α -Fe, the h.m.f. is antiparallel to the direction of the magnetic moment of iron atoms [27], so the c_1 parameter is negative. Negative values of c_1 for our sample are observed only for hyperfine fields larger than about 5 T (Fig. 2). Figure 2 also shows that a relatively large probability $p(B_{\text{hf}})$ is observed in the region close to $B_{\text{hf}} = 5$ T, much above the intensity of the external field. It is thus reasonable to suppose that B_{hf} in this region corresponds to the Fe atoms with nonzero magnetic moments. If this is so, then a nearly zero value of the c_1 parameter in Fig. 2 indicates that these moments, on average, do not contribute to the total magnetization.

4. Discussion and conclusions

A considerable enhancement of the experimental value $B_{\text{hf}}/\sigma_{\text{Fe}}$ (attaining values close to $30 \text{ T}/\mu_{\text{B}}$) in the studied Fe–Al system with respect to the values calculated for collinear systems can be explained by a transformation from ferromagnetic to non-ferromagnetic order. One should expect that the magnetization should be correlated with the z -th component of the h.m.f., B_z . This is indeed observed in our alloy $\text{Fe}_{0.48}\text{Al}_{0.52}$ (Fig. 3).

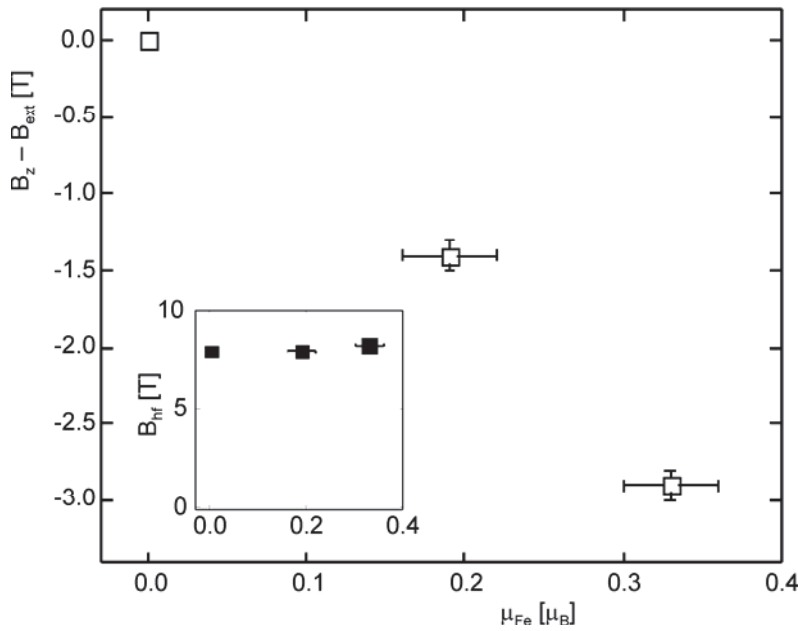


Fig. 3. Correlation between the average z -component of the h.m.f. (corrected to the external field) and the Fe magnetic moment (the inset shows a lack of correlation between the average h.m.f. and magnetic moment). Open and full symbols correspond to the z -component of the h.m.f. and the h.m.f. itself, respectively

It is reasonable to assume that the larger number of Fe atoms, the larger the observed B_{hf} . Next, it follows from EXAFS results [28] that the probabilities of finding the Fe atom in the first (I) and the second (II) coordination shells are given by $x_I = 0.10$ and $x_{II} = 0.883$, respectively. Assuming random distributions within the shells, the probability $P(k)$ that an iron atom is surrounded by $(14 - k)$ Fe and k Al atoms in the two first coordination shells is:

$$P(k) = \sum_{\substack{i,j \\ i+j=k}} \binom{8}{j} \binom{6}{i} x_I^{8-j} (1-x_I)^j x_{II}^{6-i} (1-x_{II})^i \quad (2)$$

These assumptions allow one to divide $p(B_{hf})$ into a few sections, each having the area proportional to the probability $P(k)$. The sectioning is displayed in Fig. 2 by vertical lines. The average fields estimated for each section are displayed in Fig. 4 by full symbols, while the z -components of the fields by open symbols. As expected, an increase of the field from $B_{ext} = 0.2$ T to $B_{ext} = 1.1$ T results in an increase of B_z and not B_{hf} (see the open and the overlapping full points in Fig. 4). The average $\bar{B}(k)$ for $k = 6$ (Fig. 4) is slightly above the value related to ordered Fe_3Al at low temperature [29].

It should be noted that Eq. (2) is valid under the assumption that the contributions of neighbouring atoms from the I and II coordination shells are the same, which is an approximation. The opposite approximation, in which the influence of the II coordination shell is neglected, can be made by using the binomial distribution instead of Eq. (2). The results of such treatment exhibit similar features and are not shown here (average $\bar{B}(k)$ for $k = 4$ is slightly below the value related to ordered Fe_3Al reported in [29]).

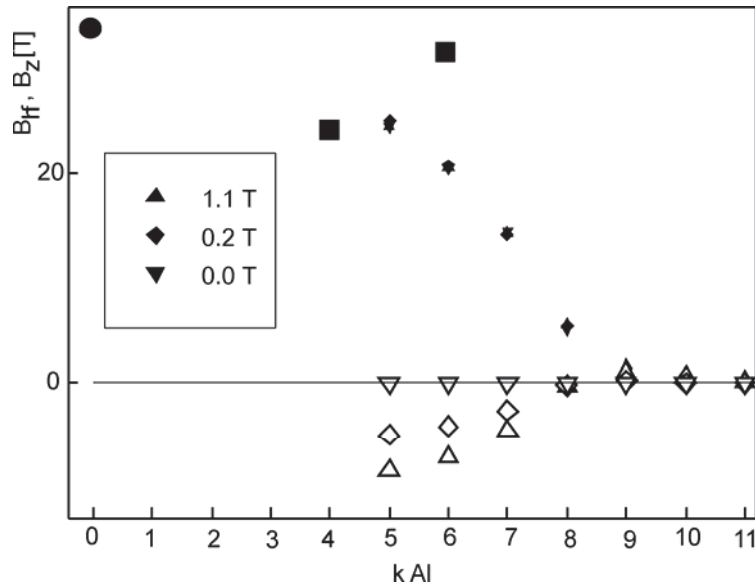


Fig. 4 Average h.m.f. and average z -th component of the field (not corrected for the external field) related to the sectors from Fig. 2, under the assumption that contributions from the first and the second coordination shells to the h.m.f. are the same. Full symbols correspond to the h.m.f., open symbols to the z -component of the h.m.f., \bullet – Ref [16], \blacksquare – Ref. [29]

The magnetization and Mössbauer data can be combined to obtain the local magnetic moments of Fe. To estimate the z -th component of the magnetic moment in the external magnetic field, we assume that it is proportional to $\bar{B}_z(k)$ and that the total contribution to the magnetization of all Fe atoms is equal to the measured magnetization. The two most important results are as follows.

An increase of the number of Al atoms in the two first coordination shells (*bcc* structure) causes a decrease of the magnetic moments and a much faster decrease of the z -component of the magnetic moments (local contribution to magnetization). Configuration (7, 1) was found as the most suitable for forming a non-collinear structure, where (k_1, k_2) denotes a Fe atom surrounded by k_1 Al atoms in the I coordination shell and k_2 Al atoms in the II coordination shell. It should be stressed that such a detailed description of the magnetic moment arrangement would hardly be possible if not for the extensive combination of experimental methods used in the present studies.

References

- [1] ARROTT A., SATO H., Phys. Rev., 114 (1959), 1420.
- [2] SATO H., ARROTT A., Phys. Rev., 114 (1959), 1427.
- [3] DANAN H., GENGNAGEL H., J. Appl. Phys., 39 (1968), 678.
- [4] HUFFMAN G.P., J. Appl. Phys., 42 (1971), 1606.
- [5] SHIGA M., NAKAMURA Y., J. Phys., Soc. Japan, 40 (1976), 1295.
- [6] NOAKES D.R., ARROTT A.S., BELK M.G., DEEVI S.C., HUANG Q.Z., LYNNJ W., SHULL R.D., WU, D., Phys. Rev. Lett., 91 (2003), 217201.
- [7] SHIGA M., NAKAMURA Y., J. Phys. Soc Japan, 40 (1976), 1295.
- [8] BESNUS M.J., HERR A., MEYER A.J.P., J. Phys. F5, (1975), 2138.
- [9] TAYLOR A., JONES R.M., J. Phys. Chem. Solids, 6 (1958), 16.
- [10] FRIEDMAN E.A., NICHOLSON W.J., J. Appl. Phys., 34 (1963), 1048.
- [11] HUFFMAN G.P., FISHER R.M., J. Appl. Phys., 38 (1967), 735.
- [12] SHIGA M., KIKAWA T., SUMIYAMA K., NAKAMURA Y., J. Magn. Soc. Japan, 9 (1985), 187.
- [13] KULIKOV N.I., POSTNIKOV A.V., BORSTEL G., BRAUN J., Phys. Rev. B, 59 (1999), 6824.
- [14] YELSUKOV E.P., VOROBYOV YU.N., ARBUSOVA T.I., SMOLYAK, I.B., J. Magn. Magn. Mater., 130 (1994), 44.
- [15] PANISSOD P., DURAND J., BUDNICK J.I., Nucl. Instr. Meth., 199 (1982), 99.
- [16] VIOLET C.E., PIPKORN D.N., J., Appl. Phys., 42, (1971), 4339.
- [17] YELSUKOV E.P., VORONINA E.V., BARINOV V.A., J. Magn. Magn. Mater., 115 (1992), 271.
- [18] MATTIS D.C., Phys. Lett., 56A (1976), 421.
- [19] ARZHNIKOV A.K., DOBYSHEVA L.V., J. Magn. Magn. Mater., 117 (1992), 87.
- [20] ARZHNIKOV A.K., DOBYSHEVA L.V., Phys. Lett., A, 195 (1994), 176.
- [21] GRETT G.S., Phys. Rev. B, 21 (1980), 165.
- [22] GONSER U., FISCHER H., [in:] *Mössbauer Spectroscopy II*, Springer-Verlag, Berlin, 1981.
- [23] WARREN B.E., B.L.AVERBACH B.L., J. Appl. Phys., 21 (1950), 595.
- [24] SZYMAŃSKI K., SATUŁA D., DOBRZYŃSKI L., Hyp. Int., 156/157 (2004), 21.
- [25] SZYMAŃSKI K., DOBRZYŃSKI L., PRUS B., COOPER M.J., Nucl. Instr. Meth. B, 119 (1996), 438.
- [26] SZYMAŃSKI K., Nucl. Instr. Meth. B, 134 (1998), 405.
- [27] HANNA S.S., HEBERLE J., LITTLEJOHN C., PERLOW G.J., PRESTON R.S., VINCENT D.H., Phys. Rev. Lett., 4 (1960), 513.
- [28] SZYMAŃSKI K., DOBRZYŃSKI L., SATUŁA D., VORONINA E., YELSUKOV E.P., MIYANAGA T., Phys. Rev. B, 72 (2005), 104409.
- [29] JOHNSON C.E., RIDOUT M.S., CRANSHAW T.E., Proc. Phys. Soc., 81 (1963), 1079.

Received 1 June 2005
Revised 10 October 2005

P11

Interpretation of the Mössbauer Spectroscopy Data by the Maximum Entropy Method

L. Dobrzyński*, A. Holas† and D. Satuła and K. Szymański**

**Institute of Experimental Physics, University of Białystok, 41 Lipowa, 15-424 Białystok, Poland
The Soltan Institute for Nuclear Studies, 05-400 Otwock-Świerk, Poland*

†*Institute of Physical Chemistry of the Polish Academy of Sciences, 44/52 Kasprzaka, 01-224
Warsaw, Poland*

***Institute of Experimental Physics, University of Białystok, 41 Lipowa, 15-424 Białystok, Poland*

Abstract. A reconstruction of the 3-dimensional distributions of the magnetic hyperfine field, quadrupole splitting and isomer shift from the measured 1-dimensional Mössbauer spectrum is extremely difficult in general case. The paper shows that reliable reconstruction can be made by means of the Maximum Entropy Method without prior assumptions concerning correlations between the parameters of interest. We also show how the prior should be chosen in order to arrive at the physically meaningful results.

Key Words: Bayesian logic, Maximum Entropy Method, Mössbauer spectra

1. INTRODUCTION

The Maximum Entropy Method (MEM) [1] was already used to analyze many spectroscopic data [2, 3, 4, 5]. This powerful method was not extensively applied to the analysis of the Mössbauer spectra where presence of the distribution of hyperfine field parameters makes the spectra complicated and the spectra interpretation becomes ambiguous because of assumptions one makes in order to get the hyperfine field distributions. The one dimensional Mössbauer spectrum contains information on the distribution of the hyperfine magnetic field (B), quadrupole splitting (QS) and the isomer shift (IS), not speaking about orientations of the hyperfine magnetic fields, which cause often a lot of problems in some experiments. We checked recently [6] that rather complicated 2-dimensional distributions in (B, IS) space can be reconstructed from the Mössbauer spectra by MEM technique. This paper deals with more difficult cases. In spite of the fact that the 3-dimensional reconstruction of (B, QS, IS) distribution from a single spectrum seems almost impossible, a well-known inherent ambiguity problem [7, 8] consisting in the fact that many distributions of the hyperfine field can fit well to the experimental spectrum, makes the situation even worse.

In short, when the Zeeman interaction is dominating, the Mössbauer spectrum consists of lines measured as a function of the source velocity $V(k)$, where $k = 1, 2, \dots, N$ with N being usually 256. In typical experiment with ^{57}Fe -based absorption, for given hyperfine magnetic field B (in Tesla), isomer shift IS (in mm/s) and quadrupole splitting QS (in

CP872, *Bayesian Inference and Maximum Entropy Methods in Science and Engineering,*
26th International Workshop, edited by Ali Mohammad-Djafari

© 2006 American Institute of Physics 978-0-7354-0371-0/06/\$23.00

mm/s), the recoilless absorption occurs at six velocities $\{v_i\}$ (Zeeman's sextet) linearly dependent on B , QS and IS , see, e.g., [6, 7, 8, 9]. In the case of infinitely thin absorber, the line intensities I_i should be as 3:2:1:1:2:3. More general formulas are given in ref. [9].

A given i th line contributes to the k th channel in the velocity spectrum the intensity proportional to

$$J_k = \frac{I_i}{(V(k) - v_i)^2 + (\Gamma/2)^2}, \quad (1)$$

where the natural width, Γ , of the line from Mössbauer source is 0.22–0.25 mm/s (in our calculations 0.24 mm/s was chosen). When the electric field gradient accompanies low magnetic hyperfine field, eight instead of six lines appear in the spectrum. The intensities have to be calculated from the solution of the so-called full Hamiltonian. In order not to complicate further considerations we shall not deal with this kind of complication, neither with another one consisting in the spectra distortions due to the finite thickness of an absorber or its possible magnetic texture.

There exist methods of reconstructing the hyperfine magnetic field distribution [10, 11, 12, 13, 14, 15, 16] from measured spectra. However, in order to make such reconstruction, one has usually to assume certain correlation between the parameters B , IS , and QS . To the best of the authors knowledge, there is no code enabling one to get, e.g., the distributions of B and IS independently of each other. Our earlier paper [6] showed that this can be done when the analysis is carried out by means of the Maximum Entropy Method. The first successful attempt to use this method for a single parameter distribution was published by Brand and Le Caër [17]. Dou et al. [18] used Bayesian inference theory to obtain the distribution of one parameter B assuming however a linear coupling of two other parameters (IS and QS) to B .

2. MAXIMUM ENTROPY METHOD

Assume that the whole 3-dimensional space of parameters was divided into pixels and the value ρ_j denotes the probability of having the values of these parameters corresponding to this particular pixel. Because the line intensities are linear in the probabilities, the intensities W_k measured (with uncertainties σ_k) at k th velocity channel will be described theoretically by:

$$T_k = \sum_{j=1}^{N_{pix}} r_{kj} \rho_j, \quad \text{where } k = 1, 2, \dots, N. \quad (2)$$

The transformation matrix $\{r_{kj}\}$ can easily be evaluated (see references given in the Introduction). We consider the distribution $\rho_j = \rho_{B, QS, IS}$, which means that the index j denotes a collection of the three indices corresponding to the variables B , QS and IS , respectively. In other words three-dimensional matrix $\{\rho_j\}$ of the probability distribution is written in eqs. (2) and (4) as a single row.

As usual one is maximizing the Lagrangian [19]:

$$L = \alpha S - \frac{1}{2} \chi^2 \quad (3)$$

under an additional constraint of normalization of the distribution $\{\rho_j\}$. In eq. (3)

$$S = - \sum_{j=1}^{N_{pix}} \rho_j \ln(\rho_j / \rho_{0j}) \quad (4)$$

and

$$\chi^2 = \sum_k \frac{1}{\sigma_k^2} (W_k - T_k)^2. \quad (5)$$

In eq. (4), ρ_{0j} denotes a prior (a model). The final equations to solve are of usual type

$$\rho_j = \frac{\rho_{0j} \exp\left(-\frac{1}{2\alpha} \frac{\partial \chi^2}{\partial \rho_j}\right)}{\sum_{j'=1}^{N_{pix}} \rho_{0j'} \exp\left(-\frac{1}{2\alpha} \frac{\partial \chi^2}{\partial \rho_{j'}}\right)}, \quad j = 1, 2, \dots, N_{pix}. \quad (6)$$

During calculations special care is taken to ensure the equality of the sum of measured intensities W_k and the sum of intensities T_k as calculated from eq. (2) for the distribution $\{\rho_j\}$.

3. AMBIGUITY PROBLEM IN THE CASE OF PARAMAGNETIC SPECTRA

Initially, the first goal of the analysis was to study the distribution of (QS, IS) parameters in $UF\text{e}_5\text{Sn}$, for which the Mössbauer spectrum was measured in paramagnetic phase [20], in which $B = 0$. In the experiment [19] well defined two quadrupole doublets were found, and from the conventional approach to the Mössbauer spectra analysis the situation looked simple and clear. The intensity ratio, appr. 4:1, of the doublets was as expected on the basis of the iron distribution among different crystallographic sites. However, the distribution obtained by MEM was unexpectedly much richer, so we decided to study the situation of simulated two doublets: $(QS, IS) = (0.287, -0.064)$ and $(0.235, 0.115)$ (all parameters are expressed in mm/s and are close to the ones found in [19]). Fig. 1A presents the simulated spectrum consisting of these doublets. The Maximum Entropy Method with the uniform prior gave again very rich landscape of $P(QS, IS)$, see Fig. 1B, almost identical with the one obtained from the experimental spectrum. It could thus seem at first that MEM produces simply wrong answers. This, however is not the case. In fact, one can easily calculate that the landscape seen in Fig. 1B shows all possible combinations of doublets and singlets which could explain the measured spectrum, and satisfy the condition of the maximum of the entropy S . The symmetry with respect to the change of the sign of QS derives simply from the absorption cross section.

Obviously, the aforementioned solution consisting of the two doublets only is hidden among other possibilities considered by MEM. In order to get unique solution within the framework of MEM one thus has either to know some physical constraints or try some tricks. In the particular case considered by us we see that the first doublet is seen in Fig.

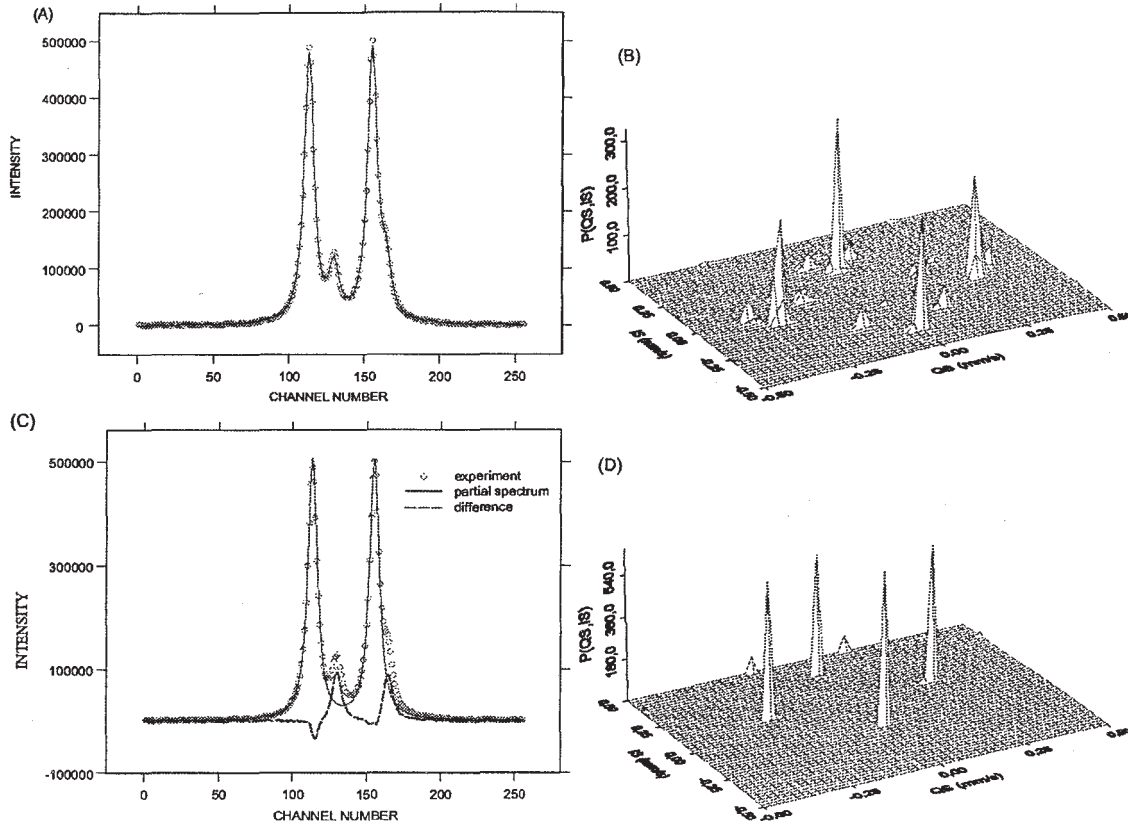


FIGURE 1. Simulated Mössbauer spectrum close to the experimentally observed for UFe_5Sn at room temperature [19]. (A) simulated (points) and reconstructed (solid line) spectrum; (B) reconstruction using uniform prior; (C) the spectrum corresponding to the strongest peak (solid line) and the difference spectrum (dashed line); (D) reconstruction from the difference spectrum.

1B with the highest intensity, i.e. it is found to be most likely. Therefore one can use it for calculating the Mössbauer spectrum which would result for this doublet only, and find its intensity so to get the best agreement with the measured spectrum in the sense of the least-square method. Next this partial spectrum can be subtracted from the total one, so the difference spectrum shown in Fig. 1C is obtained. There is a small narrow negative dip in the difference spectrum which shows that the line position or/and shape was not fitted precisely. This however, may well be due to the grid used and does not affect the final result. The MEM analysis of the difference spectrum leaves no doubts that in the total spectrum there is no more than another doublet, see Fig. 1D, in full agreement with what would be obtained from conventional analysis of the Mössbauer data. What we see in the Fig. 1D is equivalence of the doublet to two Lorentzian lines at $QS = 0$, and symmetric solution with respect to the $QS = 0$ axis. One can also note small noise in the reconstructed spectrum at the border of the range in which the reconstruction took place. This may arise from the uncertainties in the difference spectrum used for analysis and will have no physical meaning anyway.

The ambiguity problem is well-known and, as shown e.g. in ref. [13], when there is more than a single distribution of hyperfine field parameters in the paramagnetic phase,

the infinite number of distributions can be produced, all of which will be in perfect agreement with the measured Mössbauer spectrum. The Maximum Entropy Method is just giving its natural constraint which helps to find the most likely distribution. However, on the example presented above one can see that in addition to the MEM constraint which selects mathematically plausible result, one has to consider physical implications of the obtained distributions and seek eventually for the distributions with least number of features.

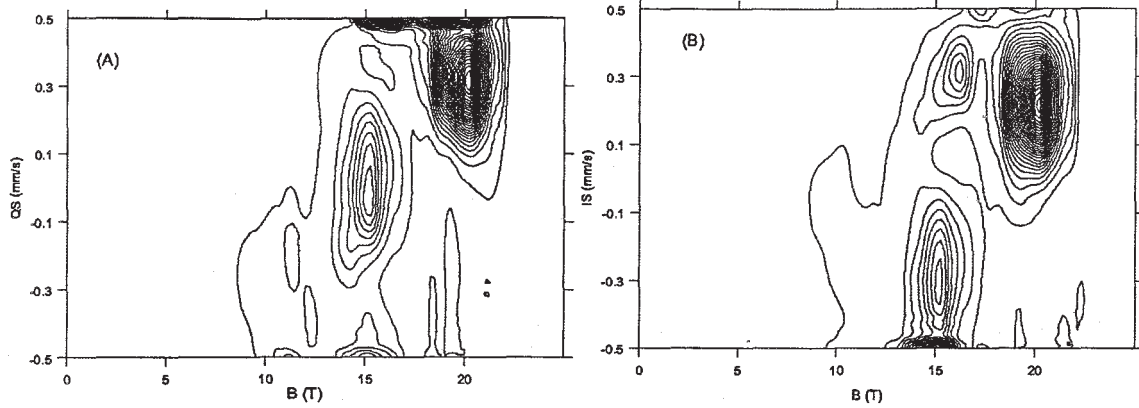


FIGURE 2. Distributions obtained with the uniform prior: (A) the marginal $P(B, QS)$; (B) the marginal $P(B, IS)$.

4. THREE-DIMENSIONAL PROBABILITY DISTRIBUTIONS

The feasibility of MEM in the case of 3-dimensional distribution was checked on the following simulated distribution:

$$\begin{aligned}
 P(B, QS, IS) = & \exp\left(-\frac{(B-20)^2}{4} - \frac{(QS-0.3)^2}{0.01} - \frac{(IS-0.2)^2}{0.01}\right) \\
 & + 0.5 \exp\left(-\frac{(B-15)^2}{4} - \frac{(QS-0.1)^2}{0.01} - \frac{(IS+0.2)^2}{0.01}\right) \\
 & + 0.25 \exp\left(-\frac{(B-10)^2}{4} - \frac{(QS+0.1)^2}{0.01} - \frac{IS^2}{0.01}\right). \quad (7)
 \end{aligned}$$

Here B is expressed in Tesla, while QS and IS in mm/s. Normalization constant is neglected as irrelevant parameter for our purpose. The calculated Mössbauer spectrum corresponding to this distribution is shown by points in Fig. 3A (the remaining content of Fig. 3 will be discussed later on). We find that the simulated distribution (7) is reconstructed perfectly if this distribution is used as a prior, so the MEM itself does not produce any substantial noise. On the other hand, although the Mössbauer spectrum is still reproduced very well, the reconstruction is rather poor if uniform prior is used. Therefore various non-uniform priors have been tried. Such priors are easily guessed if one has some experience with the Mössbauer spectra. We also noted that even in the case of poor reconstruction, the marginal probabilities [e.g., $P(B, QS) = \int P(B, QS, IS) dIS$]

are reproduced very well, and show peaks at $B = 10, 15$ and 20 , so the marginal $P(B)$ can always be used as a prior. In addition, even from the results obtained with uniform prior, see Fig. 2, one can postulate appearance of the strongest peak at $B = 20$, $QS = 0.3$ and $IS = 0.2$, and thus use the following prior

$$P(B, QS, IS) = \exp\left(-\frac{(B-20)^2}{4} - \frac{(QS-0.3)^2}{0.01} - \frac{(IS-0.2)^2}{0.01}\right) + 0.5 \left[\exp\left(-\frac{(B-15)^2}{4}\right) + \exp\left(-\frac{(B-10)^2}{4}\right) \right] \exp\left(-\frac{QS^2}{0.02} - \frac{IS^2}{0.02}\right). \quad (8)$$

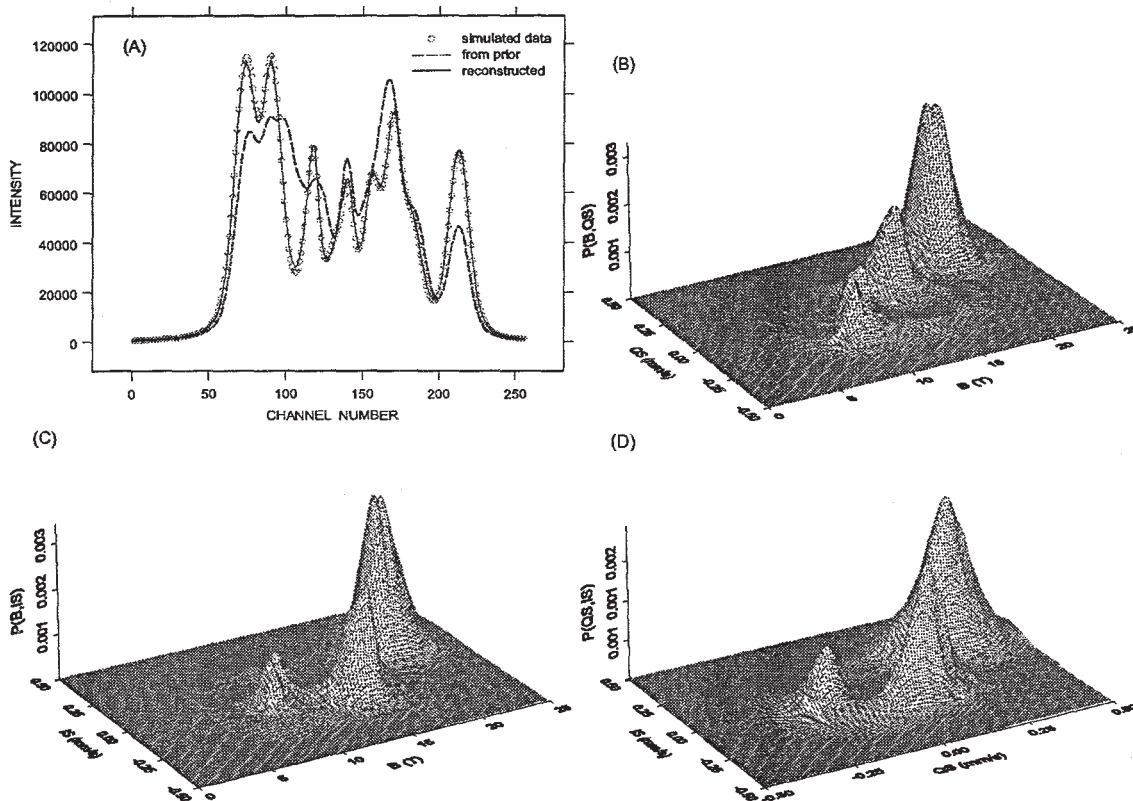


FIGURE 3. (A) The pseudo-experimental spectrum and the fitted one (solid line) with the prior as given in eq. (8). The spectrum corresponding to this prior is shown by dashed line; (B) marginal $P(B, QS)$ reconstructed from the prior (8); (c) same for $P(B, IS)$; (d) same for $P(QS, IS)$. All probabilities given in arbitrary units.

Note that although in $P(B)$ the intensities of two peaks found at $B = 15$ and $B = 10$ were apparently different, we used in (8) the same amplitude for both of them, while leaving rather large uncertainty concerning respective values of QS and IS . The spectrum corresponding to this prior (note that it is quite different from the “measured” one) and the results of the final reconstruction presented in 3-dimensional graphs are shown in Figs. 3A–D. There is no doubt that in spite of some small artefacts the reconstruction was successful. The similarity of Figs. 3C and 3D is not strange as the formula (7) indicates linear correlation of B and QS . However, this correlation had to be found by MEM!

5. CONCLUSIONS

It was shown that the reconstruction of the probability distribution of the hyperfine parameters from Mössbauer spectrum is possible, although one has to be very careful with coming to conclusions. We have shown that the Maximum Entropy Method gives the most likely distribution which, however, can have little to do with the true one. Therefore some extra work is needed for interpreting the spectrum. This does not show any weakness of the MEM method. Just the opposite is true. One should remember that all conventional methods of analysis rely on assumptions of e.g. the number of subspectra and possible correlations between hyperfine parameters. Therefore, a true advantage of MEM consists in abandoning the latter assumptions. As we showed, the MEM can successfully be applied to reconstruction of even 3-dimensional distributions from the one-dimensional Mössbauer spectra, provided, however, that a proper non-uniform prior is used.

REFERENCES

1. E. T. Jaynes, *Probability Theory. The Logic of Science*, Cambridge: Cambridge University Press, (2003).
2. G. L. Bretthorst, *Bayesian Spectrum Analysis and Parameter Estimation*, Lecture Notes in Statistics 48, Berlin: Springer-Verlag, (1988).
3. *Maximum Entropy in Action*, edited by B. Buck and V. A. Macaulay, Oxford: Clarendon Press (1991).
4. U. Gerhard, S. Marquardt, N. Schroeder, S. Weiss, Bayesian deconvolution and analysis of photoelectron or any other spectra: Fermi-liquid versus marginal Fermi-liquid behavior of the 3d electrons in Ni, *Phys. Rev. B* **58**, 6877 (1998).
5. L. Dobrzyński, "Momentum Density Studies by the Maximum Entropy Method" in *X-Ray Compton Scattering*, edited by M. J. Cooper et al., Oxford: Oxford University Press (2004), pp.188–209.
6. L. Dobrzyński, K. Szymański, D. Satuła, *Nukleonika* **49**, Suppl. 3, S89 (2004).
7. G. Le Caër, J. M. Dubois, H. Fischer, I. U. Gonser, H. G. Wagner, *Nucl. Instr. Meth.* **B5** 25 (1984).
8. G. Le Caër, R. A. Brand, General methods for the distributions of electric field gradients in disordered solids. *J. Phys.: Condens. Matter* **10**, 10715–10774 (1998).
9. K. Szymański, L. Dobrzyński, D. Satuła and B. Kalska-Szostko "Trends in Mössbauer polarimetry with circularly polarised radiation" in *Material Research in Atomic Scale by Mössbauer Spectroscopy*, edited by M. Mashlan, M. Miglierini and P. Schaaf, Nato Science Series, II Mathematics, Physics and Chemistry, Vol 94, Dordrecht: Kluwer Academic Publishers, 2003, pp. 317–328.
10. F. Varret, A. Gerard, P. Imbert, Magnetic field distribution analysis of the broadened Mössbauer spectra of zinc ferrite, *Physica Status Solidi B — Basic Research*, **43**, 723 (1971).
11. B. Window, Hyperfine field distributions from Mössbauer spectra, *J. Phys. E: Scientific Instruments*, **4**, 401 (1971).
12. T. E. Cranshaw, The deduction of the best values of the parameters from Mössbauer spectra, *J. Phys. E: Scientific Instruments*, **7**, 122–124 (1974).
13. G. Le Caër, J. M. Dubois, Evaluation of hyperfine parameter distributions from overlapped Mössbauer spectra of amorphous alloys, *J. Phys. E: Scientific Instruments*, **12**, 1083–1090 (1979).
14. S. J. Campbell, G. J. Whittle, A. M. Stewart, On the determination of the magnetic hyperfine field distribution in an amorphous alloy, *Journal of Magnetism and Magnetic Materials*, **31–34**, 1521–1522 (1983).
15. J. Hesse, A. Rubartsch, Model independent evaluation of overlapped Mössbauer spectra, *J. Phys. E: Scientific Instruments*, **7**, 526–532 (1974).
16. M. A. Chuev, O. Hupe, H. Bremers, J. Hesse, A. M. Afanas'ev, A novel method for evaluation of complex Mössbauer spectra demonstrated on nanostructured ferromagnetic FeCuNiB alloys, *Hyperfine Interactions*, **126**, 407–410 (2000).

17. R. A. Brand, G. Le Caër, Improving the validity of Mössbauer hyperfine parameter distributions: the maximum entropy formalism and its applications, *Nuclear Instruments and Methods*, **B34**, 272–284 (1988).
18. L. Dou, R. J. W. Hodgson, D. G. Rancourt, Bayesian inference theory applied to hyperfine parameter distribution extraction in Mössbauer spectroscopy, *Nuclear Instruments and Methods*, **B100**, 511 (1995).
19. J. Skilling, W. Bryan, *Mon. Not. T. Astr. Soc.*, **211**, 111-124 (1984).
20. D. Satuła, K. Szymański, V. H. Tran, L. Dobrzyński, *Nukleonika* (to be published).

P12

Hyperfine fields in UFe_5Sn compound

Dariusz Satuła,
Krzysztof Szymański,
Vinh H. Tran,
Ludwik Dobrzyński

Abstract Local hyperfine interactions on Fe nuclei in UFe_5Sn compound were determined in Mössbauer experiment. The analysis of the Mössbauer spectra measured at room temperature reveals the presence of two doublets only. Absorption line width indicates that neither distribution of quadrupole splitting nor isomer shift exists in the alloy. The measurements at 13 K show the presence of four magnetic components. Because the magnetic dipole and electric quadrupole interactions are present, full Hamiltonian was used to determine the hyperfine interactions for each iron site. Electric field gradient determined at low temperatures agrees with quadrupole splitting observed at room temperature. Absorption areas of the components at low and at high temperatures correspond well to the occupation of the crystal sites by Fe atoms.

Key words Mössbauer studies • uranium intermetallic • magnetic intermetallic

D. Satuła✉, K. Szymański
Institute of Experimental Physics,
University of Białystok,
41 Lipowa Str., 15-424 Białystok, Poland,
Tel.: +48 85 745 7242, Fax: +48 85 745 7223,
E-mail: satula@alpha.uwb.edu.pl

V. H. Tran
W. Trzebiatowski Institute of Low Temperature
and Structure Research, Polish Academy of Sciences,
50-950 Wrocław, P.O. Box 937, Poland

L. Dobrzyński
Institute of Experimental Physics,
University of Białystok,
41 Lipowa Str., 15-424 Białystok, Poland
and The Andrzej Sołtan Institute for Nuclear Studies,
05-400 Otwock-Świerk, Poland

Received: 20 June 2006

Accepted: 22 September 2006

Introduction

New intermetallic compound UFe_5Sn , discovered by A. P. Gonçalves *et al.* [3], crystallizes in orthorhombic CeCu_3Au -type structure (space group $Pnma$). The unit cell contains 4 U atoms located in $4c$ site, 4 Sn atoms in $4c$, 12 Fe atoms in $4c$ (Fe2, Fe3, Fe4) and 8 Fe atoms in $8d$ (Fe1) site [3]. The magnetization measurements carried out on a powder sample show a weak ferromagnetic behavior at room temperature and two magnetic anomalies at 248 K and 180 K [3]. The latter transition is magnetic field dependent and disappears at $B > 1$ T. Below 248 K magnetization strongly increases with decreasing temperature. More precise experiments on a single crystal [4] show that the transition at 248 K is associated with ferromagnetic ordering of iron magnetic moments along c -axis, while anomalies observed at 180 K with reorientation Fe moments towards to b -axis. This conclusion is deduced partially from Mössbauer measurements. However, the description of the spectra presented in [4] in our opinion does not fit the experimental data so well. We think that the main reason of not good agreement between the experimental and theoretical Mössbauer spectra is the use of the first order perturbation in the presence of mixed hyperfine interactions. Since the electric quadrupole interactions are not small with respect to the magnetic dipolar ones, a full Hamiltonian should be used for correct description of the Mössbauer spectra. The aim of our study is

determination of the hyperfine interactions of iron atoms located at different sites in the UFe_5Sn compound.

Sample preparation and data handling

The UFe_5Sn crystal was grown by the Czochralski method. Our sample crystallizes in the same structure as reported [3] and the lattice parameters, within the experimental errors, do not differ greatly from [3]. The powdered sample studied in the work was crushed from a single crystal, and was mixed with the LiCO_3 and epoxy glue. Such preparation results in the random distribution of the grains, so-called texture free sample. The sample thickness was $12 \text{ mg UFe}_5\text{Sn per cm}^2$.

The Mössbauer measurements at $T = 13 \text{ K}$ were carried out in a close cycle refrigerator equipped with an antivibration shroud. The source of radiation was ^{57}Co in Cr matrix. The velocity scale was calibrated with respect to $\alpha\text{-Fe}$ at room temperature.

All spectra were analysed by commercial Mössbauer package “Normos” using transmission integral [5]. Recoilless fraction of Fe atoms in UFe_5Sn was assumed to be the same as in $\alpha\text{-Fe}$ [2]. The resulting values of effective thickness of the absorber were estimated to be $\tau = 2.07 \pm 0.11$ at room temperature and $\tau = 2.41 \pm 0.11$ at $T = 13 \text{ K}$.

The spectra measured at $T = 13 \text{ K}$ were analyzed using full Hamiltonian approach for the texture free sample. Axial symmetry of the electric field gradient was assumed (asymmetry parameter $\eta = 0$) for all local environments of Fe atoms.

Results and discussion

The Mössbauer spectrum measured at room temperature was fitted by two doublets with the same values of width of the Lorentzian lines (D(1), D(2)). The result of the best fit is shown in Fig. 1 by the thick line, while parameters of the two components are listed in Table 1. The ratio of the areas of the two doublets is close to four, consistent with the assumption that doublet D(1) is created by 8 Fe atoms at $8d$ and 8 Fe atoms at $4c$

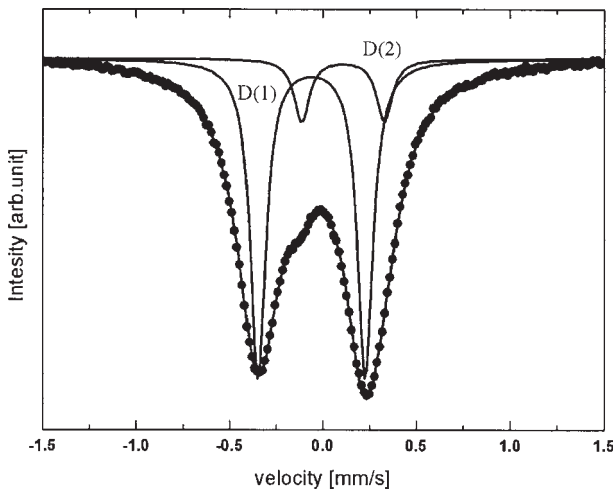


Fig. 1. Mössbauer spectrum measured at room temperature.

Table 1. The hyperfine parameters obtained from the spectrum measured at room temperature (eQ – electric quadrupole moment, V_{zz} – z component of electric field gradient, IS – isomer shift, I – intensities of the components and Γ_a – full width of the Lorentzian lines at half maximum. The width of the source was determined from calibration experiment $\Gamma_s = 0.17 \text{ mm/s}$)

	$ eQV_{zz}/2 $ [mm/s]	IS [mm/s]	I [%]	Γ_a [mm/s]
D(1)	0.54 ± 0.01	-0.06 ± 0.01	84 ± 4	0.10 ± 0.01
D(2)	0.44 ± 0.02	0.11 ± 0.01	16 ± 4	0.10 ± 0.01

sites, while D(2) doublet is created by 4 Fe atoms at $4c$ site. The difference in the isomer shift (IS) between D(2) and D(1) doublets is 0.18 mm/s . Because the Sn atoms located in the nearest neighborhood (NN) of Fe increase its IS [1], one may conclude that D(2) doublet results from the Fe2 site only, which has three Sn atoms, and being their NN located at distances ranging between $2.61\text{--}2.93 \text{ \AA}$ [3].

Despite four different local Fe sites in the unit cell, the room temperature spectra can be precisely fitted by two doublets only (see Fig. 1). The absorption lines are not broadened (their widths are equal to the widths of the lines in calibration spectrum of $\alpha\text{-Fe}$). We thus conclude that hyperfine interactions for the Fe1, Fe3 and Fe4 sites, which differ in local symmetry, result in the single doublet D(1).

The Mössbauer spectrum measured at $T = 13 \text{ K}$ is shown in Fig. 2. The shape of spectrum can be fitted by a sum of four magnetic components $S(n)$ ($n = 1, 2, 3, 4$) and a single doublet (D), all with very sharp lines ($\Gamma_a = 0.13 \pm 0.01 \text{ mm/s}$). Thick lines in Fig. 2 represent the best fit. The parameters obtained from the fit are presented in Table 2. Because the population of Fe at the $8d$ sites should be twice larger than that of Fe at each of remaining sites, one concludes that the most intense component S(1) corresponds to the Fe1 site. It was observed in U-Fe-Al [7] and in Fe-Sn [6] alloys that hyperfine magnetic field (HMF) of Fe increases with a number of Fe N.N. Assuming similar behavior in the studied compound one concludes that S(2), S(3) and

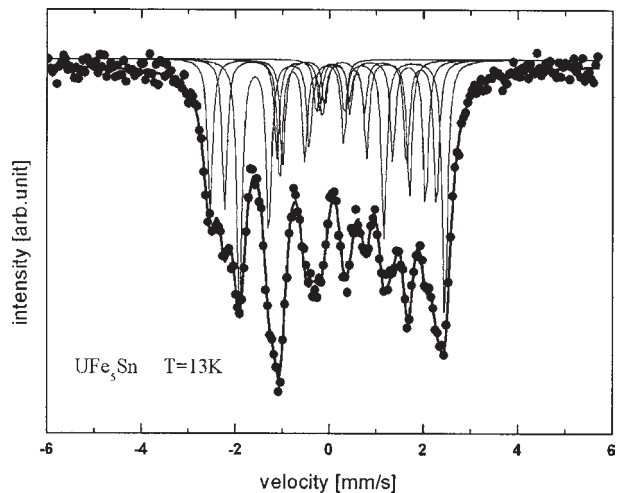


Fig. 2. Mössbauer spectrum measured at $T = 13 \text{ K}$.

Table 2. The hyperfine parameters obtained from the spectrum measured at $T = 13$ K for different local surroundings (eQ – electric quadrupole moment, V_{zz} – z component of electric field gradient, HMF – hyperfine magnetic field, I – intensities of the components)

		S(1)	S(4)	S(3)	S(2)	D
IS	[mm/s]	0.104 ± 0.005	0.094 ± 0.005	0.01 ± 0.03	0.23 ± 0.02	0.02 ± 0.02
$eQV_{zz}/2$	[mm/s]	0.46 ± 0.02	-0.63 ± 0.05	0.49 ± 0.10	0.56 ± 0.05	0.59 ± 0.04
HMF	[T]	13.4 ± 0.2	14.6 ± 0.2	13.0 ± 0.3	7.9 ± 0.2	
I	[%]	36 ± 2	22 ± 2	20 ± 4	19 ± 4	3 ± 4

S(4) comes from Fe2, Fe3 and Fe4 sites, respectively, which is consistent with [3].

In contrast to the results of [3], relative area of the doublet D observed at low temperature is twice smaller than that of the sextet (HMF = 2T) [3]. The origin of this doublet is not clear because its relative area is small. Comparison of hyperfine parameters obtained here indicates that value of IS of the doublet D is close to that of S(3) component, which in turn indicates that this doublet may have Fe3 site origin, as suggested in [3]. However, it is not clear, why part of Fe iron atoms, located at the Fe3 site is still in the paramagnetic state at $T = 13$ K. Another possibility is that the considered doublet results from a small fraction of Fe atoms located at antisite positions, U or Sn atoms.

Acknowledgment We are grateful to Prof. R. Troć for the suggestion to undertake this study.

References

1. Akai H, Blugel S, Zeller R, Dedeichs PH (1986) Isomer shifts and their relation to charge transfer in dilute Fe alloys. *Phys Rev Lett* 56:2407–2410
2. Bergmann U, Shastri SD, Siddons DP, Batterman BW, Hastings JB (1994) Temperature dependence of nuclear forward scattering of synchrotron radiation in α -⁵⁷Fe. *Phys Rev B* 50:5957–5961
3. Gonçalves AP, Godinho V, Noel H (2000) Synthesis, crystal structure, and magnetic properties of UFe₅Sn. *J Solid State Chem* 154:551–556
4. Gonçalves AP, Waerenborgh JC, Almeida M *et al.* (2003) Magnetic properties of UFe₅Sn single crystal. *J Magn Mater* 260:473–479
5. Margulies S, Ehrman JR (1961) Transmission and line broadening of resonance radiation incident on a resonance absorber. *Nucl Instrum Methods* 12:131–137
6. Vincze I, Aldred AT (1974) Mössbauer measurements in iron-base alloys with nontransition elements. *Phys Rev B* 9:3845–3853
7. Waerenborgh JC, Gonçalves AP, Almeida M (1999) Magnetization of the Fe sublattices in UFe_xAl_{12-x} ($4 \leq x \leq 5.8$) studied by Mössbauer spectroscopy. *Solid State Commun* 110:369–374

P13

Microstructure and Magnetic Properties of Iron Oxide Nanoparticles Prepared by Wet Chemical Method

D. SATUŁA^a, B. KALSKA-SZOSTKO^b, K. SZYMAŃSKI^a,
L. DOBRZYŃSKI^{a,c} AND J. KOZUBOWSKI^d

^aFaculty of Physics, University of Białystok
Lipowa 41, 15-424 Białystok, Poland

^bInstitute of Chemistry, University of Białystok
Hurtowa 1, 15-399 Białystok, Poland

^cThe Sołtan Institute of Nuclear Studies, 05-400 Otwock-Świerk, Poland

^dWarsaw University of Technology
Faculty of Materials Science and Engineering
Wołoska 141, 02-507 Warszawa, Poland

The magnetic properties of iron oxide nanoparticles prepared by the chemical decomposition of the iron chlorides with the ratio $\text{Fe}^{3+}/\text{Fe}^{2+} = 2.25$ were studied by means of transmission electron microscopy, X-ray diffraction and Mössbauer spectroscopy in- and without external magnetic field. The transmission electron microscopy studies show that the nanoparticles have spherical shape with diameter about 13 nm. The transmission electron microscopy and X-ray diffraction patterns are composed of lines that could be indexed within the cubic spinel structure. The room temperature Mössbauer spectrum shows the coexistence of the broad magnetically split part and superparamagnetic doublet. The in-field Mössbauer measurements carried out in the temperature range from room temperature down to 13 K show a gradual increase in the spin canting on the surface of the nanoparticles and decrease in the intensity of the superparamagnetic doublet. The sample was subjected to annealing process performed at elevated temperature in air atmosphere in order to change the microstructure of the nanoparticles and in consequence to change the magnetic properties of the sample. The annealing process leads to the decrease in the value of quadrupole splitting of the superparamagnetic doublets.

PACS numbers: 76.80.+y, 61.46.Df, 75.75.+a

1. Introduction

The magnetic nanoparticles are of great interest because of their novel properties, which differ considerably from that observed ones in the bulk materials [1].

The few nanometer size causes that the surface effects strongly influence magnetic properties of the nanoparticles. The fundamental mechanisms that govern their behavior are connected with single particle properties and collective interparticle interactions. It was reported that the low symmetry of the surface atoms and possible distribution of interior defects and/or microstructure can lead to the spin canting [2, 3]. Moreover, the interparticle interaction can lead to suppression of the superparamagnetic relaxation and may result in spin-glass-like ordered state at low temperatures [4, 5]. The interparticle interactions have been proposed to stabilize the magnetic order both at the nanoparticle's core and surface [6].

The aim of this work was to investigate the behavior of magnetic moments of iron atoms with decrease in temperature and an impact of the annealing process on the microstructure and in consequence on the hyperfine parameters of the iron oxide nanoparticles. The thermal annealing in air can lead to the transformation from magnetite — maghemite to hematite microstructure of the outer parts of iron oxide nanoparticles which should lead to a change of the magnetic properties — stabilization of the magnetic order of the interior nanoparticles in particular. It is expected that the gradual annealing process should influence the surface first and then the core of the nanoparticles.

2. Experiment

The iron oxide nanoparticles were synthesized following main steps from Massart's methods [7]. The particle production is divided into two main procedures. Initially the chlorides are hydrolyzed to certain hydroxides. The reaction takes place in two separated flasks. In the second step, the condensation occurs where the reagents are mixed in one bottle at elevated temperature up to 85–90°C. In the meantime the surfactant such as tetrabutylammonium hydroxide (TBAOH) is added to the solution. The nanoparticles extracted from solution were characterized by low- and high-resolution electron diffraction (TEM), X-ray diffraction (XRD) and Mössbauer spectroscopy in- and without external magnetic field. Transmission electron micrographs were taken out on a JEM 3010 microscope. The Mössbauer spectra were obtained using the equipment with a conventional constant acceleration mode spectrometer with a ^{57}Co source in chromium matrix. The reference spectra were obtained on α -Fe foil at room temperature. In-field measurements were taken with the use of external magnetic field of 1.3 T and 1 T parallel to the γ -ray direction. Low temperature measurements were carried out with the use of closed cycle refrigerator equipped with antivibrational shroud.

The powder sample was mixed with boron nitride and epoxy glue to obtain homogeneous tablets. The specimens were annealed in air atmosphere at temperature 423 K for 2 h. The procedure was repeated twice.

3. Results and discussion

The TEM images of the as prepared sample are shown in Fig. 1. The particles are roughly spherical and agglomerated. The distribution of the diameters is presented in Fig. 2. The estimated average size of the particles is (12.8 ± 1.5) nm. The high resolution picture presents clearly that the particles' cores are single crystalline. The shell of the particles is not separated. The electron diffraction patterns shows (220), (311), (400), (422), (511) and (440) rings originating from the magnetite (Fe_3O_4) and/or maghemite ($\gamma\text{-Fe}_2\text{O}_3$) structures since the positions of the diffraction patterns are almost the same in both of them [8]. The obtained ring pattern does not show any additional reflexes (rings) which could be associated with $\alpha\text{-Fe}_2\text{O}_3$ or other oxides. Small amount of crystalline organic ingredients connected with surfactant is also noticed. These results were confirmed by X-ray experiment.

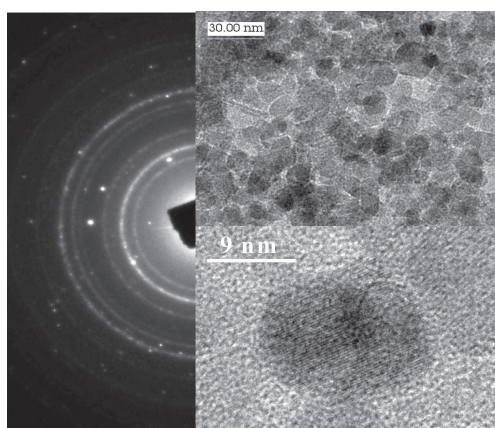


Fig. 1. TEM images and electron diffraction pattern of the sample.

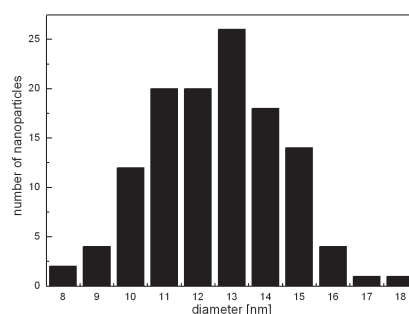


Fig. 2. Particles size distribution obtained from TEM images.

The Mössbauer spectra measured in- and without external field at room temperature are presented in Fig. 3. As one can see, the spectrum measured without external magnetic field consists of broad magnetic part and a doublet. The presence of the doublet which could be due to some superparamagnetic relaxation is rather surprising. For such materials like magnetite and maghemite which crystallize in regular structure, the superparamagnetic relaxation should be rather seen as a single line than doublets — the situation known from the measurements on bulk magnetite above T_c [9]. The superparamagnetic relaxation often observed in nanoparticles is related to the particles' size. Alternatively, one can explain the presence of superparamagnetic doublet as showing that remarkable part of Fe atoms is located in the region of the nanoparticle surface and because of broken cubic symmetry these atoms are exposed to nonzero electric field gradient.

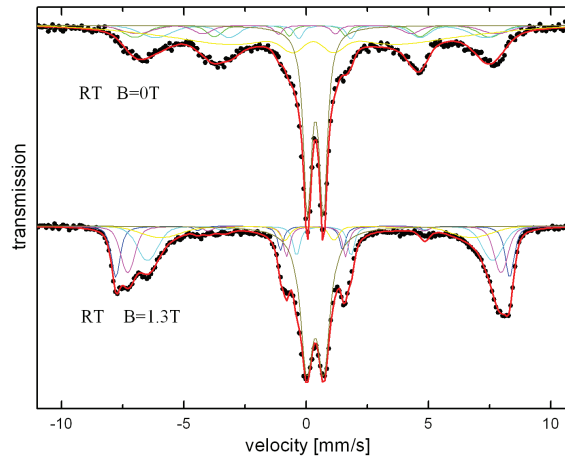


Fig. 3. The Mössbauer spectra measured at room temperature (RT) in- and without external magnetic field parallel to gamma beam.

The in-field measurements show that the magnetic part of spectra is well resolved and individual components can be extracted. Moreover, the lines 2 and 5 disappear which means that the hyperfine fields are oriented along gamma beam direction. The spectra were fitted using four sextets and one doublet. These two sextets come from the iron atoms at A and B positions connected with two different iron positions in magnetite, one sextet which comes from iron in maghemite and one broad sextet connected with superparamagnetic relaxation processes. The relative intensity of the doublet is $(37 \pm 4)\%$ of the spectra and within the experimental accuracy does not change for in- and without external magnetic field measurements. Assuming that the outer layer is solely responsible for the presence of the doublets, one can estimate that the thickness of this layer must be (2.0 ± 0.5) nm. This value is over twice larger than the lattice parameter for maghemite which for nanoparticles varies from 0.833 to 0.838 nm [10].

The Mössbauer spectra measured in the temperature range 300 K down to 13 K are presented in Fig. 4. Two main features follow from inspection of the observed spectral shapes. The quadrupole components decrease and disappear at $T = 50$ K and the gradual increase in the intensities connected with the lines 2 and 5 is observed when the temperature decreases. This can be interpreted as suppression of the superparamagnetic relaxation processes and formation of the static disordered spin structure. This confirms that the doublet is connected with the atoms located at the outer part of the particle. The gradual increase in the intensities of the lines 2 and 5 with decrease in the temperature were observed in maghemite nanoparticles (7 nm) in the work [11] and interpreted as strongly canted iron magnetic moments from B-sites ions.

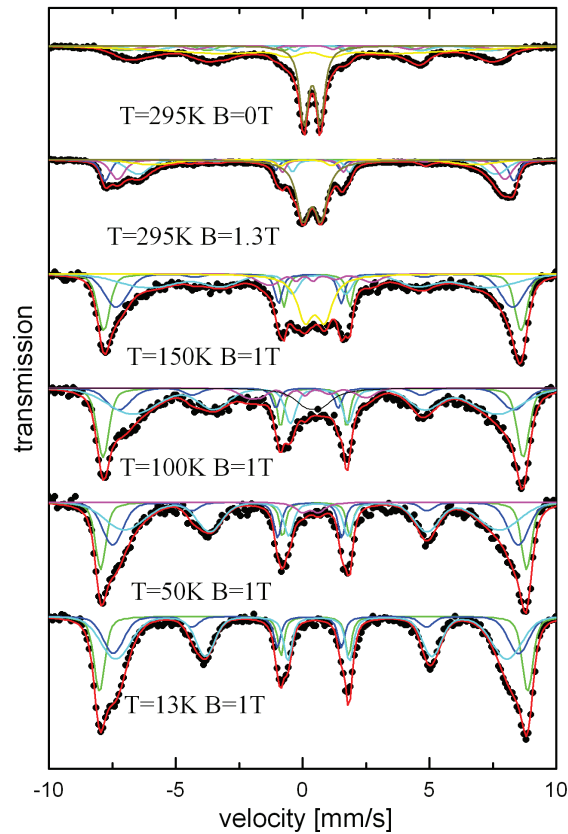


Fig. 4. The Mössbauer spectra measured at temperature range 13 K to RT.

The Mössbauer spectra measured at room temperature for sample subjected to different annealing process are presented in Fig. 5. The intensities of the superparamagnetic doublets decrease with increase in the annealing time. Moreover, the results show that value of the quadrupole splitting decreases from

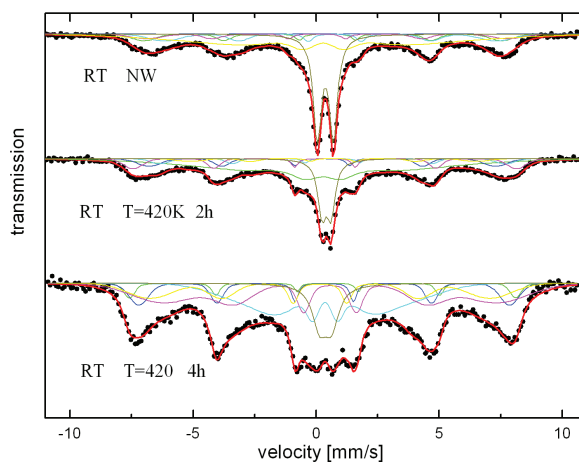


Fig. 5. The room temperature Mössbauer spectra measured for samples subjected to different annealing processes.

(0.65 ± 0.03) mm/s for as prepared sample to (0.37 ± 0.04) mm/s for sample annealed for 2 h. Further annealing does not change the value. The decrease in quadrupole splitting can be caused by a change of the outer layer morphology or by coating the particles by hematite. The small components of the hematite were detected in the in-field Mössbauer spectra of the sample subjected to 4 h annealing. We cannot exclude a possibility of surfactant decomposition resulting in an increase in dipolar interaction between the particles.

4. Conclusions

TEM measurements, X-ray diffraction and Mössbauer spectroscopy show that using the chemical wet method the magnetite/maghemite iron oxide nanoparticles with the size of (12.8 ± 1.5) nm were produced. The Mössbauer spectra at room temperature consist of the superparamagnetic doublet and the magnetic part. The applied external magnetic field exerts strong influence on the magnetic part of the spectra and does not change the superparamagnetic part. The Mössbauer measurements carried out in the temperature from room temperature down to 13 K show gradual suppression of the superparamagnetic component and formation of static spin disordered structure. The procedure of annealing of the nanoparticles in air leads to the change of the value of the quadrupole interaction of the iron atoms in the outer layer of the nanoparticles and partially suppression of the superparamagnetic phenomenon.

Acknowledgments

The work was partially supported as a research project by the funds allocated for scientific research for years 2008–2011.

References

- [1] J.L. Dormann, D. Fiorani, E. Tronc, *Adv. Chem. Phys.* **98**, 283 (1997).
- [2] J.M.D. Coey, *Phys. Rev. Lett.* **27**, 1140 (1971).
- [3] S. Morup, *J. Magn. Magn. Mater.* **266**, 110 (2003).
- [4] S. Mørup, F. Bodker, P.V. Hendriksen, S. Linderoth, *Phys. Rev. B* **52**, 287 (1995).
- [5] Y. Sun, M.B. Salamon, K. Garnier, R.S. Averback, *Phys. Rev. Lett.* **91**, 167206 (2003).
- [6] V. Skumryev, S. Stoyanov, Y. Zhang, G. Hadjipanayis, D. Givord, J. Nauues, *Nature* **423**, 850 (2003).
- [7] R. Massart, V. Cabuil, *J. Chim. Phys.* **84**, 967 (1987).
- [8] S. Sun, H. Zeng, D.B. Robinson, S. Raoux, P.M. Rice, S.X. Wang, G. Li, *J. Am. Chem. Soc.* **126**, 273 (2004).
- [9] J.M. Florez, J. Mazo-Zuluaga, J. Restrepo, *Hyperfine Interact.* **161**, 161 (2005).
- [10] S. Nasrazadani, A. Raman, *Corros. Sci.* **34**, 1355 (1993).
- [11] Ö. Helgason, H. Rasmusen, S. Mørup, *J. Magn. Magn. Mater.* **302**, 413 (2006).

P14

Mössbauer data analysis based on invariants and application to UFe₅SnD. Satuła,¹ K. Szymański,¹ L. Dobrzyński,^{1,2} V. H. Tran,³ and R. Troć³¹University of Białystok, Faculty of Physics, Lipowa 41, 15-424 Białystok, Poland²The Soltan Institute of Nuclear Studies, 05-400 Otwock-Świerk, Poland³W. Trzebiatowski Institute of Low Temperature and Structure Research, Polish Academy of Sciences, P.O. Box 1410, 50-950 Wrocław, Poland

(Received 11 March 2008; revised manuscript received 7 May 2008; published 7 July 2008)

A method for Mössbauer data treatment is proposed for texture-free samples. Parameters of hyperfine interactions, Debye temperature, temperature dependence of the electric-field gradient components, site occupancies, and magnetic moments of the ground state are measured for UFe₅Sn. Spin reorientation is evidenced and anomalous temperature dependence of magnetic moments at specific sites is revealed. The presented results do not contain full information about parameters of hyperfine interactions but are free of ambiguity typical for 3/2–1/2 nuclear-spin transitions because only experimentally available information is being considered. It is proven that the presented method could be easily employed with the help of widely used standard Mössbauer packages when some constraints are applied.

DOI: 10.1103/PhysRevB.78.014411

PACS number(s): 75.25.+z, 76.80.+y, 75.50.Bb, 71.20.Lp

I. INTRODUCTION

It was recognized already in the 1960's that details of the hyperfine structure cannot be unambiguously determined from the Mössbauer spectrum of a randomly oriented, thin absorber in which mixed interactions (e.g., magnetic dipole and electric quadrupole) are present.¹ This limitation applies even to the simplest case of a single site and is called the ambiguity problem.^{2–5} Application of the external magnetic field,⁶ use of single crystals,⁷ or polarimetric methods^{8,9} are helpful issues in the complete determination of the hyperfine interactions. More serious problem arise when many sites are present or when distribution of hyperfine interactions causes an overlap of the absorption lines.^{10,11}

Although the randomly oriented absorber information obtained by Mössbauer spectroscopic methods is poorer than in the case of using single crystals, obviously the availability of powders and difficulties in some single-crystal growth make the use of powdered absorbers still highly desirable. Thus, the ambiguity problem has to be properly treated. This paper demonstrates an effective method of Mössbauer data treatment, applied to the particular case of a UFe₅Sn intermetallic alloy. An additional advantage of the presented method stems from the possibility of using (under proposed interpretation) the results obtained by standard Mössbauer packages equipped in full Hamiltonian formalism.

This paper is organized as follows. We present exact, explicit solutions for the positions and amplitudes of absorption lines in the case of 3/2–1/2 mixed transitions. Next, it is shown how to obtain a set of all possible hyperfine parameters, which realizes the specific absorption spectrum. The shape of the spectrum is given by a set of invariants. Then we show how to find the set and how to easily find its representation by the parameters of hyperfine interactions. Finally, the method is applied to the analysis of experimental data of UFe₅Sn. Spin reorientation in this compound is clearly evidenced by a discontinuity in the temperature dependence of invariants.

II. INVARIANTS IN THE CONTEXT OF THE AMBIGUITY PROBLEM

Line positions in the Mössbauer spectra are calculated by diagonalization of the spin-Hamiltonian matrix, while line amplitudes are given by a product of the eigenstates.¹² Since one has to deal with 4 × 4 matrices, the discussion of the spin Hamiltonian of the eigenvalues and thus line intensities is rather difficult for spin 3/2. We have shown in Ref. 13 that the concept of the intensity tensor^{14–17} leads to the line intensities, which are given explicitly by scalars S_0 , S_1 , and S_2 , constructed from the electric-field-gradient (EFG) tensor \mathbf{V} and hyperfine magnetic-field (hmf) pseudovector \mathbf{B} :

$$S_0 = a\sqrt{\text{Tr } \mathbf{V}^2},$$

$$S_1 = a\mathbf{m}^T \cdot \mathbf{V} \cdot \mathbf{m},$$

$$S_2 = a\sqrt{\mathbf{m}^T \cdot \mathbf{V}^2 \cdot \mathbf{m}}, \quad (1)$$

where

$$a = eQc/E_\gamma \quad (2)$$

is the proportionality constant between EFG components [in (V/m²) SI units] and invariants expressed conveniently for applications in (mm/s). Q is the nuclear quadrupole moment, e is the elementary charge, c is the speed of light, and E_γ is the energy between the ground and the excited state (≈ 14.4 keV). In Eq. (1), $\mathbf{m} = \mathbf{B}/B$ (B is the modulus of \mathbf{B}) is the unit vector parallel to \mathbf{B} .

The invariants S_0 , S_1 , and S_2 (or $\text{Tr } \mathbf{V}^2$, $\mathbf{m}^T \mathbf{V} \mathbf{m}$, and $\mathbf{m}^T \mathbf{V}^2 \mathbf{m}$) have a clear physical interpretation. In Eq. (1), $6^{-1/2}S_0$ appears to be equal to $aV_{zz}(1 + \eta^2/3)^{1/2}/2$ and would be just a separation between $I_e = 3/2$ nuclear sublevels when the hmf is zero, or would be a separation between the absorption lines in the paramagnetic state. The asymmetry parameter η has the common meaning, i.e., defined by the diagonal components of the \mathbf{V} : $\eta = (V_{xx} - V_{yy})/V_{zz}$. The diagonal components V_{ii} are chosen so that $|V_{xx}| \leq |V_{yy}| \leq |V_{zz}|$, resulting in $0 \leq \eta \leq 1$.

$m^T V m$ is the component of the EFG tensor V in the direction of the hmf, and its sign may be positive or negative. The average value of $m^T V m$ [when m is randomly oriented in the principal-axis system (PAS) of the V] is zero.¹⁸ S_1 is proportional to the shift of the absorption lines 2, 3, 4, 5 with respect to the 1 and 6 in the Zeeman sextet caused by a small quadrupole interaction in the first-order approximation.¹⁹

The invariant $m^T V^2 m$ is the component of the V^2 in the direction of the hmf, $V_{zz}^2(1-\eta)^2/4 \leq m^T V^2 m \leq V_{zz}^2$. It also shows the length of Vm . Indeed, $m^T V^2 m = (Vm) \cdot (Vm)$. Some additional properties of invariants [Eq. (1)] are given in the Appendix. Finally, it should be noted that the choice of the invariants [Eq. (1)] is not unique.

Some results from Ref. 13 are essential to the present considerations, and are recalled as follows. The secular equation for the eigenvalues E of the excited $I_e=3/2$ state is

$$\lambda^4 + p\lambda^2 + q\lambda + r = 0, \quad (3)$$

$$\lambda = 2E/v_B,$$

where $v_B = g_{3/2}\mu_N Bc/E_\gamma$ is the Zeeman splitting between $I_e=3/2$ sublevels expressed in velocity units, μ_N is the nuclear magneton, and $g_{3/2}$ is the nuclear g -factor of the excited state. The coefficients p , q , and r are

$$p = -10 - \frac{1}{3}(S_0/v_B)^2,$$

$$q = -8S_1/v_B,$$

$$r = \frac{1}{4}(p+4)^2 - 4(S_2/v_B)^2. \quad (4)$$

The absorption line intensity for a randomly oriented absorber in the case of a $3/2 \rightarrow 1/2$ magnetic dipolar transition is proportional to the trace of the intensity tensor $I_{\alpha\beta}$, and the explicit form is (Ref. 13)

$$\text{Tr } I_{\alpha\beta} = \frac{3}{8} + \beta \frac{40\lambda_\alpha^2 - 4q\lambda_\alpha + (p+4)(p+16) - 4r}{16(4\lambda_\alpha^3 + 2p\lambda_\alpha + q)}. \quad (5)$$

The index $\beta = \pm 1$ corresponds to two ground states, while four eigenvalues λ_α are roots of secular Eq. (3).

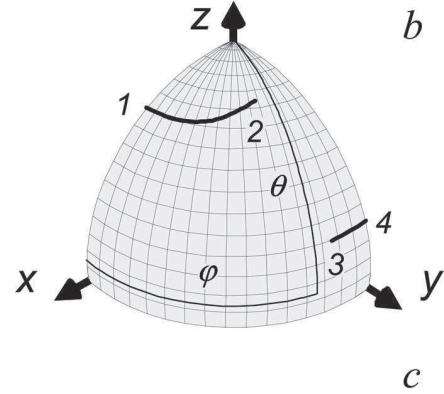
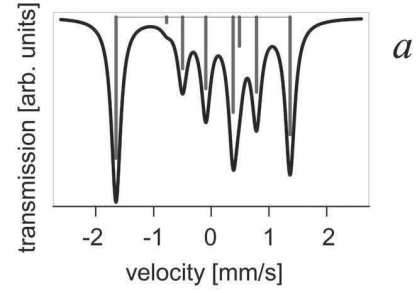
The explicit form of the roots can be found in Ref. 18. The line positions $v_{\alpha\beta}$ (expressed conveniently in the velocity units) are

$$v_{\alpha\beta} = (\lambda_\alpha - \beta g_{1/2}/g_{3/2})v_B/2, \quad (6)$$

where $g_{1/2}$ is the nuclear g -factor of the ground state.

The results [Eqs. (1), (5), and (6)], fully determining the absorption line positions and intensities, depend on four invariants only: B , S_0 , S_1 , and S_2 , while there are five independent hyperfine parameters: B , θ , φ , V_{zz} , and η , where θ and φ are polar and azimuthal angles of the B vector in PAS of the V tensor.

It would be helpful to consider a typical example (for instance, assuming no accidental relations between parameters), which illustrates the ambiguity problem. Let us take $eQcV_{zz}/E_g = -2$ mm/s, $B = |eQV_{zz}/(4g_{3/2}\mu_N)| (=7.364\dots\text{T})$,



no	R	η	θ	φ
1	2.152	0.278	0.588	0.000
2	1.887	1.000	0.455	1.047
3	-1.887	1.000	1.181	1.331
4	-1.947	0.872	1.171	1.571

FIG. 1. (a) Simulated Mössbauer absorption spectrum for hyperfine field $B = |eQV_{zz}/(4g_{3/2}\mu_N)| (=7.3641\text{ T})$, and invariants S_0 , S_1 , and S_2 (1) equal to $(57/8)^{1/2}$, $-5/4$, $(217/64)^{1/2}$ (all in mm/s), respectively. (b) Thick lines drawn on part of the unit sphere show possible values of the polar θ and azimuthal φ angles of the B vector in the principal axes system of the electric-field-gradient tensor V . At some points marked by numbers 1, 2, 3, 4, (c) values of the main diagonal component V_{zz} [$R = eQV_{zz}/(2g_{3/2}\mu_N)$, see text after Eqs. (1) and (3) for explanation of the symbols], the asymmetry parameter η and angles θ and φ are given in the table. For all points located on the thick lines, the values of the invariants do not change. This means that the spectrum shown in (a) remains unchanged.

$\eta = 3/4$, $\theta = \pi/6$, and $\varphi = \pi/4$. So, S_0 , S_1 , and S_2 invariants [Eq. (1)] are equal to $(57/8)^{1/2}$, $-5/4$, $(217/64)^{1/2}$ (all in mm/s), respectively. The line positions [Eq. (6)] and intensities [Eq. (5)] as well as the absorption spectrum are shown in Fig. 1(a). In Fig. 1(b), as thick lines, we show all possible values of the V_{zz} , η , θ , and φ for which the invariants S_0 , S_1 , and S_2 and thus the spectrum remains unchanged. For clarity, only $0 \leq \theta \leq \pi/2$ and $0 \leq \varphi \leq \pi/2$ are shown in Fig. 1(b). Other values, such as V_{zz} , η , θ , and φ , can be obtained by mirror reflections with respect to the xy , xz , and yz planes in the PAS of the V tensor. Some numerical values, such as V_{zz} , η , θ , and φ , are given in Fig. 1(c).

Two important specific cases (e.g., for special choice of the hyperfine parameters) have to be mentioned. (i) If $\eta = 0$,

the problem has axial symmetry, and thus, in Fig. 1(b), there are additional circles ($\theta = \text{const}$, $0 \leq \varphi \leq 2\pi$). (ii) If in the considered case of axial symmetry the angle θ is a magic angle, i.e., $\cos \theta = 3^{-1/2}$, all invariants [Eq. (1)] expressed by $(V_{zz}, \eta, \theta, \varphi)$ will not contain terms linear in V_{zz} , thus making the determination of the sign of V_{zz} impossible. In that case, the pair of circles (for $\pm V_{zz}$) would overlap in Fig. 1(b).

III. PRINCIPLES OF DATA TREATMENT BASED ON THE INVARIANTS METHOD

Because line intensities and their positions are fully determined by four invariants: B , S_0 , S_1 , and S_2 , it is obvious that only these values (or their functions) could be extracted if no other information is available. Thus, it would be desirable to have a method in which fitted or simulated parameters were expressed in terms of B , S_0 , S_1 , and S_2 . In principle, one can construct such a routine based on Eqs. (1), (5), and (6), however, we propose a more convenient solution. The observation is that the thick lines, which show possible values of φ and θ [Fig. 1(b)] for constant values of B , S_0 , S_1 , and S_2 , always cross the meridian $\varphi = 0$ or $\varphi = \pi/2$, or equator $\theta = \pi/2$. This is quite a general situation, which is shown in the Appendix. Thus, one could use standard fitting packages, which properly treat mixed interactions, and in order to find hyperfine parameters describing the experimental data, one must check all possibilities related to the main meridians and the equator. By doing so, e.g., traveling on the main meridians and the equator with the angles θ and φ , we are sure of probing all possibilities of S_0 , S_1 , and S_2 invariants (see the Appendix for a mathematical proof).

IV. PROPERTY OF INTERMETALLIC UFe_5Sn COMPOUND

The intermetallic compound UFe_5Sn , discovered by Gonçalves *et al.*,²⁰ crystallizes in an orthorhombic CeCu_5Au -type structure (space group Pnma). The unit cell contains 4 U atoms located on the $4c$ site, 4 Sn atoms on $4c$, 8 Fe atoms on $8d$ (Fe1), and 12 Fe atoms on $4c$ (Fe2, Fe3, and Fe4) sites.²⁰ The relative populations of the iron atoms at the four different sites fulfill the 2:1:1:1 ratio. The iron atoms Fe1 and Fe3 have identical chemical nearest surroundings (3 uranium, 2 tin, 7 iron atoms), however, they differ by the arrangement of atoms. The surroundings of Fe2 and Fe4 are (3 uranium, 3 tin, 5 iron atoms) and (3 uranium, 1 tin, 8 iron atoms), respectively. According to magnetization data performed on a powder sample, UFe_5Sn shows a weak ferromagnetic behavior at room temperature and undergoes two magnetic transitions at 248 and 180 K.²⁰ The latter transition was reported to be magnetic-field dependent and disappears for $B_{\text{ext}} > 1$ T. It was reported also that the magnetization below 248 K strongly increases with decreasing temperature. More precise experiments on a single crystal²¹ have revealed that the transition at 248 K is associated with the ferromagnetic ordering of iron magnetic moments along the c axis, while anomalies observed at 180 K are associated with re-orientation of Fe moments toward the b axis. This conclusion was deduced partially from Mössbauer measurements. How-

ever, in our opinion, a more exact description of the UFe_5Sn spectra can be obtained by using the mixed hyperfine interactions instead of the first-order perturbation theory presented in Ref. 21. Since the electric quadrupolar interactions are not small with respect to the magnetic dipolar ones, the full Hamiltonian should be used for a correct description of the Mössbauer spectra.

An important initial step in the analysis involves the determination of the temperature behavior of parameters of hyperfine interactions expressed by invariants, which may describe properly the experimental Mössbauer spectrum.

V. SAMPLE PREPARATION

A single crystal of UFe_5Sn was grown by the Czochralski method. The sample characterization is given elsewhere.²² The powdered sample studied in this work was made by crushing part of a large single crystal, and the obtained powder was mixed with both Li_2CO_3 and epoxy glue. Such a preparation ensures the random distribution of the grains, resulting in a texture-free sample. The sample thickness used in our experiment was 12 mg UFe_5Sn per cm^2 .

VI. MÖSSBAUER MEASUREMENTS AND QUALITATIVE DESCRIPTION OF THE SPECTRA

Mössbauer measurements at various temperatures were carried out in a closed-cycle refrigerator equipped with an antivibration shroud. The source of radiation was ^{57}Co in a Cr matrix. The velocity scale was calibrated with respect to $\alpha\text{-Fe}$ at room temperature.

All spectra were analyzed initially by a commercial Mössbauer package "Normos" using a transmission integral.²³ Recoilless fraction of Fe atoms in UFe_5Sn was assumed to be the same as in $\alpha\text{-Fe}$.²⁴ The resulting values of the effective thickness of the absorber extrapolated to $T=0$ was estimated to be $\tau = 2.41 \pm 0.11$.

The Mössbauer spectrum measured at room temperature was fitted using two doublets with the same values of the width of the Lorentzian lines [$D(1), D(2)$], shown on the top of Fig. 2. The ratio of the areas of these two doublets is close to four, consistent with an assumption that a stronger doublet $D(1)$ is created by 8 Fe atoms at $8d$ and by 8 Fe atoms at $4c$ sites, while the $D(2)$ doublet is created by 4 Fe atoms at the $4c$ site. The difference of the isomer shift (IS) between the $D(2)$ and $D(1)$ doublets is 0.18 mm/s. Because the Sn atoms located in the nearest neighborhood (NN) of Fe should increase its IS,²⁵ the $D(2)$ doublet must be ascribed uniquely to the Fe2 site, which has three Sn atoms in the NN shell; NNs are located at distances ranging from 2.61 to 2.93 Å.²⁰ However, the overall situation may be more complicated. In particular, the Fe4 site has only one atom Sn in NN, with an interatomic distance of 2.77 Å, and no extra doublet connected with this site is resolved in the measured spectrum. The absorption lines are almost not broadened (their widths are almost equal to the widths of the lines in the calibration spectrum of $\alpha\text{-Fe}$). It is puzzling that three different sites (Fe1, Fe3, and Fe4) could be fitted by a single doublet. We will show in Sec. VII that some reasonable assumption about

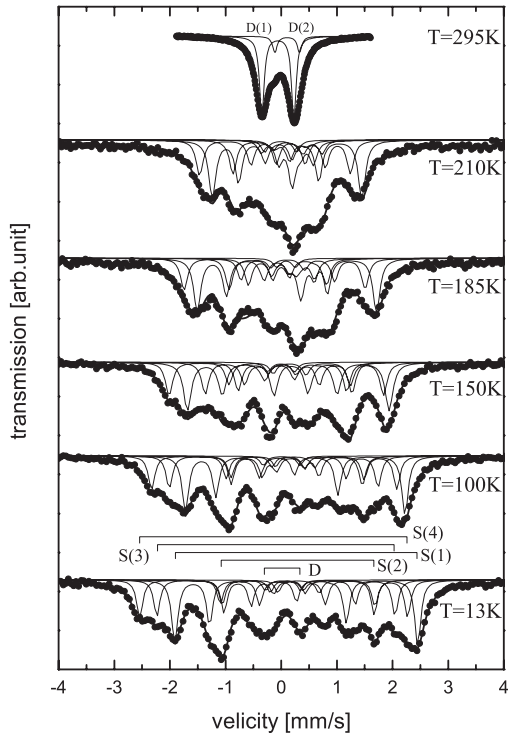


FIG. 2. Selected Mössbauer spectra taken at different temperatures. Solid lines represent the best simultaneous fit described in Sec. VIII.

temperature dependences of hyperfine interactions leads to the conclusion that these three sites have in fact slightly different parameters of hyperfine interactions, and the proposed method of invariants allows us to derive these parameters.

The selected Mössbauer spectra measured in the temperature range 13–295 K are presented in Fig. 2. The spectra from room temperature down to 250 K contain doublets only.

At $T=240$ K, the spectrum starts to broaden, indicating that from room temperature down to 240 K, the magnetic hyperfine field is equal to zero and the iron ions are in the paramagnetic state. The temperature where the broadening of the doublet is observed corresponds well with the first transition temperature previously reported in the magnetization measurements.²⁰ The spectra taken between 240 and 13 K exhibit a complicated magnetically split pattern, whose behavior must be connected with the four different local iron surroundings. The local values of the hmf gradually increase with decreasing temperature.

VII. RESULTS OF ANALYSIS WITH UNCONSTRAINED INVARIANTS METHOD

An initial analysis of the magnetically split spectra measured at 13 K was done using a full Hamiltonian and fitting four magnetic components $S(n)$ ($n=1,2,3,4$), and one doublet (D) located in the central part of spectra, all exhibiting very sharp lines (the width of the lines connected with the absorber is $\Gamma_a=0.13 \pm 0.01$ mm/s). Each sextet was fitted as described in Sec. III, and we were able to find the set of the invariants, which describe well the measured spectrum. Be-

cause the population of Fe at the 8d sites should be two times larger than those of the remaining sites, one expects that the most intense component $S(1)$ corresponds to the Fe1 site. Assuming that the hmf of Fe increases with the number of Fe atoms in the NN, such as in the case of U-Fe-Al (Ref. 26) and in Fe-Sn (Ref. 27) systems, one suspects that $S(2)$, $S(3)$, and $S(4)$ come from the Fe2, Fe3, and Fe4 sites, respectively. This conjecture is consistent with that reported in Ref. 21 and agrees well with the identification of the NN surrounding the small doublet observed in room-temperature data. However, in contrast to the previous results,²¹ the relative area under the doublet D observed at low temperatures is two times smaller than that of the sextet ($B_{hf}=2$ T).²¹ Because its relative area is small, the origin of this doublet is not clear at present. Nevertheless, a comparison of the hyperfine parameters obtained here indicates that the value of IS for the doublet D is close to that of the $S(3)$ component, which in turn implies that this doublet can be rather associated with the Fe3 site. However, it is difficult to understand why part of the iron atoms at the Fe3 site should be paramagnetic at $T=13$ K. Therefore, it seems more likely that the considered doublet results from a small fraction of Fe atoms located at an antisite positions, U, or Sn atoms. Two additional features, evidenced in the change in shapes of measured spectra, should be noticed.

The first important feature is visible on the left-hand side of the spectra measured at 13, 100, and 150 K shown in Fig. 2. The change in the first three lines located at velocities -2.6 , -2.2 , and -2.0 (mm/s, $T=13$ K) are attributed to the Fe4, Fe3, and Fe1 surroundings. The visible sequence of the intensities of respective lines at $T=13$ K and 100 K is: small, small, and large. If one looks at the spectrum obtained at $T=150$ K, this sequence is different: small, large, and small. This situation might occur if the hmf of the component due to the Fe3 surrounding decreases much faster with increasing temperature than the B_{hf} intensity of Fe1 and Fe4 sites.

The second feature visible in the change of spectral shapes appears between 150 and 185 K. The singlelike line seen in the central part of the spectra (at $v=0.3$ mm/s) at 185 K (Fig. 2) disappears at 150 K. Assuming that the EFG in metals is rather slightly dependent on temperature, a strong rearrangement of the line positions and the change in intensities are then presumably associated with a strong change of the direction of local magnetic moments in the PAS of the EFG for at least one iron position.

VIII. RESULTS OF SIMULTANEOUS FITS WITH CONSTRAINED INVARIANTS

Using invariants, we were able to find reasonably good fits to the spectra measured at low temperatures, where many absorption lines were narrow and relatively well separated. At temperatures higher than $T=200$ K, the spectra are strongly collapsed and there is a little hope for their proper decomposition. In this situation, we decided to fit simultaneously all measured spectra under some constraints stemming from physics of the problem:

(i) The relative intensities of the local components were kept constants for all spectra;

TABLE I. The local invariants ($6^{-1/2}S_0, S_1, S_2$), isomer shift (IS), and relative intensities extrapolated to $T=0$ K. The last row shows the site occupancies resulting from the crystal structure.

	$S(1)$	$S(4)$	$S(3)$	$S(2)$	D
IS (mm/s)	0.113 ± 0.005	0.078 ± 0.005	0.052 ± 0.03	0.23 ± 0.01	0.08 ± 0.01
$6^{-1/2}S_0$ (mm/s)	0.74	0.68	0.67	0.50	0.65
S_1 (mm/s)	0.8	-0.9	-0.5	0.52	—
S_2 (mm/s)	1.02	1.06	0.71	0.91	—
hmf (T)	13.3 ± 0.2	14.9 ± 0.2	13.1 ± 0.3	8.1 ± 0.2	0.0
I (%)	33 ± 2	23 ± 2	23 ± 4	17 ± 4	4 ± 3
$I_{\text{cryst.str.}}$ (%)	40	20	20	20	

(ii) the temperature behavior of the second-order Doppler (SOD) shift was approximated by the Debye model with the same value of the characteristic temperature for all iron sites;

(iii) the $T^{3/2}$ law for the EFG components was assumed. The experimental fact is that the temperature dependence of the EFG in various noncubic metals is approximated reasonably well by $V_{ij}(T) = V_{ij}(0)(1 - AT^{3/2})$, which results from the mean-square displacement of the host atoms.²⁸

The best results of simultaneous fit to all the spectra are presented in Fig. 2 by solid lines for all performed temperature measurements. The measured spectra are described very well although there are small misfits in the central part of spectra. The hyperfine parameters extrapolated to $T=0$ K are presented in Table I. The values of hyperfine parameters of the ground state presented can be directly compared with electronic structure calculations. The behavior of the isomer shift (and SOD shift) and hmf versus temperature are presented in Figs. 3(a) and 3(b), respectively. As one can see, the results of the IS can be divided into two groups. The surrounding of the Fe2 has clearly higher values of IS than those of the three remaining sites (Fe1, Fe3, and Fe4). If one considers the composition the NN, thus one can conclude that the increase in the IS of Fe2 sites is connected with a higher number of Sn atoms in the NN. The Sn atoms as a NN increase the value of the IS observed in the Fe nuclei.²⁵ In spite of that, such an influence is not visible on the Fe4 atoms that have only one Sn atom in the NN. Moreover, in spite of similar composition of the NN, the IS for Fe1 and Fe3 is different. It means that the IS depends not only on the composition of the NN but also on other factors, such as the symmetry and the local distances of the NN atoms. The Debye temperature that corresponds to the SOD shift shown in Fig. 3(a) is equal to (301 ± 10) K for all types of surroundings, in agreement with the value previously obtained by Gonçalves *et al.*²¹ The observed value is in the range typical for so-called 151 uranium compounds, UCu_5Al (329 K) (Ref. 29) and UCu_5Sn (250 K).³⁰

The temperature dependence of the local hmf is presented in Fig. 3(b). The onset of the nonzero hmf is visible slightly below 250 K, which agrees well with the temperature of the first transition observed in the magnetization measurements. Moreover, the unusual behavior of hmf of Fe3 is clearly observed. Its hmf decreases apparently faster than the hmf of the remaining components. The fastest decrease in the hmf for Fe3 is observed when the temperature approaches 170 K,

where the second anomaly was observed.^{20,21} In addition, one can see that the hmf of Fe1 and Fe4 have different values at $T=13$ K, and they become almost equal to each other at $T=170$ K.

The dependence of the local hyperfine field extrapolated to $T=0$ K on the number of iron atoms located in NN show an almost linear relation between these two quantities. The Fe atom in the NN increases the hmf by (2.3 ± 0.2) T.

Let us estimate the local iron magnetic moments at the ground state on the basis of the hmf extrapolated to $T=0$ K. In order to do that, one has to estimate the coupling constant between the hmf and iron magnetic moment on the basis of neutron and Mössbauer results for a similar class of compounds. One of the best choices is UFe_4Al_8 , which crystallizes in the tetragonal ThMn_{12} -type structure and under-

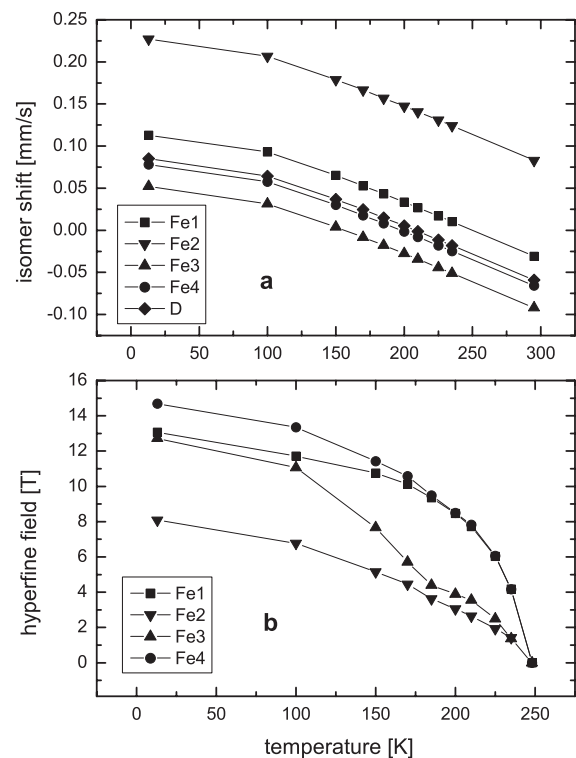


FIG. 3. The local isomer shift (a) and hyperfine magnetic field (b) vs temperature. The points on the isomer shift are calculated from the Debye model. The lines are guides to the eye.

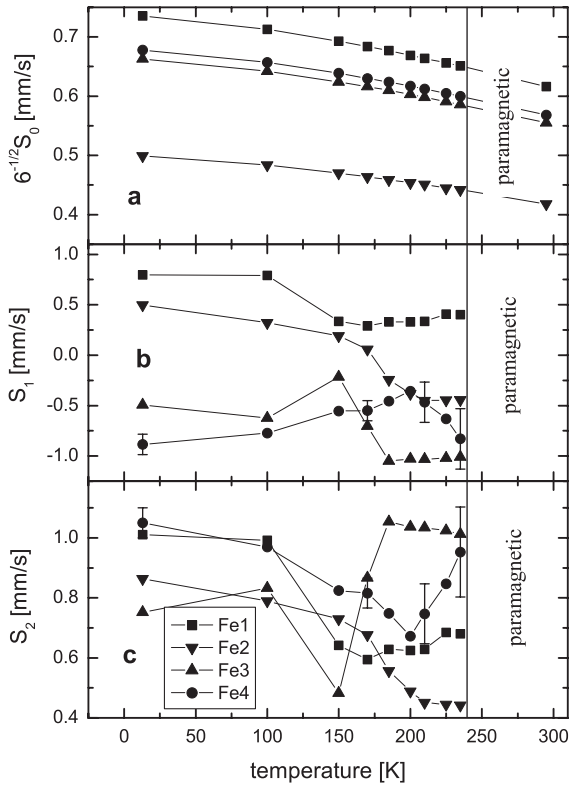


FIG. 4. Temperature dependence of invariants $6^{-1/2}S_0$, S_1 , S_2 for different Fe sites. The lines in (b) and (c) are guides to the eye.

goes a transition to magnetic state at $T=155$ K. The hmf of the latter compound at 13 K equals 11 T and the iron magnetic moment inferred from neutron-diffraction measurements is $\mu_{\text{Fe}}=1.04 \mu_B$.³¹ So in this case the coupling constant is equal to $0.095 \mu_B/\text{T}$. Using this value, the estimated local Fe magnetic moments in UFe_5Sn are $\mu_{\text{Fe1}}=1.27 \mu_B$, $\mu_{\text{Fe2}}=0.76 \mu_B$, $\mu_{\text{Fe3}}=1.24 \mu_B$, and $\mu_{\text{Fe4}}=1.41 \mu_B$. Based on the value of the saturation magnetic moment per formula unit extrapolated to $T=0$ K and being equal to $5 \mu_B$,²⁰ occupations of the local sites by iron atoms, and taking also the assumption that the Fe moments are collinear, the uranium atom would acquire a magnetic moment of $\mu_{\text{U}}=-0.79 \mu_B$. In other words, the direction of the uranium magnetic moments becomes opposite to the direction of the iron magnetic moments, as expected from the results given in Ref. 32.

The temperature dependence of invariants S_0 , S_1 , and S_2 are presented in Figs. 4(a)–4(c), respectively. The invariant S_0 reflects a $(1-A \cdot T^{3/2})$ dependence assumed above. The obtained value $A=(3.0 \pm 0.1) \times 10^{-5} \text{ K}^{-3/2}$ confirms our assumption about the lattice dynamics' origin of the EFG temperature dependence. Indeed, recent *ab initio* calculations show that A is a positive constant in a range 10^{-4} – $10^{-5} \text{ K}^{-3/2}$ and in many cases reproduces well the temperature dependence of the V_{zz} .³³ Values of the S_0 parameter for different Fe sites, similar to the IS, can be divided into two groups. The values observed for Fe2 have smaller values compared to those of the remaining sites. Moreover, the values for the sites with the same average volumetric constraints Fe1 and Fe3 show different values. It means that the value of the EFG reflects the symmetry of local surroundings rather than the

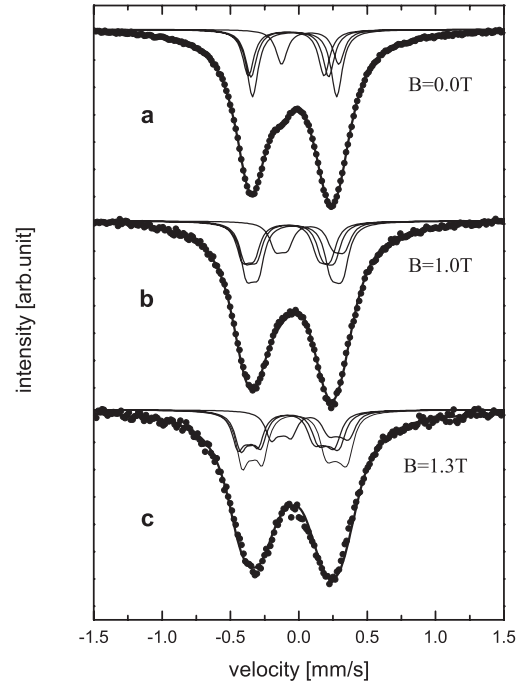


FIG. 5. The Mössbauer spectra measured at room temperature in the external magnetic field parallel to the gamma beam. The solid thick lines in (a) represent the best simultaneous fits for the first model from Sec. VIII. The solid thick lines in (b) and (c) represent the best fit using fixed values of invariants obtained in the simultaneous fit and assuming $\eta=0$ for all local iron sites. The experimental data for $B=0$ are the same as shown on the top of Fig. 2.

distances and composition of the NN. The use of constraints for temperature dependence of some hyperfine parameters allow us to show that the singlelike doublet in the room-temperature spectrum, discussed in Sec. VI, should be considered as three components for Fe1, Fe3, and Fe4 sites with a similar value for parameter S_0 , while this parameter for Fe2 differs clearly from those of the remaining Fe sites, as shown in Fig. 5(a) and Table II.

The invariants S_1 and S_2 , which reflect an orientation of the hmf pseudovector in the PAS of the EFG, show a clear discontinuity around $T=170$ K for Fe3 sites [Figs. 4(b) and 4(c)]. This discontinuity is much more visible on the invariant S_2 than for S_1 . This is correlated with a fast decrease in the value of the hmf. The behavior of the S_1 invariant of Fe2 shows relatively high amplitudes of change and also a change in the sign in the temperature range 170–200 K. The

TABLE II. Invariant $6^{-1/2}S_0$ and isomer shift (IS) from room-temperature measurement.

	$6^{-1/2}S_0$	IS (mm/s)
$S(1)$	0.62	-0.031 ± 0.005
$S(2)$	0.42	0.083 ± 0.005
$S(3)$	0.56	-0.092 ± 0.005
$S(4)$	0.57	-0.066 ± 0.005
D	0.54	-0.059 ± 0.005

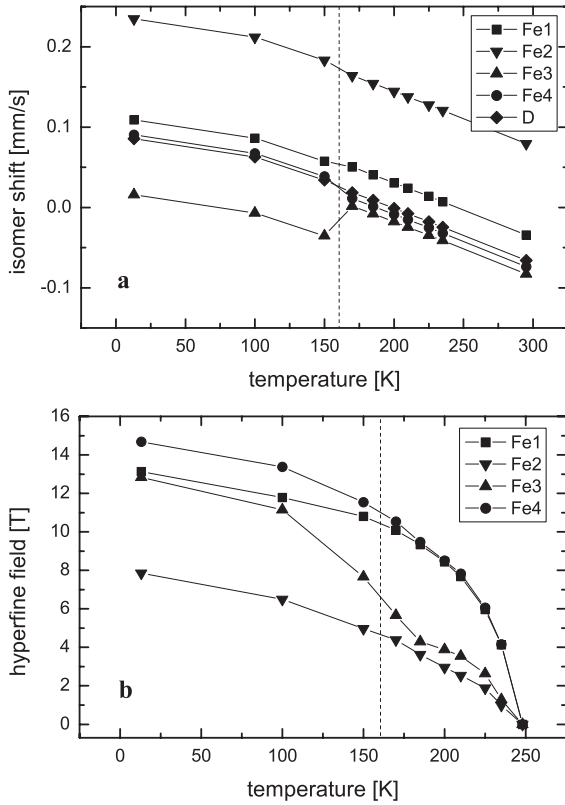


FIG. 6. The isomer shifts (a) and hyperfine magnetic fields (b) vs temperature. The second-order Doppler shift was calculated within the second model described in the text.

invariants for the remaining sites behave much more smoothly, although even these for Fe1 show a decrease but in the temperature between 150 and 170 K.

The invariants S_1 and S_2 can be determined only in the temperature range for which the hmf is nonzero. Thus, the increase of S_1 with a temperature for Fe4 at around $T = 235$ K is, in our opinion, connected with an analysis of poorly resolved spectra and has no physical meaning. Since the temperature dependences of S_1 and S_2 indicate a sudden change around $T = 170$ K, one has to consider a possibility of the phase transition and thus the change in the electronic structure. We have performed simultaneous fits under an assumption that is similar to that discussed at the beginning of this section, where the possibility of the temperature discontinuity in both the IS and EFG was allowed (in the vicinity of $T = 170$ K). This was made in such a way that for every Fe surrounding a step function was used, e.g., for the center shift (CS) of the components: $CS = SOD(T) + IS$ for $T < 170$ K, while $CS = SOD(T) + IS + \delta IS$ for $T > 170$ K, where δIS was an additional free parameter [see Fig. 6(a)]. Similarly, for the components of the EFG: $V_{ij}(T) = V_{ij}(0)(1 - A \cdot T^{3/2})$ for $T < 170$ K, while $V_{ij}(T) = [V_{ij}(0) + \delta V_{ij}](1 - A \cdot T^{3/2})$ for $T > 170$ K, where δV_{ij} were additional free parameters, see Fig. 7(a). This model fits slightly better for all the measured spectra, particularly in their central part. The obtained results of the IS and hmf are presented in Figs. 6(a) and 6(b), respectively. The behavior of the local hmf shows practically the same picture as that in the first model. It

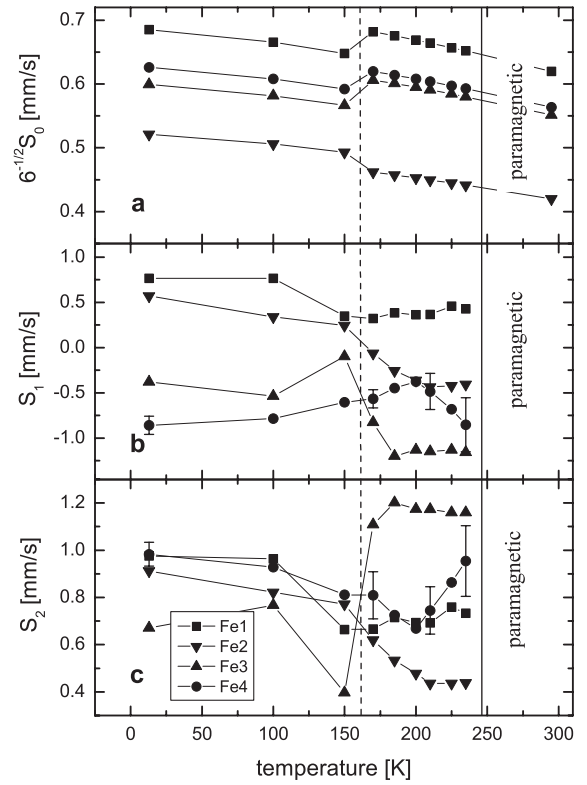


FIG. 7. Temperature dependence of invariants $6^{-1/2}S_0$, S_1 , S_2 for different Fe sites assuming the possibility of a transition at a temperature of about 170 K. The lines are guides to the eye.

means that this parameter is not sensitive to the assumption about discontinuity. On the other hand, the behavior of the isomer shift [Fig. 6(a)] shows a distinct discontinuity for the Fe3 site, while those for the remaining sites are disturbed weakly. Within the scope of this model, the strong reduction of the Fe3 hmf is presumably associated with the change in the electronic structure, and also reflected in the IS at this site.

The temperature dependence of the S_0 , S_1 , and S_2 invariants is presented in Figs. 7(a)–7(c), respectively. As one can see, the possibility of the transition around 170 K is connected with the discontinuity of the S_0 invariant clearly visible on all iron sites. For the Fe2 site the invariant decreases crossing 170 K toward a higher temperature, while for the remaining sites the invariants increase. The results obtained for the invariants S_1 and S_2 do not differ much from the results found within the first model. So, the conclusions are the same as for the first model.

To recapitulate, the results presented above lead to the following conclusions:

- (i) The hmf on Fe3 sites decreases with increasing temperature much faster than those on the remaining sites, and the fastest change takes place at around 170 K.
- (ii) The discontinuity in the temperature dependence of the invariants S_1 and S_2 for the Fe3 sites is connected with a change of orientation of the magnetic moments of Fe3 with respect to the PAS.
- (iii) The invariant S_0 reflects a $(1 - A \cdot T^{3/2})$ dependence originating from lattice dynamics with the value $A = (3.0 \pm 0.1) \times 10^{-5} \text{ K}^{-3/2}$.

(iv) The electronic structure of the studied compound may change at around 170 K.

IX. IN EXTERNAL MAGNETIC-FIELD ROOM-TEMPERATURE MEASUREMENTS

In order to get the iron local invariants in the paramagnetic state, measurements in $B_{\text{ext}}=1$ T and 1.3 T external magnetic fields parallel to the gamma beam were carried out. The measured spectra are presented in Figs. 5(b) and 5(c). As one can see, the influence of the external magnetic field on the shape of the spectra is rather small. The spectra were analyzed according to the procedure given by Blaes *et al.*,³⁴ where random distribution of the EFG and the fixed direction of the hmf (B_{hf}) induced by an external magnetic field have been assumed. In principle, this kind of analysis can provide information about the local asymmetry parameter as well as the values of the local EFG. Unfortunately, because the applied field is too small with respect to the quadrupole interactions, the spectra presented in Figs. 5(b) and 5(c) are not well resolved, so the separation of these two quantities is a difficult task. Future experiments in higher external fields are needed in order to obtain these quantities. The solid thick lines in Fig. 5 represent the fits with invariants obtained by the method described in Sec. VII with the assumption of $\eta=0$ for all iron local surroundings. It should be stressed that only one free parameter, namely, the hmf, was used in the fit. As one can see, the theoretical curves fit well to the experimental points. However, the analysis reveals that the observed hyperfine fields are 0.61 T and 0.38 T for $B_{\text{ext}}=1.3$ T and 1 T, respectively. It means that the induced local hmf's are relatively large and directed antiparallel to the applied external field. This observation agrees well with the results of magnetization measurements, where one could detect a weak ferromagnetic component in the compound still existing at room temperature, i.e., fairly far above T_c .

X. CONCLUSIONS

High quality texture-free absorbers, prepared from a powdered UFe_5Sn single crystal and the use of a constrained invariant method, allowed us to interpret the shapes of the Mössbauer spectra at different temperatures, in terms of the contributions coming from separated Fe components. The theoretical intensities agree very well with the site occupancies resulting from the crystal structure. The presented method of invariants, dedicated for texture-free samples, may have potential application in material science and geology, where powdered absorbers are widely used.

Parameters of hyperfine interactions including hmf, IS, and invariants constructed from the EFG tensor and the hmf pseudovector for the ground state of UFe_5Sn were determined. These values could be directly compared with the results of electronic band-structure calculations. The proposed method of data treatment avoids any inconsistency caused by an ambiguity problem, although the hyperfine information is still incomplete.

Mössbauer spectra of UFe_5Sn measured at different temperatures show that all iron ions in the compound are para-

magnetic at room temperature. The measurements carried out in the external magnetic field show that the hmf's observed on Fe nuclei are much smaller than those of an applied B_{ext} .

The temperature behavior of the hmf shows that the iron atoms order magnetically at $T=250$ K, indicating that the transition is mainly due to the ordering of the iron magnetic moments.

Our Mössbauer data imply that the transition observed in the magnetization data at $T\sim 180$ K is associated with a much faster decrease of hmf with temperature on Fe3 atoms (as compared with the behavior of the other local hmf's), and with the distinct change of the invariants S_1 and S_2 for Fe3, and likely for Fe2 sites.

The analysis of Fe at different sites—the spectrum measured at $T=13$ K—shows that the magnetic moments of Fe at different sites are linearly correlated with the number of NN iron atoms. Using a coupling constant derived from the UFe_4Al_8 compound,³¹ the contribution of the iron magnetic moments to the spontaneous magnetization per formula unit was found to be $\mu=5.79 \mu_B$, and the magnetic moments of uranium atoms are estimated to be $-0.79 \mu_B$, which are antiparallel to the iron magnetic moments.

ACKNOWLEDGMENTS

The authors thank J. Cieśliński and A. P. Gonçalves for helpful discussions. The work was partially supported as a research project by the funds allocated for scientific research for the years 2008–2011.

APPENDIX

1. Lemma 1

Let \mathbf{V} and \mathbf{m} be a traceless, symmetric, real tensor, and a unit vector, respectively (both in \mathbb{R}^3). Let us define p , q , and r according to Eqs. (1) and (4). Without losing generality, we may assume that $a=v_B=1$, because this results in simple scaling of all components of \mathbf{V} . There exists the traceless, symmetric, real tensor $\mathbf{\Omega}$ and the unit vector \mathbf{n} for which equalities Eqs. (1) and (4) hold (upon replacement $\mathbf{V}\rightarrow\mathbf{\Omega}$ and $\mathbf{m}\rightarrow\mathbf{n}$) and \mathbf{n} is perpendicular to one of the diagonal directions of $\mathbf{\Omega}$.

Proof

Without losing generality, we may choose $\mathbf{n}^T=(100)$. We will find an explicit form of the $\mathbf{\Omega}$. Let us assume that the diagonal direction is (001). Thus

$$\mathbf{\Omega} = \begin{bmatrix} \Omega_{11} & \Omega_{12} & 0 \\ \Omega_{21} & \Omega_{22} & 0 \\ 0 & 0 & -\Omega_{11} - \Omega_{22} \end{bmatrix}, \quad (\text{A1})$$

then

$$\mathbf{n}^T \cdot \mathbf{\Omega} \cdot \mathbf{n} = \Omega_{11},$$

$$\mathbf{n}^T \cdot \mathbf{\Omega}^2 \cdot \mathbf{n} = \Omega_{11}^2 + \Omega_{12}\Omega_{21},$$

$$\text{Tr } \boldsymbol{\Omega}^2 = 2\Omega_{11}^2 + 2\Omega_{22}^2 + 2\Omega_{11}\Omega_{22} + 2\Omega_{12}\Omega_{21}. \quad (\text{A2})$$

Thus, using definition (2) and solving Eq. (A2), four solutions are obtained:

$$\begin{aligned} \Omega_{11} &= \frac{-q}{16}, \\ \Omega_{12} = \Omega_{21} &= \pm \frac{1}{16} \sqrt{64 + 4p(8+p) - q^2 - 16r}, \\ \Omega_{22} &= \frac{1}{32} [q \pm \sqrt{q^2 - 16p(32+p) + 64(r-64)}]. \end{aligned} \quad (\text{A3})$$

Among these four solutions, there are two pairs. Each pair has the same eigenvalues and the eigenvectors, which differ by mirror reflection with respect to the xy , xz , or yz planes. Thus, Eq. (A3) is an explicit expression for the traceless, symmetric tensor $\boldsymbol{\Omega}$. Equation (A3) is real only when the expressions under square roots are not negative. Using abbreviations (1) and (4), these two conditions are equivalent to

$$\mathbf{m}^T \cdot \mathbf{V}^2 \cdot \mathbf{m} - (\mathbf{m}^T \cdot \mathbf{V} \cdot \mathbf{m})^2 \geq 0, \quad (\text{A4})$$

$$(\mathbf{m}^T \cdot \mathbf{V} \cdot \mathbf{m})^2 + 2 \text{Tr } \mathbf{V}^2 - 4\mathbf{m}^T \cdot \mathbf{V}^2 \cdot \mathbf{m} \geq 0. \quad (\text{A5})$$

Inequality (A4) follows from the properties of the scalar product. Indeed, for any two vectors \mathbf{a} and \mathbf{b} , we have

$$a^2 b^2 \geq (\mathbf{a} \cdot \mathbf{b})^2. \quad (\text{A6})$$

Let us take $\mathbf{a} = \mathbf{V} \cdot \mathbf{m}$, $\mathbf{b} = \mathbf{m}$. Inserting these \mathbf{a} and \mathbf{b} into Eq. (A6), we get Eq. (A4). Inequality (A5) is valid for any traceless Hermitian matrix in R^3 , as a result of Lemma 2.

2. Lemma 2

For a traceless, Hermitian matrix V in R^3 and a unit vector \mathbf{m} , the following inequality holds:

$$(\mathbf{m}^T \cdot \mathbf{V} \cdot \mathbf{m})^2 + 2 \text{Tr } \mathbf{V}^2 - 4\mathbf{m}^T \cdot \mathbf{V}^2 \cdot \mathbf{m} \geq 0. \quad (\text{A7})$$

Proof

Without losing generality we may choose a coordination system in which \mathbf{m} will have only one nonzero coordinate, e.g., $\mathbf{m}^T = (1, 0, 0)$. In this system,

$$(\mathbf{m}^T \cdot \mathbf{V} \cdot \mathbf{m}) = V_{11},$$

$$(\mathbf{m}^T \cdot \mathbf{V}^2 \cdot \mathbf{m}) = V_{11}^2 + V_{12}V_{21} + V_{13}V_{31},$$

$$\text{Tr } \mathbf{V}^2 = V_{11}^2 + V_{22}^2 + V_{33}^2 + 2(V_{12}V_{21} + V_{13}V_{31} + V_{23}V_{32}). \quad (\text{A8})$$

Let us abbreviate:

$$F \equiv (\mathbf{m}^T \cdot \mathbf{V} \cdot \mathbf{m})^2 + 2 \text{Tr } \mathbf{V}^2 - 4\mathbf{m}^T \cdot \mathbf{V}^2 \cdot \mathbf{m}, \quad (\text{A9})$$

thus

$$\begin{aligned} F &= V_{11}^2 + 2(V_{11}^2 + V_{22}^2 + V_{33}^2) + 4(V_{12}V_{21} + V_{13}V_{31} + V_{23}V_{32}) \\ &\quad - 4(V_{11}^2 + V_{12}V_{21} + V_{13}V_{31}) \\ &= (V_{22}^2 + V_{33}^2) - V_{11}^2 + 4V_{23}V_{32}. \end{aligned} \quad (\text{A10})$$

For the traceless and Hermitian matrix

$$V_{11} = -(V_{22} + V_{33}) \quad \text{and} \quad V_{23}V_{32} \geq 0, \quad (\text{A11})$$

hence,

$$F = (V_{22} - V_{33})^2 + 4V_{23}V_{32} \geq 0. \quad (\text{A12})$$

¹S. W. Karyagin, Fiz. Tverd. Tela (Leningrad) **8**, 493 (1966) [Sov. Phys. Solid State **8**, 391 (1966)].

²P. G. L. Williams and G. M. Bancroft, Moessbauer Eff. Methodol. **7**, 39 (1971).

³L. J. Dąbrowski, J. Piekoszewski, and J. Suwalski, Nucl. Instrum. Methods **91**, 93 (1971).

⁴L. J. Dąbrowski, J. Piekoszewski, and J. Suwalski, Nucl. Instrum. Methods **103**, 545 (1972).

⁵J. Dongen Torman, R. Jagannathan, and J. M. Trooster, Hyperfine Interact. **1**, 135 (1975).

⁶H. Spiering, Nucl. Instrum. Methods **154**, 295 (1978).

⁷G. K. Wertheim, Phys. Rev. **121**, 63 (1961).

⁸D. Barb, D. Tarina, A. Ito, and S. Morimoto, J. Phys. C **14**, 497 (1981).

⁹K. Szymański, Phys. Rep. **423**, 295 (2006).

¹⁰G. Le Caër and R. A. Brand, J. Phys.: Condens. Matter **10**, 10715 (1998).

¹¹L. Dobrzyński, K. Szymański, and D. Satuła, Nukleonika **49**, S89 (2004).

¹²T. C. Gibb and N. N. Greenwood, *Mössbauer Spectroscopy* (Chapman and Hall, London, UK, 1971), pp. 63–72.

¹³K. Szymański, J. Phys.: Condens. Matter **12**, 7495 (2000).

¹⁴P. Zory, Phys. Rev. **140**, A1401 (1965).

¹⁵R. Ingalls, K. Ono, and L. Chandler, Phys. Rev. **172**, 295 (1968).

¹⁶R. Zimmermann, Nucl. Instrum. Methods **128**, 537 (1975).

¹⁷R. Zimmermann, Chem. Phys. Lett. **34**, 416 (1975).

¹⁸L. Häggström, University of Uppsala Report No. UIIP-851, 1974 (unpublished).

¹⁹O. C. Kistner and A. W. Sunyar, Phys. Rev. Lett. **4**, 412 (1960).

²⁰A. P. Gonçalves, M. Godinho, and H. Noel, J. Solid State Chem. **154**, 551 (2000).

²¹A. P. Gonçalves, J. C. Waerenborgh, M. Almeida, M. Godinho, I. Catarino, G. Bonfait, and H. Noel, J. Magn. Magn. Mater. **260**, 473 (2003).

²²R. Troć, C. Sułkowski, and H. Misiorek (to be published).

²³S. Margulies and J. R. Ehrman, Nucl. Instrum. Methods **12**, 131 (1961).

²⁴U. Bergmann, S. D. Shastri, D. P. Siddons, B. W. Batterman, and J. B. Hastings, Phys. Rev. B **50**, 5957 (1994).

²⁵H. Akai, S. Blugel, R. Zeller, and P. H. Dederichs, Phys. Rev. Lett. **56**, 2407 (1986).

²⁶J. C. Waerenborgh, A. P. Gonçalves, and M. Almeida, Solid State

- Commun. **110**, 369 (1999).
- ²⁷I. Vincze and A. T. Aldred, Phys. Rev. B **9**, 3845 (1974).
- ²⁸B. Kolk, *Studies of Dynamical Properties of Solids with the Mössbauer Effect* (Elsevier Science, New York, 1984).
- ²⁹V. H. Tran, R. Troć, J. Stepień-Damm, T. Komatsubara, F. Steglich, R. Hauser, and E. Bauer, Phys. Rev. B **66**, 054421 (2002).
- ³⁰V. H. Tran, R. Troć, A. Czopnik, Z. Henkie, A. Jeżowski, D. Włosewicz, and F. Steglich, Acta Phys. Pol. B **34**, 1133 (2003).
- ³¹K. Rećko, M. Biernacka, L. Dobrzyński, K. Perzyńska, D. Satuła, K. Szymański, J. Waliszewski, W. Suski, K. Wochowski, G. Andre, and F. Bouree, J. Phys.: Condens. Matter **9**, 9541 (1997).
- ³²A. Szajek and W. L. Malinowski, Phys. Status Solidi B **236**, 548 (2003).
- ³³D. Torumba, K. Parlinski, M. Rots, and S. Cottenier, Phys. Rev. B **74**, 144304 (2006).
- ³⁴N. Blaes, H. Fisher, and U. Gonser, Nucl. Instrum. Methods Phys. Res. B **9**, 201 (1985).

P15

The method of invariants applied to the analysis of ^{57}Fe Mössbauer spectra

K. Szymański · D. Satuła · L. Dobrzyński

Published online: 1 April 2009
© Springer Science + Business Media B.V. 2009

Abstract A method for Mössbauer data treatment is proposed for texture-free samples, easily obtained as powdered absorbers. Although the results of the analysis do not contain full information about the parameters of hyperfine interactions, they are free of ambiguity typical for $3/2-1/2$ nuclear-spin transitions because only experimentally available information is being considered. The method is particularly useful in cases where mixed interactions, e.g. magnetic dipole and electric quadrupole interactions are present. The method could be easily employed with the help of widely used standard Mössbauer packages when some constraints are applied. Advantages of the suggested procedure are illustrated on the example of interpretation of the Mössbauer spectra of UFe_5Sn alloy characterized by many inequivalent sites of iron.

Keywords Data analysis · Methodology · Intermetallics · Ambiguity problem · UFe_5Sn

1 Introduction

The details of the hyperfine structure cannot be unambiguously determined from the Mössbauer spectrum of a randomly oriented, thin absorber in which mixed interactions e.g., magnetic dipole and electric quadrupole are present [1] and relates to the so called ambiguity problem. The information obtained by Mössbauer spectroscopic methods for randomly oriented absorber is poorer than in the case of using single

K. Szymański (✉) · D. Satuła · L. Dobrzyński
Faculty of Physics, University of Białystok, Lipowa, 41 15-424, Białystok, Poland
e-mail: kszym@alpha.uwb.edu.pl

L. Dobrzyński
The Andrzej Sołtan Institute for Nuclear Studies, 05-400, Otwock-Świerk, Poland

crystals. However availability of powders and difficulties with some single-crystal growth make use of powdered absorbers still highly desirable. Thus, the ambiguity problem has to be properly treated. The aim of the paper is a demonstration of an effective method of Mössbauer data treatment. An unquestionable advantage of the method stems from the possibility of using (under proposed interpretation) the results obtained by standard Mössbauer packages equipped in full Hamiltonian formalism.

2 Mössbauer spectrum expressed by invariants

Line positions in the Mössbauer spectra of texture free absorbers can be given explicitly by invariants S_0 , S_1 , S_2 constructed from the electric field gradient (*EFG*) tensor \mathbf{V} and the hyperfine magnetic field (*hmf*) pseudovector \mathbf{B} [2]:

$$\begin{aligned} S_0 &= a\sqrt{\text{Tr}\mathbf{V}^2}, \\ S_1 &= a\mathbf{m}^T \cdot \mathbf{V} \cdot \mathbf{m}, \\ S_2 &= a\sqrt{\mathbf{m}^T \cdot \mathbf{V}^2 \cdot \mathbf{m}}, \end{aligned} \quad (1)$$

where

$$a = eQc/E_\gamma \quad (2)$$

is the proportionality constant between the *EFG* components (in [V/m²] SI units) and the invariants expressed conveniently for applications in [mm/s]. Q is the nuclear quadrupole moment, e is the elementary charge, c is the speed of light, E_γ is the energy between the ground and the excited state, $\mathbf{m} = \mathbf{B}/B$.

The invariants S_0 , S_1 , and S_2 have clear physical interpretation. In Eq. 1, $6^{-1/2}S_0$ appears to be equal to $aV_{zz}(1 + \eta^2/3)^{1/2}/2$ and would be just a separation between $I_e = 3/2$ nuclear sublevels when the *hmf* is zero. The S_1 is the component of the *EFG* tensor \mathbf{V} in the direction of the *hmf*. Its sign may be positive or negative and S_1 is proportional to the shift of the absorption lines 2, 3, 4, 5 with respect to the lines 1 and 6 in the Zeeman sextet, caused by a small quadrupole interaction in the first-order approximation. The square of invariant S_2 is the component of the \mathbf{V}^2 in the direction of the *hmf*. S_2 is also the length of the vector \mathbf{Vm} .

The secular equation for the eigenvalues E of the excited $I_e = 3/2$ state is

$$\lambda^4 + p\lambda^2 + q\lambda + r = 0, \quad \lambda = 2E/v, \quad (3)$$

where $v = g_{3/2}\mu_N Bc/E_\gamma$ is the Zeeman splitting between $I_e = 3/2$ sublevels expressed in velocity units, μ_N nuclear magneton, $g_{3/2}$ nuclear g -factor of the excited state. The coefficients p , q , and r are:

$$\begin{aligned} p &= -10 - \frac{1}{3}(S_0/v)^2, \\ q &= -8S_1/v, \\ r &= \frac{1}{4}(p+4)^2 - 4(S_2/v)^2. \end{aligned} \quad (4)$$

The absorption line intensity for a randomly oriented absorber in the case of a $3/2 \rightarrow 1/2$ magnetic dipolar transition is proportional to the trace of the intensity tensor $\mathbf{I}_{\alpha\beta}$ [3]:

$$\text{Tr } \mathbf{I}_{\alpha\beta} = \frac{3}{8} + \beta \frac{40\lambda_\alpha^2 - 4q\lambda_\alpha + (p+4)(p+16) - 4r}{16(4\lambda_\alpha^3 + 2p\lambda_\alpha + q)} \quad (5)$$

The index $\beta = \pm 1$ corresponds to two ground states, while four eigenvalues λ_α are roots of secular Eq. 3. The line positions $\nu_{\alpha\beta}$ (expressed conveniently in the velocity units) are:

$$\nu_{\alpha\beta} = (\lambda_\alpha - \beta g_{1/2}/g_{3/2}) \nu/2 \quad (6)$$

where $g_{1/2}$ nuclear g -factor of the ground state.

The results (Eqs. 1, 5 and 6) uniquely determining the absorption line positions and intensities, depend on four invariants only: B , S_0 , S_1 , S_2 , while there are five independent hyperfine parameters: B , θ , φ , V_{zz} , and η , where θ , φ are polar and azimuthal angles of the \mathbf{B} vector in the principal axes system (PAS) of the \mathbf{V} tensor, η is the asymmetry parameter [1, 2]. Because the spectrum depends on only four independent invariants, there is continuum of different values of hyperfine parameters (B , θ , φ , V_{zz} , and η) resulting in the same shape of the Mössbauer spectrum. This is the cause of the aforementioned ambiguity.

3 Data treatment based on the invariants method

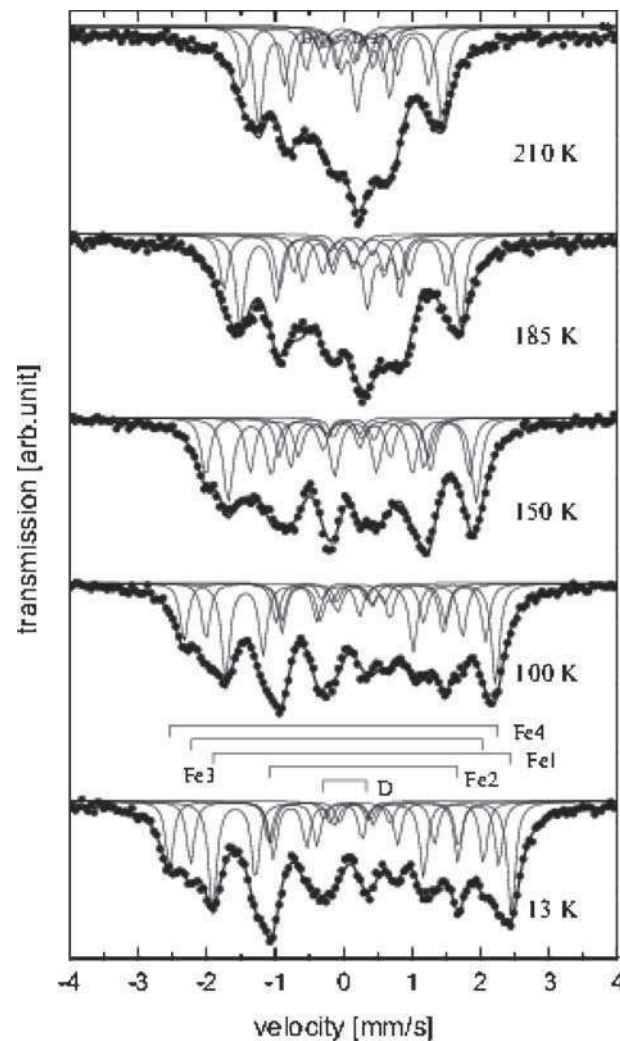
From previous paragraph it follows that the only information which can be extracted unambiguously from the Mössbauer spectrum are the values of four invariants: B , S_0 , S_1 and S_2 (or their functions). It was proved [3] that the commonly used parameters: B , V_{zz} , η and properly constrained orientation of the \mathbf{B} in the PAS of the EFG guarantee correct determination of invariants (1).

The practical recipe for fitting of texture free absorber is as follows. One has to use any Mössbauer package equipped in full Hamiltonian option and perform fit with free parameters B , θ , φ , V_{zz} , η under the constraint: $\varphi = 0$ or $\varphi = \pi/2$ or $\theta = \pi/2$ (which is equivalent that the \mathbf{B} is perpendicular to one of the main axis of the PAS of the EFG). The parameters θ , φ , V_{zz} , and η , have to be used for calculation of invariants (1) with explicit form:

$$\begin{aligned} S_0 &= \frac{a|V_{zz}|}{\sqrt{6}} \sqrt{1 + \frac{1}{3}\eta^2}, \\ S_1 &= \frac{aV_{zz}}{2} (3 \cos^2 \theta - 1 + \eta \cos 2\varphi \sin^2 \theta), \\ S_2 &= \frac{a|V_{zz}|}{2} \sqrt{4 - (3 - 2\eta \cos 2\varphi + \eta^2) \sin^2 \theta}, \end{aligned} \quad (7)$$

These invariants (and the hyperfine magnetic field B) are the physically valid parameters, which can be extracted from the spectra of texture free absorbers. The

Fig. 1 Selected Mössbauer spectra taken at different temperatures. *Solid lines* represent the best simultaneous fit of the components dependent on the constrained invariants

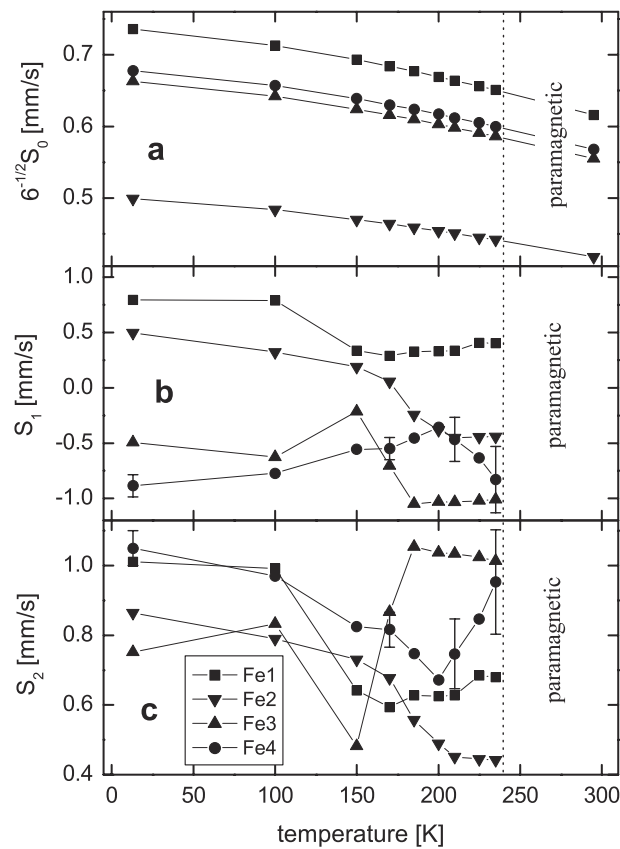


invariants (1) can be compared with theoretical calculations in which all hyperfine parameters, e.g. B , θ , φ , V_{zz} , and η , are available.

4 Example of application: UFe_5Sn studies

The UFe_5Sn compound crystallizes in an orthorhombic CeCu_5Au -type structure (space group Pnma) [4]. The unit cell contains 4 U atoms located on the 4c site, 4 Sn atoms on 4c, 8 Fe atoms on 8d (Fe1), and 12 Fe atoms on 4c (Fe2, Fe3, and Fe4) sites [4]. The relative populations of the iron atoms at the four different sites fulfil the 2:1:1:1 ratio. According to magnetization data performed on a powder sample, UFe_5Sn shows a weak ferromagnetic behaviour at room temperature and undergoes two magnetic transitions at 248 and 180 K [4]. Experiments on a single crystal [5] have

Fig. 2 Temperature dependence of invariants $6^{-1/2}S_0$, S_1 , S_2 for different Fe sites. The *lines* in **a** shows $T^{3/2}$ dependence while in **b** and **c** are guides to the eye

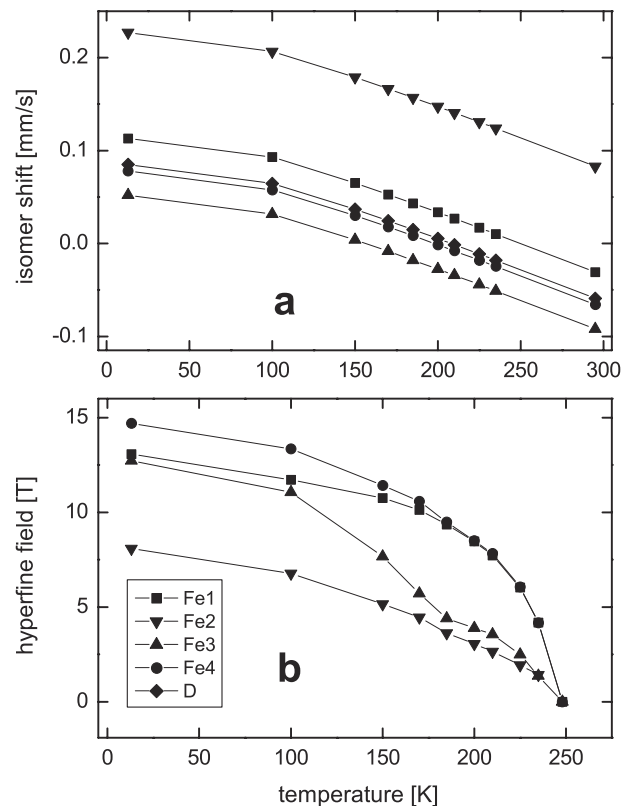


revealed that the transition at 248 K is associated with the ferromagnetic ordering of iron magnetic moments along the c axis, while anomalies observed at 180 K are associated with reorientation of Fe moments toward the b axis. The results of Mössbauer measurements of UFe_5Sn show apparent inconsistencies with first order perturbation approximation [5], since the ratio of quadrupolar electric to dipolar magnetic interaction is not a small parameter. Thus the full Hamiltonian has to be used for proper analysis.

All spectra measured in the temperature range 13–295 K were fitted simultaneously under some constraints stemming from physics of the problem: (i) the relative intensities of the local components were kept constants for all spectra; (ii) the temperature behaviour of the second-order Doppler (SOD) shift was approximated by the Debye model; (iii) the $T^{3/2}$ law for the EFG components was assumed [6]. Selected spectra and results of fits are shown in Fig. 1. The temperature dependence of invariants S_0 , S_1 , and S_2 are presented in Fig. 2. The invariant S_0 reflects assumed $(1 - A \cdot T^{3/2})$ dependence. The obtained value $A = (3.0 \pm 0.1) \cdot 10^{-5} \text{ K}^{3/2}$ agrees with recent *ab initio* calculations [6].

The results of the isomer shift is shown in Fig. 3a. The Debye temperature that corresponds to the SOD shift shown in Fig. 3a is equal to (301 ± 10) K for all types of surroundings, in agreement with the reported value [5].

Fig. 3 The local isomer shift and the second order Doppler shift calculated within Debye approximation (a) and hyperfine magnetic field (b) vs temperature. The lines are guides to the eye



The temperature dependence of the local *hmf* is presented in Fig. 3b. The onset of the nonzero *hmf* is visible slightly below 250 K, which agrees well with the temperature of the first transition observed in the magnetization measurements. Moreover, the unusual behaviour of *hmf* of Fe3 is clearly observed. Its *hmf* decreases apparently faster than the *hmf* of the remaining components. The fastest decrease in the *hmf* for Fe3 is observed when the temperature approaches 170 K, where the second anomaly was observed [4, 5].

The relative fractions of Fe1, Fe2, Fe3, Fe4 were 0.33 ± 0.02 , 0.23 ± 0.02 , 0.23 ± 0.04 , 0.17 ± 0.04 , respectively, and agree very well with the site occupancies resulting from the crystal structure (2:1:1:1).

The inherent ambiguity does not permit to perform fits using standard set of parameters B , θ , φ , V_{zz} , and η , for each magnetic component. The use of the constrained invariant method, allowed us to interpret the shapes of the Mössbauer spectra at different temperatures, in terms of the contributions coming from separated Fe components. It can be stressed, that presented method is quite general, free of ambiguity and may have potential applications in material science, biology and geology, where powdered absorbers are widely used.

Acknowledgements The work was partially supported by the funds allocated for scientific research for the years 2008–2011 as a research project NN202172335.

References

1. Karyagin, S.W.: K opredelenyu parametrov lokalnogo pola po sts spektra Mössbauera. *Fiz. Tverd. Tela (Leningr.)* **8**, 493–499 (1966) [*Sov. Phys. Solid State* **8**, 391–397 (1966)]
2. Szymański, K.: Explicit expression for the intensity tensor for $3/2\text{--}1/2$ transitions and solution of the ambiguity problem in Mössbauer spectroscopy. *J. Phys., Condens. Matter.* **12**, 7495–7507 (2000)
3. Satuła, D., et al.: Mössbauer data analysis based on invariants and applications to UFe_5Sn . *Phys. Rev., B* **77**, 014411 (2008)
4. Gonçalves, A.P., et al: Synthesis, crystal structure, and magnetic properties of UFe_5Sn . *J. Solid State Chem.* **154**, 551 (2000)
5. Gonçalves, A.P., et al: Magnetic properties of UFe_5Sn single crystals. *J. Magn. Magn. Mater.* **260**, 473 (2003)
6. Torumba, D., Parliński, K., Rots, M., Cottenier, S.: Temperature dependence of the electric-field gradient in hcp-Cd from first principles. *Phys. Rev., B.* **74**, 144304 (2006)

P16

Determination of the Mössbauer absorption cross section and reconstruction of hyperfine field distribution by the maximum entropy method

This article has been downloaded from IOPscience. Please scroll down to see the full text article.

2010 J. Phys.: Condens. Matter 22 296005

(<http://iopscience.iop.org/0953-8984/22/29/296005>)

View [the table of contents for this issue](#), or go to the [journal homepage](#) for more

Download details:

IP Address: 212.33.73.17

The article was downloaded on 06/09/2010 at 09:44

Please note that [terms and conditions apply](#).

Determination of the Mössbauer absorption cross section and reconstruction of hyperfine field distribution by the maximum entropy method

D Satuła¹, K Szymański¹ and L Dobrzyński^{1,2}

¹ Faculty of Physics, University of Białystok, 41 Lipowa Street, 15-424 Białystok, Poland

² The Soltan Institute for Nuclear Studies, 05-400 Otwock-Świerk, Poland

E-mail: satula@alpha.uwb.edu.pl

Received 18 March 2010, in final form 20 May 2010

Published 29 June 2010

Online at stacks.iop.org/JPhysCM/22/296005

Abstract

Determination of the Mössbauer absorption cross section, $\sigma(E)$, and accurate reconstruction of the hyperfine field distributions of the invar alloy, Fe₆₄Ni₃₆, by the maximum entropy method (MEM) is presented. The procedure consists of three steps: deconvolution of the Mössbauer spectra with the instrumental resolution function using MEM, nonlinear transformation of the deconvoluted spectrum into $\sigma(E)$, and reconstruction of the hyperfine field distribution. In order to test the procedure of the deconvolution and correction for thickness effect, several simulated spectra with thickness parameter $1 < t < 50$ and different values of Lorentzian FWHM of the source and absorber were analyzed. It is shown that the procedure of the deconvolution and extraction of $\sigma(E)$ works well for spectra whose lines contain at least five experimental points per FWHM. Reconstructed distributions of hyperfine field parameters, based on the extracted Mössbauer cross section of the Fe–Ni invar alloy, measured with and without application of an external magnetic field, are discussed. The reconstruction has been made to test the earlier postulated non-collinear ferromagnetic state of invar without referring to any specific model in the analysis of the Mössbauer results. It is shown that marginal probability distribution of hyperfine magnetic field consists of the main maximum at about 28 T and a broad tail extending down to 5 T. Observed isomer shift of the main maximum is small and positive. The isomer shift decreases with magnetic field and attains negative values at the lowest fields. It is shown that the magnetic texture parameter does not depend on the hyperfine magnetic field. One thus concludes that in the invar Ni–Fe alloys, in contrast to some theoretical predictions, there is no evidence for different arrangements of the iron magnetic moments as a function of the magnetic hyperfine field.

(Some figures in this article are in colour only in the electronic version)

1. Introduction

In Mössbauer spectroscopy, description of the Mössbauer spectra by a set of Lorentzian absorption lines or a set of sextets is the method most often used in their analysis. The method assuming thin absorber approximation is the simplest one and good enough to extract information attached uniquely to the

velocity scale of the spectrum. However, information from the line intensities contains systematic errors if effective thickness exceeds unity, which is due to the nonlinear dependence of the intensities on this parameter. Thus the analysis of the Mössbauer spectra within the thin absorber approximation will thus lead to systematic errors for thick samples. A number of methods of reconstructing the hyperfine parameter distribution

from Mössbauer spectra have been reported so far [1–7]. However, general deficiency of these methods consists in the need of postulating some correlations between hyperfine parameters, for example linear dependence of the hyperfine magnetic field and the isomer shift. The finite thickness of the sample creates another problem in the proper interpretation of the results.

One of the model-free methods for the analysis of spectroscopic data is the maximum entropy method (MEM). The MEM stems from the so-called Bayesian logics [8] and was used to analyze many spectroscopic data [9–11]. The first successful reconstruction of the single parameter distribution in Mössbauer spectroscopy was published in [12] and then reconstructions of multi-dimensional hyperfine field distribution were reported [13–15]. In order to use MEM in a proper way one should make suitable choice of so-called *prior*, which in the case of Mössbauer measurements is the distribution of hyperfine field, based on the available information about the system under study. In order to use MEM in an efficient way, one should build the prior containing or at least closely resembling our knowledge about the system.

The discovery of the invar effect [16] has stimulated many experimental and theoretical studies of this phenomenon. According to most popular, so-called 2γ -state models [17], the invar can be explained by the existence of two states of iron with different arrangement of the magnetic moments, one state with high moments, high volume and ferromagnetic order, and the second state with low moments and low volume. In recent years, along with possibilities of *ab initio* computation of the non-collinear spin alignments it was shown that invar phenomena are connected with continuous transition from ferromagnetic ordering of Fe spins for high volumes to approximately uniform angular distribution of Fe spins with slightly reduced local moment for low volumes [18]. In order to test such a hypothesis the neutron scattering experiments on Fe₆₅Ni₃₅ invar alloy with polarization analysis of the incident and scattered beams have been made [19]. The results of this work suggest that the invar exhibits collinear ferromagnetic arrangement of magnetic moments. Mössbauer spectroscopy seems to be a powerful tool to study this prediction because it is sensitive to the iron magnetic hyperfine field (proportional to local Fe moment) distribution and delivers information on different arrangements of the iron magnetic moments through relative intensity of the lines $z = I_5/I_4 = I_2/I_3$. In light of earlier results [20] iron magnetic moments in the sample may have different values but their ordering is the same. The measured Mössbauer spectra with and without external magnetic field, as well as with a circularly polarized gamma ray source, were analyzed [20] assuming that $P(B)$ is a superposition of three Gaussian distributions with the following free parameters: average hyperfine magnetic field, its standard deviation, and the relative intensities and z parameter for each Gaussian distribution. The conclusion concerning the possibility of different magnetic states of iron follows from the obtained z values for individual Gaussian shapes. Because the z value was the same for all three components, the paper [20] claimed that there is no evidence for different arrangements of magnetic moments corresponding to observed magnetic hyperfine fields.

The goal of this paper is to check the validity of the hyperfine field distribution obtained by us earlier for invar Fe–Ni alloy [20], using much more elaborate techniques of the interpretation of the measured spectra. The relation between the magnetic hyperfine field and texture parameter z , which indicates how the field is oriented with respect to the gamma beam direction, is studied. The computer code of MEM was developed to find a distribution $P(B, IS, z)$ (quadrupole splitting parameter $QS = 0 \text{ mm s}^{-1}$ for Fe–Ni cubic structure) from the Mössbauer cross section. The analysis of $P(B, IS, z)$ obtained for Fe–Ni invar alloy confirms our earlier conclusions [20] that there are no different iron magnetic moment arrangements. The parameter z is shown to be independent of the magnetic hyperfine field while distribution of the latter is compared with the one found in [20]. Moreover, quite unexpected correlation between the isomer shift (IS) and magnetic hyperfine field, B , was found.

After a brief description of the experiment, the paper consists of three sections: (i) description of the method of extraction of the Mössbauer absorption cross section from the spectra of known thickness parameter, (ii) tests of the deconvolution procedure by the MEM on the simulated Mössbauer spectra and extraction of the Mössbauer absorption cross section from such spectra, (iii) application of the method for extraction of the cross section and then reconstruction of the hyperfine field distribution $P(B, IS, z)$ for Fe–Ni invar alloy measured with and without external magnetic field parallel to the gamma ray direction.

2. Experimental details

The Mössbauer spectra of Fe₆₄Ni₃₆ foil with $t = 2.35$ were collected at room temperature on a conventional ⁵⁷Co spectrometer. The data were calibrated using iron foil at room temperature. The line FWHM of the source Γ_s which was used in the deconvolution procedure was obtained from the analysis of the Mössbauer spectrum of the iron foil ($t = 3.03(2)$) using a transmission integral [21] with fixed natural line width of the absorber $\Gamma_a = 0.097 \text{ mm s}^{-1}$. The measurements of the Fe–Ni alloy in the external magnetic field parallel to the gamma beam were carried out using permanent magnets with the field $B = 1 \text{ T}$. The principle of the maximum entropy code used in the analysis of Mössbauer spectra was described in [13, 14].

3. Evaluation of the absorption cross section

Mössbauer spectrum in the transmission geometry and with an infinitely thin source can be approximated by [21]:

$$S(V) = C \left(1 - f_s + f_s \frac{\Gamma_s}{2\pi} \times \int_{-\infty}^{\infty} \frac{1}{(E - V)^2 + \Gamma_s^2/4} e^{-t\sigma(E)} dE \right) \quad (1)$$

C is a constant dependent on the geometry of the experiment and electronic absorption in the sample and is proportional to the accumulation time of the spectra and activity of the source; f_s is the recoilless fraction of the source; Γ_s the FWHM of the Lorentzian distribution of the photons emitted by the

source; V the Doppler shift between the source and absorber, $V = (v/c)E_\gamma$; v the velocity of the source with respect to the absorber; $\sigma(E)$ the absorption cross section of the absorber; t the effective thickness of the absorber given by:

$$t = \sigma_0 f_a n, \quad (2)$$

where σ_0 is the absorption cross section at resonance [21]; f_a the recoilless fraction of the ^{57}Fe in the absorber; n the number of ^{57}Fe atoms per unit area of the absorber.

$\sigma(E)$ is the absorption cross section proportional to the sum of the Lorentzian lines:

$$\sigma(E) = \sum_{i=1}^n \frac{a_i \Gamma_a \Gamma_0 / 4}{(E - E_i)^2 + \Gamma_a^2 / 4}, \quad (3)$$

with normalized intensities:

$$\sum_{i=1}^n a_i = 1, \quad (4)$$

or, in case of continuous distribution of the hyperfine interactions:

$$\sigma(E) = \int_{-\infty}^{\infty} \frac{a(x) \Gamma_a \Gamma_0 / 4}{(E - x)^2 + \Gamma_a^2 / 4} dx, \quad \int_{-\infty}^{\infty} a(x) dx = 1, \quad (5)$$

Γ_0 is the natural width of the Mössbauer transition which is equal to 0.097 mm s^{-1} [22], Γ_a is the FWHM of the absorption line in the absorber which includes possible broadening of the lines. Because of the normalization of the amplitudes, the cross section is normalized:

$$\int_{-\infty}^{\infty} \sigma(E) dE = \frac{\pi \Gamma_0}{2}. \quad (6)$$

The goal is to extract $\sigma(E)$ from the measured $S(V)$ spectra (1). The value of parameter t can be estimated from the composition and Fe content per unit area of the sample used in the experiment. Parameter C can be determined from the experimental spectra as the number of counts far from the resonance. In a real experiment, because of finite resolution of the detector (usually proportional counter), parameter f_s in (1) is influenced by nonresonant background and is smaller than the Lamb–Mössbauer factor of the source [23]. Thus in practice f_s is a constant dependent on the experimental conditions and has to be determined for each measurement.

Let us define $Y^*(x, \Gamma)$ as the deconvolution of $Y(v)$ with Lorentzian shape:

$$Y(v) = \frac{\Gamma}{2\pi} \int_{-\infty}^{\infty} \frac{1}{(v - x)^2 + \Gamma^2 / 4} Y^*(x, \Gamma) dx. \quad (7)$$

Function Y^* is to be obtained from the deconvolution of Y and can be expressed as a result of the linear operator F_Γ acting on function Y :

$$Y^*(x, \Gamma) = F_\Gamma[Y](x). \quad (8)$$

Let us define the normalized spectrum $s(V)$ as:

$$s(V) = 1 - \frac{S(V)}{C} \quad (9)$$

where C is defined in (1). Normalized spectrum $s(V)$ is nonnegative and is proportional to $1/v^2$ for velocities far from the resonance. From equation (1) it is clear that the normalized spectrum (9) is a convolution:

$$s(V) = f_s \frac{\Gamma_s}{2\pi} \int_{-\infty}^{\infty} \frac{1}{(E - V)^2 + \Gamma_s^2 / 4} (1 - e^{-t\sigma(E)}) dE, \quad (10)$$

which can be deconvoluted by operator F_{Γ_s} :

$$1 - e^{-t\sigma(E)} = \frac{1}{f_s} F_{\Gamma_s}[s](E), \quad (11)$$

and finally

$$\sigma(E) = \frac{-1}{t} \ln \left(1 - \frac{1}{f_s} F_{\Gamma_s}[s](E) \right). \quad (12)$$

The concept of the deconvolution of Mössbauer spectra was suggested already in [24]. However, the procedure was not widely used because of two problems: an unknown value of f_s and deconvolution of a function usually affected by statistical noise. The first problem can be solved by examining the normalization condition (6). Indeed, after a single deconvolution of the normalized spectrum $s(V)$ one obtains the $F_{\Gamma_s}[s](E)$ function and from the normalization condition (6) applied to (12) one gets a nonlinear equation for single unknown f_s . For the second problem, a natural solution is the use of the MEM [8] resulting in smooth and nonnegative results. Summarizing, determination of the resonant cross section from the data with statistical noise is performed in the following steps:

- in the independent calibration experiment parameter Γ_s is determined. In the case of pure, annealed, and thin iron foil $\Gamma_a = \Gamma_o$ was assumed. The Γ_s value is usually higher than Γ_o because of broadening of the source which depends on the commercial supplier. The broadening caused by the spectrometer can also be included in Γ_s ;
- the Mössbauer measurement $S(V)$ is performed on the absorber with thickness t ;
- the deconvolution $F_{\Gamma_s}[s](E)$ is performed on the normalized spectrum $s(V)$ by the MEM;
- the numerical solution for x must satisfy the equation:

$$\int_{-\infty}^{\infty} \ln \left(1 - \frac{1}{x} F_{\Gamma_s}[s](E) \right) dE = -\frac{\pi \Gamma_o t}{2}; \quad (13)$$

- the resonant cross section is finally determined as (12) with $f_s = x$ determined from (13).

4. Mössbauer absorption cross section from the simulated spectra

The first problem of the deconvolution in the presence of noise is the non-uniqueness of the solution. One of the ways to solve such a problem is the application of MEM in which the noise is treated as an important part of information used. In order to examine the usefulness of the MEM in the deconvolution problem, some simulated Mössbauer spectra (single line and sextet in 256 channels) with different values of Γ_s and Γ_a , and

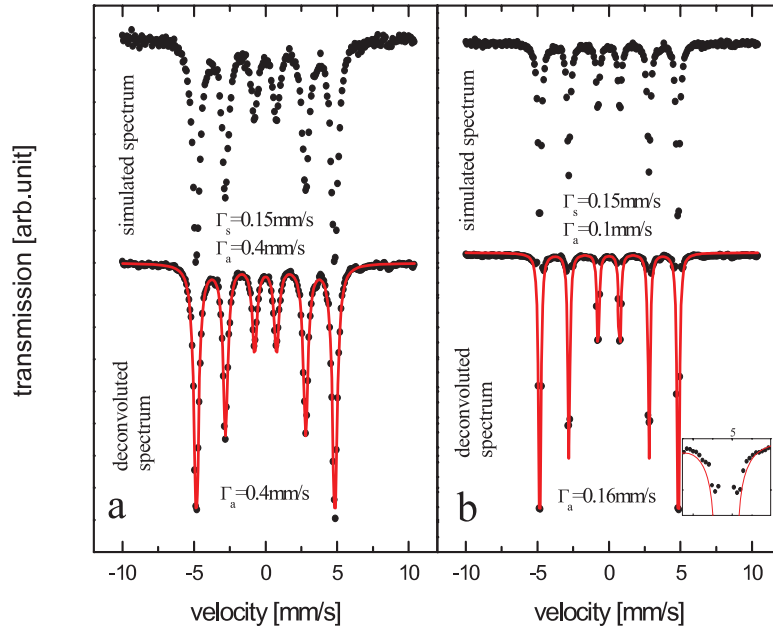


Figure 1. The simulated spectra and $F_{\Gamma_s}[s](E)$ function after MEM deconvolution. Solid lines represents the best fitting in a thin absorber approximation.

thickness parameter in the range $2 < t < 20$ were produced and subsequently analyzed.

As follows from equation (9), the spectrum of interest presents a convolution of the real spectrum with the Lorentzian function described by the width Γ_s . The deconvolution procedure delivers function $F_{\Gamma_s}[s](E)$ which depends on the cross section, the thickness parameter t and unknown constant parameter f_s which generally depends on the recoilless fraction of the source and the efficiency of the gamma ray detector.

4.1. Problem of the number of channels per absorption line

In order to test the sensitivity of the deconvolution using the MEM procedure to the sharpness of the spectrum, several simulated magnetically split Mössbauer patterns with $t = 2$, $\Gamma_s = 0.15 \text{ mm s}^{-1}$ (typical for ^{57}Co source), and different values Γ_a between 0.1 mm s^{-1} and 0.85 mm s^{-1} were analyzed (Γ_a includes possible broadening of the lines). One should point out that the simulated spectrum with $\Gamma_a = 0.1 \text{ mm s}^{-1}$ corresponds to the spectrum of the iron foil used for calibration.

An example of simulated spectra with $\Gamma_a = 0.4 \text{ mm s}^{-1}$ and $\Gamma_a = 0.1 \text{ mm s}^{-1}$ with added Gaussian noise are shown in the upper part of figures 1(a) and (b), respectively. Next, the simulated spectra were deconvoluted using MEM with flat (ignorant) prior. The result of such a deconvolution is shown in the bottom part of figures 1(a) and (b). As a rule, the Lagrange parameter in the MEM procedure [25] was chosen so as to obtain the χ^2 value close to one, where

$$\chi^2 = \sum_i \frac{1}{\sigma_i^2} (I_i - I_i^{\text{rec}})^2, \quad (14)$$

where I_i and I_i^{rec} denote measured and reconstructed intensity in the i th channel, and σ_i is the uncertainty of the measured intensity.

The solid lines represent the best fits to $F_{\Gamma_s}[s](E)$ functions using a Lorentzian shape in the thin absorber approximation. The obtained value for a broader spectrum, $\Gamma_a = (0.40 \pm 0.02) \text{ mm s}^{-1}$, is in agreement with the value used in the simulation while for a sharp spectrum $\Gamma_a = (0.18 \pm 0.02) \text{ mm s}^{-1}$ and is almost twice as large as the value used in the simulation. It can be also noted that the shape of the lines obtained after deconvolution is not Lorentzian, see inset in figure 1(b).

The values of Γ_a used in the simulated spectra (full circles) and Γ_a obtained after deconvolution (open circles) are shown in figure 2(a). The behavior of χ^2 as a function of the number of channels per FWHM, i.e. $\Gamma = \Gamma_a + \Gamma_s$, is shown in figure 2(b). As one can see, the Γ_a used in the simulated spectra is reproduced well, i.e. within the error bar, when Γ is about 2.5 times broader than the FWHM of the resolution function. In our experiment it means that the Γ should cover at least five channels. The same conclusion can be inferred from the behavior of χ^2 (figure 2(b)) which suddenly increases for the deconvolution performed for Γ narrower than five channels.

4.2. Deconvolution and transformation to the absorption cross section

The results of the deconvolution of the simulated spectra indicated that the MEM can be successfully used for deconvolution of the Mössbauer data, especially when the hyperfine field distribution is broad, leading to the broadening of absorption lines.

As it was shown using the MEM procedure for deconvolution of the Mössbauer spectra, one can get function $F_{\Gamma_s}[s](E)$, equations (7) and (8), which depends on the unknown parameter f_s and thickness t . In order to extract the Mössbauer cross section one should numerically solve

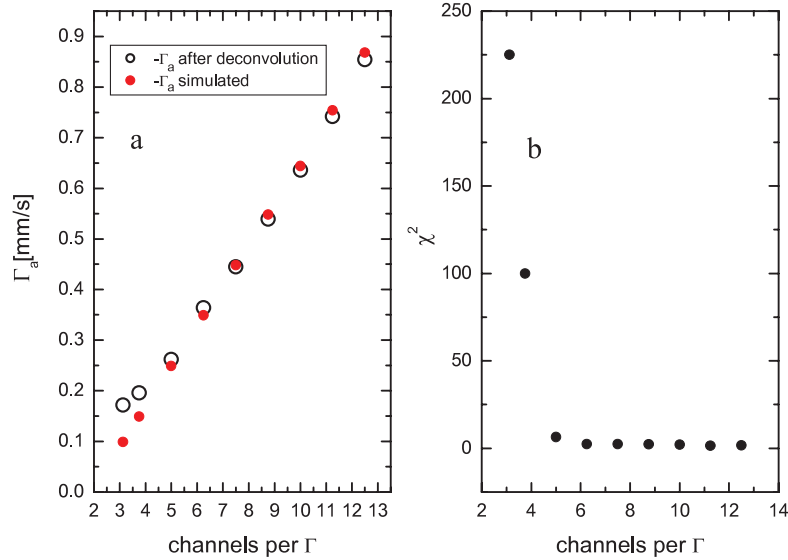


Figure 2. The behavior of (a) Γ_a after deconvolution and (b) χ^2 as a function of number of channels per FWHM.

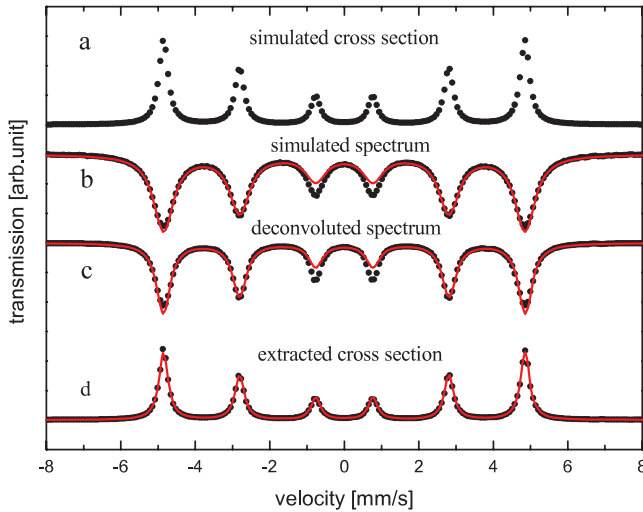


Figure 3. The simulated (a) cross section, (b) Mössbauer spectrum, (c) deconvoluted spectrum, and (d) extracted cross section. The solid lines represent the best fitting in the thin absorber approximation.

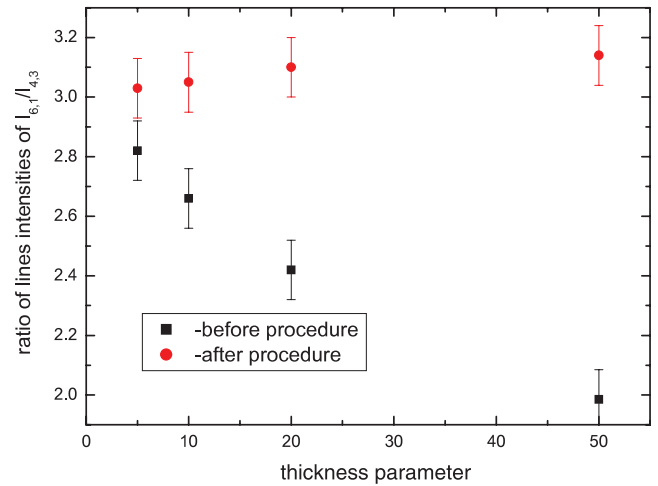


Figure 4. The line intensities ratio $I_{6,1}/I_{4,3}$ obtained from simulated spectra and from the cross sections within the framework of the thin absorber approximation.

equation (13) with the known thickness parameter t (see equation (2)).

Let us test the procedure of extraction of the cross section on the deconvoluted texture free spectrum of a thick absorber for t between 5 and 50. As an example, the simulated cross section with $\Gamma_a = 0.3 \text{ mm s}^{-1}$ is shown in figure 3(a). The simulated spectrum with $\Gamma_a = 0.3 \text{ mm s}^{-1}$, $\Gamma_s = 0.15 \text{ mm s}^{-1}$, and $t = 10$, deconvoluted functions using MEM and extracted cross sections are shown in figures 3(b)–(d). The solid lines in figures 3(b)–(d) represent the best fit in the thin absorber approximation with fixed relative line intensities $I_{6,1}/I_{4,3} = 3$ expected for texture free thin absorbers. Because of large thickness parameter $t = 10$, the simulated spectrum as well as the deconvoluted function (figures 3(b) and (c)) cannot be fitted well within the thin absorber approximation. The main

misfit is clearly seen on the lines 3 and 4 where simulated lines are much deeper than theoretical ones. Under applied nonlinear transformation, equation (12), the extracted cross section is fitted well by a Zeeman sextet in the thin absorber approximation (figure 3(d)). Such procedures were repeated for simulated spectra with t between 5 and 50. The results of the line intensity ratio $r = I_{6,1}/I_{4,3}$ (r treated as a free parameter in the fitting) as a function of thickness parameter for simulated spectra and extracted cross sections are presented in figure 4. As one can see, the r parameter decreases with increasing t for the simulated spectra while r is equal to three, within the error bars, for all extracted cross sections. One should stress that for a spectrum with $t = 50$ the shapes of the lines in the simulated spectrum are clearly not Lorentzian while after the transformation equation (12) Lorentzian shape in the extracted cross section is recovered.

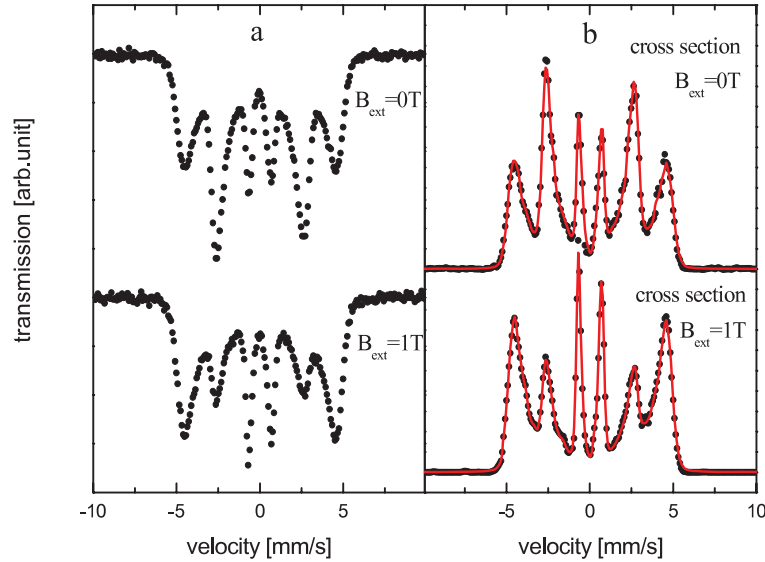


Figure 5. (a) Measured spectra and (b) absorption cross section of Fe–Ni measured in and without external magnetic field. The solid lines in (b) represent the best fits obtained by the MEM method.

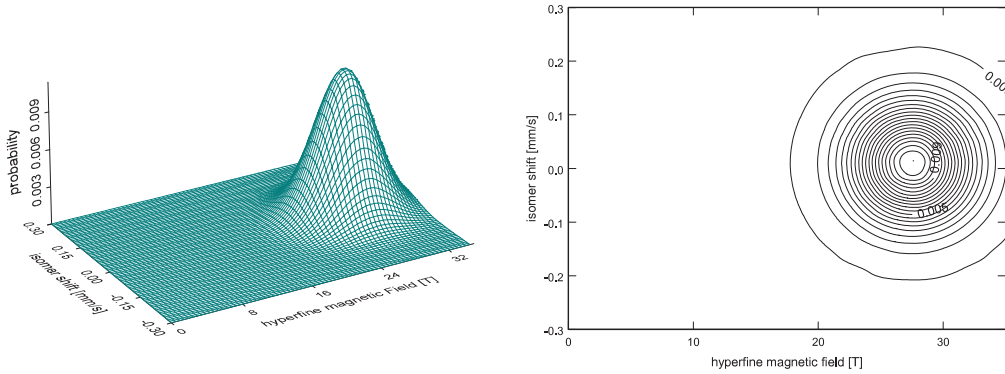


Figure 6. The marginal $P_o(B, IS)$ followed from the prior (15) used in the reconstruction of the $P(B, IS, z)$ and its projection.

5. Reconstruction of the hyperfine field distribution of the Fe–Ni invar alloy

The MEM was used for reconstruction of the hyperfine field distribution $P(B, IS, z)$ from the spectra measured for Ni–Fe invar alloy with and without external magnetic field. The cross sections were extracted and the primary goal was to check whether different iron magnetic moment arrangements exist in Fe–Ni.

Mössbauer spectra of Fe–Ni invar alloy measured in external magnetic field parallel to the gamma beam, and in zero magnetic field (figure 5(a)) and the extracted cross sections, are shown in figure 5(b). The absorption lines in the Mössbauer spectra are broad enough, so there are many more than five channels per FWHM. There is a clear change of intensities of lines 2 and 5 in the cross sections (figure 5(b)) which means that applied external magnetic field of 1 T causes substantial iron magnetic moment rearrangement.

5.1. Prior construction

From the shape of the Mössbauer spectra one can infer that there is hyperfine magnetic field distribution with the main

maximum at about 27.5 T (the velocities of the outer lines are -4.5 and 4.5 mm s $^{-1}$). The isomer shift was estimated to be centered around 0.01 mm s $^{-1}$. Therefore the prior $P_o(B, IS, z)$ was chosen in the form of (see figure 6) a Gaussian peak, as a smooth, symmetrical and the simplest shape, with $B_o = 27$ T and $\sigma_B = 4.5$ T, $IS_o = 0.01$ mm s $^{-1}$ and $\sigma_{IS} = 0.1$ mm s $^{-1}$, and z_o and $\sigma_z = 0.3$ according to the following expression

$$P_o(B, IS, z) = \exp\left(-\frac{(B - B_o)^2}{\sigma_B^2}\right) \exp\left(-\frac{(IS - IS_o)^2}{\sigma_{IS}^2}\right) \times \exp\left(-\frac{(z - z_o)^2}{\sigma_z^2}\right) \quad (15)$$

where z_o is the initial texture parameter and was estimated directly from the measured spectra and equal to 1.0 and 2.8 for in-field and zero external magnetic field, respectively. Both values arise from a brief inspection of the raw data.

5.2. Reconstruction of the distributions

In order to analyze the reconstructed $P(B, IS, z)$ distribution the marginal probabilities were calculated according to the

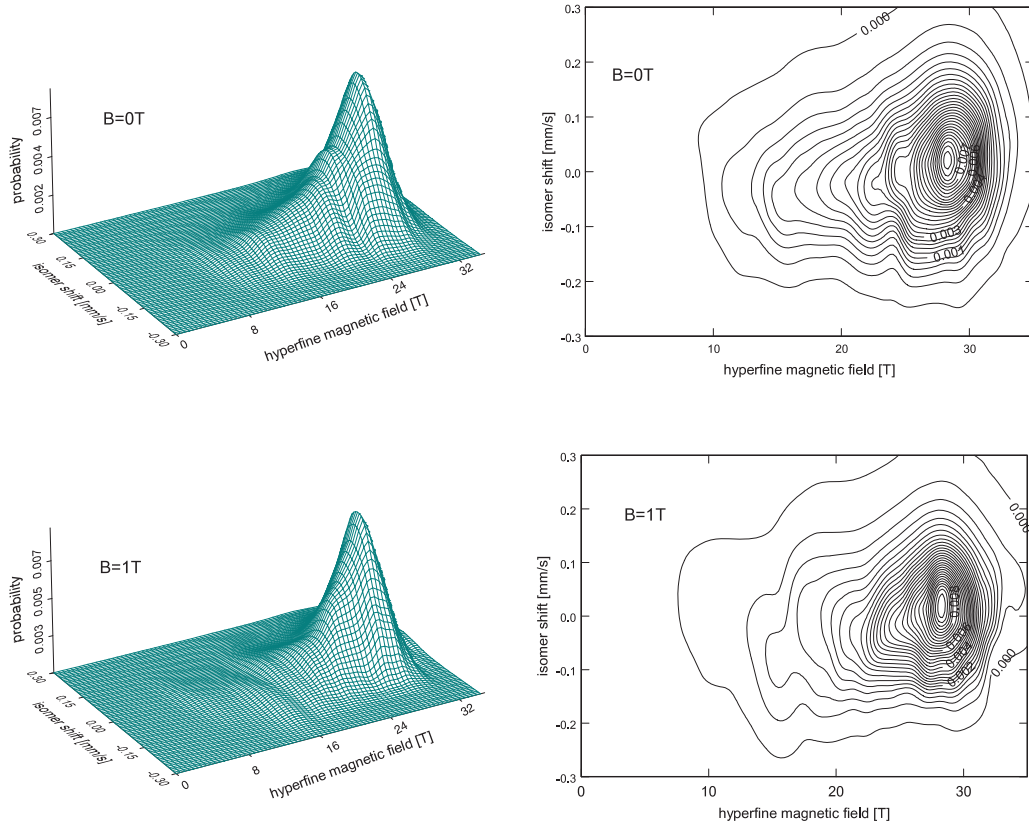


Figure 7. The marginal (with respect to z) probability distribution $P(B, IS)$ and its projection obtained for in-field and without external magnetic field measurements.

scheme:

$$P(B, IS) = \int P(B, IS, z) dz \quad (16)$$

$$P(B) = \int P(B, IS, z) dIS dz \quad (17)$$

and a mean value of z as a function of magnetic hyperfine field

$$\bar{z}(B) = \int zP(B, IS) dIS. \quad (18)$$

The reconstructed marginal probability distributions $P(B, IS)$ for the in-field and without-field measurements are presented in figure 7. The solid lines in figure 5(b) represent the best fit to the cross sections using the MEM procedure. A large peak centered at B about 28 T is seen in figure 8 for reconstructions of both spectra, in external magnetic field and in zero external field. The maximal probability for the isomer shift when B is decreasing is pointing to descending values. The observed IS is positive and small for the main maximum in the distribution while isomer shifts exhibit negative values at lower fields. This result indicates clearly the presence of correlation between hyperfine field and isomer shift. This correlation is consistent with observations of [26, 27] of the average hyperfine magnetic field and isomer shift in the concentration range of 60–70% of Fe in Fe–Ni alloys. An increase of iron content leads to a decrease of both hyperfine field and isomer shift.

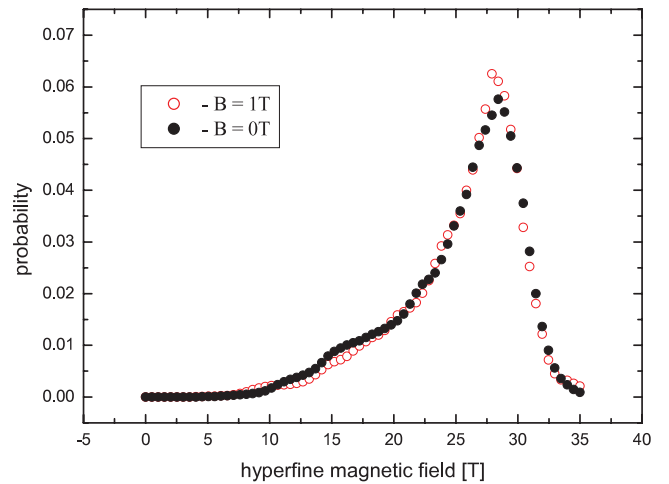


Figure 8. The marginal probability distribution $P(B)$ of Fe–Ni invar alloy for in- and without-field measurements.

Our model-free MEM treatment reveals that the asymmetry in the shape of the spectra of Fe₆₅Ni₃₅ can be explained as correlation between hyperfine field and isomer shift and this correlation can hardly be approximated by linear dependence. Indeed, assuming linear and positive correlation between hyperfine magnetic field and IS, one expects to observe amplitudes of lines 1, 2, and 3 larger than 6, 5, and 4, respectively. What is observed, however, is that amplitudes

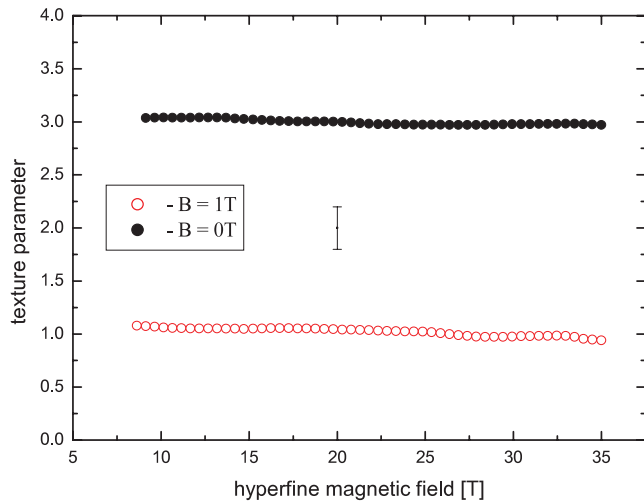


Figure 9. The mean values $z(B)$ obtained from the in-field and zero-external-field measurements. Systematic uncertainties are indicated by error bars.

of lines 2 and 3 are larger than 5 and 4, respectively while lines 1 and 6 do not show asymmetry in amplitudes in figure 5(b) (this work). Similarly, in figure 1 (65 at.% Fe) and in figure 12 ($T = 4.2$ K) of [26] the asymmetry of lines 1 and 6 is opposite to the asymmetry of pairs 2, 5 and 3, 4. The results of fitting in [26] show that a slope of $IS(B)$ dependence is positive at room temperature and negative at $T = 14$ K. One should also point out that the fitted curves in [26] do not reproduce well all absorption line intensities, particularly for low temperature measurements. Most probably the assumption of linear correlation between IS and B is oversimplified.

In figure 8 the marginal distributions $P(B)$ are presented for in-field and without-field measurements. As one can see, the maximum of hyperfine field distribution is slightly moved towards smaller hyperfine magnetic field. This reflects the influence of external magnetic field on the magnetic hyperfine field which has opposite sign. The reconstructed shapes of these distributions are almost the same (figure 8). The only small deviation is visible around 15 T and can be attributed to the texture effect. It means that external magnetic field of order of 1 T does not change significantly $P(B)$.

The most important information related to the magnetic arrangement of iron magnetic moments in invar Fe–Ni alloy can be inferred from the behavior of mean values of $z(B)$. The behavior of $z(B)$ for zero- and in-field measurements is shown in figure 9. It is clearly seen that z does not depend on hyperfine magnetic fields, neither for the zero nor for the external magnetic field acting on the sample. Such behavior of texture parameter allows us to conclude that there is no evidence for a change of the magnetic moment arrangement with the value of the magnetic moments. This does agree with the conclusion of [19] where the results of neutron study with polarization analysis of Fe–Ni invar alloy were presented.

6. Conclusion

A new method of extraction of the absorption cross section was presented. The method was checked on simulated spectra

and proved to work for thin as well as for thick absorbers. After extraction of the cross section one can perform further analysis in the thin absorber approximation without generating systematic deviations in the line intensities by the thickness effects.

It was demonstrated that deconvolution of the spectra can be performed safely by MEM when absorption peaks are not very sharp, which in practice means that there should be at least five channels per FWHM of the absorption peak. It was shown that the Γ_a used in the simulated spectra is reproduced well, i.e. within the error bar, when Γ is about 2.5 times broader than the FWHM of the resolution function. The reconstructed hyperfine field probability distributions, $P(B, IS, z)$ for Fe–Ni invar alloy, show the presence of the broad magnetic hyperfine field with the main maximum at 28 T and a long tail which extends down to 5 T. The isomer shift for the main maximum of $P(B)$ is small and positive. It changes to negative values with decreasing B . It was shown that the behavior of the mean value of the texture parameter does not depend on magnetic hyperfine field. Within the used model-free treatment no evidence that local arrangement of iron magnetic moments is correlated with the value of magnetic moment in the Fe–Ni invar alloy was found.

Acknowledgment

The work was partially supported by the funds allocated for scientific research for the years 2008–2011 as research project NN202172335.

References

- [1] Campbell S J, Whittle G J and Stewart A M 1983 *J. Magn. Magn. Mater.* **31–34** 1521–2
- [2] Chuev M A, Hupe O, Bremers H, Hasse J and Afanas'ev A M 2000 *Hyperfine Interact.* **126** 407–10
- [3] Cranshaw T E 1974 *J. Phys. E: Sci. Instrum.* **7** 122–4
- [4] Hesse J and Rübartsch A 1996 *J. Phys. E: Sci. Instrum.* **7** 526–32
- [5] Le Caer G and Brand R A 1998 *J. Phys.: Condens. Matter* **10** 10715–74
- [6] Varret F, Gerard A and Imbert P 1971 *Phys. Status Solidi b* **43** 723–30
- [7] Window B 1971 *J. Phys. E: Sci. Instrum.* **14** 401–2
- [8] Jaynes E T 2003 *Probability Theory. The Logic of Science* (Cambridge: Cambridge University Press)
- [9] Dobrzyński L 2004 *X-Ray Compton Scattering* (Oxford: Oxford University Press) pp 188–209
- [10] Gerhard U, Marquardt S, Schroeder N and Weiss S 1998 *Phys. Rev. B* **58** 6877–91
- [11] Buck B and Macaulary V A 1991 *Maximum Entropy in Action* (Oxford: Clarendon)
- [12] Brand R A and Le Caer G 1988 *Nucl. Instrum. Methods Phys. Res. B* **34** 272–84
- [13] Dobrzyński L, Szymański K and Satuła D 2004 *Nukleonika* **49** S89
- [14] Dobrzyński L, Holas A, Satuła D and Szymański K 2006 *Bayesian Inference and Maximum Entropy Methods in Science and Engineering, 26th Int. Workshop* ed A Mohammad-Djafari American Institute of Physics
- [15] Bentley P M and Kilcoyne S H 2006 *J. Phys.: Condens. Matter* **18** 7751–9

- [16] Guillaume C E 1897 *C. R. Acad. Sci., Paris* **125** 235–8
- [17] Weiss R J 1963 *Proc. R. Soc. A* **82** 281–2
- [18] van Schilfgaarde M, Abrikosov I A and Johansson B 1999 *Nature* **400** 46–9
- [19] Cowlam N and Wildes A R 2003 *J. Phys.: Condens. Matter* **15** 521–30
- [20] Satuła D, Szymański K, Dobrzyński L, Rečko K and Waliszewski J 2003 *Nukleonika* **40** S71–4
- [21] Margulies S and Ehrman J R 1961 *Nucl. Instrum. Methods* **12** 131
- [22] Robinson J W (ed) 1981 *Handbook of Spectroscopy* (Boca Raton, FL: CRC Press)
- [23] Housley R M 1965 *Nucl. Instrum. Methods Phys. Res.* **35** 77
- [24] Lin T M and Preston R S 1974 *Mössbauer Effect Method* **9** 205
- [25] Skilling J and Bryan R K 1984 *Mon. Not. Trans. Astron. Soc.* **211** 111–24
- [26] Ping J Y, Rancourt D G and Dunlap R A 1992 *J. Magn. Magn. Mater.* **103** 285–313
- [27] Lagarec K, Rancourt D G, Bose S K, Sanyal B and Dunlap R A 2001 *J. Magn. Magn. Mater.* **236** 107–30

P17

The method of invariants in ^{57}Fe Mössbauer spectroscopy on selected examples

This article has been downloaded from IOPscience. Please scroll down to see the full text article.

2010 J. Phys.: Conf. Ser. 217 012010

(<http://iopscience.iop.org/1742-6596/217/1/012010>)

View [the table of contents for this issue](#), or go to the [journal homepage](#) for more

Download details:

IP Address: 212.33.73.17

The article was downloaded on 19/01/2011 at 11:09

Please note that [terms and conditions apply](#).

The method of invariants in ^{57}Fe Mössbauer spectroscopy on selected examples

K Szymański¹, D Satuła¹, L Dobrzyński², K Rećko¹, W Olszewski¹,
K Brzózka³ and J Jankowska-Kisielińska⁴

¹University of Białystok, Faculty of Physics, Lipowa 41 15-424 Białystok, Poland

²also: The Andrzej Sołtan Institute for Nuclear Studies, 05-400 Otwock-Świerk, Poland

³Department of Physics, Technical University of Radom, Malczewskiego 29, Radom 26-600, Poland

⁴Institute of Atomic Energy, 05-400 Otwock-Świerk, Poland

corresponding author's e-mail address: kszym@alpha.uwb.edu.pl

Abstract. The method of invariants is an effective tool for decomposition of Mössbauer spectra into components resulting from electric quadrupole and magnetic dipole interactions. The invariants can be next analysed to obtain all possible values of hyperfine interaction parameters. In some cases it is possible to determine the parameters with satisfactory precision. The method was applied to not fully ordered UFe_4Al_8 . Obtained results indicate that the dominant component of the electric field gradient is negative and is oriented almost perpendicularly to the direction of the hyperfine magnetic field. Another example shows that the method of invariants results in substantial reduction of the number of calculated components in modeling of hyperfine interactions in $\gamma\text{-FeMn}$.

1. Introduction

Mixed hyperfine interactions, e.g. magnetic dipole and electric quadrupole ones, in case of 1/2-3/2 spin transition cause difficulties in the interpretation of Mössbauer spectra because of the ambiguity problem [1]. Derivation of complete set of hyperfine parameters corresponding to specified values of invariants was considered in [2]. The proposed treatment was, however, not widely used. Explicit formulas for the intensity tensor [3] allow one to use the invariants (instead of hyperfine fields) for description of the absorption line positions and intensities as well. The method of Mössbauer spectra analysis making use of the invariants for proper description of the spectra components was recently proposed in [4]. Although the method described in [4] does not allow determination of the complete set of hyperfine interactions parameters, of invariants, and the analysis proposed in [2], may lead to satisfactory characterisation of the system. In particular the method is sensitive to the changes of local direction of hyperfine magnetic field (*HMF*) with respect to the electric field gradient (*EFG*) diagonal directions, see [4] for details.

UFe₄Al₈ intermetallic compound attracted considerable interest and the magnetic structure was recently determined [5,6]. Although the unit cell of UFe₄Al₈ is tetragonal, local symmetry of Fe is low [5], see Fig. 1a. The orientation of the *EFG* axes can not be simply deduced from the structure. Also experiments with ¹⁸¹Ta local probe in UFe₄Al₈ [7] were not conclusive and to our best knowledge *EFG* at Fe(8f) in UFe₄Al₈ is not known. This motivated us to analyze the Mössbauer data of UFe₄Al₈ by the method of invariants. Unfortunately, probably because of the sample quality, the spectra collected close to the transition temperature could not be characterized by single site static behaviour. We thus restrict the analysis to the spectra measured at low temperatures only. The spectrum measured in paramagnetic phase will be analysed as well.

Another selected example was disordered γ -FeMn antiferromagnetic alloy, interesting for spintronics. The Mössbauer spectra of this alloy have been already measured in sixties [8], however orientation of hyperfine fields and strength of the *EFG* is still not exactly known [9,10]. The invariants offer strict description of the spectra components at temperatures close to the transition temperature and thus spectra measured in the wide temperature range can simultaneously be analysed. This results in information on the hyperfine interactions in poorly resolved spectra.

2. Example of UFe₄Al₈

Mössbauer measurements were performed on the powdered sample of UFe₄Al₈ (reported in [11]) at different temperatures. The spectra shown in Fig. 1b were simultaneously analysed using the set of four components. The line positions and intensities can be given explicitly by invariants S_0, S_1, S_2 constructed from the *EFG* tensor V and the *HMF* pseudovector B [3]:

$$\begin{aligned} S_0 &= a\sqrt{\text{Tr}V^2}, \\ S_1 &= a\mathbf{m}^T \cdot V \cdot \mathbf{m}, \\ S_2 &= a\sqrt{\mathbf{m}^T \cdot V^2 \cdot \mathbf{m}}, \end{aligned} \quad (1)$$

where

$$a = eQc / E_\gamma \quad (2)$$

is the proportionality constant between the *EFG* components (in [V/m²] in SI units) and the invariants expressed conveniently for applications in [mm/s]. Q is the nuclear quadrupole moment, e is the elementary charge, c is the speed of light, E_γ is the energy between the ground and the excited state, $\mathbf{m}=\mathbf{B}/B$. Because of presence of weak intensity components, constraints were applied to their center shifts according to the Debye model. The isomer shift at $T=0$ was a free parameter for each component. Constraints were also applied to the areas under subspectra and $T^{3/2}$ dependence of the *EFG* components on temperature. The invariants S_0, S_1, S_2 extracted from the spectra at temperatures 12, 35 and 80 K are shown in Fig. 1c for the main component (Fe(8f)). The measurements were also performed at higher temperatures close to the magnetic transition temperature (not shown). However, observed shape of the spectra indicate that simple approximation which uses constant number of subspectra is not sufficient.

All possible values of hyperfine parameters $B, V_{zz}, \eta, \theta, \varphi$, corresponding to a point in Fig. 1c, were next extracted by a method similar to those presented in [2]. We note that the treatment described in [2] does not include situation when invariants are closely related to condition:

$$2S_0^4 + 18S_2^4 - 3S_0^2(S_1^2 + 4S_2^2) = 0 \quad (3)$$

shown by the lines in Fig. 1c. This case corresponds to the axially symmetric *EFG* and full discussion of the data treatment will be published elsewhere. The results obtained for all possible values of $V_{zz}, \eta, \theta, \varphi$ are shown in Fig. 1d

Low temperature measurements indicate presence of six line patterns, in agreement with earlier reports [5,6,11]. However, room temperature spectra consist of a slightly asymmetric doublet. It is hard to expect that Goldanski-Karyagin effect can be responsible for the asymmetry because

a tetragonal axis of symmetry is perpendicular to the local two-fold axis of iron. More likely explanation can be searched in distribution of *EFG* originated due to chemical disorder in the crystal. One cannot also exclude presence of small amount of other phases, for example FeAl. That is why four components were used for simultaneous fit shown in Fig. 1b.

The method of invariants and constrained simultaneous fit allowed us to decompose the spectra into the main and other components. Although invariants are not single valued functions of hyperfine parameters, the results obtained for the main component in UFe_4Al_8 (Fig. 1d) are located within relatively narrow ranges. The V_{zz} component of the *EFG* is negative and the angle between the V_{zz} axis and the hyperfine magnetic field is close to $\pi/2$. No systematic changes of the orientation of hyperfine field with respect to the *EFG* axes were detected in the temperature range 13-80K.

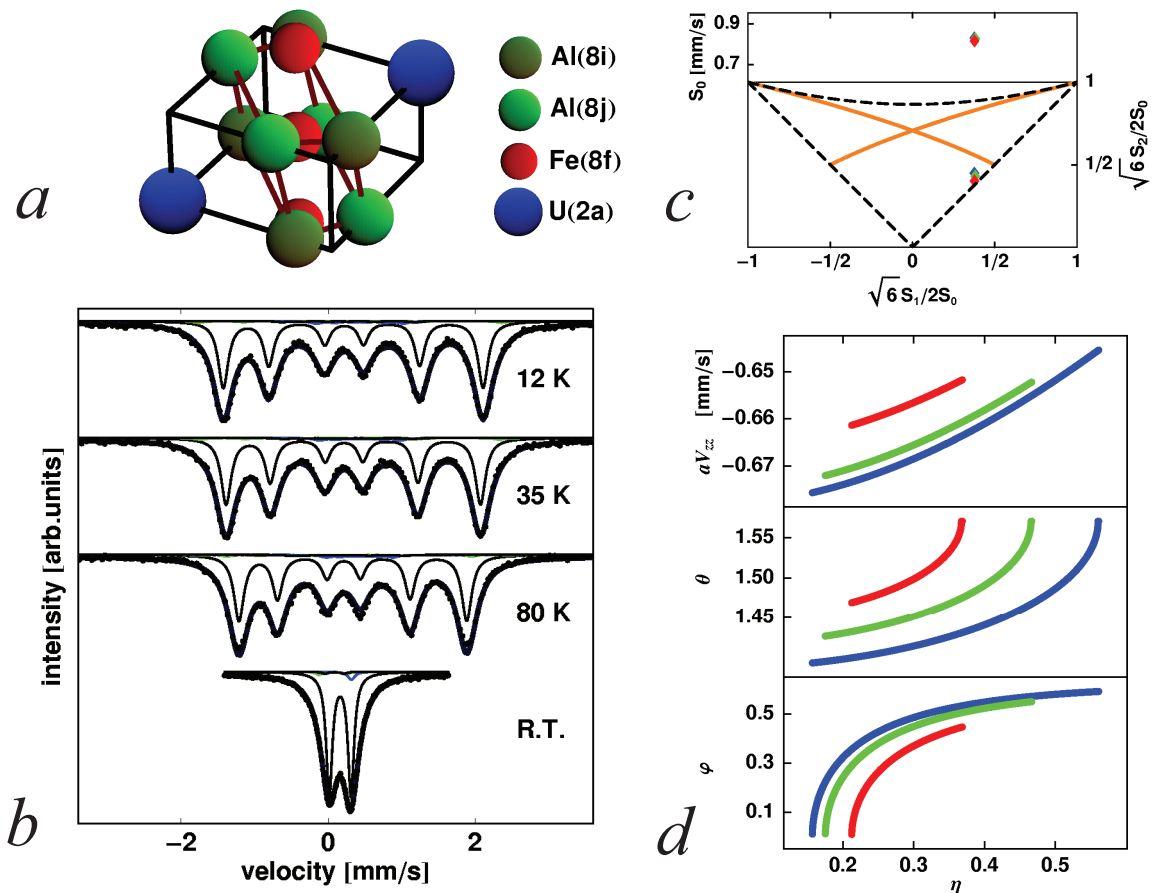


Figure 1 a) Local structure of Fe at $8f$ site in UFe_4Al_8 , b) Mössbauer spectra of Fe in UFe_4Al_8 and results of simultaneous fit (weak-area components are reduce practically to horizontal lines in the figure c). Invariants S_0 , S_1 , S_2 of the main component (different temperatures are indicated by different colors, however the symbols overlap). Dashed lines indicate the region of all physically possible values of the invariants. Orange lines correspond to values of axially symmetric *EFG*, see eq. (3), d) All possible values of V_{zz} , η , θ , φ parameters for the S_0 , S_1 , S_2 invariants shown in c) (θ and φ in radians). Blue, green and red colours correspond to $T=12, 35$ and 80 K, respectively.

3. Example of γ -FeMn

Chemical disorder in cubic alloys causes breaking of local symmetry and creation of nonzero *EFG*. This was demonstrated in the case of bcc Fe-V alloys [12]. Similar situation may be present in

disordered fcc Fe-Mn alloys. In case of magnetic order, number of different local environments is large. For exemplary estimation let us assume that local magnetization in fcc Fe-Mn is oriented along one of (111) directions. If the *EFG* gradient is next assumed to depend on the chemical configuration of the nearest neighbours (screened Coulombic pseudopotential [13]), one finds 2^{12} different chemical configurations and 8 different orientations of the local hyperfine fields (see example in Fig 2a) which makes $8 \cdot 2^{12} = 32768$ different local environments for which diagonalisation has to be performed for correct calculation of the mixed hyperfine interactions. The problem, however, may be greatly simplified if the invariants are calculated. For all considered configurations only 160 different sets of invariants (S_0, S_1, S_2) exist. These invariants, once calculated, may be used in the fitting procedures. Efficiency of this procedure is shown in Fig.2 which displays excellent fit performed for the spectra measured in a wide temperature range (for details see [14]).

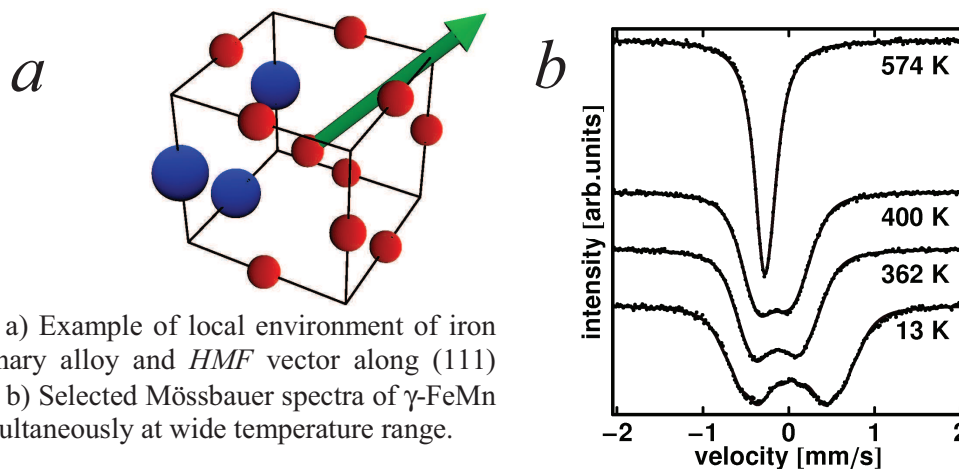


Figure 2 a) Example of local environment of iron at fcc binary alloy and *HMF* vector along (111) direction. b) Selected Mössbauer spectra of γ -FeMn fitted simultaneously at wide temperature range.

Acknowledgments:

The work was supported by a research project NN202172335.

References

- [1] Karyagin S W 1966 *Fiz. Tverd. Tela* (Leningrad) **8** 493, 1966 *Sov. Phys. Solid State* **8** 391
- [2] Dąbrowski L J, Piekoszewski J and Suwalski J 1972 *Nucl. Instrum. Methods* **103** 545
- [3] Szymański K 2000 *J. Phys.: Condens. Matter* **12** 7495
- [4] Satuła D, Szymański K, Dobrzyński L, Tran V H and Troć R 2008 *Phys. Rev.* **B 78** 014411
- [5] Paixao J A, Lebech B, Goncalves A P, Brown P J, Lander G H, Burllet P, Delapalme A, and Spirlet J C 1997 *Phys.Rev.* **B 55** 14370
- [6] Waerenborgh J C, Goncalves A P, Bonfait G, Godinho M and Almeida M 1999 *Phys. Rev.* **B 60** 4074
- [7] Marques J, Barradas N, Alves E, Ramos A, Goncalves A P, da Silva M and Soares J 2001 *Hyp. Int.* **136** 333
- [8] Ishikawa Y and Endoh Y 1967 *J. Phys. Soc. Jpn.* **23** 205
- [9] Kennedy S J and Hicks T J 1987 *J Phys. F: Met. Phys.* **17** 1599
- [10] Szymański K, Olszewski W, Dobrzyński L, Satuła D and Jankowska-Kisielińska J 2004 *Nukleonika* **49** S75.
- [11] Szymański K, Rečko K, Dobrzyński L and Satuła D 1999 *J.Phys.Condens. Matter*, **11** 6451
- [12] Preston R S, Lam D J, Nevitt M V and Ostenburg D O 1966 *Phys. Rev.* **149** 440
- [13] Scholte P M L O, Tegze M, van der Woude F, Buschow K H J and Vincze I 1986 *Hyp. Int.* **27** 437
- [14] Szymański K, Olszewski W, Satuła D, Dobrzyński L, Brzózka K and Jankowska-Kisielińska J 2009 *J. Phys. Soc. Jap.* **78** in press

P18

Maximum Entropy Method in Mössbauer Spectroscopy — a Problem of Magnetic Texture

D. SATUŁA^{a,*}, K. SZYMAŃSKI^a AND L. DOBRZYŃSKI^{a,b}

^aFaculty of Physics, University of Białystok, 41 Lipowa Str., 15-424 Białystok, Poland

^bThe Soltan Institute for Nuclear Studies, 05-400 Otwock-Świerk, Poland

A reconstruction of the three dimensional distribution of the hyperfine magnetic field, isomer shift and texture parameter z from the Mössbauer spectra by the maximum entropy method is presented. The method was tested on the simulated spectrum consisting of two Gaussian hyperfine field distributions with different values of the texture parameters. It is shown that proper prior has to be chosen in order to arrive at the physically meaningful results.

PACS: 76.80.+y, 02.60.-x

1. Introduction

The analysis of the hyperfine parameter distribution in the Mössbauer spectroscopy have a long history. The first algorithms for the deconvolution problem was published by Varret et al. [1] with later modification by Hesse Rübartsch [2] and Window [3]. The method presented in [1, 2] uses a matrix formulation for reconstruction of weight function $P(x)$ (x — hyperfine parameter). In [3] an expansion of the distribution in the basis of the trigonometric functions was formulated. The problem of both methods are some mathematical artefacts which lead to unphysical oscillations in the calculated distributions from noisy Mössbauer spectra. On the other hand, deficiency of these methods consist in the necessity of postulating of some correlations between hyperfine parameters, for example linear dependence of hyperfine magnetic field and the isomer shift. A different approach is to find $P(x)$ distribution of single parameter by the maximum entropy method presented by Brandt and Le Caer [4].

The maximum entropy method (MEM) stems from the Bayesian logic [5] was already used to analyze many spectroscopic data [6, 7, 8]. This model-free method was not frequently used to the analysis the Mössbauer spectra where presence of the distributions of hyperfine field parameters makes the spectra complicated and interpretation becomes dependent on assumptions one makes in order to get the hyperfine fields distributions. The one dimensional Mössbauer spectra contain information on the hyperfine magnetic fields (B), isomer shift (IS), quadrupole splitting (QS), and orientation of the hyperfine magnetic field with respect to gamma beam

direction through magnetic texture parameter z defined as:

$$z = \frac{I_{2,5}}{I_{1,6}} = \frac{3 \sin^2 \theta}{\frac{9}{4}(1 + \cos^2 \theta)}, \quad (1)$$

where θ is an angle between direction of gamma ray and local hyperfine magnetic field. It was shown recently that two dimensional distribution in (B, IS) space [9] and three dimensional distribution in (B, IS, QS) [10] space can be reconstructed from Mössbauer spectra by the MEM technique in the first order approximation approach, where the quadrupole interaction is considered as a small parameter. The problem not discussed in [9, 10] is reconstruction of the hyperfine field distribution for not very thin samples for which there is nonlinear dependence of the intensities of Mössbauer lines and the thickness parameter. This can lead to artifacts in the reconstructed distribution. The method of extraction of cross section from the Mössbauer spectra using MEM is described in [11]. In specific problems, where a spatial arrangement of the hyperfine magnetic field depends on the field B , one needs to make reconstruction of the $P(B, IS, z)$ distribution. The aim of this work is to test whether such reconstruction by MEM is feasible in the first order perturbation approach.

2. Maximum entropy method

In the application of maximum entropy method to the analysis of the Mössbauer spectra we divide whole 3-dimensional space into pixels and the value ρ_j denotes the probability of having given values of the chosen three parameters within j 'th pixel. Because the line intensities are linear in probability, the intensities W_k measured with uncertainties σ_k at k 'th velocity channel are described theoretically by a sum:

* corresponding author; e-mail: satula@alpha.uwb.edu.pl

$$W_k = \sum_{j=1}^{N_{pix}} r_{kj} \rho_j, \quad (2)$$

where $r_{k,j}$ is the transformation matrix.

As usual one is maximizing the Lagrangian

$$L = \alpha S - \frac{1}{2} \chi^2, \quad (3)$$

where S is the information entropy described as:

$$S = - \sum_{J=1}^{N_{pix}} \rho_j \ln \left(\frac{\rho_j}{\rho_{oj}} \right), \quad (4)$$

where ρ_j and ρ_{oj} are reconstructed and initial (prior) distributions.

The final equations to solve are of type:

$$\rho_j = \frac{\rho_{oj} \exp \left(-\frac{1}{2\alpha} \frac{\partial \chi^2}{\partial \rho_j} \right)}{\sum_{j'=1}^{N_{pix}} \rho_{oj'} \exp \left(-\frac{1}{2\alpha} \frac{\partial \chi^2}{\partial \rho_{j'}} \right)}. \quad (5)$$

In practical applications one encounters a problem with choosing prior as this choice can influence the response of the MEM procedure.

3. Results and discussion

In order to test the possibility of the reconstruction of $P(B, IS, z)$ using maximum entropy method, the simulated spectrum in thin absorber approximation approach shown in Fig. 1a was used. The spectrum consists of two sextets with Voigt line shapes with hyperfine parameters, (B, σ_B, IS, QS, z) , equal to $(30 \text{ T}, 3 \text{ T}, 0 \text{ mm/s}, 0 \text{ mm/s}, 2)$ $(20 \text{ T}, 4 \text{ T}, 0 \text{ mm/s}, 0 \text{ mm/s}, 1)$. The integrated intensities of both sextets were assumed to be equal. Assumed hyperfine field distribution is shown in the inset of Fig. 1a. The Gaussian noise on the level of 1% of effective absorption was added to the simulated spectrum. Assumed behavior of $z(B)$ is shown in Fig. 1b. One can should point out that the reconstruction of such simulated spectrum presents one of the most difficult tasks because the lines no 1, 2 and 5, 6 of low field component are located in the positions of lines no. 2 and 5 of the high field component. One can thus expect a strong correlations between reconstructed texture parameters of both components.

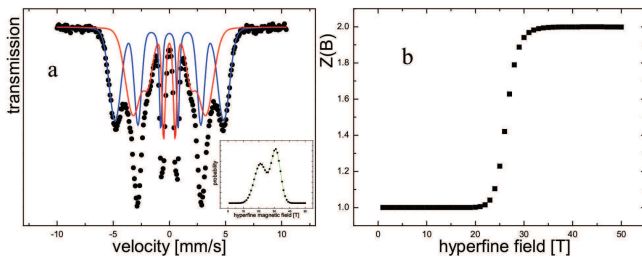


Fig. 1. a) The simulated Mössbauer spectrum and b) its $z(B)$ function. The hyperfine magnetic field distribution is shown as a inset.

At first, flat initial prior was assumed. It means that the response of MEM to the complete lack of knowledge of the distribution was tested. The results of MEM procedures are presented in Fig. 2a. As one can see the theoretical line fit well to the simulated spectrum. The reconstructed marginal distribution $P(B, IS)$ (see Fig. 2b) shows two distinct maxima located at $B \approx 20 \text{ T}$ and 30 T what qualitatively agree with assumption done in simulated spectra. One notes that the distribution of IS parameter, originally assumed to be delta-like, appeared to be rather broad. This shows a degree of uncertainty of this parameter hidden in the simulated spectrum, arising from correlations between reconstructed field B and the isomer shift IS . On the other hand, such broad distribution of IS reflects our state of knowledge on this parameter. Because of the inherent property of the Maximum Entropy Method, a flat prior used in the IS reconstruction results in much broader distribution (Fig. 2b) than those obtained with Gaussian prior (Fig. 3b). The shape of the reconstructed marginal $P(B)$ distribution (Fig. 2c) is wider than the simulated one. Moreover, the low magnetic field component is moved towards lower values of B (Fig. 2c). When behavior of $z(B)$ (Fig. 2d) is concerned, one notices that it is quantitatively clearly different than the one used in simulation, yet it indicates that there are different texture values for high magnetic fields than for lower. In conclusion, one can say that the use of flat prior results in good description of the Mössbauer spectrum but only in a qualitatively good reconstruction of the simulated distribution of hyperfine parameters.

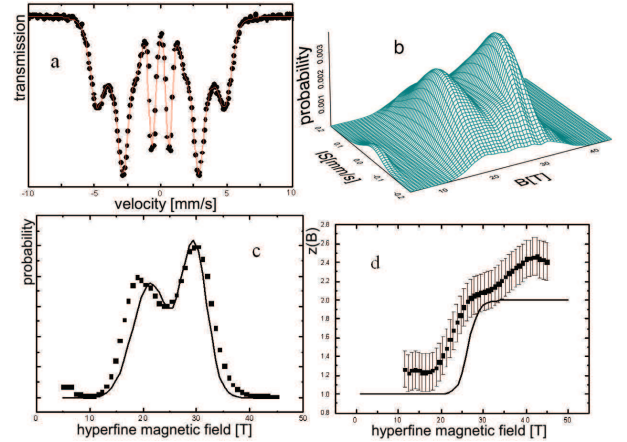


Fig. 2. a) The simulated Mössbauer spectrum (points) and fitting line (solid line); b) marginal $P(B, IS)$ distribution; c) marginal $P(B)$ distribution and d) $z(B)$ are obtained using flat prior. The solid lines in (c) and (d) represents the results of simulation.

In the second step, the prior was assumed to be a superposition of two broad Gaussian shapes (see Fig. 3a) which follow from quick inspection of the simulated Mössbauer spectrum. The position of the spectroscopic lines in the simulated spectrum shows beyond the doubts that at least two components, one at about $B \approx 30 \text{ T}$ and sec-

ond somewhere in the central part of spectra, must characterize the distribution of hyperfine parameters. The response of MEM to the chosen prior is such presented in Figs. 3b, 3c and 3d for $P(B, IS)$, $P(B)$ and $z(B)$, respectively. As it follows from inspection of these Figures, this time the reconstructed distributions agree much better with the simulated ones than previously. $P(B)$ distribution differs from the assumed one a little only, and the behavior of $z(B)$ also fits better to the simulated one, and shows existence of two magnetic configurations of iron magnetic moments.

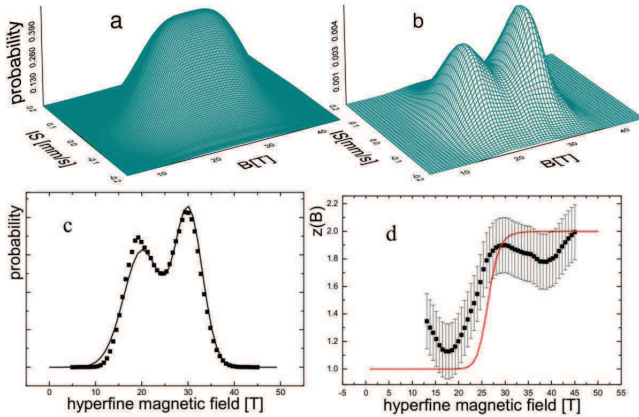


Fig. 3. a) The assumed prior distribution; b) marginal $P(B, IS)$ distribution; c) marginal $P(B)$ distribution and d) $z(B)$. The solid lines in (c) and (d) represents the results of simulation.

4. Conclusion

The results of our analysis show that even in very difficult case like the one analyzed in this paper, one can obtain reliable distributions of the hyperfine parameters, and obtain good indication concerning the magnetic moment configuration distribution in the considered sample. The paper shows that the use of biased prior (flat one in our case), i.e. much different from the one clearly evident from the observed spectrum, leads to distorted dis-

tributions with respect to the real ones. This paper also strengthens conclusions drawn from similar analysis [11] carried out for Fe-Ni Invar alloy for which a non-collinear arrangement of magnetic moments was predicted theoretically. The results of this paper show that the MEM can be used in situations where different magnetic moment arrangements of iron are expected. As a minimum, a qualitative picture of the real $P(B, IS, z)$ distributions can be obtained and may serve as an excellent starting point to the interpretation of complicated Mössbauer spectra.

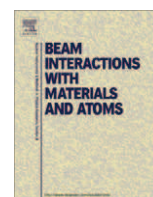
Acknowledgments

The work was partially supported by the funds allocated for scientific research for the years 2008–2011 as a research project NN202172335.

References

- [1] F. Varet, A. Gérard, P. Imbert, *Phys. Status Solidi B* **43**, 723 (1971).
- [2] J. Hesse, A. Rübarsch, *J. Phys. E: Sci. Instrum.* **7**, 526 (1974).
- [3] B. Window, *J. Phys. E: Sci. Instrum.* **4**, 401 (1971).
- [4] R.A. Brand, G. Le Caer, *Nucl. Instrum. Methods Phys. Res., Sect. B* **34**, 272 (1988).
- [5] E.T. Jaynes, *Probability Theory. The Logic of Science*, Cambridge University Press, 2003.
- [6] L. Dobrzyński, *X-ray Compton scattering*, Oxford University Press, 2004, pp. 188–209.
- [7] U. Gerhard, S. Marquardt, N. Schroeder, S. Weiss, *Phys. Rev. B* **58**, 6877 (1998).
- [8] B. Buck, V.A. Macaulary, *Maximum entropy in action*. Clarendon Press, Oxford 1991.
- [9] L. Dobrzyński, K. Szymański, D. Satula, *Nukleonika* **49**, S89 (2004).
- [10] L. Dobrzyński, A. Holas, D. Satuła, K. Szymański, in: *Bayesian Inferencje and Maximum Entropy Methods in Science and Engineering, 26th International Workshop*, Ed. A. Mohammad-Djafari, American Institute of Physics, 2006.
- [11] D. Satula, K. Szymański, L. Dobrzyński, *J. Phys. Condens. Matter* **22**, 296005 (2010).

P19



A single line linearly polarized source for Mössbauer spectroscopy

D. Satuła^{a,*}, K. Szymański^a, L. Dobrzyński^{a,b}

^a Faculty of Physics, University of Białystok, 41 Lipowa Street, 15-424 Białystok, Poland

^b The Soltan Institute for Nuclear Studies, 05-400 Otwock-Świerk, Poland

ARTICLE INFO

Article history:

Received 16 February 2011

Received in revised form 8 July 2011

Available online 29 July 2011

Keywords:

Mössbauer spectroscopy

Monochromatic polarized radiation

Magnetic texture

ABSTRACT

A single line source of linearly polarized radiation in a conventional Mössbauer setup working at room temperature with ⁵⁷Co in Cr matrix was constructed. The ordered Fe₃Si was used as a filter. The estimated degree of polarization of the source depends on the preparation and thickness of the polarizer. The best polarization degree (92 ± 8)% was achieved. The measurements with polarized radiation lead to significant simplification of the complex spectra and allow to study components arising from various polarizations separately. In particular, it is possible to extract $\Delta m = (1, -1)$ and $\Delta m = 0$ transitions by use of a linearly polarized beam. Moreover polarized beam can be used for determination of texture parameters related to spatial arrangements of spins in the plane perpendicular to the radiation beam. Such parameters are not easily measurable by other methods. The Mössbauer spectra of invar Fe₆₅Ni₃₅ measured by monochromatic linearly polarized radiation are shown as an example.

© 2011 Elsevier B.V. All rights reserved.

1. Introduction

The usefulness of polarized gamma rays was recognized soon after discovery of Mössbauer effect [1,2] and was used to determine information about electric field gradient [3], the direction of the magnetic hyperfine field (m.h.f.) vector [4] and spin structure for single crystal absorbers [5]. A number of methods was developed in order to obtain polarized resonant radiation. Most of them were cumbersome and too complicated for regular studies. The recently developed multiline linearly polarized Mössbauer source was reported [6]. However, the most promising approach is to use the filter technique which allows one to obtain single line polarized beam [7–10].

The monochromatic circularly polarized Mössbauer source constructed by us [8] allow for very easy determination of the sign of the hyperfine magnetic field. The method is site selective and is particularly attractive for studying the magnetic moments configuration in materials with nonhomogeneous magnetization distribution. The usefulness of the method was demonstrated on ferrimagnetic HoFe₂ [8] in which the magnetic moments of iron are known to be oriented antiparallel to the direction of the magnetization. Another example is magnetite measured in external field with circularly monochromatic radiation. Two nonequivalent Fe sites [11] are separated in the spectrum so the numerical analysis is not required for detection of antiparallel orientation of magnetic moments of the two sites. The next example showing advantage of the Mössbauer polarimetry is ferrimagnetic Er-Fe-B

amorphous material with compensation temperature. Reversal of the sign of magnetic moments of Fe with temperature was unambiguously shown [12]. In general, the application of polarized radiation simplifies the measured spectrum and allows correct determination of the complex hyperfine magnetic field distribution [13].

In the case of Mössbauer polarimetry with a monochromatic, linearly polarized radiation, one notes that some of the published constructions suffer from use of chemical materials not stable at ambient conditions [14,15]. Very convenient system which can be operated for long time was constructed in our laboratory. The single line linearly polarized Mössbauer source allows a remarkable simplification of measured absorption spectra and separation of the nuclear transitions arising from $\Delta m = (1, -1)$ and $\Delta m = 0$. Thus complex spectra can be unraveled by analyzing components for various polarization separately.

One of serious problems in study of magnetic materials is determination of the magnetic texture. The relative line intensities of magnetically splitted Mössbauer spectra yield information on the angular distribution of the magnetic hyperfine field vectors described by the polar angles θ and φ , defined in the inset in Fig. 1. Using unpolarized radiation, an information about $\langle \cos^2\theta \rangle$ (θ is the angle between gamma direction and hyperfine magnetic field vectors, the brackets, $\langle \rangle$, denote averaging with magnetic texture function and will be explained later) can be obtained in single measurement. The Mössbauer polarimetry brings more information. In the case of circularly polarized source it is possible to determine $\langle \cos\theta \rangle$ which allows also to determine direction of hyperfine magnetic field vector. The linearly polarized radiation offers the possibility of determination of additional magnetic texture parameter

* Corresponding author.

E-mail address: satula@alpha.uwb.edu.pl (D. Satuła).

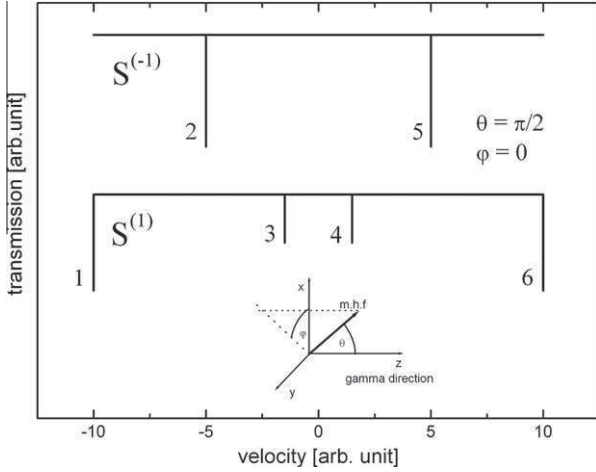


Fig. 1. Schematic presentation of single site Mössbauer spectra of monochromatic linearly polarized gamma ray.

$\langle \cos^2 \varphi \sin^2 \theta \rangle$ where φ is an angle in the absorber plane. In particular, for $\theta = \pi/2$ this parameter contains information about angular distribution of the m.h.f. vector in the sample plane perpendicular to the beam.

2. Intensities of the absorption lines for single line source of linearly polarized radiation

In case of completely polarized gamma radiation and the hyperfine magnetic field oriented at angles θ and φ , a single site Mössbauer spectrum consists of six lines with normalized intensities I_i^p ($i = 1, 2, 3, 4, 5, 6$) [16]:

$$I_{1,6}^{(1)} : I_{2,5}^{(1)} : I_{3,4}^{(1)} = \left(\frac{3}{8}(1 - ss) \right) : \left(\frac{ss}{2} \right) : \left(\frac{1}{8}(1 - ss) \right) \quad (1)$$

$$I_{1,6}^{(-1)} : I_{2,5}^{(-1)} : I_{3,4}^{(-1)} = \left(\frac{3}{8}(1 - cs) \right) : \left(\frac{cs}{2} \right) : \left(\frac{1}{8}(1 - cs) \right) \quad (2)$$

where $ss = \sin^2 \varphi \sin^2 \theta$ and $cs = \cos^2 \varphi \sin^2 \theta$ and p refer to two orthogonal polarization states $p = 1$, or $p = -1$. It follows from (1) and (2) that $I_{1,6}^p : I_{3,4}^p = 3$. Also, in the special case of $\theta = \pi/2$, $\varphi = 0$, the intensities of the absorption lines are $I_{1,6}^{(1)} : I_{2,5}^{(1)} : I_{3,4}^{(1)} = 3/8 : 0 : 1/8$ and $I_{1,6}^{(-1)} : I_{2,5}^{(-1)} : I_{3,4}^{(-1)} = 0 : 1/2 : 0$. It is clear that a single line linearly polarized gamma source allows for a remarkable simplification of absorption spectra in the Mössbauer experiment and the determination of φ angle of the m.h.f. vector in the absorber plane. Let us abbreviate sextets $S^{(1)}$ and $S^{(-1)}$ described by relations (1) and (2), respectively. Schematic Mössbauer spectra $S^{(1)}$ and $S^{(-1)}$ for aforementioned special values of angles θ and φ are presented in Fig. 1.

In case of incomplete polarization of the radiation emitted by the source, the total spectrum is a linear combination of $S^{(1)}$ and $S^{(-1)}$:

$$n_{(1)} S^{(1)} + n_{(-1)} S^{(-1)} \quad (3)$$

where $n_{(1)}$ and $n_{(-1)}$ are the fractions of photons with each polarization in the beam. Using the normalization condition $n_{(1)} + n_{(-1)} = 1$, the degree of polarization p can be defined as:

$$p = n_{(1)} - n_{(-1)}. \quad (4)$$

One should stress that in such definition of degree of polarization the p value can vary in the range from 1 to -1 . In our notation (1) and (2) $p > 0$ corresponds to $(n_{(1)} > n_{(-1)})$ while $p < 0$ corre-

sponds to $(n_{(1)} < n_{(-1)})$. For $n_{(1)} = n_{(-1)}$ the radiation is unpolarized and $p = 0$. Using relations (1)–(4) the normalized line intensities are:

$$I_{1,6}^p : I_{2,5}^p : I_{3,4}^p = \left(\frac{3(p+1)}{16}(cs - ss) + \frac{3}{8}(1 - cs) \right) : \left(\frac{(p+1)}{4}(ss - cs) + \frac{cs}{2} \right) : \left(\frac{(p+1)}{16}(cs - ss) + \frac{1}{8}(1 - cs) \right) \quad (5)$$

In special case of unpolarized beam, $p = 0$, one gets from (5):

$$I_{1,6}^0 : I_{2,5}^0 : I_{3,4}^0 = \left(\frac{3}{16}(1 + cc) \right) : \left(\frac{1}{4}(1 - cc) \right) : \left(\frac{1}{16}(1 + cc) \right) \quad (6)$$

where $cc = \cos^2 \theta$. Eq. (6) is equivalent to the sum of two spectra measured with two opposite polarizations, p and $-p$. Because of the identity $ss + cs + cc \equiv 1$ and Eq. (6), the line intensities I_2 and I_5 measured with unpolarized radiation are described by the relation:

$$4I_{2,5}^0 = cs + ss \equiv 1 - cc \quad (7)$$

3. Determination of the magnetic texture

The foregoing analysis was sufficient for the consideration of the problem of a single m.h.f. direction in the absorber. In real cases one has to consider a problem of the m.h.f. direction having certain angular distribution known as the magnetic texture function $P(\theta, \varphi)$. This distribution is usually represented as a series of spherical harmonics [17,18]. Mössbauer measurements with unpolarized radiation bring information about $\langle \cos^2 \theta \rangle$, while circularly polarized beam allows one to determine $\langle \cos \theta \rangle$. The sign of $\langle \cos \theta \rangle$ is related to the orientation of m.h.f. vector with respect to gamma beam direction. The averaging is performed in standard way:

$$\langle \circ \rangle = \frac{1}{4\pi} \int_{\text{sphere}} (\circ) P(\theta, \varphi) \sin \theta d\theta d\varphi \quad (8)$$

The Mössbauer measurements using linearly polarized beam deliver additional information about the texture function $P(\theta, \varphi)$ through the averages $\langle cs \rangle$ or $\langle ss \rangle$. When $\theta = \pi/2$, parameters $\langle cs \rangle$ and $\langle ss \rangle$ give information about preferred orientation of the m.h.f.s. in the plane of the studied sample. The linearly polarized gamma radiation with polarization degree equal p allows to determine the texture parameter $\langle cs \rangle$ using Eqs. (5) and (7). Because $I_{1,6}^p = 3I_{3,4}^p$ (see. Eq. (5)) and normalization condition the parameter:

$$\langle cs \rangle = \frac{2(I_{2,5}^0(1+p) - I_{2,5}^p)}{p} \quad (9)$$

Parameters $\langle cs \rangle$ and $\langle ss \rangle$ are not easily available in single measurement with unpolarized or circularly polarized beam. Determination of $\langle cs \rangle$ and $\langle ss \rangle$ requires multitude of measurements, see details described in Refs. [17,19–21].

4. Construction of the linearly polarized monochromatic source

Source of the monochromatic, linearly polarized radiation, constructed in our lab is working at room temperature on the commercially available ^{57}Co source in Cr matrix and is shown schematically in Fig. 2 together with the definition of the orientation of the m.h.f. in the absorber (θ, φ). The polarizer is made from magnetically ordered $^{57}\text{Fe}_{2.85}\text{Si}_{1.15}$ alloy glued to the source and mounted on the standard Mössbauer transducer working in constant acceleration mode. The detailed procedure of selection of the material of the polarizer is described in Ref. [7]. In order to test an influence of the method of preparation of the polarizer on its quality, five different filters presented in Table 1 were tested. For all polarizers the powder of Fe-Si was mixed with epoxy glue.

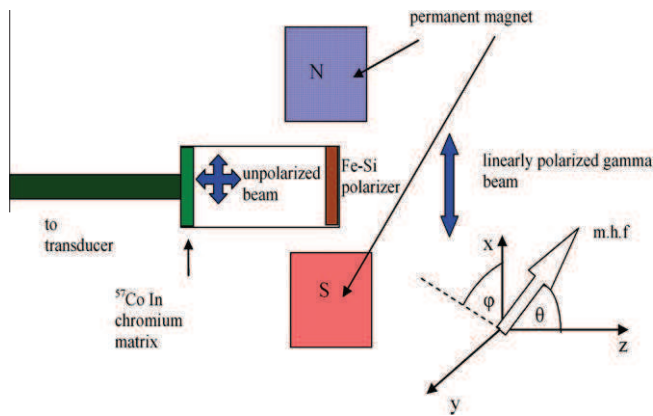


Fig. 2. The schematic layout of the polarized source. Direction of the polarized beam is in the z axis.

Table 1
Polarizers made of $^{57}\text{Fe}_{2.85}\text{Si}_{1.15}$ used in the experiment.

Symbol	Area density (mg/cm ²)	Description
A	20	Solidified in magnetic field
B	30	Solidified in magnetic field
C	40	Solidified in magnetic field
D	34	Solidified in magnetic field, slightly different degree of structural ordering and different size of grain of the powder
E	40	Solidified without magnetic field

Polarizers abbreviated by A, B, C and D with different density of Fe-Si (20, 30, 40 and 34 mg/cm² respectively) were solidified in an external magnetic field parallel to the plane of the filter. Moreover, the polarizer D, prepared at initial stage of project, was made of Fe-Si alloys with probably slightly different size of grains and degree of structural order. Polarizer E with density 40 mg/cm² was solidified without usage of external magnetic field. The external magnetic field during preparation of the polarizers was used in order to induce an easy axis of magnetization which should cause easier saturation of the filter. The external magnetic field of about 1T produced by a setup of permanent magnets acts in the plane of the polarizer and aligns its magnetic moments. The schematic construction of permanent magnets is shown in Fig. 3. The gamma beam transmitted through the ideally polarizing filter contains the polarization orthogonal to that absorbed by the filter. The Mössbauer measurements for two states of polarization of the beam for all filters were carried out on the α -Fe foil with thickness

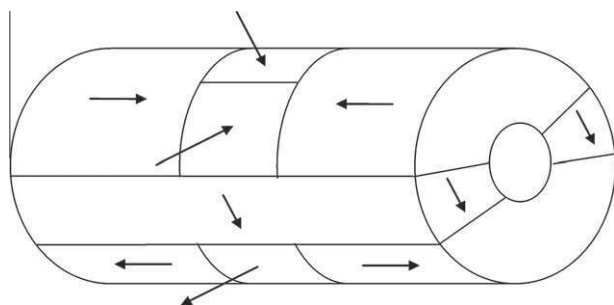


Fig. 3. The schematic view of permanent magnets used to magnetize polarizer. The arrows indicate directions of permanent magnetization. The polarizer is located in the center of the cylinder and the magnetic field acts in its plane, perpendicular to the cylinder axis.

6 μm placed in the identical permanent magnets as used for magnetization of the polarizer. For the polarizer with highest degree of polarization the invar alloy Fe₆₅Ni₃₅ as an example was measured.

5. Determination of the degree of polarization

Based on relation (9) one can easily obtain an equation which allows to estimate the degree of polarization of the source:

$$p = \frac{2(I_{2,5}^0 - I_{2,5}^p)}{\langle cs \rangle - 2I_{2,5}^0} \quad (10)$$

In order to determine polarization degree p , one needs an information about $\langle cs \rangle$ for the absorber and intensities of the lines of Mössbauer spectra measured with polarized as well as unpolarized beam. The intensities of line $I_{2,5}^0$ can be determined in two ways. One can carry out measurements with unpolarized radiation (7) or to add the two spectra measured with polarizations p and $-p$.

Fig. 4 presents the spectra measured for both polarization states on α -Fe foil in the external magnetic field $B = 1\text{ T}$ with direction along x axis ($(\theta, \varphi) = (\pi/2, 0)$). In order to determine line intensities for p and $-p$ transmission integrals were used. The solid lines in Fig. 4 represent the best fits. The determination of the lines intensities $I_{2,5}^p$ for both polarization states give directly the information about line $I_{2,5}^0$. Because all measurements were carried out on the same iron foil the alignment of the magnetization in the absorber is the same for all measurements and equal $I_{2,5}^0 = (0.24 \pm 0.01)$.

As one can see, the spectra for all polarizers show six absorption lines for both polarization states of beam, p and $-p$. The lines nos 2 and 5 for p and lines nos 1,3,4 and 6 for $-p$ are suppressed according to relations (1) and (2), respectively. Such shapes of spectra can arise because of the following two reasons. One is connected with incomplete polarization of the gamma beam, and second can be connected with not perfect magnetization of the measured iron foil. Incomplete polarization of the beam can follow from not perfect magnetization, too small thickness and not perfect homogeneity of the polarizer. The homogeneity of the filter is the crucial for the quality of the filter. The lack of perfect homogeneity causes that some parts of the beam do not interact with the polarizing medium. Thus some unpolarized radiation is transmitted through filter. It is clear that intensity lines nos 1,3,4,6 for polarization p and lines nos 2 and 5 for $-p$ decrease with the increasing area density of polarizer (polarizers A, B, C). Polarizers C and E have the same Fe-Si density, differ in the field applied during solidification (see Table 1) and produce spectra of the same shape (compare C and E in Fig. 4). It means that the alignment of the m.h.f. vectors

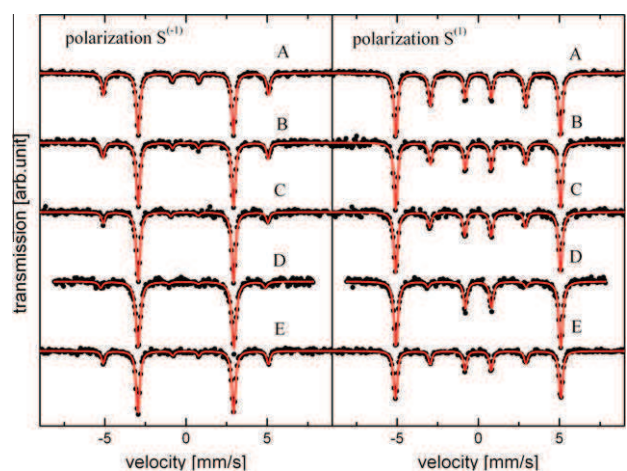


Fig. 4. Polarized Mössbauer spectra measured of α -Fe foil for different polarizers. The solid line represents the best fit using transmission integral procedure.

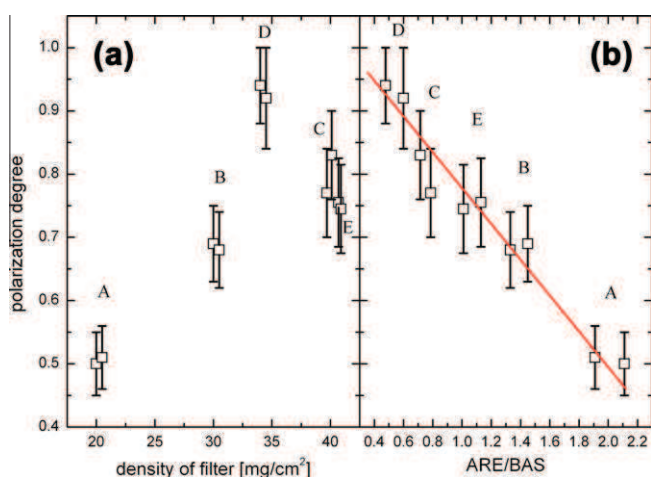


Fig. 5. Polarization degree $|p|$ for different polarizer (a) as a function of area density of the filter, (b) as a function of rate of total area under spectrum and background. The points at (a) for particular filters were moved a little in the x axis for better presentation. The solid lines are guide only.

in the polarizers C and E caused by the external magnetic field $B = 1\text{ T}$ are similar. So in external field solidification does not cause detectable improvement. The best spectra showing minute contamination of unwanted lines were obtained for polarizer D.

In order to determine low limit of $\langle cs \rangle$ parameter it was assumed that best polarizer D transmits fully polarized beam. It means that all nonexpected lines come from not perfect alignment of m.h.f. vector in the absorber. Using Eq. (9) and intensities of the absorption lines from the fit one gets $\langle cs \rangle = (0.93 \pm 0.02)$. The upper limit of $\langle cs \rangle$ is equal unity. In that case, all unwanted lines are associated with not fully polarized beam. Such values of $\langle cs \rangle$ together with intensities of the absorption lines were used to estimate the degree of polarization p for all filters. The obtained results of $|p|$ for both states of polarization are presented in Fig. 5a as a function of area density of the filters. It is clear that there is no systematic relation between $|p|$ and area density of polarizer. The polarizer D ($34\text{ mg}/\text{cm}^2$) has the highest degree of polarization $|p| = (0.92 \pm 0.08)$. Lack of monotonic relation between density and degree of polarization results from the effects of homogeneity in the polarizer. In Fig. 5b the value of $|p|$ versus ratio of total area under spectrum (ARE) and background (BAS) is shown. Such presentation reflects in much better way possible reasons of incomplete polarization of the beam. The results lead to conclusion that solidification of filters in the external field improves the arrangements of the m.h.f. vector of polarizers but does not lead to better degree of polarization because of worse homogeneity of the filters. Such behavior was observed much more clear in the study of circularly polarized beam. Fig. 6 displays two Mössbauer spectra of iron foil using two filters which differed only by solidification in or without external magnetic field perpendicular to their surface. In the case of Mössbauer spectra measured using circularly polarized beam presented in Fig. 6 the unwanted lines are nos. 1, 2, 4 and 5. As one can see, much better degree of polarization was obtained for filter not solidified in magnetic field. It means that homogeneity of the filters were lost during solidification process. The detailed rapport concerning the filters for circularly polarized beam will be published elsewhere.

The linearly polarized radiation was tested on the invar alloy $\text{Fe}_{65}\text{Ni}_{35}$ measured in the external field 1T. Spectra with two orthogonal linear polarizations together with the measurement using unpolarized beam are presented in Fig. 7. Apparently in the spectrum for p state of the beam, polarization lines 2 and 5 are suppressed, while for $-p$ the lines 1, 3, 4, 6 are suppressed. This shows how easy separation of $\Delta m = (1, -1)$ and $\Delta m = 0$ transitions is by use of a linearly polarized beam.

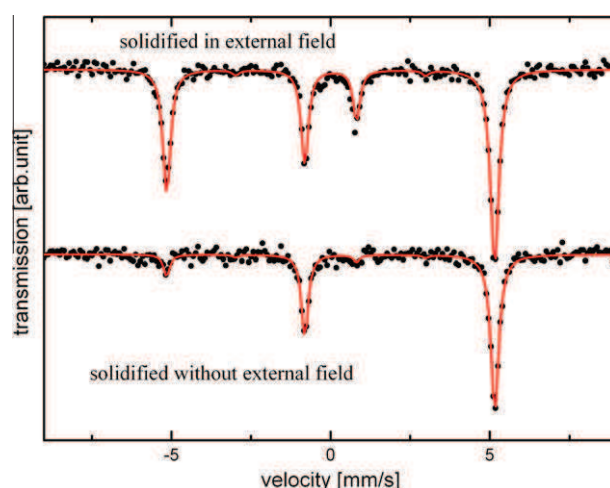


Fig. 6. Mössbauer spectra of $\alpha\text{-Fe}$ foil measured by beam filtered by filters of the same thickness and prepared in two different way: one solidified in the external field and in zero field.

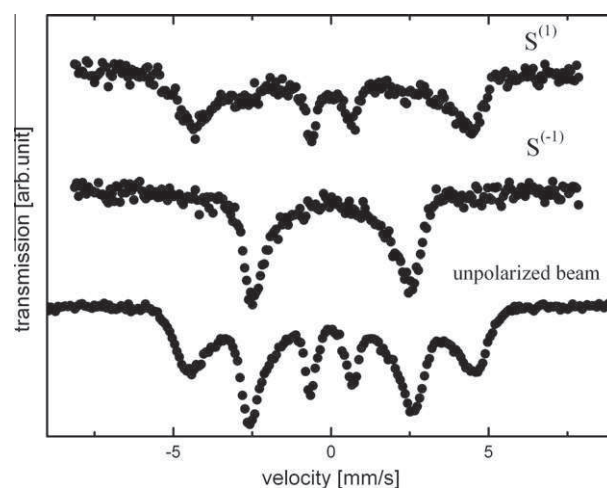


Fig. 7. Mössbauer spectra of $\text{Fe}_{65}\text{Ni}_{35}$ invar alloy measured with linearly polarized radiation and with unpolarized beam.

6. Conclusion

The paper describes successful construction of the monochromatic, linearly polarized Mössbauer source of 14.4 keV working in a conventional Mössbauer setup at room temperature with single line unpolarized $^{57}\text{Co}:\text{Cr}$. The different methods of preparation of polarizers were tested. It was concluded that the quality of the polarizer strongly depends on the homogeneity of the filter. The latter can be lost during solidification process in the external magnetic field. In that case the better arrangements of the magnetization vectors in the polarizers do not lead to better degree of polarization of the beam because of worse homogeneity of filter.

A useful correlation between polarization degree p and (ARE/BAS) ratio was found. This correlation is of great practical importance since one is able to predict how much intensity is lost when approaching to high polarization degree.

The best degree of polarization achieved in the experiment was equal $92 \pm 8\%$. The monochromatic single line linearly polarized source serves as very effective tool for determination of the texture parameter $\langle \cos^2\varphi \sin^2\theta \rangle$ which give the information about the distribution of m.h.f. vectors in the sample plane. Moreover, the Mössbauer measurements carried out using linearly polarized

source results in remarkably simplified spectra. This in turn helps a lot in interpretation of the magnetic hyperfine field distribution for absorber characterized by broadened and overlapped absorption lines.

Acknowledgement

The work was partially supported by funds allocated for scientific research for the years 2008–2011 as a Research Project NN202172335.

References

- [1] S.S. Hanna, J. Heberle, C. Littlejohn, G.J. Perlow, R.S. Preston, D.H. Vincent, *Phys. Rev. Lett.* 4 (1960) 177.
- [2] H. Fraunfelder, D.E. Nagle, R.D. Taylor, D.R.F. Cochran, W.M. Visscher, *Phys. Rev.* 126 (1962) 1065.
- [3] C.E. Johnson, W. Marshall, G.J. Perlow, *Phys. Rev.* 126 (1962) 1503.
- [4] N. Blum, L. Grodzins, *Phys. Rev.* 136 (1964) A133.
- [5] U. Gonser, R.W. Grant, H. Wiederseich, S. Geller, *Appl. Phys. Lett.* 9 (1966) 18.
- [6] F. Tanczikó, L. Deák, D.L. Nagy, L. Bottyán, *Nucl. Instr. Meth. B* 226 (2004) 461.
- [7] J.P. Stampfel, P.A. Flinn, *Mössbauer Effect Methodol.* 6 (1970) 95.
- [8] K. Szymański, L. Dobrzyński, B. Prus, M.J. Cooper, *Nucl. Instr. Meth. B* 119 (1996) 438.
- [9] J. Jäschke, H.D. Rüter, E. Gerdau, G.V. Smirnov, W. Sturhahn, J. Pollmann, *Nucl. Instr. Meth. B* 155 (1999) 189.
- [10] W. Olszewski, K. Szymański, D. Satuła, L. Dobrzyński, L. Bottyán, F. Tanczikó, *Nucl. Instr. Meth. B* 266 (2008) 3319.
- [11] K. Szymański, D. Satuła, L. Dobrzyński, *Hyp. Int.* 156 (/157) (2004) 21.
- [12] B. Kalska, K. Szymański, L. Dobrzyński, D. Satuła, R. Wäppling, A. Broddefalk, P. Norblad, *Hyp. Int.* 141 (/142) (2002) 161.
- [13] K. Szymański, D. Satuła, L. Dobrzyński, *J. Phys. Condens. Matter* 11 (1999) 881.
- [14] F. Varret, P. Imbert, G. Jehanno, R. Saint-James, *Phys. Stat. Sol.* 27 (1975) K99.
- [15] S. Shtrikman, S. Somekh, *Rev. Sci. Instr.* 40 (1969) 1151.
- [16] R.A. Brand, *Nucl. Instr. Meth. B* 28 (1987) 417.
- [17] H.D. Pfannes, H. Fisher, *Appl. Phys.* 13 (1977) 317.
- [18] H.D. Pfannes, R.M. Paniago, *Hyp. Int.* 71 (1992) 1499.
- [19] J.M. Greneche, M. Henry, F. Varret, *J. Magn. Magn. Mater.* 26 (1982) 153.
- [20] J.M. Greneche, F. Varret, *J. Phys.* 43 (1982) L-233.
- [21] K. Brzózka, P. Sovák, B. Gôrka, T. Szumiata, M. Gawroński, *Acta Phys. Polonica A* 119 (2011) 33.